Universität Stuttgart

Institut für Wasser- und Umweltsystemmodellierung

Mitteilungen

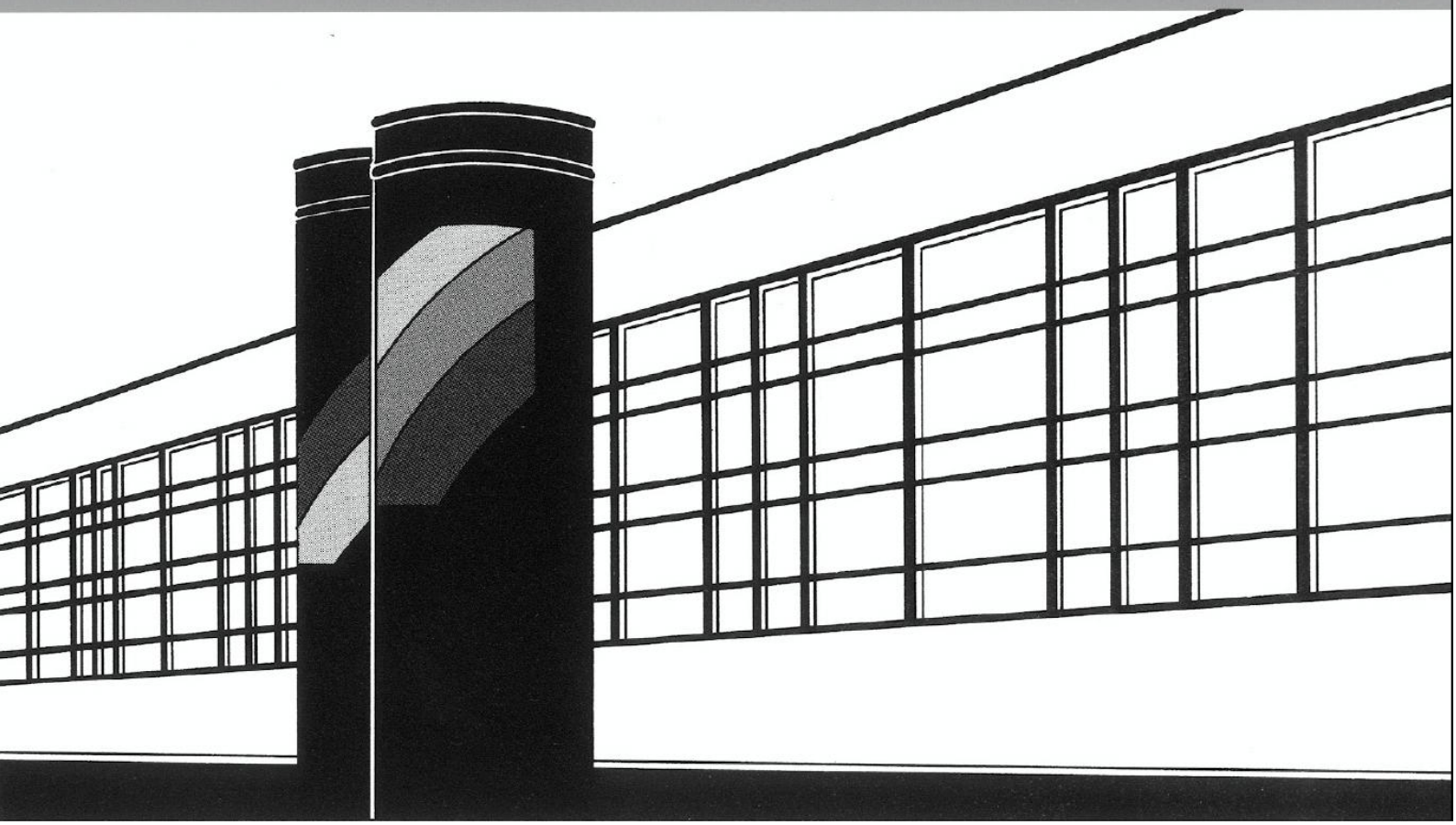

Heft 259 Thomas Fetzer

Coupled Free and Porous-Medium Flow Processes Affected by Turbulence and Roughness – Models, Concepts and Analysis

Coupled Free and Porous-Medium Flow Processes Affected by Turbulence and Roughness
–
Models, Concepts and Analysis

von der Fakultät Bau- und Umweltingenieurwissenschaften der Universität Stuttgart zur Erlangung der Würde eines Doktor-Ingenieurs (Dr.-Ing.) genehmigte Abhandlung

vorgelegt von

Thomas Fetzer

aus Tübingen, Deutschland

Hauptberichter:	Prof. Dr.-Ing. Rainer Helmig
Mitberichter:	Prof. Dr. Patrick Jenny
	Prof. Kathleen M. Smits, PhD
	Prof. Dr. Jan Vanderborght

Tag der mündlichen Prüfung: 20. Februar 2018

Institut für Wasser- und Umweltsystemmodellierung
der Universität Stuttgart
2018

Heft 259

Coupled Free and Porous-Medium Flow Processes Affected by Turbulence and Roughness – Models, Concepts and Analysis

von
Dr.-Ing.
Thomas Fetzer

Eigenverlag des Instituts für Wasser- und Umweltsystemmodellierung
der Universität Stuttgart

D93 Coupled Free and Porous-Medium Flow Processes Affected by Turbulence and Roughness – Models, Concepts and Analysis

Bibliografische Information der Deutschen Nationalbibliothek
Die Deutsche Nationalbibliothek verzeichnet diese Publikation in der Deutschen Nationalbibliografie; detaillierte bibliografische Daten sind im Internet über http://www.d-nb.de abrufbar

Fetzer, Thomas:
Coupled Free and Porous-Medium Flow Processes Affected by Turbulence and Roughness – Models, Concepts and Analysis, Universität Stuttgart. - Stuttgart: Institut für Wasser- und Umweltsystemmodellierung, 2018

(Mitteilungen Institut für Wasser- und Umweltsystemmodellierung, Universität Stuttgart: H. 259)
Zugl.: Stuttgart, Univ., Diss., 2018
ISBN 978-3-942036-63-4

NE: Institut für Wasser- und Umweltsystemmodellierung <Stuttgart>: Mitteilungen

Herausgegeben 2018 vom Eigenverlag des Instituts für Wasser- und Umweltsystem-modellierung

Druck: DCC Kästl e.K., Ostfildern

Danksagung

Ich möchte hier all denen danken, die mich auf dem Weg zur Fertigstellung dieser Arbeit unterstützt haben. Zuerst danke ich meiner wunderbaren Frau Anja für ihr geduldiges Zuhören und ihre Motivation. Auch meinen Eltern und Schwiegereltern danke ich für ihre Unterstützung, insbesondere der liebevollen Betreuung unserer Tochter Magdalena in meiner intensiven Schreibphase.
Rainer Helmig hat mich mit seinem ansteckenden, endlosen Enthusiasmus und Optimismus immer wieder aufs Neue motiviert. Seine fachliche Kompetenz zusammen mit seiner menschlichen, zugewandten Art die Arbeitsgruppe zu führen, haben mich geprägt und beeindruckt. Darüber hinaus danke ich ihm für unterhaltsame S-Bahn Fahrten und den ein oder anderen Tratsch am Marktstand. Thanks to Kate Smits, Jan Vanderborght and Patrick Jenny for writing the reports, the inspiring discussions and their willingness to share knowledge and experimental data. I want to thank Kate Smits, Tissa Illangasekare and Andrew Trautz for hosting me in Golden and the great time I have had there.
Maria Costa, Stefanie Siegert, Prudence Lawday, Michelle Hartnick und David Werner danke ich für ihre Hilfe bei bürokratischen Hürden und Computerproblemen. Den Mitentwicklern von DuMu$^{\mathrm{x}}$, unter der Regie von Bernd Flemisch, danke ich für die produktive Zusammenarbeit. Für die großartige, entspannte Arbeitsatmosphäre am LH^2 bedanke ich mich bei allen meinen Kollegen. Mit ihnen konnte ich jederzeit alle fachlichen Fragen diskutieren und bei ihnen wertvolle Tipps einholen. In diesem Sinne danke ich besonders meinen Zimmerkollegen Johannes Hommel, Christoph Grüninger, Dennis Gläser, Martin Beck und Martin Schneider. Christoph Grüninger bin ich dankbar, dass er als Mitentwickler der Kopplung und bei gemeinsamen Joggingrunden ein treuer Wegbegleiter war. Durch ihn wurden meine Fähigkeiten der Softwareentwicklung immens bereichert. Nathanael und Benedikt danke ich für die vielen Gespräche und Ablenkung vom Promotionsalltag bei den gemeinsamen Essenspausen.
Der DFG danke ich für die finanzielle Unterstützung verschiedener Projekte von denen ich profitieren durfte: das Graduiertenkolleg NUPUS (IRTG 1398), die internationale Forschergruppe MUSIS (FOR 1083) und das Einzelprojekt SAtIn.

Contents

List of Figures

List of Tables

Nomenclature

Greek Symbols

α_ω	k-ω model constant	–
α_{BJ}	Beavers-Joseph coefficient	–
α_{VG}	Van Genuchten coefficient	$^1/_{\mathrm{Pa}}$
β	Thermal conductivity lumping coefficient	–
β_ω	k-ω model constant	–
β_{BJS}	Auxiliary condition for the Beavers-Joseph-Saffman condition	–
β_{k}	k-ω model constant	–
χ	Spalart-Allmaras model function	–
δ	Boundary layer thickness	m
Δt	Temporal discretization width	s
$\Delta x, \Delta y, \Delta z$	Spatial discretization width	m
ε	Dissipation	$^{\mathrm{m}^2}/_{\mathrm{s}^3}$
$\tilde{\varepsilon}$	Dissipation (in Low-Re k-ε model)	$^{\mathrm{m}^2}/_{\mathrm{s}^3}$
κ	Karman constant ($\kappa \approx 0.41$)	–
λ	Thermal conductivity	$^{\mathrm{W}}/_{\mathrm{m\,K}}$
λ_{BC}	Brooks-Corey coefficient	–
μ	Dynamic viscosity	$\mathrm{Pa\,s}$
ν	Kinematic viscosity	$^{\mathrm{m}^2}/_{\mathrm{s}}$
Ω	Domain	–
ω	Turbulence frequency	$^1/_{\mathrm{s}}$
$\tilde{\omega}$	k-ω model function	$^1/_{\mathrm{s}}$
ϕ	Porosity	–

φ	Primary variable/unknown	
ϱ	Density	$\mathrm{kg/m^3}$
$\varrho_{\mathrm{g}}^{\mathrm{w}}$	Water vapor concentration	$\mathrm{kg/m^3}$
ϱ_{mol}	Molar density	$\mathrm{mol/m^3}$
σ	Surface tension	$\mathrm{mN/m}$
σ_ε	k-ε and Low-Re k-ε model constant	–
$\sigma_{\tilde{\nu}}$	Spalart-Allmaras model constant	–
σ_{d}	k-ω model function	–
σ_{k}	Two-equation turbulence model constant	–
τ	Tortuosity factor	–
Θ	Contact angle	$^\circ$
θ	Water content	–

Latin Symbols

A	Amplitude height	m
a	Thermal diffusivity	$\mathrm{m^2/s}$
B	Log law parameter for rough surfaces	–
C	Log law integration constant ($C = 5$ to 5.5)	–
$C_{1\varepsilon}$	k-ε model constant	–
$C_{1\tilde{\varepsilon}}$	Low-Re k-ε model constant	–
$C_{2\varepsilon}$	k-ε model constant	–
$C_{2\tilde{\varepsilon}}$	Low-Re k-ε model constant	–
C_μ	Two-equation turbulence model constant	–
C_{F}	Forchheimer drag coefficient	–
c_{b1}	Spalart-Allmaras model constant	–
c_{b2}	Spalart-Allmaras model constant	–
c_{f}	Skin friction coefficient	–
c_{p}	Specific heat capacity at constant pressure	$\mathrm{J/kg\,K}$
c_{v1}	Spalart-Allmaras model constant	–
c_{w1}	Spalart-Allmaras model constant	–
c_{w2}	Spalart-Allmaras model constant	–

c_{w3}	Spalart-Allmaras model constant	–
D	Diffusion coefficient	m^2/s
D_ε	Low-Re k-ε damping function	m^2/s^3
D_{disp}	Dispersion coefficient	m^2/s
d	Diameter	m
d_{50}	Median sand grain diameter	m
d_{hy}	Hydraulic diameter	m
E	Log law integration constant ($E = 9.793$)	–
E_k	Low-Re k-ε damping function	m^2/s^4
e	Evaporation rate	mm/d
F	Baldwin-Lomax model function	m/s
F_{kleb}	Baldwin-Lomax model function	–
F_{wake}	Baldwin-Lomax model function	m^2/s
f	Darcy friction factor	–
f_1	Low-Re k-ε model constant	–
f_2	Low-Re k-ε model constant	–
f_μ	Low-Re k-ε damping function	–
f_{v1}	Spalart-Allmaras model function	–
f_{v2}	Spalart-Allmaras model function	–
f_w	Spalart-Allmaras model function	–
g	Grid grading factor	–
g_w	Spalart-Allmaras model function	–
H	Henry coefficient	Pa
h	Specific enthalpy	J/kg
I	Turbulence intensity	–
J	Leverett J-function	–
K	Intrinsic permeability	m^2
k	Turbulent kinetic energy	m^2/s^2
k_J	Johansen coefficient	–
k_r	Relative permeability	–
k_s	Sand grain roughness	m

k_s^+	Dimensionless sand grain roughness	–
ℓ	Turbulent length scale	m
l_mix	Mixing length	m
M	Molar mass	$^\mathrm{kg}/_\mathrm{mol}$
m_VG	Van Genuchten coefficient ($m_\mathrm{VG} = 1 - {}^1/_{n_\mathrm{VG}}$)	–
MC	Moisture content	–
n	Number of cells	–
n_H	Haaland parameter	–
n_mole	Number of moles	–
n_VG	Van Genuchten coefficient	–
$\mathcal{P}$	P-function	–
P	Period length	m
p	Pressure	Pa
p_c	Capillary pressure	Pa
p_d	Entry pressure	Pa
p_g^κ	Partial pressure	Pa
p_sat^κ	Saturated vapor pressure	Pa
Pr	Prandtl number	–
q^w	Total water mass flux	$^\mathrm{kg}/_{\mathrm{m}^2\mathrm{s}}$
R	Universal gas constant ($R \approx 8.3146\,{}^\mathrm{J}/_\mathrm{mol\,K}$)	$^\mathrm{J}/_\mathrm{mol\,K}$
R_α	Specific gas constant	$^\mathrm{J}/_\mathrm{kg\,K}$
r	Transfer resistance	$^\mathrm{s}/_\mathrm{m}$
r_w	Spalart-Allmaras model function	–
Re	Reynolds number	–
RH	Relative humidity	–
$\mathcal{S}$	S-function	–
S	Saturation	–
S_r	Residual saturation	–
$\tilde{S}$	Modified effective strain rate	$^1/_\mathrm{s}$
Sc	Schmidt number	–
T	Temperature	K

t	Time	s
u	Specific internal energy	$\mathrm{J/kg}$
u^+	Dimensionless velocity	–
u_τ	Wall friction velocity	$\mathrm{m/s}$
V	Volume	m^3
X	Mass fraction	–
x	Mole fraction	–
y	Wall distance	m
y^+	Dimensionless wall distance	–
$y^+_{\mathrm{threshold}}$	Threshold for using the law of the wall	–

Vectors

$\boldsymbol{\omega}$	Vorticity	$\mathrm{1/s}$
$\boldsymbol{f}$	Conductive energy flux	$\mathrm{J/m^2 s}$
$\boldsymbol{g}$	Gravitational acceleration: $\boldsymbol{g} = (0, \dots, -9.81\,\mathrm{m/s^2})^\intercal$	$\mathrm{m/s^2}$
$\boldsymbol{j}_{\mathrm{mass}}$	Diffusive mass flux	$\mathrm{kg/m^2 s}$
$\boldsymbol{j}_{\mathrm{mol}}$	Diffusive molar flux	$\mathrm{mol/m^2 s}$
$\boldsymbol{n}$	Normal vector	–
$\boldsymbol{t}$	Tangential vector	–
$\boldsymbol{v}$	Velocity: $\boldsymbol{v} = (v_\mathrm{x}, v_\mathrm{y}, \dots)^\intercal$	$\mathrm{m/s}$
$\boldsymbol{x}$	Space coordinates: $\boldsymbol{x} = (x, y, \dots)^\intercal$	m

Tensors

$\boldsymbol{\Omega}$	Rotation rate	$\mathrm{1/s}$
$\boldsymbol{\tau}$	Shear stress	$\mathrm{kg/s^2 m}$
$\mathbf{I}$	Identity matrix	–
$\mathbf{S}$	Strain rate	$\mathrm{1/s}$

Subscripts

α	Phase index: gas (g), liquid (l), or solid (s)
char	Characteristic

d	Diameter
eff	Effective
fc	Fully coupled
g	Gas phase
l	Liquid phase
max	Maximum
min	Minimum
n	Non-wetting
nom	Nominal
p	Matching point
s	Solid phase
t	Turbulent/eddy
vs	Viscous sublayer
wf	Wall function
w	Wetting

Superscripts

∞	Free stream
κ	Component index: air (a) or water (w)
$\bar{a}$	Temporal-average of quantity 'a'
a'	Fluctuation of quantity 'a'
a	Air component
bl	Boundary layer
c	Cell
eq	Equilibrium
if	Interface
pm	Porous medium
ref	Reference
w	Water component

Abstract

Understanding the coupled exchange processes between a free flow and flow through a porous medium is important for a wide spectrum of applications in many fields of research. Possible applications arise from environmental science, medical science, aerospace engineering, civil engineering, process engineering, energy supply, safety issues, and technical design problems. A common feature in all these applications is the interface between the free-flow and the porous-medium flow domain. In the vicinity of this interface, processes in both domains control the coupled exchange fluxes. Therefore, modeling the interface region is a key challenge and requires the consideration of various processes on different scales with varying physical complexity, and thus the application of adequate modeling strategies.

First, understanding the relevant processes and the key properties in the free flow (e.g. turbulence, boundary layer formation), in the porous medium (e.g. capillary flow, thermal conduction), and at their common interface (e.g. roughness) is important for the analysis of resulting coupled exchange fluxes. Second, bridging scales by properly accounting for effects occurring on smaller spatial and temporal scales is important for an efficient simulation and accurate results. Third, for the numerical modeling, numerical stable and mass conservative schemes are required. In addition, inside the two domains the relevant scales and processes are different and a sufficiently high resolution in interface-normal direction is required for a good approximation of the exchange fluxes. Fourth, comparing numerical simulations with laboratory experiments is difficult due the coupled interplay of mass, momentum, and energy transport composed of advective and diffusive transport mechanisms which occur in a small area around the interface.

The focus of this thesis is on improving the model concept for multi-phase porous-medium flow coupled to a turbulent free flow, both including multi-component and energy transport. It is aimed to develop an REV-scale two-domain concept which can handle two models in two separated subdomains and to couple them via appropriate coupling conditions at a sharp interface. One goal is to perform this coupling without introducing additional degrees of freedom on the interface. An existing porous-medium model, using the equations by Darcy or Forchheimer and discretized with the cell-centered finite volume method, is coupled to a (Reynolds-Averaged) Navier-Stokes model discretized with a marker-and-cell scheme (also known as staggered grid), cf. Grüninger et al. [2017]. In this framework, eddy-viscosity based turbulence models of different complexity are presented and implemented. In addition, simplifications of the coupling conditions are introduced and discussed. The implementation

is performed using the software modules DuMu^x and DUNE. A fully implicit Euler method is used and the resulting monolithic matrix is solved with a Newton method and the help of a direct linear solver.

Numerical results for the analysis of different model concepts, parameters, and setups are presented. In a first step, the developed model concepts and coupling methods are compared to a previous work which uses the box method for spatial discretization, cf. Mosthaf [2014]. The results for both discretization methods are in a good agreement. The investigated turbulence models produce differences in stage-I evaporation rates of about $\pm 12\%$ compared to their mean rate. Under specific conditions, simplifications of the free-flow model concept can speed-up the simulations by preserving the quality of the results. The analyses of the turbulent Schmidt number, the turbulent Prandtl number, and the Beavers-Joseph coefficient show an influence of up to $+10\%$ on stage-I evaporation rates when each value is varied from unity to other physical meaningful values.
In a second study, the model results are compared to different evaporation experiments from the literature and show a good qualitative and quantitative agreement. Most difficulties are observed in reproducing the temperature evolution over time, or the transition from stage-I to stage-II evaporation. The results show that the model predictions are sensitive to the boundary conditions, the considered model dimension, and the porous-medium properties.
Finally, the effect of three different kinds of roughness is analyzed: heterogeneities, roughness resulting from the sand-grains and from porous obstacles. The roughness of the porous medium has a strong influence on the entire evaporation process and may add additional stages to the typical evaporation stages known from flat and homogeneous media.
Based on the previous analyses and with respect to the research hypotheses, the following conclusions are drawn:

Discretizations and Interface Model Concepts The discretization around the interface is important. If degrees of freedom are located on the interface, grid-independent stage-I evaporation rates can be shown for a minimum discretization of $\Delta y^+ < 5$ at the interface. For mainly interface-parallel flow, the proposed coupling methods without additional degrees of freedom on the interface converge against the same results but with a stronger restriction: $\Delta y^+ < 1$. For flow normal toward a porous medium with multiple mobile phases, all methods produce different results, because of the different ways to account for the phases' resistance to flow.

Turbulence Models and Simplifications Compared to the fully-coupled model concept, all presented simplifications are shown to speed-up the simulation. Simplifying the free flow

is possible, e.g. by setting one-dimensional models as boundary conditions for the porous medium or by calculating mass and energy transport on a given flow field without feedback on the momentum transport. Wall functions for the k-ε model are especially helpful for larger setups. Further, the choice of the turbulence model affects the predicted stage-I evaporation rates.

Processes and Properties in Vicinity of the Interface The influence of the turbulent Prandtl number and the turbulent Schmidt number on the stage-I evaporation rate is in a similar range as the effect of the different turbulence models. The effect of the Beavers-Joseph coefficient is minor. The comparison of simulation results with data from various experiments and the case of a sharp heterogeneity without conductive energy transfer indicate the importance of the energy transport inside the porous medium, but also across the porous-medium free-flow interface or the insulation of the porous medium. A model which includes the sand-grain roughness of an impermeable surface, is tested for its usage in the application of evaporation through a permeable interface. Its influence on the stage-I evaporation rate only depends on the dimensionless sand-grain roughness length k_s^+. Finally, different porous obstacles are analyzed. Any change to the flat surface increases the stage-I evaporation rate, but also leads to a shorter duration of stage-I. The area which is available for free-flow porous-medium exchange inside one cavity between two porous obstacles has a distinct influence on the stage-II evaporation rate.

Zusammenfassung

Für ein breites Spektrum an Anwendungen aus vielen Forschungsgebieten ist es wichtig, die gekoppelten Austauschprozesse zwischen einer freien Strömung und einer Strömung durch ein poröses Medium zu verstehen. Mögliche Anwendungen finden sich in Umweltwissenschaften, Medizin, Luft- und Raumfahrttechnik, Bauingenieurwesen, Verfahrenstechnik, Energieversorgung, Sicherheitsaspekten oder Fragen des technischen Designs wieder. Eine Gemeinsamkeit all dieser Anwendungen ist die Schnittstelle des Gebiets der freien Strömung mit dem Gebiet der porösen Strömung (von hier an *Interface*). In unmittelbarer Nähe dieses Interfaces kontrollieren Prozesse in beiden Gebieten die gekoppelten Austauschflüsse; deshalb ist die Modellierung der Interface-Region eine der Hauptherausforderungen und erfordert die Berücksichtigung von unterschiedlichen Prozessen auf unterschiedlichen Skalen und mit unterschiedlicher physikalischer Komplexität und damit auch die Anwendung von passenden Modellierungsstrategien.

Zuerst gilt es, die relevanten Prozesse und Eigenschaften in der freien Strömung (z. B. Turbulenz, Grenzschichtentwicklung), im porösen Medium (z. B. kapillarer Fluss, thermische Leitfähigkeit) und an dem gemeinsamen Interface (z. B. Rauigkeit) zu verstehen, um die resultierenden Austauschflüsse zu analysieren. Zweitens ist es wichtig, die unterschiedlichen Skalen zu überbrücken um genaue Ergebnisse zu erzielen und die Simulationen effizient durchzuführen. Hierfür müssen Effekte auf kleineren örtlichen und zeitlichen Skalen entsprechend integriert werden. Drittens sind für das numerische Modellieren numerisch stabile und massenerhaltende Methoden erforderlich. Darüber hinaus sind die relevanten Skalen und Prozesse in den beiden Gebieten unterschiedlich und eine entsprechend hohe Auflösung der Richtung normal zum Interface ist notwendig, um eine gute Annäherung der Austauschflüsse sicherzustellen. Zuletzt bleibt die Schwierigkeit, numerische Simulationen mit Laborexperimenten zu vergleichen, da das gekoppelte Zusammenspiel von Masse-, Impuls-, und Energie-Transport, bestehend aus advektiven und diffusiven Transportmechanismen, in einem sehr kleinen Bereich um das Interface stattfindet.

Das Hauptaugenmerk dieser Arbeit liegt auf der Verbesserung des Modellkonzeptes für eine poröse Mehrphasenströmung, die an eine turbulente freie Strömung gekoppelt ist; beide Strömungen berücksichtigen den Transport mehrerer Komponenten und der Energie. Ein REV-skaliger Zwei-Gebiets-Ansatz, der zwei Modelle in zwei getrennten Teilgebieten berücksichtigen kann, wird angestrebt. Diese beiden Teilgebiete sollen über entsprechende Bedingungen an einem gemeinsamen, scharfen Interface gekoppelt werden. Ein Ziel ist es, diese

Kopplung umzusetzen ohne zusätzliche Freiheitsgrade auf dem Interface einzuführen. Ein bestehendes Modell des porösen Mediums, basierend auf der Darcy oder der Forchheimer Gleichung und mit der zell-zentrierten Finiten-Volumen-Methode diskretisiert, wird mit einem (Reynolds-gemittelten) Navier-Stokes Modell, diskretisiert mit der Marker-and-Cell-Methode (auch bekannt als verschobenes Gitter), gekoppelt, siehe Grüninger et al. [2017]. In diesem Rahmen werden unterschiedlich komplexe Wirbelviskosität-Turbulenzmodelle vorgestellt und implementiert. Darüber hinaus werden Vereinfachungen der Kopplungsbedingungen eingeführt und diskutiert. Die Implementierung findet in den Software-Modulen DuMu$^{\text{x}}$ und DUNE statt. Es wird die voll-implizite Euler-Methode benutzt und die resultierende, monolithische Matrix wird mit der Newton-Methode und mit Hilfe eines direkten linearen Lösers gelöst.

Mit den Ergebnissen numerischer Simulationen werden verschiedene Modellkonzepte, Parameter und Aufbauten untersucht. Im ersten Schritt werden die entwickelten Modellkonzepte und Kopplungsmethoden mit einer vorherigen Arbeit verglichen, die die box-Methode für die örtliche Diskretisierung benutzt, siehe Mosthaf [2014]. Die Ergebnisse beider Diskretisierungsmethoden sind in guter Übereinstimmung. Die Verdunstungsraten der implementierten Turbulenzmodelle weichen im ersten Abschnitt um bis zu $\pm 12\%$ von deren Mittel ab. Unter bestimmten Voraussetzungen können, bei gleichbleibender Qualität der Ergebnisse, vereinfachte Modellkonzepte für die freie Strömung die Simulationen beschleunigen. In einer Parameterstudie wird der Einfluss der turbulenten Schmidt-Zahl, der turbulenten Prandtl-Zahl und des Beavers-Joseph Koeffizienten analysiert. Eine Variation dieser Parameter von eins auf andere physikalisch sinnvolle Werte ergibt eine Veränderung von bis zu $+10\%$ auf die Verdunstungsraten im ersten Abschnitt.
In einer zweiten Studie werden die Modellergebnisse mit verschiedenen Verdunstungsexperimenten aus der Literatur verglichen und zeigen eine gute qualitative und quantitative Übereinstimmung. Die größten Schwierigkeiten werden bei dem Abbilden der zeitlichen Temperaturverläufe und dem Übergang zwischen dem ersten und dem zweiten Verdunstungsabschnitt beobachtet. Die Ergebnisse zeigen, dass die Modellvorhersagen sehr sensitiv bezüglich der Randbedingungen, der berücksichtigten Modelldimensionen und der Eigenschaften des porösen Mediums sind.
Zum Abschluss wird der Effekt von drei unterschiedlichen Arten von Rauheit analysiert: Heterogenitäten, Sandkornrauheit und poröse Hindernisse. Die Rauheit eines porösen Mediums hat einen starken Einfluss auf das gesamte Verdunstungsverhalten und kann den typischen Verdunstungsabschnitten, die von flachen und homogenen Medien bekannt sind, zusätzliche Abschnitte hinzufügen.
Basierend auf diesen Analysen und in Bezug auf die Forschungshypothesen, werden folgende Schlussfolgerungen gezogen:

Diskretisierungen und Modellkonzepte des Interfaces Die Diskretisierung am Interface zwischen dem porösem Medium und der freien Strömung ist wichtig. Falls Freiheitsgrade auf dem Interface vorhanden sind, kann gezeigt werden, dass die Verdunstungsraten im ersten Abschnitt für eine minimale Diskretisierungsweite von $\Delta y^+ < 5$ gitterunabhängig werden. Die Kopplungsmethoden ohne zusätzliche Freiheitsgrade am Interface konvergieren gegen die gleichen Ergebnisse, für den Fall einer interface-parallelen Strömung, erfordern aber mit $\Delta y^+ < 1$ größere Einschränkungen. Für eine Strömung die normal zum Interface stattfindet und die mehrere mobile Phasen umfasst zeigen alle Methoden unterschiedliche Ergebnisse, da sie in unterschiedlicher Weise den Fließwiderstand der Phasen berücksichtigen.

Turbulenzmodelle und Vereinfachungen Im Vergleich zum voll-gekoppelten Modellkonzept können für alle vorgestellten Vereinfachungen kürzere Simulationszeiten gezeigt werden. Eine Vereinfachung der freien Strömung ist möglich, indem eindimensionale Modelle als Randbedingungen für das poröse Medium gesetzt werden oder indem der Massen- und Energietransport auf einem vorgegeben Strömungsfeld, ohne Rückkopplung auf den Impulstransport, gerechnet wird. Eine Vereinfachung des k-ε Modells mit Wandfunktionen ist besonders für größere Szenarien hilfreich. Darüber hinaus beeinflusst das gewählte Turbulenzmodell die Verdunstungsraten im ersten Abschnitt.

Prozesse und Eigenschaften der interface-nahen Region Der Einfluss der turbulenten Prandtl-Zahl und der turbulenten Schmidt-Zahl auf die Verdunstungsraten im ersten Abschnitt ist vergleichbar mit dem der unterschiedlichen Turbulenzmodelle. Der Einfluss des Beavers-Joseph Koeffizienten ist geringer. Der Vergleich von Simulationsergebnissen mit verschiedenen Experimenten, aber auch Ergebnisse für den Fall eines porösen Mediums mit einer scharfen Heterogenität, die keinen konduktiven Energietransfer zulässt, lassen auf die Wichtigkeit des Energietransportes schließen. Dies umschließt den Energietransport innerhalb des porösen Mediums, über das Interface mit der freien Strömung und die Isolation des porösen Mediums. Die Anwendbarkeit eines Modells, das die Sandkornrauheit auf einer undurchlässigen Oberfläche beschreibt, wird bezüglich des Massentransports über ein durchlässiges Interface getestet. Der Einfluss auf die Verdunstungsraten des ersten Abschnitts beruht allein auf der dimensionslosen Sandkornrauheitslänge k_s^+. Zum Abschluss werden die Auswirkungen von porösen Hindernissen analysiert. Jegliche Änderung an der flachen Oberfläche erhöht die Verdunstungsraten im ersten Abschnitt, führt aber auch zu einer kürzeren Dauer des ersten Abschnitts. Die Fläche des Interfaces, das für den Austausch zwischen der freien und der porösen Strömung zwischen zwei porösen Hindernissen zur Verfügung steht, hat einen ausgeprägten Einfluss auf die Verdunstungsraten im zweiten Abschnitt.

1 Introduction

Understanding the coupled exchange processes between a free flow and flow through a porous medium is important for a wide spectrum of applications in many fields of research. Possible applications arise from *environmental science* [Das et al., 2002, Sophocleous, 2002, Ren and Packman, 2005, Furman, 2008, Davarzani et al., 2014, Mosthaf et al., 2014, Jambhekar et al., 2016, Broecker et al., 2018], *medical science* [Discacciati and Quarteroni, 2009, Baber et al., 2016], *aerospace engineering* [Dahmen et al., 2014, Chen et al., 2016], *civil engineering* [Buccolieri et al., 2009, Defraeye, 2011, Defraeye et al., 2012b, Belleghem et al., 2014], *process engineering* [Nassehi, 1998, Verboven et al., 2006, Targui and Kahalerras, 2008], *energy supply* [Salinger et al., 1994, Gurau et al., 2008, Baber et al., 2016, Suga, 2016], *safety issues* [Das et al., 2001, Oldenburg and Unger, 2004, Smits et al., 2013, Masson et al., 2016], or *technical and design problems* [Iliev and Laptev, 2004, Cimolin and Discacciati, 2013]. Modeling these applications requires the consideration of various processes on different scales with varying physical complexity, and thus the application of adequate modeling strategies. Tab. 1.1 gives an application-oriented overview on studies modeling coupled porous-medium free-flow problems and the complexity of the models used therein. A common feature in all these applications is the interface between the free-flow and the porous-medium flow domain. In the vicinity of this interface, processes in both domains control the coupled interactions and exchange processes. Therefore, modeling the interface region is a key challenge and it is demanding for various reasons.

First, *understanding* the relevant processes and the key properties in the free flow (e.g. turbulence, boundary layer formation, buoyancy, radiation), in the porous medium (e.g. capillary flow, preferential transport, thermal conduction, turbulent pumping, vaporization/condensation), and at their common interface (e.g. roughness, slip condition) is important for the interpretation and the analysis of resulting coupled exchange fluxes, see Fig. 1.1.

Second, *bridging scales* by properly accounting for effects occurring on smaller scales, a so-called upscaling, is important for an efficient simulation and accurate results. This upscaling has to be performed for both domains and the interface. For example, upscaling is necessary for simulating larger-scale hazards such as the evaporation-driven soil salinization for

motivation/application	publications, e.g.	multiple mobile phases	multiple components	non-isothermal	turbulence	experimental data	mechanics/solid precipitation	reactions	local non-equilibrium
CO_2 leakage	Oldenburg and Unger [2004]	●	●	○	●	○	○	○	○
cooling in helmets	Cimolin and Discacciati [2013]	○	○	○	○	○	○	○	○
cooling of food	Verboven et al. [2006]	○	○	●	●	○	○	○	●
cooling of rockets	Dahmen et al. [2014]	○	●	●	●	●	○	○	○
drying of porous material	Defraeye et al. [2012a]	●	●	●	●	○	○	○	○
	Belleghem et al. [2014]	●	●	●	●	●	○	○	○
filtration	Nassehi [1998]	○	○	○	○	○	○	○	○
	Hanspal et al. [2006]	○	○	○	○	●	○	○	○
flow in human bodies	Discacciati and Quarteroni [2009]	○	○	○	○	○	●	○	○
fuel cells	Gurau et al. [2008]	●	●	○	○	○	○	●	●
	Baber et al. [2016]	●	●	●	○	○	○	○	○
heat transfer	Targui and Kahalerras [2008]	○	○	○	●	○	○	○	○
	Nimvari et al. [2012]	○	○	●	●	○	○	○	○
ignition of coal stockpiles	Salinger et al. [1994]	○	●	●	○	○	○	●	○
landmine detection	Das et al. [2001], Smits et al. [2013]								
nuclear waste storage	Masson et al. [2016]	●	●	●	●	○	○	○	○
oil filters	Iliev and Laptev [2004]	○	○	○	○	○	○	○	○
preferential transport	Das et al. [2002]	○	○	○	○	○	○	○	○
river bed interactions	Sophocleous [2002], Ren and Packman [2005], Broecker et al. [2018]								
soil salinization	Jambhekar et al. [2016]	●	●	●	○	●	●	●	○
soil water evaporation	Davarzani et al. [2014]	●	●	●	●	●	○	○	●
	Mosthaf et al. [2014]	●	●	●	●	●	○	○	○
urban air flow	Buccolieri et al. [2009]	○	●	○	●	●	○	○	○
	Defraeye [2011]	●	●	●	●	●	○	○	○

Table 1.1: Applications affected by coupled exchange processes between a porous-medium and a free flow. Publications using coupled porous-medium free-flow numerical models are listed together with their features. Features in the scope of this thesis (•) and beyond (•) are indicated.

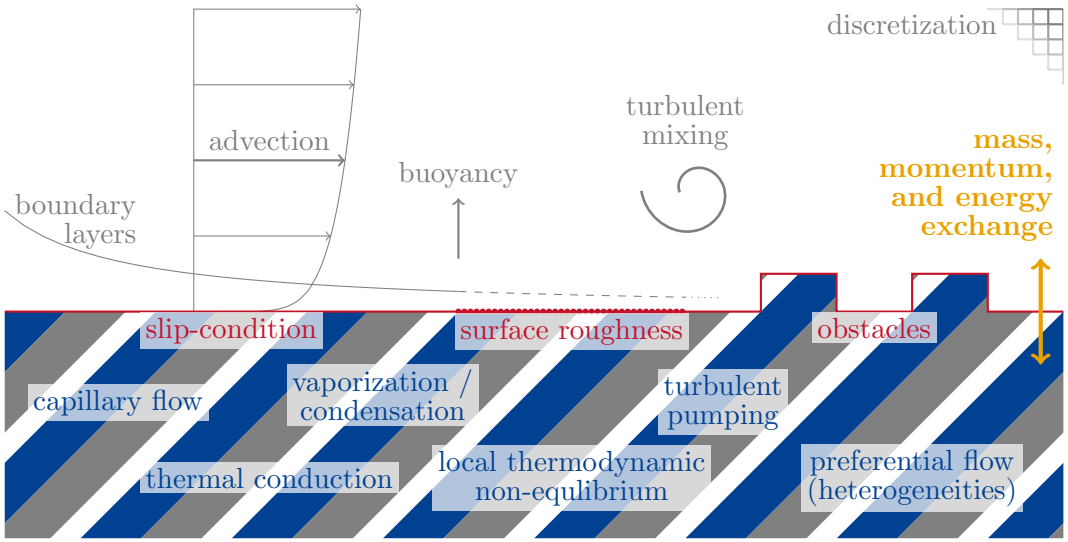

Figure 1.1: Relevant processes, properties, and challenges for coupled porous-medium free-flow problems, based on the example of soil water evaporation, after Fetzer et al. [2016].

agriculture. In such an application, a detailed simulation would exceed the computational capacity.

Third, the *numerical modeling* requires stable and mass-conservative schemes. In most cases, the interest is on the lateral distribution of fluxes and state variables at the interface. For a good approximation of these fluxes and variables, all processes in interface-normal direction have to be described with a sufficiently high resolution. In turn, this oftentimes reduces the lateral resolution, the desired output. In addition, inside the two domains or over time, the relevant scales and processes are different and thus numerical or physical decoupling strategies or adaption techniques might be helpful.

Fourth, *comparing* numerical simulations with laboratory experiments is difficult due to the coupled interplay of mass, momentum, and energy transport composed of advective and diffusive transport mechanisms. Finally, the driving processes occur in a small area around the interface, which affects the quality and quantity of the experimental data.

1.1 Research Goal and Hypotheses

The goal of this thesis is to improve the model concept for coupled porous-medium and free flow problems under turbulent conditions. The influence of properties and processes in vicinity of the interface is analyzed and it is aimed to contribute to the following research hypotheses by considering the application of soil water evaporation.

Hypothesis 1: For modeling coupled porous-medium free flow problems, the discretization and conceptualization of the interface are important. Mosthaf et al. [2014] show that a model concept for coupling free flow and porous-medium flow using the collocated box method [cf. Mosthaf et al., 2011, Baber et al., 2012] can successfully be applied to simulate evaporation fluxes from a porous medium into a mainly parallel free flow.
Nevertheless, some disadvantages and advantages are associated with this concept. First, Baber [2014] shows that this method leads to stable pressure oscillations which may influence the local exchange behavior between the two domains. Therefore, it may not be suited for modeling mainly interface-normal flow. In this case, the pressure at the interface is necessary to induce the flow through the porous medium and thus pressure fluctuations would lead to unphysical lateral fluxes inside the porous medium. Hanspal et al. [2006] also mention the importance of the near-interface discretization for the free flow field. Second, the box discretization scheme reveals difficulties to handle interface-corner points, which are necessary for modeling non-planar surfaces. A major advantage of the box method is that a good approximation of the gradients at the interface, by using information from one subdomain only, is possible. All relevant properties are available at the porous-medium free-flow interface from each side. For cell-centered methods, which are used in this thesis, this is not straightforward, cf. Grüninger [2017].

Hypothesis 2: It is possible to include the effects of turbulence while reducing the overall model complexity. Solving coupled flow and transport processes using one coefficient matrix (monolithic scheme) while including information from the next time level (implicit) is computationally expensive. Numerical techniques, as spatial and temporal decoupling are available and show to reduce the computational cost, e.g. Rybak et al. [2015], Discacciati et al. [2016], Masson et al. [2016]. However, it is also possible to reduce the complexity of the physical model, if some limitations are respected. Compared to the full complex model, the computational and qualitative performance as well as the limitations of models with reduced complexity are explored.
Based on hypothesis 1, the developed full complex model is replaced by simpler approximations of the exchange fluxes: (i) neglecting lateral transport inside the free flow, so that only the one-dimensional interface-normal fluxes have to be described, (ii) neglecting feedbacks of the transported quantities on the momentum transport, and (iii) including wall functions to approximate the exchange fluxes on a coarse mesh.

Hypothesis 3: The properties and processes in the vicinity of the porous-medium free-flow interface strongly affect the resulting exchange fluxes. A common feature of flow along a boundary with different properties than the main flow are the strong gradients which prevail

in the resulting boundary layers. Driven by these strong gradients, the diffusive processes through the boundary layers have a substantial impact on the resulting evaporation fluxes, see Haghighi et al. [2013], Mosthaf et al. [2014]. The relevance of boundary layers for flow and transport phenomena is well known and described in various textbooks, e.g. Schlichting and Gersten [2006], Bird et al. [2007]. The properties of and at the interface will alter the boundary layers and thus the resulting exchange fluxes.
First, the surface of the porous medium may not always be perfectly smooth, roughness can occur on different scales and will have an impact on the model results. Therefore, this study aims at extending the concepts for flat and smooth surfaces and include roughness concepts and highlight the influence of different aspects of roughness: (i) roughness resulting from the sand grains themselves and (ii) roughness as discrete, porous objects. Second, heterogeneities in porous-medium properties will affect the local fluxes across the interface and induce lateral fluxes inside the porous medium. This is especially relevant if these heterogeneities are located at the porous-medium surface. Third, at the porous-medium surface, the coupling of tangential momentum [Beavers and Joseph, 1967] or the concept of a slip-velocity condition [Saffman, 1971] involves a new parameter for which few experimental data is available. It will be discussed, whether these aspects influence flow and transport under turbulent free flow conditions.

1.2 Related Studies

For the numerical modeling of such coupled applications, two main approaches are found in literature, the so-called *one-domain* and *two-domain* approaches.
In one-domain approaches, one set of equations is used in the entire problem area. With a detailed knowledge of the (porous) structure, of the boundary conditions, and high spatial and temporal resolutions, a direct numerical simulation (DNS) is possible. DNS studies are performed for turbulent, single-phase flow above a well-defined pore geometry [e.g. Hahn et al., 2002, Breugem and Boersma, 2005, Kuwata and Suga, 2016], but also above real porous media [e.g. Krafczyk et al., 2015, Fattahi et al., 2016]. A DNS is computationally very expensive, especially when non-isothermal, multi-phase, and multi-component flow processes are included. The one-domain method by Brinkman [1949] uses one set of averaged equations in which the features of both subdomains are integrated. By changing the parameters via a specified region, a gradual transition from one subdomain to the other is achieved. This is usually done for coupling laminar free flow with creeping flow in the porous medium. The author is not aware of Brinkman-like approaches for multi-phase flow and turbulent conditions.
In two-domain approaches, two different sets of equations are used in the two subdomains and

connected by appropriate conditions on an interface with no thickness. This interface can be modeled as a *sharp simple* interface [e.g. Mosthaf et al., 2011] or a *sharp complex* interface, which allows to store mass at the interface, e.g. to account for drop formation [Baber et al., 2016]. Discacciati et al. [2014] propose a decomposition approach using interface conditions at the edges of an *overlap* region. Le Bars and Worster [2006] extend the influence of the free-flow region, via a *viscous transition zone*, into the porous-medium domain. The two-domain approaches offer the opportunity for adapting the model complexity to the needs of each subdomain. The free flow and the porous-medium flow are usually modeled by upscaled models. This study uses an upscaled two-domain approach based on Mosthaf et al. [2014] and Grüninger [2017]. Therefore, the following literature study highlights different aspects of such models and underlines their differences with respect to the free flow, the porous-medium flow, their common interface, and numerical techniques. Finally, the attention is drawn to the application of (soil water) evaporation.

Free Flow The effect of turbulence is usually captured by time-averaged turbulence models, based on the Reynolds-averaged Navier-Stokes equations (RANS). These turbulence models are classified by the number of partial differential equations for the transport of turbulent properties. Available are relatively simple algebraic or zero-equation models [e.g. Baldwin and Lomax, 1978, Cebeci and Smith, 1974], intermediate one-equation models [e.g. Spalart and Allmaras, 1992], and more complex and more general two-equation models [cf. Patel et al., 1985, Bardina et al., 1997]. To avoid the necessity for simulating the entire free flow, boundary layer models can be used to mimic the exchange through a diffusion-dominated boundary layer. The effect of roughness, as roughness elements on an impermeable surface, on the free-flow processes is intensively discussed in fluid dynamics textbooks as Schlichting and Gersten [2006]. Studies on roughness of permeable surfaces are discussed in the next paragraphs.

Mosthaf et al. [2014] compare boundary layer approaches and zero-equation models to simulate soil water evaporation. Kuznetsov and Becker [2004] use a zero-equation model with extensions for surface roughness as proposed in Cebeci [1978] to analyze heat transfer mechanisms. The more complex two-equation turbulence models, like the k-ε, Low-Re k-ε, or k-ω turbulence models, are applied for a dimensionless analysis on heat transfer [Nimvari et al., 2012, Jamarani et al., 2017], heat transfer over rough surfaces [Kuznetsov, 2004], drying problems [Defraeye et al., 2010, Belleghem et al., 2014], cooling applications [Dahmen et al., 2014], or problems including turbulence inside the porous medium [Pedras and de Lemos, 2001, de Lemos, 2009]. For the k-ε model, wall functions are required for a correct modeling of the low-Reynolds flow near the wall. Even for smooth surfaces, these wall functions are found to increase the transfer coefficients and thus the exchange fluxes by up to 50% compared to

other methods [Defraeye, 2011]. Wall-function models which includes a parametrization of roughness are also available, e.g. Blocken et al. [2007]. Flow over discrete porous/non-porous obstacles is a key topic in building physics [e.g. Lien et al., 2004, Buccolieri et al., 2009, Defraeye et al., 2010], but also in limnology [e.g. Broecker et al., 2018], combustion processes [e.g. Suga et al., 2013, Suga, 2016], or heat exchangers [e.g. Targui and Kahalerras, 2008, Nimvari et al., 2012, Jamarani et al., 2017]. Haghighi and Or [2015] perform experiments to analyze how arrangements of bluff non-evaporating obstacles affect the evaporation rate and surface temperature distribution. Sugita and Kishii [2002] conduct experiments with different distributions of evaporating obstacles and analyze the influence of different spacing by simple roughness parametrizations.

Porous Medium The porous medium is normally described with one of the following up-scaled/averaged models: the multi-phase Darcy law [e.g. Mosthaf et al., 2011, Baber et al., 2012, Mosthaf et al., 2014], liquid-phase flow via Richards equation [e.g. Defraeye, 2011], or the Forchheimer extension including inertia effects [e.g. Dahmen et al., 2014]. Nevertheless, two-domain approaches with a pore representation of the porous medium are also available. Beyhaghi et al. [2016] present a method for an isothermal coupling of turbulent free flow to flow and transport in a pore-network model.
Characteristics of coupled exchange fluxes depend on the processes and properties inside the porous medium. The influence of properties of homogeneous porous media on the evaporation behavior is analyzed via numerical [e.g. Mosthaf et al., 2014] and experimental studies [e.g. Shokri and Or, 2011]. Heterogeneities alter the evaporation behavior. Horizontal layers with a coarse structure, so-called mulches, reduce the evaporation by restricting the flow of liquid water [Modaihsh et al., 1985, Diaz et al., 2005, Shokri et al., 2010]. Iliev and Laptev [2004] include anisotropic porous media which promote flow in certain directions. Porous-medium models are oftentimes built on the assumption that locally all processes are in an equilibrium state (local thermodynamic equilibrium). However, the multi-phase effects of evaporation, the small time scale for phase transition, and the associated heat transfer, may indicate that the underlying assumptions for local thermodynamic equilibrium are not always valid. The effects of non-equilibrium models are analyzed for pure porous-medium systems [Smits et al., 2011, Trautz et al., 2015] or including a pseudo free flow, which is a region with a large porosity and permeability [Nuske et al., 2014].

Coupling and Interface Modeling The importance of the porous-medium free-flow interface is known in soil science. For agricultural purposes, tillage is used to modify the interface or surface behavior and thus the evaporation fluxes: Capillary pathways are destroyed, soil portions with different hydraulic properties and water contents are brought to the surface

[Unger and Cassel, 1991], or the increased roughness of the soil surface may influence the net radiation [Potter et al., 1987]. The effect of vegetation is not considered here, even though it plays a huge role in real applications [Shukla and Mintz, 1982].
Only few studies are performed regarding the influence of rough and permeable surfaces, especially in conjunction with flow and transport in the porous medium. Krafczyk et al. [2015] and Kuwata and Suga [2016] use DNS to simulate single-phase flow above a porous bed. Pokrajac and Manes [2009] and Manes et al. [2011] show that the effect of roughness of an impermeable and of a permeable surface is different. At the porous-medium free-flow interface, non-zero tangential velocities may occur as proposed and discussed in Beavers and Joseph [1967], Saffman [1971], Sahraoui and Kaviany [1992], Auriault [2010]. According to references given in Nield [2009], the resulting coefficient depends on the flow direction, Reynolds number, the extend of the free flow domain, and the structure of the porous-medium surface. However, it does neither explicitly include these parameters nor the effects of turbulence, roughness, or the presence of multiple phases. Apart from Beavers et al. [1974], few experimental work is performed on determining this coefficient. The sensitivity of evaporation rates to a slip condition at the interface is analyzed for low velocities [Baber et al., 2012, Davarzani et al., 2014] but not for higher velocities (turbulent conditions). A review on the interface as a hydrodynamic boundary condition for the porous medium can be found in Nield and Bejan [2017, Ch. 1.6] and is intensively discussed in Shavit [2009]. The interface is not only interesting regarding its hydrodynamic properties, but also for mass and energy transport mechanisms. The distribution of evaporating pores at the interface yields compensation mechanisms which allow the porous medium to maintain a high evaporation rate, although its surface is only partially wetted, see Suzuki and Maeda [1968], Schlünder [1988], Haghighi and Or [2015].

Numerical Modeling Techniques A large variety is found when looking at the discretization schemes for two-domain approaches. Finite volume methods using collocated grids [Mosthaf et al., 2011, Baber et al., 2012], pure staggered-grid schemes [Iliev and Laptev, 2004], combined staggered and collocated approaches [Rybak et al., 2015, Masson et al., 2016, Grüninger, 2017], or in combination with finite element methods [Defraeye, 2011, Dahmen et al., 2014] are applied. In addition, spatial [Dahmen et al., 2014, Discacciati et al., 2016, Masson et al., 2016] or temporal decoupling [Rybak et al., 2015] of the two subdomains helps to improve the model performance. A fully implicit monolithic scheme is also used by e.g. Mosthaf et al. [2011], whereas the majority of the other publications applies an explicit scheme. The uniqueness of this work is, that it combines a fully implicit monolithic scheme on an oscillation-free spatial discretization to simulate turbulent free flow coupled to multi-phase flow inside the porous medium.

(Soil Water) Evaporation This thesis focuses on the coupled modeling of soil water evaporation. In this field of research, detailed numerical studies are performed for laminar flow and turbulent flow using simple turbulence models [Mosthaf et al., 2014], laminar flow using dispersion coefficients and local thermodynamic non-equilibrium [Davarzani et al., 2014], and laminar flow including salinization [Jambhekar et al., 2016]. More work is performed on analyzing the influence of evaporation on the soil processes and improving the boundary conditions for the soil water modeling [Schneider-Zapp et al., 2010, Smits et al., 2012, Haghighi et al., 2013, Tang and Riley, 2013].
Also, many experiments are performed to analyze soil water evaporation. Some of these experiments are conducted without a forced free flow to analyze pore-scale effects [Laurindo and Prat, 1998, Belhamri and Fohr, 1996, Assouline et al., 2010, Shahraeeni and Or, 2010, Haghighi et al., 2013] or to analyze processes on the averaged scale [e.g. Schneider-Zapp et al., 2010, Zhang et al., 2015].
Other studies include an atmospheric free flow in a wind tunnel. Shahraeeni et al. [2012] analyze the effect of discrete pores on the evaporation process. Yamanaka et al. [1997] vary the atmospheric boundary conditions and demonstrate the significance of the depth of the evaporating surface. Sugita and Kishii [2002] put their focus on different obstacle arrangements. Experiments with focus on bound water are performed by Lu et al. [2005]. The influence of evaporation from different porous roofing materials on the roof temperature is investigated by Wanphen and Nagano [2009]. Combining experimental and numerical studies to analyze free and porous-medium flow properties is done in Davarzani et al. [2014], Mosthaf et al. [2014]. In Trautz et al. [2015] different numerical models which account for non-equilibrium processes are compared. Trautz [2015] presents various soil water evaporation experiments on different scales and compares them with modeling results from porous-medium and coupled models. Evaporation chambers are examined in Song et al. [2014] or in Aluwihare and Watanabe [2003] under outdoor conditions.
Since a long period, evaporation experiments are carried out in the field. Penman [1948] suggests theoretical estimates for the evaporation rate and compares them with different data sets form all over the world. A review of near-surface wind speeds by McVicar et al. [2012] implies the importance of atmospheric conditions on evaporation. Collecting and interpreting evaporation data sets is still, with improving measurement techniques, an issue in soil science [Vanderborght et al., 2010].

1.3 Structure of the Thesis

This chapter outlines the main motivation and goals of this thesis. Further, it contains a literature review on publications related to this work. Chapter two introduces the relevant

physical definitions and concepts. In the third chapter, the physical models and mathematical equations are explained. The fourth chapter illustrates the numerical models and their implementations. Chapter five presents numerical results for various applications and setups. Finally, chapter six summarizes the thesis and gives an outlook beyond the scope of this work.

2 Fundamentals

This chapter provides the necessary basic definitions and conceptual background for the further understanding of this work. In section 2.1, the fundamental terms are defined and explained. Section 2.2 includes information about modeling equilibrium-based processes. Afterward, in section 2.3, the attention is drawn to material properties. Then, the defining processes and properties of fluid flow (section 2.4), of porous media (section 2.5), and of the interface (section 2.6) are highlighted.

2.1 Basic Definitions

In this section, some basic definitions are given.

2.1.1 Scales

Coupled processes between a free flow and flow in a porous medium occur on different *spatial* and *temporal* scales with varying importance, which will be defined here.

Spatial Scales On the *molecular scale*, the interest is on the interactions between individual molecules of one or more substances, e.g. attraction, collision, and polarity. If many molecules are considered, average quantities can be constructed, e.g. pressure, density, and viscosity. On this *continuum scale*, these quantities are continuous in space. This work is based on continuum-scale considerations.
On the *pore scale*, all information about pore sizes and shapes, the distribution of pores, and the connectivity between pores is available. For experimental and numerical works with real porous media it is challenging to collect this information. Non-destructive measurement technologies like x-ray or neutron tomography are needed to gain insight into the states and processes while running the experiments [Wildenschild and Sheppard, 2013]. Resolving all geometrical details for simulations results in many unknowns and high computational demands [Blunt et al., 2013]. To enable the simulation of more complex problems or larger domains,

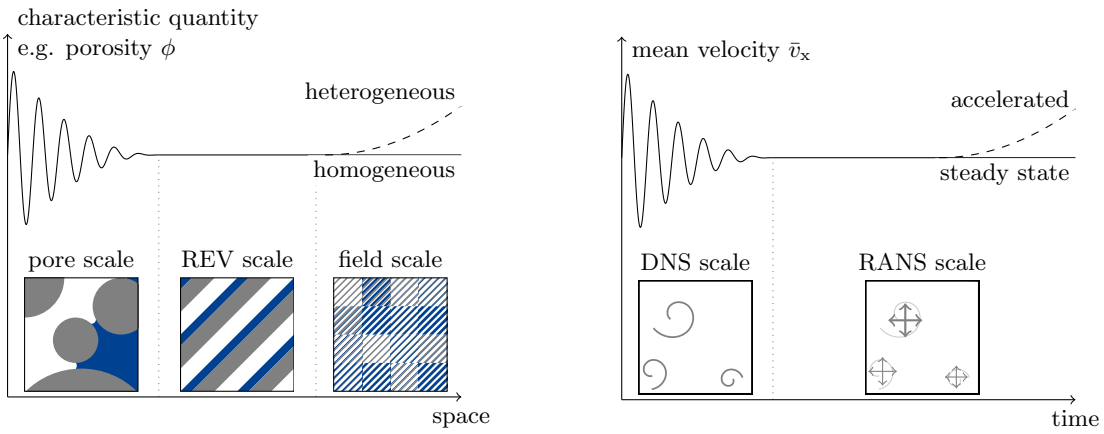

Figure 2.1: Averaging of quantities for the spatial scale in a porous medium (left, after Bear [1988] and Mosthaf [2014]), and the temporal scale in a turbulent free flow (right).

as for the transition from molecular to continuum scale, an averaging is neceassary. Here, it is averaged over several pore volumes with the goal to obtain a *representative elementary volume* (REV). Consequently, this is called the *REV scale*. On this scale, the information about the pores is converted to volume-averaged quantities, as the porosity or the permeability. An REV is achieved, if these characteristic quantities do not change, when changing the size of the averaging volume, see Fig. 2.1 (left). Consequently, the lower and upper limits of the REV size cannot be defined arbitrarily, but are limited by strong variations in the beginning and the risk of averaging over heterogeneous parts of the porous medium [Bear, 1988]. The REV scale typically covers a range of centimeters to meters. For larger domains, ranging from meters to kilometers, REV-scale models are still valid, however, the respective volumes become larger and therefore this is often referred as *field scale*. Modeling on the field scale is predominantly motivated by large-scale applications, like groundwater flow, oil or gas production, geothermal power plants, CO_2 storage, or soil remediation. The additional loss of information caused by large REVs is traded for an efficient and practical model.

Temporal Scales On the one hand, the temporal scale is important for the porous medium to ensure local thermodynamic equilibrium. The assumption of local thermodynamic equilibrium typically does not hold if the temporal scale is too small for the relevant processes to reach an equilibrium state. Reasons might be slow heat and mass transfer between the different phases under the presence of high fluid velocities as it occurs in soil remediation [Ahrenholz et al., 2011, Armstrong et al., 1994] or in the presence of a heat source. Smits et al. [2011] show that non-equilibrium models can help to improve predictions for soil water evaporation. However, non-equilibrium models are not the focus of this thesis.
On the other hand, the temporal scale is important for simulating turbulent flow. Then,

the detailed flow structure, influenced by so-called turbulent eddies, has to be resolved by the spatial and temporal discretization. For such *direct numerical simulation* (DNS) the Kolmogorov length and time scales give an approximation for the discretization requirements. These turbulent scales depend on the viscosity of the fluid and the dissipation of the flow, e.g. Kolmogorov [1941, 1991], Pope [2006], Schlichting and Gersten [2006]. In a turbulent flow, larger eddies decay to smaller eddies until they finally dissipate into heat. The smallest eddies which can exist are limited by the viscosity of the fluid. Because of the high computational cost for simulating turbulence (all eddies have to be resolved by the spatial and temporal discretization), turbulence is oftentimes not simulated but modeled (the effect of eddies on the flow field is parametrized). Therefore, the velocity and other relevant quantities are time-averaged. Small-scale velocity fluctuations, which cause viscous-like effects, can be upscaled using turbulence models of different complexity, e.g. Wilcox [2006]. To achieve appropriate results, the averaging period has to be much larger than the time scales of the relevant turbulent fluctuations, see Fig. 2.1 (right). White [2011] suggests an averaging period $\Delta t \approx 5\,\mathrm{s}$ for gas and water.

2.1.2 Phases, Components, and their Interactions

This section defines terms which are relevant for multi-phase, multi-component systems.

Phases In general, a phase (α) is composed of one or more substances. The substances in one phase have the same physical state: solid, liquid, supercritical, or gaseous. On the continuum scale, the phase state is defined by its thermodynamic state, this means by pressure and temperature. In multi-phase systems, the different phases are separated by a sharp interface and a discontinuity of fluid properties. Theoretically, several liquid and solid phases can coexist, but only one gas phase is possible. For the application of soil water evaporation two fluid phases are considered: the liquid water phase (subscript l) and the gaseous air phase (subscript g). The solid phase (subscript s) is rigid and immobile.

Components Each phase consists of at least one component (κ). The same component may exist in different phases and may change between these phases by different processes like vaporization, condensation, dissolution, or degassing. In this work, two components are considered: water/water vapor (superscript w) and air (superscript a). In reality, air has a variable composition of different substances (e.g. nitrogen, oxygen, etc.), here air is treated as one pseudo-component and its properties do not depend on composition.

Mole and Mass Fractions Different expressions can be used to define the composition of a phase. The mole fraction of a component in a phase (x_α^κ) is defined as the ratio of the number of moles (n_{mole}):

$$x_\alpha^\kappa := \frac{n_{\text{mole},\alpha}^\kappa}{n_{\text{mole},\alpha}} = \frac{n_{\text{mole},\alpha}^\kappa}{\sum_{i\in\{a,w\}} n_{\text{mole},\alpha}^i} \,. \tag{2.1}$$

Similar, the mass fraction of a component in a phase (X_α^κ) is defined as the ratio of masses. The mole fractions can be converted in mass fraction by using the molar mass (M):

$$X_\alpha^\kappa := \frac{x_\alpha^\kappa M^\kappa}{M_\alpha} = \frac{x_\alpha^\kappa M^\kappa}{\sum_{i\in\{a,w\}} x_\alpha^i M^i} \,. \tag{2.2}$$

From the definition of the mole and mass fractions follows that in a phase the sum of mole or mass fractions equals one:

$$\sum_{\kappa\in\{a,w\}} x_\alpha^\kappa = \sum_{\kappa\in\{a,w\}} X_\alpha^\kappa = 1 \,. \tag{2.3}$$

2.1.3 Interfaces

In the context of evaporation, different interfaces occur on different scales. Moeckel [1975] defines an interface as: *"... a singular surface at which three-dimensional thermodynamic fields possess discontinuities."*. On the pore scale, *fluid-solid interfaces* can be found between the soil grains and the adjacent gas or liquid phase and induce shear stresses. *Fluid-fluid interfaces* separate mobile phases such as liquid and gas, and allow the transport of mass and energy between these phases, e.g. by means of vaporization. *Fluid-fluid-solid interfaces* are responsible for capillary forces that affect the phase distributions within the pores. All effects of these pore-scale interfaces have to be integrated/upscaled in REV-scale models, as their information is lost by the averaging process.
On the REV scale, *material interfaces* are present between different soil types or at heterogeneities. Also, the transition from the porous medium to the free flow domain is often approximated by a sharp *porous-medium free-flow interface*. On the pore scale these are no interfaces but continuous transitions. If the term *interface* is used in this work without further specification, then it refers to the porous-medium free-flow interface.

2.1.4 Dimensionless Numbers

Dimensionless numbers can be helpful to analyze flow regimes with different fluids, flow properties, or geometrical features. The dimensionless numbers are used to draw qualitative

conclusions about important processes, dominating forces, or relevant scales.

Reynolds Number The Reynolds number (Re) relates inertia and viscous forces and gives information about the flow regime and the turbulence of a flow:

$$Re := \frac{\text{inertia force}}{\text{viscous force}} = \frac{v_{\text{char}}\, x_{\text{char}}}{\nu}\,. \tag{2.4}$$

A characteristic velocity (v_{char}) and a characteristic length scale (x_{char}), together with the kinematic fluid viscosity (ν), can be used to define different types of Reynolds numbers. The characteristic velocity usually is the mean or maximum velocity. For pipe flows, the diameter is oftentimes taken to identify the expected flow regime, whereas using a run length helps to approximate boundary layer thicknesses or to estimate the flow regime for flow along a flat plate.

Schmidt Number The Schmidt number (Sc) relates viscous and diffusive forces, which are represented by the diffusion coefficient (D):

$$Sc := \frac{\text{viscous force}}{\text{diffusive force}} = \frac{\nu}{D}\,. \tag{2.5}$$

Prandtl Number The Prandtl number (Pr) relates viscous and conductive forces:

$$Pr := \frac{\text{viscous force}}{\text{conductive force}} = \frac{\nu}{a} = \frac{\nu\, \varrho\, c_{\text{p}}}{\lambda}\,, \tag{2.6}$$

in which a is the thermal diffusivity, ϱ the density, c_{p} the specific heat capacity, and λ the thermal conductivity of the fluid.

2.2 Equilibrium Processes and Assumptions

This work is based on the assumption that all thermodynamic properties are locally in equilibrium and thus the processes are in an equilibrium state. This means that kinetic phases change is not be considered.

2.2.1 Local Thermodynamic Equilibrium

The local thermodynamic equilibrium can be split in three parts, cf. Helmig [1997]. *Mechanical equilibrium* is fulfilled if all forces acting on a certain body cancel out. This means that all phase pressures are in equilibrium. In a porous medium pressure jumps can still occur, but originate from capillary forces, see section 2.5.2. *Chemical equilibrium* is satisfied, if all components have the same chemical potential. Finally, *thermal equilibrium* assumes that in one REV all phases have the same temperature. Favorable conditions for the local thermodynamic equilibrium are: low flow velocities, small storage capacities, and small source terms, e.g. Nuske et al. [2014]. More information on local thermodynamic non-equilibrium processes can be found, e.g. in Nuske et al. [2014], Trautz et al. [2015], Nield and Bejan [2017].

2.2.2 Ideal Gas Law

The equation of state for a hypothetical, ideal gas is called ideal gas law:

$$\varrho_\mathrm{g} = \frac{p_\mathrm{g} M_\mathrm{g}}{RT} = \frac{p_\mathrm{g}}{R_\mathrm{g} T} \,. \tag{2.7}$$

The universal gas constant ($R \approx 8.3146\,{}^{\mathrm{J}}/_{\mathrm{mol\,K}}$) or the specific gas constant ($R_\mathrm{g} := {}^{R}/_{M_\mathrm{g}}$) are used together with the pressure (p) and the temperature (T).

2.2.3 Phase Change and Phase Composition

In this section, the basic laws for determining the composition of a phase are explained.

Dalton's Law Under the assumption that the ideal gas law can not only be used to describe pure substances but also mixtures, Dalton's law states that the sum of all partial pressures (p_g^κ) equals the total gas-phase pressure:

$$p_\mathrm{g} = \sum_\kappa p_\mathrm{g}^\kappa \,. \tag{2.8}$$

The partial pressure is the hypothetical pressure of a component if it would occupy the entire volume. For ideal gases, the partial pressure can be calculated with the help of its mole fraction:

$$p_\mathrm{g}^\kappa = p_\mathrm{g} x_\mathrm{g}^\kappa \,. \tag{2.9}$$

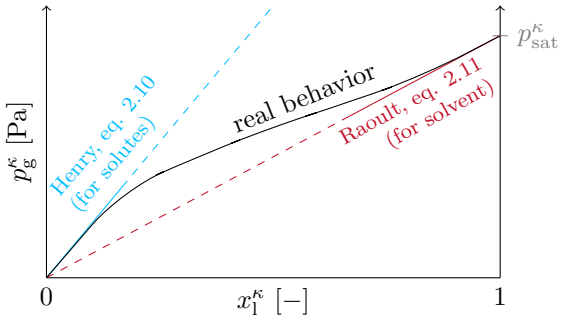

Figure 2.2: Schematic sketch of Henry's and Raoult's law for calculating the partial pressure of a component above a liquid phase, after Class [2001] and Fetzer [2012]. The black line shows the real behavior in contrast to Henry's and Raoult's law.

Henry's Law and Raoult's Law Fig. 2.2 shows the behavior of the partial pressure of one component above a liquid mixture. For the solute, the component which has a very low mole fraction ($x_{\mathrm{l}}^{\kappa} \ll 1$), the vapor pressure can be described by Henry's law:

$$p_{\mathrm{g}}^{\kappa} = x_{\mathrm{l}}^{\kappa} H_{\mathrm{l}}^{\kappa} \,, \tag{2.10}$$

in which the Henry coefficient (H) describes the tendency of a component to leave the liquid phase. For the solvent, the major component of the liquid phase ($x_{\mathrm{l}}^{\kappa} \gg 0$), the vapor pressure can be calculated by Raoult's law with the help of the saturated vapor pressure ($p_{\mathrm{sat}}^{\kappa}$).

$$p_{\mathrm{g}}^{\kappa} = x_{\mathrm{l}}^{\kappa} p_{\mathrm{sat}}^{\kappa} \,. \tag{2.11}$$

With the help of Dalton's, Henry's and Raoult's law and the constitutive relation given in (2.3), the composition of the liquid and gas phase can be described.

Relative Humidity and Equilibrium Mole Fraction The relative humidity (RH) of the gas phase is expressed as the ratio of the partial pressure of the liquid component, here water, to its saturated vapor pressure:

$$RH := \frac{p_{\mathrm{g}}^{\mathrm{w}}}{p_{\mathrm{sat}}^{\mathrm{w}}} = \frac{p_{\mathrm{g}} x_{\mathrm{g}}^{\mathrm{w}}}{p_{\mathrm{sat}}^{\mathrm{w}}} \,. \tag{2.12}$$

By comparing the definition of the relative humidity (2.12) and Raoult's law (2.11), it is found that $RH = x_{\mathrm{l}}^{\mathrm{w}}$. Oftentimes the influence of the diluted component on the partial pressure is neglected. If the liquid phase is present, this leads to $p_{\mathrm{g}}^{\mathrm{w}} = p_{\mathrm{sat}}^{\mathrm{w}}$ and thus $RH = 1$. In this case, the gas and the liquid phase are in equilibrium and an equilibrium mole fraction can be calculated as

$$x_{\mathrm{g}}^{\mathrm{w,eq}} := \frac{p_{\mathrm{sat}}^{\mathrm{w}}}{p_{\mathrm{g}}} \tag{2.13}$$

2.2.4 Diffusion and Dispersion

The diffusive molar flux ($\boldsymbol{j}_{\mathrm{mol}}$) in a phase is modeled by Fick's first law [Fick, 1855] using the molar density (ϱ_{mol}):

$$\boldsymbol{j}^{\kappa}_{\mathrm{mol},\alpha} = -D^{\kappa}_{\alpha}\varrho_{\mathrm{mol},\alpha}\nabla x^{\kappa}_{\alpha}\,. \tag{2.14}$$

Fick's first law is a good approximation for a binary system (a phase consisting of two components), with a very diluted solute component which diffusion coefficient does not depend on composition. If a phase is a binary system, the mole fraction gradients are related by: $\nabla x^{\mathrm{solute}}_{\alpha} = -\nabla x^{\mathrm{solvent}}_{\alpha}$. Further, the net diffusive molar flux in one phase is zero:

$$\sum_{\kappa} \boldsymbol{j}^{\kappa}_{\mathrm{mol},\alpha} = 0\,, \tag{2.15}$$

and thus the diffusion coefficients in one phase have to be identical. Normally they are identical to the one of the solute component: $D_{\alpha} = D^{\mathrm{solute}}_{\alpha}$. The molar fluxes can be converted to diffusive mass fluxes ($\boldsymbol{j}$) by the molar mass of each component:

$$\boldsymbol{j}^{\kappa}_{\mathrm{mass},\alpha} = \boldsymbol{j}^{\kappa}_{\mathrm{mol},\alpha}M^{\kappa} = -D^{\kappa}_{\alpha}\varrho_{\mathrm{mol},\alpha}M^{\kappa}\nabla x^{\kappa}_{\alpha}\,. \tag{2.16}$$

For systems with more than two components or larger mole fractions of the solute component, diffusion becomes more complex. Then, the interactions between the different solutes have to be considered and the diffusion coefficients may depend on the composition of the phase. These effects can be modeled using the Maxwell-Stefan equation for multi-component diffusion. However, this work assumes binary, Fickian diffusion and for a more detailed discussion of the Maxwell-Stefan equation, it is referred to Bird et al. [2007].
Another diffusion-like phenomenon is dispersion. Dispersion originates from the underlying velocity field. Reasons leading to dispersion are tortuous pathways and velocity distributions in a porous medium or velocity fluctuations in a turbulent free flow. Bear [1988] combines diffusion and dispersion (D_{disp}) to an effective or hydrodynamic dispersion (D_{eff}):

$$D^{\kappa}_{\mathrm{eff}} = D^{\kappa}_{\alpha} + D_{\mathrm{disp}}\,. \tag{2.17}$$

This hydrodynamic dispersion results in a spreading of a transported component *"beyond the region it is expected to occupy according to the average flow alone"* [Bear, 1988].

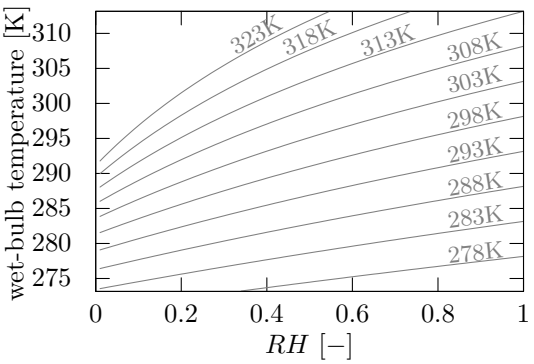

Figure 2.3: Wet-bulb temperatures for different temperature (gray lines) and humidity conditions (x-axis) of the ambient air. Data is obtained from a script provided by the TU München[1]. However, it can also be extracted manually from a Mollier diagram or a psychrometric chart, as presented in Grassmann and Widmer [1974].

2.2.5 Thermal Conduction

Fourier's law of heat conduction describes the conductive energy flux ($\boldsymbol{f}$) which is driven by a temperature gradient together with the thermal conductivity:

$$\boldsymbol{f} = -\lambda \nabla T \,. \tag{2.18}$$

This law does not include the portion of energy transported with advective or diffusive mass fluxes. In the above-mentioned form, it only applies for isotropic media: this is the case for fluids, but solids may have preferred directions, see Bird et al. [2007] for a list of references.

2.2.6 Wet Bulb Temperature

The minimum temperature which can be reached by water evaporation only is called wet-bulb temperature. The wet-bulb temperature at the evaporating surface depends on the energy supply, and thus the temperature of the ambient air and its water vapor content. During the evaporation process, the temperature at the evaporating surface will decrease and finally form an equilibrium between energy supplied by the ambient air and energy extracted by the vaporization process. Resulting wet-bulb temperatures are shown in Fig. 2.3.

[1] `https://web.archive.org/web/20141019115010/http://www.td.mw.tum.de:80/tum-td/de/studium/lehre/thermo_2/kgtsite/TD_KGT.htm`, accessed on December 28, 2017 (in German).

properties	components	phases	references
density	$\varrho^{\mathrm{a}}(p,T)$		ideal gas law (2.7)
	$\varrho^{\mathrm{w}}(p,T)$		[IAPWS, 2007]
		$\varrho_{\mathrm{g}} = \sum_\kappa \varrho^\kappa x_{\mathrm{g}}^\kappa$	
		$\varrho_{\mathrm{l}}(\varrho^{\mathrm{w}}, x_{\mathrm{g}}^\kappa, M^\kappa)$	[Class et al., 2002]
dynamic viscosity	$\mu^{\mathrm{a}}(p,T)$		[Lemmon and Jacobsen, 2004]
	$\mu^{\mathrm{w}}(p,T)$		[IAPWS, 2008]
		$\mu_{\mathrm{g}}(\mu^\kappa, x_{\mathrm{g}}^\kappa)$	[Poling et al., 2001]
		$\mu_{\mathrm{l}} = \mu^{\mathrm{w}}$	
diffusion coefficient		$D_{\mathrm{g}}^{\mathrm{w}}(p,T)$	[Vargaftik, 1975, Walker et al., 1981]
		$D_{\mathrm{l}}^{\mathrm{a}}(T)$	[Ferrell and Himmelblau, 1967]
Henry coefficient		$H_{\mathrm{l}}^{\mathrm{a}}(T)$	[Finsterle, 1993]
saturated vap. pressure	$p_{\mathrm{sat}}^{\mathrm{w}}(T)$		[IAPWS, 2007]
specific heat capacity	$c_{\mathrm{p}}^{\mathrm{a}}(T)$		[Kays et al., 2009]
	$c_{\mathrm{p}}^{\mathrm{w}}(p,T)$		[IAPWS, 2007]
		$c_{\mathrm{p,g}}(c_{\mathrm{p}}^\kappa, x_{\mathrm{g}}^\kappa)$	
		$c_{\mathrm{p,l}} = c_{\mathrm{p}}^{\mathrm{w}}$	
specific enthalpy	$h^{\mathrm{a}}(T)$		[Kays et al., 2009]
	$h^{\mathrm{w}}(p,T)$		[IAPWS, 2007]
		$h_{\mathrm{g}}(h^\kappa, X_{\mathrm{g}}^\kappa)$	[Class, 2001]
		$h_{\mathrm{l}} = h^{\mathrm{w}}$	
thermal conductivity	$\lambda^{\mathrm{a}} = \text{const.}$		
	$\lambda^{\mathrm{w}}(p,T)$		[IAPWS, 2011]
		$\lambda_{\mathrm{g}} = \lambda^{\mathrm{a}}$	
		$\lambda_{\mathrm{l}} = \lambda^{\mathrm{w}}$	

Table 2.1: Used material laws for the components and the phases.

2.3 Material Properties

This section describes basic features of the gas and the liquid phase. Tab. 2.1 shows the main material laws for the components and the phases and their references. Further details on the applied material laws can be found in the documentation and the inside-code comments of DuMu$^{\mathrm{x}}$ 2.12 [Fetzer et al., 2017a].

Air Component and Gas Phase As already mentioned, the gas phase mainly consists of the pseudo component air. Although the composition of air is variable in reality, a constant

composition is assumed: 78 Vol.% nitrogen, 22 Vol.% oxygen. The influence of other gases, e.g. argon, carbon dioxide, is neglected. The properties of the gas phase depend on pressure, temperature, and mole fractions of air and water vapor, see Fig. 2.4 (left figures) and Tab. 2.1. During the evaporation process, the gas phase cools down and gets more humid at the same time. Fig. 2.4 shows that for room conditions ($T = 273 \pm 10\,\mathrm{K}$), the influence of the temperature on the gas-phase density is stronger than the influence of the composition. This leads to higher densities for the gas above the evaporating surface and thus a more stable layering.

Water Component and Liquid Phase The properties of water are essential for the liquid phase. In contrast to the gas phase, in which substantial amounts of water vapor can occur, air hardly dissolves into liquid water. Thus, many features of the liquid phase are mainly influenced by the property of water, see Tab. 2.1. One unique feature of water is that its highest density occurs at 4 °C, which can be seen in Fig. 2.4. In contrast to the gases, the dynamic viscosity of liquids decreases with increasing temperature.

2.4 Fluid Flow

When talking about fluid flow, the Reynolds number is an important quantity. Based on the Reynolds number, different flow regimes can be classified. The Reynolds-number-based classification is a good rule of thumb, however other factors as roughness, geometry, and fluctuations in inflow conditions affect the real behavior, cf. White [2011]. This section is used to present the different flow regimes and their special features. Another important phenomenon presented in this section is the development of boundary layers. Further information about fluid flow and involved processes can be found in: Pope [2006], Schlichting and Gersten [2006], Wilcox [2006], White [2011].

2.4.1 Creeping Flow

In the absence of inertia forces compared to viscous forces ($Re \leq 1$), the flow is called creeping. Creeping flow is a basic assumption for many porous-medium models as well as for the (unsteady) Stokes equation.

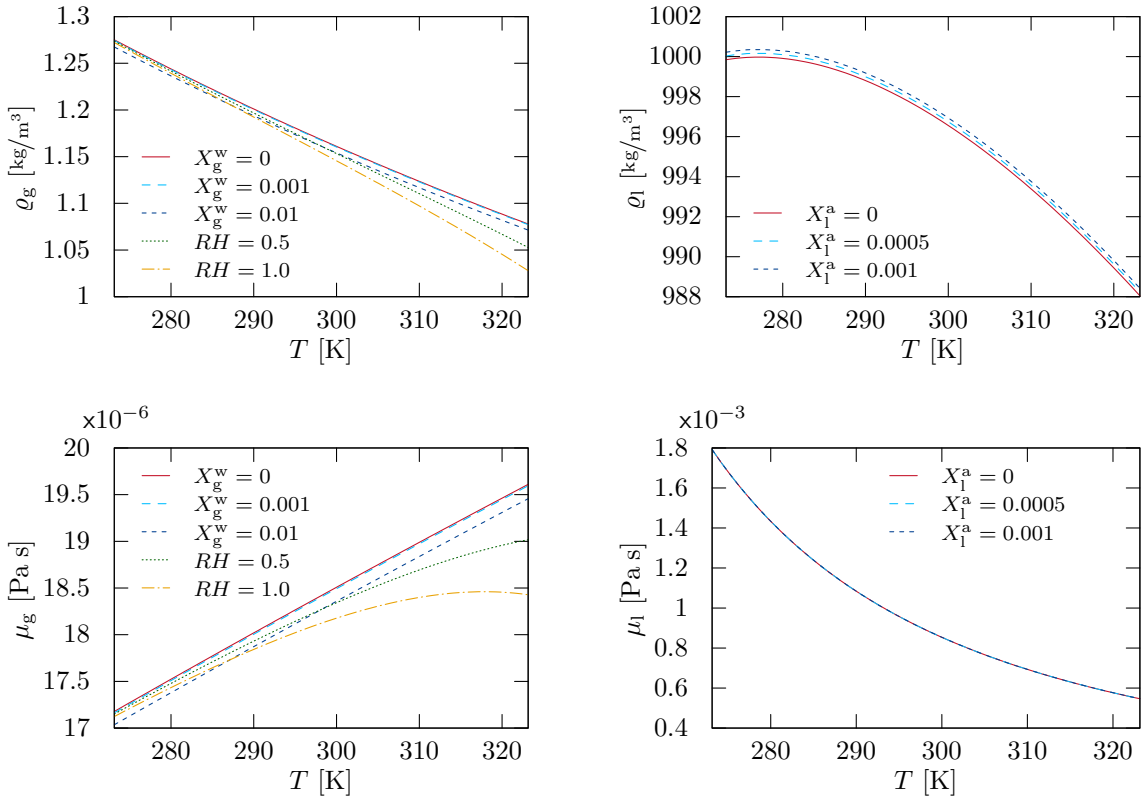

Figure 2.4: Density (top) and dynamic viscosity (bottom) of the gas phase (left) and the liquid phase (right), as implemented in DuMu^x 2.12. The variation of these properties for different compositions are given over a temperature range at a pressure of $p_\alpha = 1\,\text{Pa}$.

2.4.2 Laminar Flow

Laminar flow can be regarded as a system of well-ordered layers with little interaction. It is characterized by a high momentum diffusion (viscous forces), but a low momentum advection (inertia forces), however the inertia forces cannot be neglected.

2.4.3 Laminar-Turbulent Transition

Until now, the transition from laminar to turbulent flow is not fully understood and depends on different processes and properties. This transition does not occur suddenly, but turbulence starts with little disturbances and local turbulence, which gradually become larger. With increasing Reynolds number, the non-linear nature of the inertia forces become more and more important, and the viscous forces are not strong enough to overcome this effect. For flow along a flat plate, Schlichting and Gersten [2006] and Pope [2006] propose a length-based Reynolds number of $Re_{\mathrm{x}} = 5\mathrm{E}5 \sim 1\mathrm{E}6$ for the transition from laminar to turbulent conditions. For flow in a pipe, the diameter-based Reynolds number $Re_{\mathrm{d}} = 2300$ can be considered as a critical value above which the flow is turbulent [Pope, 2006].

2.4.4 Turbulent Flow

Turbulent flow is always irregular and chaotic, forming three-dimensional eddies which can stretch and shrink. Therefore, turbulence is always a three-dimensional phenomenon. These eddies are spreading over a wide-ranging length scale: The largest eddies reach sizes in the order of magnitude of the domain size, the smallest eddies are determined by viscosity and measure even less than millimeters. Kinetic energy is transferred from larger eddies to smaller eddies and ultimately, by a process called dissipation, transformed into heat, see Kolmogorov [1941, 1991]. With respect to component transport, the most prominent difference to laminar flow is the enhanced mixing of the transported substances, see Schlichting and Gersten [2006, Fig. 1.6]. More information about turbulent flow can be found in textbooks such as Oertel [2011], Pope [2006], White [2011], Wilcox [2006].

2.4.5 Boundary Layers

When a fluid flows along a boundary with different properties, boundary layers will evolve. The evolving boundary layers for mass, momentum, and energy can have different shapes and properties. The most prominent example is a fluid flowing along a solid wall at which a

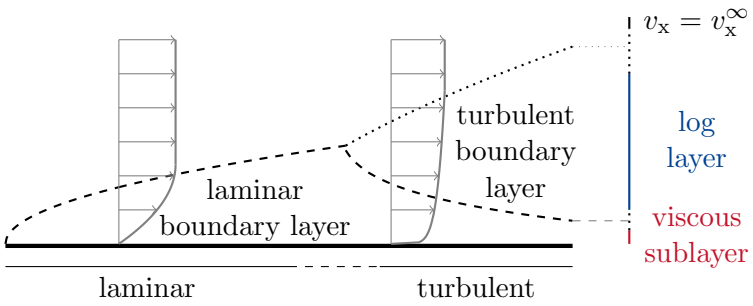

Figure 2.5: Schematic sketch of boundary layer evolution for flow along a flat plate, after Schlichting and Gersten [2006], Fetzer et al. [2016], Grüninger [2017].

zero velocity is assumed (no-slip condition). In that case, the end of the boundary layer is typically defined as the point at which 99% of the maximum or free stream velocity is reached [Pope, 2006]. Boundary layers evolve for all above-mentioned flow regimes, but with different thicknesses (δ). The laminar boundary layer thickness evolves as a function of the square root of the flow length, as specified by the Blasius equation:

$$\delta_{\text{laminar}} \approx \frac{5x}{\sqrt{Re_x}} = \frac{5\sqrt{x\nu}}{\sqrt{v_x}} \,. \tag{2.19}$$

The total turbulent boundary layer thickness can be estimated, according to White [2011], by:

$$\delta_{\text{turbulent}} \approx \frac{0.16x}{Re_x^{1/7}} \,. \tag{2.20}$$

After the transition to turbulent flow, different layers inside the turbulent boundary layer can be discerned. Although the total turbulent boundary layer is thicker than the laminar one, the viscous-dominated layer (viscous sublayer) is much smaller, see Fig. 2.5. Estimations for the viscous sublayer thickness, which are crucial for the near-wall processes or exchange across the porous-medium free-flow interface, are discussed in Chapter 3.

For a detailed study of the turbulent boundary layer, the wall friction velocity (u_τ) is an important quantity. It is calculated based on the velocity gradient or shear stress ($\boldsymbol{\tau}$) at the wall:

$$u_\tau := \sqrt{\frac{\tau_{\text{xy,wall}}}{\varrho}} = \sqrt{\left|\frac{\partial v_x}{\partial y}\right|_{\text{wall}} \nu} \,. \tag{2.21}$$

The wall friction velocity is used to scale the main velocity and the wall distance (y):

$$u^+ := \frac{v_{\text{main}}}{u_\tau} \,, \quad y^+ := \frac{y\, u_\tau}{\nu} \,. \tag{2.22}$$

region	position	property
viscous sublayer	$y^+ < 5$	inertia/turbulence forces are negligible compared to viscous forces
buffer layer	$5 < y^+ < 30$	region between viscous sublayer and log layer
log layer	$y^+ > 30$	region in which the log law holds, turbulence is dominating
viscous wall region	$y^+ < 50$	viscosity is contributing to total shear stress (turbulent + viscous)
outer layer	$y^+ > 50$	no direct effects of viscosity on mean velocity

Table 2.2: Boundary layer regions and defining properties, after Pope [2006]. Note that different values, especially for the end of the viscous sublayer, can be found in literature.

The normalized wall distance (y^+) allows a classification of different regions of the turbulent boundary layer. These regions and their defining properties are listed in Tab. 2.2. The most important regions thereof are the viscous sublayer and the log layer. In the viscous sublayer ($y^+ < 5$) the normalized velocity (u^+) scales linearly with the normalized wall distance:

$$u^+ = y^+ \,. \tag{2.23}$$

In the log or turbulent layer ($y^+ > 30$) the relation between the two values is log linear:

$$u^+ = \frac{1}{\kappa} \ln\left(y^+\right) + C \,, \tag{2.24}$$

with the Karman constant $\kappa \approx 0.41$ and the integration constant C for which values between 5 and 5.5 can be found for flow along smooth boundaries. Fig. 2.6 visualizes these laws of the wall in a dimensionless and real velocity profile. For rough surfaces, e.g. Schlichting and Gersten [2006] and Wilcox [2006] give the following equation:

$$u^+ = \frac{1}{\kappa} \ln\left(\frac{y}{k_\mathrm{s}}\right) + B(k_\mathrm{s}) \,, \tag{2.25}$$

with the sand grain roughness k_s and a parameter $B(k_\mathrm{s})$.

2.5 Porous Medium

Theoretically, a porous medium can be described and simulated on the pore scale. Practically, oftentimes only an abstraction of the real pore geometry is used in pore-network models. However, state-of the art measurement techniques are required and the simulation and modeling are computationally demanding and not suited for large scales. Therefore, this thesis

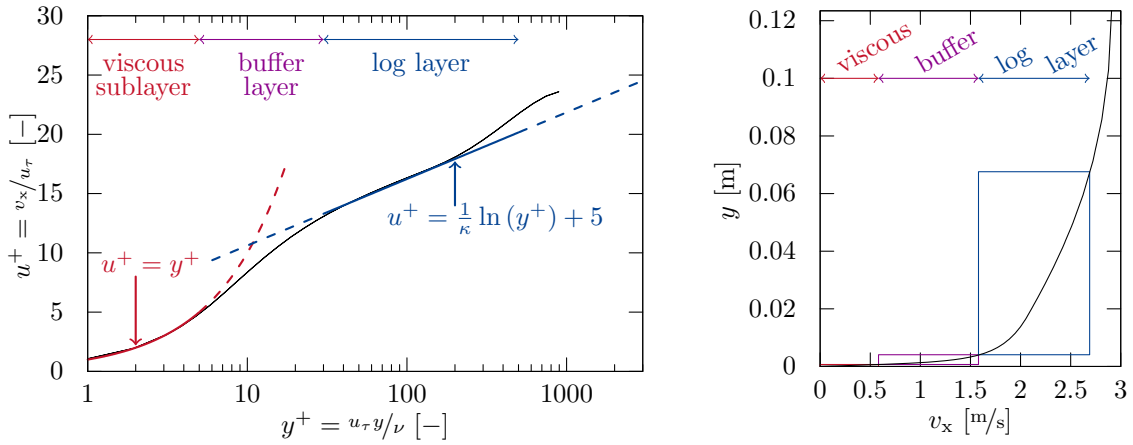

Figure 2.6: Dimensionless velocity profile with the law of the wall (left) and its corresponding velocity profile (right). In addition, the different boundary layers are indicated after Pope [2006].

focuses on volume-averaged porous-medium models on the REV scale. More information on the volume-averaging theory can be found in Bear [1988], Whitaker [1986], Helmig [1997].

2.5.1 REV-Scale Quantities

In the following, some basic quantities arising from the volume averaging over an REV are explained. First, the porosity (ϕ) of an REV is defined as the ratio of the pore volume and the total volume of an REV:

$$\phi := \frac{V_{\text{pore}}}{V_{\text{REV}}} \,. \tag{2.26}$$

The saturation (S) of an REV with a certain phase α is given as:

$$S_\alpha := \frac{V_\alpha}{V_{\text{pore}}} \,. \tag{2.27}$$

Finally, the sum of all saturations equals one:

$$\sum_\alpha S_\alpha := 1 \,. \tag{2.28}$$

In non-technical porous media, saturations of 0 or 1 can hardly be achieved, almost always a certain amount remains in the porous medium. This residual saturation (S_r) is used to formulate an effective saturation:

$$S_{\text{eff}} := \frac{S_\text{l} - S_{\text{r,l}}}{1 - S_{\text{r,g}} - S_{\text{r,l}}} \quad \text{for} \quad S_{\text{r,l}} \leq S_\text{l} < 1 - S_{\text{r,g}} \,. \tag{2.29}$$

In soil science and hydrology, the water content (θ) is oftentimes used to describe the ratio of liquid water to the total REV volume:

$$\theta = \frac{V_\mathrm{l}}{V_\mathrm{REV}} = \phi S_\mathrm{l} \,. \tag{2.30}$$

2.5.2 Multi-Phase Effects

In contrast to single-phase free flow, the presence of multiple mobile phases and the influence of the solid matrix ask for additional concepts. These effects strongly depend on the preference of the fluids to cover or wet a certain solid material. Therefore, indices for the wetting phase (w) and the non-wetting phase (n) are used. In hydrophilic porous media, as considered in this thesis, liquid water is the wetting phase and gas is the non-wetting phase.

Capillary Pressure A prominent example is that the wetting phase rises in a capillary tube. The capillary pressure (p_c) is defined as the pressure difference between the two phases:

$$p_\mathrm{c} := p_\mathrm{n} - p_\mathrm{w} \tag{2.31}$$

On the pore scale, the capillary pressure is described by the Young-Laplace equation, cf. Bear [1988]. On the REV scale, many empirical or semi-empirical relationships for upscaling capillary-driven effects can be found. The most prominent capillary pressure–saturation relationships are those proposed by Brooks and Corey [1964]:

$$p_\mathrm{c} = p_\mathrm{d} S_\mathrm{eff}^{-1/\lambda_\mathrm{BC}} \,, \tag{2.32}$$

or by van Genuchten [1980]:

$$p_\mathrm{c} = \frac{1}{\alpha_\mathrm{VG}} \left(S_\mathrm{eff}^{-1/m_\mathrm{VG}} - 1 \right)^{1/n_\mathrm{VG}} \,. \tag{2.33}$$

Both relationships, which mimic the primary drainage process, are visualized in Fig. 2.7. Even if not considered in this thesis, it shall be mentioned that under the influence of reversing flow directions, like switching from evaporation to condensation or precipitation, the capillary pressure–saturation relationship is not unique and hysteresis effects occur, cf. Bear [1988], Helmig [1997], Roth [2012]. The coefficients of the van Genuchten model are related by: $m_\mathrm{VG} = 1 - 1/n_\mathrm{VG}$.
If a residual water saturation exists, as shown in Fig. 2.7, the soil is not able to dry out. Once the saturation approaches the residual threshold, the capillary forces become infinitely strong and water would be supplied from any other soil portions or the capillary forces will hinder

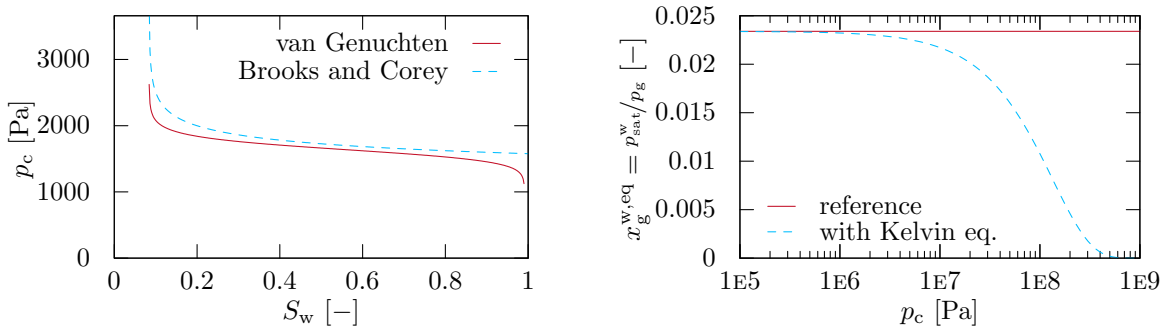

Figure 2.7: The left figure shows the capillary pressure–saturation relationships for a sandy soil using different models: by van Genuchten [1980] and by Brooks and Corey [1964]. The right figure shows the influence of the capillary pressure used in the Kelvin equation (2.34) on the saturated vapor pressure and thus the equilibrium water mass fraction compared to the reference calculated with IAPWS [2007].

further vaporization (see next paragraph). To force a complete drying, the p_c-S_w curve has to be regularized. The soil parametrizations in thesis always use a regularization. Mosthaf [2014] has analyzed the influence of different regularizations on the drying characteristics.

Saturated Vapor Pressure and Kelvin Equation Above strongly curved liquid-gas interfaces, like they occur in small capillaries, the effective saturated vapor pressure of the wetting phase is lower than above an infinitely large interface, because of the surface tension. This effect is reported by Lord Kelvin and therefore named Kelvin equation, cf. Thomson [1871], Class [2007]:

$$p_{sat,Kelvin}^w := p_{sat}^w \exp\left(-\frac{p_c M^w}{\varrho_l R T}\right) . \tag{2.34}$$

Fig. 2.7 illustrates the resulting equilibrium water mass fraction with and without considering the capillary effect. The curves start to deviate at a capillary pressure of $p_c = 1\text{E}6\,\text{Pa}$. This pressure is usually not reached when linearizing the p_c-S_w curve for sandy soils.

Relative Permeability If multiple phases are present, they mutually constrain their possibility to flow by occupying and thus blocking different pores and pathways. This effect is described by a dimensionless quantity called relative permeability ($k_{r,}$). The relative permeabilities are usually described as a function of the saturation and can derived by combining pore-network models with capillary pressure–saturation relationships, see Helmig [1997]. As for the capillary pressure, the most common models, visualized in Fig. 2.8, are those based

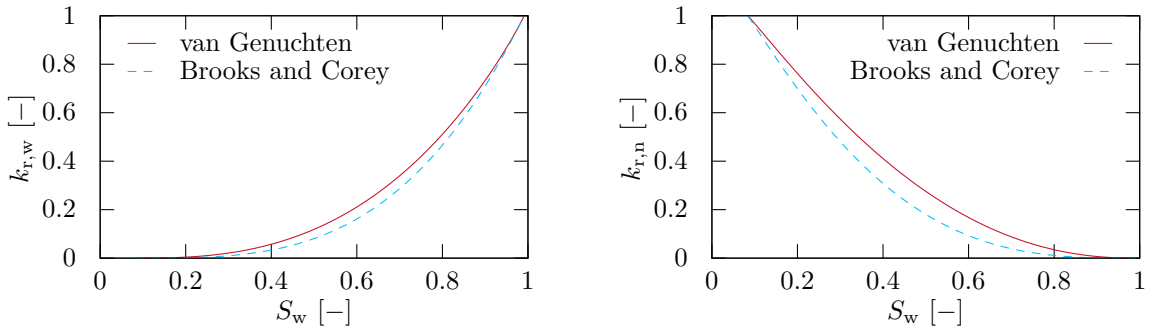

Figure 2.8: Relative permeability–saturation relationships, for the same sandy soil as in Fig. 2.7, using models by van Genuchten [1980] and by Brooks and Corey [1964]. The figures show the wetting phase (left) and the non-wetting phase (right).

on Brooks and Corey [1964]:

$$k_{r,w} = S_{eff}^{\frac{2+\lambda_{BC}}{\lambda_{BC}}} , \tag{2.35}$$

$$k_{r,n} = (1 - S_{eff})^2 \left(1 - S_{eff}^{\frac{2+\lambda_{BC}}{\lambda_{BC}}}\right) , \tag{2.36}$$

or on van Genuchten [1980]:

$$k_{r,w} = \sqrt{S_{eff}} \left(1 - \left(1 - S_{eff}^{\frac{1}{m_{VG}}}\right)^{m_{VG}}\right)^2 , \tag{2.37}$$

$$k_{r,n} = (1 - S_{eff})^{\frac{1}{3}} \left(1 - S_{eff}^{\frac{1}{m_{VG}}}\right)^{2m_{VG}} . \tag{2.38}$$

Diffusion and Tortuosity Diffusion in the porous medium is slower than in a free-flow region due to tortuous pathways. This effect can be included by accounting for a tortuosity factor (τ), see Millington [1959]. According to Helmig [1997], the effective porous-medium diffusion coefficient (D^{pm}) and the molecular diffusion coefficient (D) can be related by:

$$D_\alpha^{pm} = D_\alpha \tau \phi S_\alpha , \tag{2.39}$$

with the following tortuosity factor

$$\tau_\alpha = \phi^{1/3} S_\alpha^{7/3} . \tag{2.40}$$

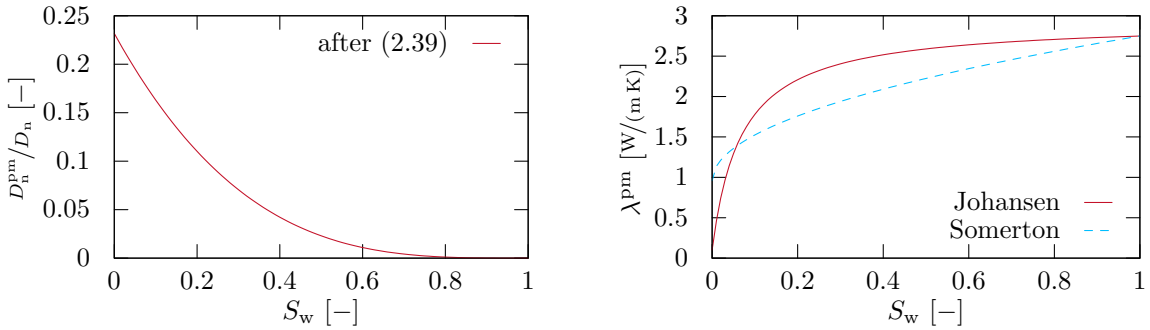

Figure 2.9: Effective diffusivity reduction (left) and different effective thermal conductivity models (right) in a porous medium.

This changes the diffusive fluxes inside the porous medium to:

$$\boldsymbol{j}_\alpha^{\kappa,\mathrm{pm}} = -D_{\mathrm{mass},\alpha}^{\mathrm{pm}} \varrho_{\mathrm{mol},\alpha} M^\kappa \nabla x_\alpha^\kappa \,. \tag{2.41}$$

Thermal Conductivity In an REV, different phases contribute to the conductive heat transfer and lead to a total porous-medium thermal conductivity (λ^{pm}), which depends on all phases (fluids and solid). Dong et al. [2015] compare different kinds of models for λ^{pm}: Mixing models, empirical models, and mathematical models. In this work, the empirical models by Somerton et al. [1974] and Johansen [1975] are used, see Fig. 2.9. Both use the basic relation:

$$\lambda^{\mathrm{pm}} = \lambda_{\mathrm{dry}} + \beta \left(\lambda_{\mathrm{sat}} - \lambda_{\mathrm{dry}}\right) \,, \tag{2.42}$$

with the following functions after Somerton et al.:

$$\lambda_{\mathrm{dry}} = \lambda_{\mathrm{s}}^{1-\phi} \lambda_{\mathrm{n}}^{\phi} \,, \quad \lambda_{\mathrm{sat}} = \lambda_{\mathrm{s}}^{1-\phi} \lambda_{\mathrm{w}}^{\phi} \,, \quad \beta = \sqrt{S_{\mathrm{w}}} \,,$$

or after Johansen:

$$\lambda_{\mathrm{dry}} = \frac{0.135 \varrho_{\mathrm{s}} \phi + 64.7\,\mathrm{kg/m^3}}{\varrho_{\mathrm{s}} - 0.947 \varrho_{\mathrm{s}} \phi} \frac{\mathrm{W}}{\mathrm{m\,K}} \,, \quad \lambda_{\mathrm{sat}} = \lambda_{\mathrm{s}}^{1-\phi} \lambda_{\mathrm{w}}^{\phi} \,, \quad \beta = \frac{k_{\mathrm{J}} S_{\mathrm{w}}}{1 + (k_{\mathrm{J}} - 1) S_{\mathrm{w}}} \,,$$

in which $k_{\mathrm{J}} = 15.6$ is fitted to Quartz sand [Smits et al., 2010].

2.6 Interface

At the interface between the free-flow region and the porous medium, mass, momentum, and energy is exchanged between the two flows. In addition, there is an interaction between the

solid matrix of the porous medium and the free flow above.

2.6.1 Roughness

According to Wikipedia[2], the German Institute for Standardization (DIN) defines roughness as deviation in shape ("Gestaltsabweichung"). This deviation in shape includes quite noticeable deviations like furrows/ripples but goes down to roughness resulting from the surface/porous-medium texture. The second includes surface roughness resulting from the sand grains of a, on the REV scale homogeneous medium, but also roughness as a heterogeneity resulting from different solid materials. Fluid dynamic textbooks avoid a definition of roughness only based on the shape of the surface. Pope [2006] states that roughness, as a departure from an ideal, is *"to a first approximation ... characterized by a lengthscale of protrusions or indentations"*. More crucial in fluid dynamics is whether the roughness affects the free flow and transport processes. This is expressed with the help of the sand grain roughness (k_s) and the dimensionless sand grain roughness (k_s^+):

$$k_\mathrm{s}^+ := \frac{k_\mathrm{s} u_\tau}{\nu} \,. \tag{2.43}$$

Fig. 2.10 depicts different surface configurations influencing the free-flow behavior. The different turbulent flow schemes are defined according to Schlichting and Gersten [2006] and with respect to the viscous sublayer thickness (δ_vs):

$$\begin{aligned}
k_\mathrm{s}^+ = 0 \quad &\rightarrow \text{ smooth } (k_\mathrm{s} = 0\,\mathrm{m}) \\
k_\mathrm{s}^+ < 5 \quad &\rightarrow \text{ hydraulically smooth } (k_\mathrm{s} < \delta_\mathrm{vs}) \\
5 \leq k_\mathrm{s}^+ \leq 70 \quad &\rightarrow \text{ transitionally rough } (\delta_\mathrm{vs} < k_\mathrm{s}) \\
70 < k_\mathrm{s}^+ \quad &\rightarrow \text{ fully rough } (\delta_\mathrm{vs} < k_\mathrm{s})
\end{aligned}$$

For densely packed grains on an impermeable plate, as e.g. on a sandpaper, Schlichting and Gersten [2006] define k_s to be the sand grain diameter. They also propose different equivalent values for common materials. The definition of k_s for a porous medium is more challenging, as no baseline like an impermeable plate is available, cf. Fig. 2.10. Kuznetsov [2004] gives an approximation based on porous-medium properties ($k_\mathrm{s} = 0.5\, d_{50}$). The work by Manes et al. [2011], who experimentally analyzed the friction factors over permeable beds, indicates the effects of roughness in conjunction with permeable media behaves different than roughness on an impermeable plate.

[2] `https://de.wikipedia.org/wiki/Rauheit`, accessed on July 03, 2017.

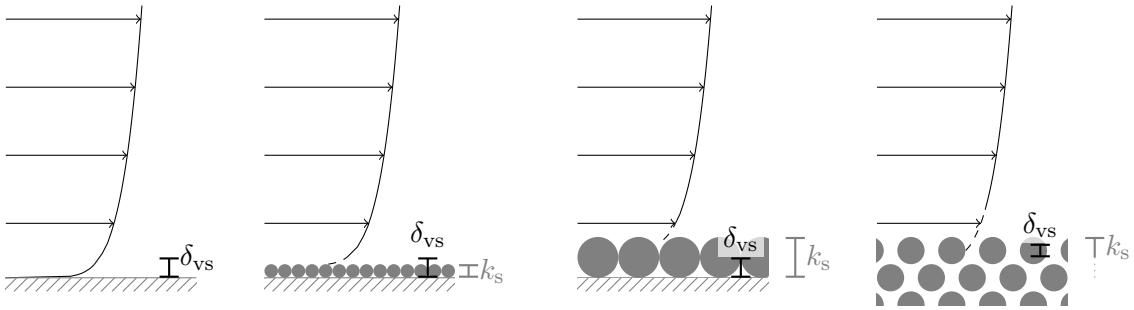

$k_s^+ = 0$	$k_s^+ < 5$	$5 < k_s^+$	$5 < k_s^+$
smooth	hydraulically smooth	(transitionally) rough	(transitionally) rough
impermeable	impermeable	impermeable	permeable

Figure 2.10: Schematic sketch of turbulent flow over rough surfaces.

2.6.2 Evaporation

A lot of work on analyzing coupled porous-medium free-flow exchange processes is performed in the field of water evaporation from bare soil surfaces, e.g. van Brakel [1980], Brutsaert [1982], Or et al. [2013]. During the evaporation process mainly two different stages are discerned, depending on the source they are called stage-I/stage-II [e.g. Lehmann et al., 2008], or constant-rate period (CRP)/falling-rate period (FRP) [e.g. Yiotis et al., 2007].

The stage-I period is characterized by higher and relatively constant evaporation rates, see Fig. 2.11. In this thesis, the evaporation rate (e) is defined as the total water mass flux across the porous-medium free-flow interface. This flux q^w in $\mathrm{kg/m^2\,s}$ contains all advective and diffusive water (vapor) fluxes in the liquid and in the gas phase:

$$e := \frac{q^w}{\varrho^w} \cdot 1000\,\mathrm{mm/m} \cdot 86400\,\mathrm{s/d} \approx q^w \cdot 86400\,\mathrm{s/d} \tag{2.44}$$

In stage-I, liquid water is present at the interface and thus the evaporation rate is constrained by the atmospheric demand (vapor/partial-pressure gradient). As reported in Shahraeeni et al. [2012], Or et al. [2013], the stage-I evaporation rate is not necessarily constant. In the presence of very thin boundary layers, the evaporation rate can already drop during stage-I. Another reason for a falling rate is that the system is far from its equilibrium state, e.g. due to strong evaporative fluxes and the combined cooling effect [Lu et al., 2005, Mosthaf et al., 2014]. During the drying process, a pattern of wet pores evolves at the interface. Shahraeeni et al. [2012] and Or et al. [2013] show that this is an efficient but limited compensation mechanism: The evaporation rate per pore increases as a result of switching from one-dimensional to three-dimensional diffusion. Mosthaf et al. [2014] and Fetzer et al. [2017c] show that REV-scale simulations, without concepts accounting for pore-scale compensation effect as proposed by

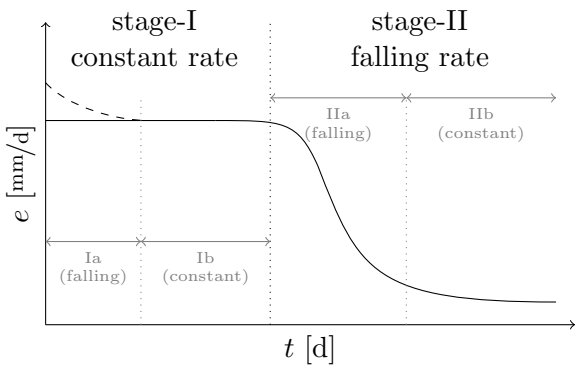

Figure 2.11: Schematic sketch of the evaporation rate evolution over time, after Mosthaf [2014].

Suzuki and Maeda [1968], Schlünder [1988], Haghighi et al. [2013], are not able to predict a decrease in stage-I evaporation rate from a homogeneous medium once an equilibrium state is formed. As soon as the compensation mechanism fails, the capillary effects are not strong enough to deliver water from deeper depth to fulfill the evaporative demand, or the capillary forces in the remaining pores are too strong to allow further evaporation (cf. section 2.5.2), the evaporation rate starts to drop and the second stage of evaporation is reached.

Evaporation in stage-II is diffusion-limited and depends on the vapor transport through the unsaturated soil, e.g. Shokri et al. [2009], Shokri and Or [2011]. The stage-II period, is characterized by starting with a falling rate period (oftentimes referred to as stage-IIa or transition), followed by a period with a constantly low rate [Or et al., 2013].

3 Physical and Mathematical Model

In this chapter, the continuum-scale models are presented. First, the models for the two subdomains, the free flow (section 3.1) and the porous medium (section 3.2) are explained, then the coupling conditions are introduced (section 3.3).

3.1 Free Flow

The free flow is modeled with the Navier-Stokes equations. Further, the following assumptions are made: (i) single-phase gas flow, composed of two components: water vapor (w) and air (a), (ii) Newtonian fluid without dilation, and (iii) equilibrium processes, especially Fickian diffusion.

3.1.1 Mass and Momentum Balance

The total mass balance is given by:

$$\frac{\partial \varrho_{\mathrm{g}}}{\partial t} + \nabla \cdot (\varrho_{\mathrm{g}} \boldsymbol{v}_{\mathrm{g}}) + \sum_{\kappa} \nabla \cdot \boldsymbol{j}^{\kappa,\mathrm{ff}}_{\mathrm{mass,eff}} = 0 \,. \tag{3.1}$$

The total mass balance includes effective diffusive-dispersive fluxes ($\boldsymbol{j}^{\kappa,\mathrm{ff}}_{\mathrm{mass,eff}}$), which will be discussed in section 3.1.3. As shown in section 2.2.4, the mass-based diffusive-dispersive fluxes for both components are not equal and have to be considered in the total mass balance. For modeling momentum transport in the free flow region, the Navier-Stokes equations are used:

$$\frac{\partial \left(\varrho_{\mathrm{g}} \boldsymbol{v}_{\mathrm{g}}\right)}{\partial t} + \nabla \cdot \left(\varrho_{\mathrm{g}} \boldsymbol{v}_{\mathrm{g}} \boldsymbol{v}_{\mathrm{g}}^{\mathsf{T}}\right) - \nabla \cdot \boldsymbol{\tau}_{\mathrm{g}} + \nabla \cdot (p_{\mathrm{g}} \mathbf{I}) - \varrho_{\mathrm{g}} \boldsymbol{g} = 0 \,. \tag{3.2}$$

The shear stress tensor is defined as:

$$\boldsymbol{\tau}_{\mathrm{g}} := 2 \varrho_{\mathrm{g}} \nu_{\mathrm{g}} \mathbf{S} = \varrho_{\mathrm{g}} \nu_{\mathrm{g}} \left(\nabla \boldsymbol{v}_{\mathrm{g}} + \nabla \boldsymbol{v}_{\mathrm{g}}^{\mathsf{T}}\right) \,, \tag{3.3}$$

with the strain rate tensor $\mathbf{S} = \frac{1}{2}\left(\nabla \boldsymbol{v}_\mathrm{g} + \nabla \boldsymbol{v}_\mathrm{g}^\mathsf{T}\right)$. In addition, the identity matrix ($\mathbf{I}$) and the gravitational acceleration $\boldsymbol{g} = (0, \ldots, -9.81\,\mathrm{m/s^2})^\mathsf{T}$ are needed. For laminar flow, the Navier-Stokes equations can be solved quite easily (compared to the computational effort for turbulent flow conditions). Then, as discussed in section 2.4, viscous/diffusive forces are stronger than inertia/convective forces. The effect of turbulence, when the inertia forces are dominating, is discussed in the next section. For creeping flow ($Re < 1$) and the absence of gravitational forces, the Navier-Stokes equations simplify to the transient Stokes equations:

$$\frac{\partial\left(\varrho_\mathrm{g}\boldsymbol{v}_\mathrm{g}\right)}{\partial t} - \nabla\cdot\boldsymbol{\tau}_\mathrm{g} + \nabla\cdot\left(p_\mathrm{g}\mathbf{I}\right) = 0\,. \tag{3.4}$$

3.1.2 Turbulence Modeling

Two main approaches for simulating turbulent flow can be discerned. If specific requirements are fulfilled, a direct numerical simulation (DNS) of the turbulent flow is possible. Otherwise, the effects of the turbulent flow have to be modeled.

3.1.2.1 From DNS to RANS[3]

For the direct simulation of turbulent free flow, even the smallest eddies have to be resolved correctly, otherwise physically unrealistic results are obtained. Therefore, the smallest eddies have to be estimated. Referring to the Kolmogorov energy cascade [Kolmogorov, 1941], energy is transferred from larger to smaller eddies and finally dissipates into heat. The kinematic viscosity is a crucial quantity and determines the Kolmogorov micro scale, the smallest possible eddy size. Eddies are always three-dimensional, so a microscale of 20 μm and thus an equidistant discretization with 10 μm would result in $1 \cdot 10^{12}$ cells for simulating a cube of 0.1 m length. This results in a high computational demand, especially if non-linear material laws or the influence of component and energy transport are considered. Examples for direct numerical simulations of coupled porous-medium free-flow processes can be found e.g. in Krafczyk et al. [2015] or Fattahi et al. [2016].

Large eddy simulations (LES) include first simplifications of the turbulent flow processes. LES methods assume that the small-scale eddies are universal. As a consequence, the effect of small-scale eddies is modeled with simpler turbulence models, whereas the larger eddies are still simulated. More information about LES models can be found e.g. in Rodi et al. [2013].

[3]This section is based on T. Fetzer: Numerical analysis of the influence of turbulence on exchange processes between porous-medium and free flow, *Master's Thesis*, Universität Stuttgart, 2012.

The next level of model abstraction includes the loss of information about the detailed, instantaneous flow structure. The *Reynolds decomposition* assumes that any transported quantity (e.g. the instantaneous velocity v_x), is composed of a mean value (e.g. $\bar{v}_\mathrm{x}$) and the fluctuations around this mean value (e.g. v'_x):

$$v_\mathrm{x} = \bar{v}_\mathrm{x} + v'_\mathrm{x}\,. \tag{3.5}$$

The mean values are a result of an averaging in time, in space, or over ensembles. Here, the time-averaging method is considered, cf. Fig. 2.1. In a second step, the *Reynolds averaging*, all decomposed quantities are inserted in the governing balance equations. Then, all balance equations are time-averaged. For more information on the Reynolds averaging it is referred to standard fluid mechanics textbooks as Pope [2006], Wilcox [2006], White [2011], or Oertel [2012]. When the Reynolds averaging is applied on the Navier-Stokes equations (3.2), the Reynolds-averaged Navier-Stokes equations (RANS) are obtained under the assumptions of (i) steady state turbulence, meaning the mean value is in a steady state and (ii) negligible influence of pressure fluctuations:

$$\frac{\partial\left(\varrho_\mathrm{g}\bar{\boldsymbol{v}}_\mathrm{g}\right)}{\partial t} + \nabla\cdot\left(\varrho_\mathrm{g}\bar{\boldsymbol{v}}_\mathrm{g}\bar{\boldsymbol{v}}_\mathrm{g}^\mathsf{T}\right) + \nabla\cdot\left(\varrho_\mathrm{g}\overline{\boldsymbol{v}'_\mathrm{g}\boldsymbol{v}'^\mathsf{T}_\mathrm{g}}\right) - \nabla\cdot\bar{\boldsymbol{\tau}}_\mathrm{g} + \nabla\cdot\left(\bar{p}_\mathrm{g}\mathbf{I}\right) - \varrho_\mathrm{g}\boldsymbol{g} = 0\,. \tag{3.6}$$

The overbar indicates that a quantity or expression is time-averaged. The mass balance remains unchanged, the instantaneous values are only replaced by the mean values.

The Reynolds averaging yields a new expression: $\varrho_\mathrm{g}\overline{\boldsymbol{v}'_\mathrm{g}\boldsymbol{v}'^\mathsf{T}_\mathrm{g}}$. Even though this term results from the advection term, it leads to viscous or diffusive effects. It is called Reynolds stress tensor ($\boldsymbol{\tau}_\mathrm{t}$), which is a symmetric tensor with 3×3 entries. This leads to a closure problem, because no further relations to describe these additional Reynolds stresses (or turbulent stresses) are provided. Models which find expressions for all six entries of this symmetric tensor are called Reynolds stress models (RSM). Under specific simplifications, namely those published by Boussinesq [1877], that turbulent stresses act in analogy to viscous stresses, the number of unknowns is reduced. The Reynolds stresses are then modeled by an additional viscosity, called eddy viscosity (ν_t), plus the contribution of the turbulent kinetic energy (k):

$$\varrho_\mathrm{g}\overline{\boldsymbol{v}'_\mathrm{g}\boldsymbol{v}'^\mathsf{T}_\mathrm{g}} = -\bar{\boldsymbol{\tau}}_\mathrm{t} = -\varrho_\mathrm{g}\nu_\mathrm{t}\left(\nabla\bar{\boldsymbol{v}}_\mathrm{g} + \nabla\bar{\boldsymbol{v}}_\mathrm{g}^\mathsf{T}\right) + \frac{2}{3}\varrho_\mathrm{g}k\mathbf{I}\,. \tag{3.7}$$

The name *eddy* accounts for the fact, that the eddy viscosity is a flow property and fully depends on the turbulent flow field and not on the fluid. The turbulent kinetic energy is defined via the turbulent velocity fluctuations, $k := {}^1\!/_2\left({v'_{\mathrm{g,x}}}^2 + {v'_{\mathrm{g,y}}}^2 + {v'_{\mathrm{g,z}}}^2\right)$. Therefore, it has to be included in (3.7) to match its definition for incompressible flow. Later, turbulence models are presented which do not model the turbulent kinetic energy and thus do not include the last term in (3.7). For simplicity, the contributions of the fluid shear stresses and the

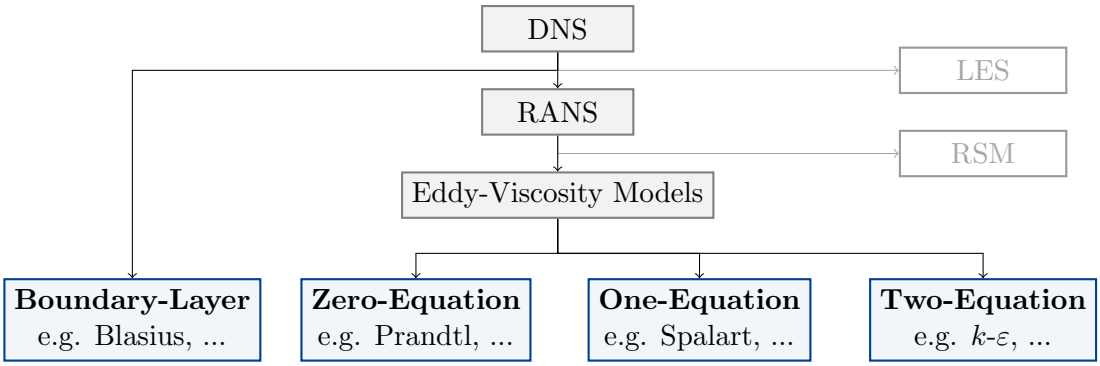

Figure 3.1: Hierarchy of turbulence models, after Fetzer [2012] and Trautz [2015]. The models highlighted in blue are used in this work.

turbulent/Reynolds stresses are combined to an effective stress term ($\bar{\boldsymbol{\tau}}_{\mathrm{eff}}$):

$$\bar{\boldsymbol{\tau}}_{\mathrm{eff}} = \bar{\boldsymbol{\tau}}_{\mathrm{g}} + \bar{\boldsymbol{\tau}}_{\mathrm{t}} = \varrho_{\mathrm{g}}\nu_{\mathrm{g}}\left(\nabla\bar{\boldsymbol{v}}_{\mathrm{g}} + \nabla\bar{\boldsymbol{v}}_{\mathrm{g}}^{\intercal}\right) + \varrho_{\mathrm{g}}\nu_{\mathrm{t}}\left(\nabla\bar{\boldsymbol{v}}_{\mathrm{g}} + \nabla\bar{\boldsymbol{v}}_{\mathrm{g}}^{\intercal}\right) - \frac{2}{3}\varrho_{\mathrm{g}}k\mathbf{I}\,. \tag{3.8}$$

The turbulent flow field is strongly affected by the presence of solid walls. In this case, the turbulence is *wall-bounded*, the fluid velocity decreases towards the wall and viscous effects become more dominant. Also the porous-medium free-flow interface functions as such a wall for the turbulent free flow. Therefore, it is crucial to correctly account for these walls and to predict their influence on the turbulent flow field, which in turn influences the exchange processes across the interface.

Various parametrizations of different complexity are available for calculating the eddy viscosity, see Fig. 3.1. The eddy-viscosity models are characterized by the number of partial differential equations (PDE) which have to be solved for the turbulent flow properties. Pope [2006] writes that the two-equation turbulence models are complete in a sense that both, the turbulent length and time scale are modeled and not predefined. These two scales can be derived based on the turbulent kinetic energy (k) together with the dissipation (ε) or the turbulence frequency (ω). These three turbulent quantities are linked by the following relation:

$$\varepsilon = \omega k\,. \tag{3.9}$$

The one-equation models use one PDE for one turbulent quantity together with a turbulent length scale, here the mixing length (l_{mix}), which depends on geometrical information, namely the wall distance. Spalart [2015] explains that also one-equation models are complete in a sense that the turbulent quantity contains a turbulent length and time scale. The zero-equation models are the simplest eddy-viscosity models and do not include an additional PDE. The eddy viscosity is calculated based on geometrical features, the mixing length, and

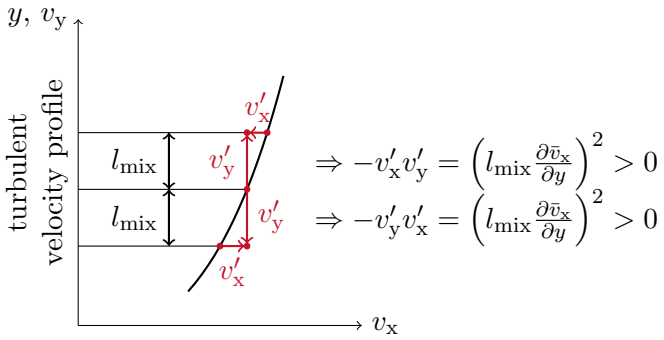

Figure 3.2: Mixing-length concept, after Schlichting and Gersten [2006].

properties of the mean flow field, the velocity gradient, see Fig. 3.2. This means that the two-equation models have the least geometrical requirements. When the exchange across the wall or across the porous-medium free-flow interface is modeled, the most drastic simplification which still accounts for the effects of the turbulent flow field is to take the information about the resulting boundary layers to model this exchange, cf. e.g. Mosthaf et al. [2014], Fetzer et al. [2016]. For more information on the theory of turbulence it is referred to Pope [2006]. Wilcox [2006] and Versteeg and Malalasekra [2009] approach this topic from a modeler perspective.

For the sake of readability, from here on the overbars which indicate mean values are dropped. For all equations and results, if a turbulence model is included, the quantities are always considered to be time-averaged.

3.1.2.2 Two-Equation Models

Reviews on two-equation turbulence models can be found in Wilcox [2006], in which their applicability to various test cases is compared. Similarly, Bardina et al. [1997] provides qualitative rankings of four two-equation turbulence models. Two main groups of two-equation models can be found: the classic k-ε model, which is suited for high-Reynolds number flows and low-Reynolds number models, which are also valid in the near-wall region, as the Low-Re k-ε model and the k-ω model.

K-Epsilon (k-ε) According to Pope [2006] and Wilcox [2006] the k-ε turbulence model is the most popular one. The k-ε model was originally introduced by Jones and Launder [1972]. It was further developed by Launder and Sharma [1974], there the standard values for the model constants are published. The model solves two balance equations to model the turbulent

kinetic energy and the dissipation which are combined to calculate the eddy viscosity:

$$\nu_\mathrm{t} = C_\mu \frac{k^2}{\varepsilon} \,. \tag{3.10}$$

As explained in section 3.1.2, the turbulent kinetic energy is defined via the velocity fluctuations. Unfortunately, these fluctuations are unknown in RANS models. Therefore, the turbulent kinetic energy is modeled by the following balance equation:

$$\frac{\partial (k)}{\partial t} + \nabla \cdot (\boldsymbol{v}_\mathrm{g} k) - \nabla \cdot \left(\left(\nu_\mathrm{g} + \frac{\nu_\mathrm{t}}{\sigma_\mathrm{k}} \right) \nabla k \right) - 2\nu_\mathrm{t} \mathbf{S} \cdot \mathbf{S} + \varepsilon = 0 \,. \tag{3.11}$$

The tensor scalar product of the strain rate tensor is: $\mathbf{S} \cdot \mathbf{S} = \sum_i \sum_j S_{ij} S_{ij}$. In addition, a balance equation for the dissipation is needed. The dissipation can be seen as an energy-flow rate in the energy cascade [Pope, 2006, Wilcox, 2006]:

$$\frac{\partial (\varepsilon)}{\partial t} + \nabla \cdot (\boldsymbol{v}_\mathrm{g} \varepsilon) - \nabla \cdot \left(\left(\nu_\mathrm{g} + \frac{\nu_\mathrm{t}}{\sigma_\varepsilon} \right) \nabla \varepsilon \right) - C_{1\varepsilon} \frac{\varepsilon}{k} 2\nu_\mathrm{t} \mathbf{S} \cdot \mathbf{S} + C_{2\varepsilon} \frac{\varepsilon^2}{k} = 0 \,. \tag{3.12}$$

According to Pope, the model equation for the dissipation is *"best viewed as being entirely empirical"* and not based on the exact equation which may also be derived.
The constants for both equations are, according to Launder and Sharma [1974]:

$$\sigma_\mathrm{k} = 1.00 \,,\ \sigma_\varepsilon = 1.30 \,,\ C_{1\varepsilon} = 1.44 \,,\ C_{2\varepsilon} = 1.92 \,,\ C_\mu = 0.09 \,.$$

If the k-ε model is considered to be a purely high-Reynolds turbulence model, it holds that $\nu_\mathrm{t} \gg \nu_\mathrm{g}$. Nevertheless, formulations including the kinematic fluid viscosity ν_g can be found in Wilcox [2006] and OpenFOAM, whereas it is neglected in Versteeg and Malalasekra [2009] and Pope [2006]. The k-ε model is, in the presented form, not suited for flow with strong viscous effects as they occur near walls. Possible remedies are explained in the subsequent paragraphs.

Wall Functions: Wall functions use the law of the wall and its solution for the logarithmic layer (2.24) and are, according to Pope [2006], originally proposed by Launder and Spalding [1972]. Wall functions are generally useful, if the geometries are simple and the law of the wall is valid. This might not be the case, e.g. for surface mass injection as reported by Andersen et al. [1972] or [Wilcox, 2006, Fig. 4.27]. The wall-function method has constantly been developed over the past years: e.g. Craft et al. [2002] adopted the wall-function treatment for better predictions or Blocken et al. [2007] analyzed the influence of wall functions including sand-grain roughness parametrizations for atmospheric boundary layer flow over buildings. Based on the analytical law-of-the-wall solution, the wall shear stress and the wall friction

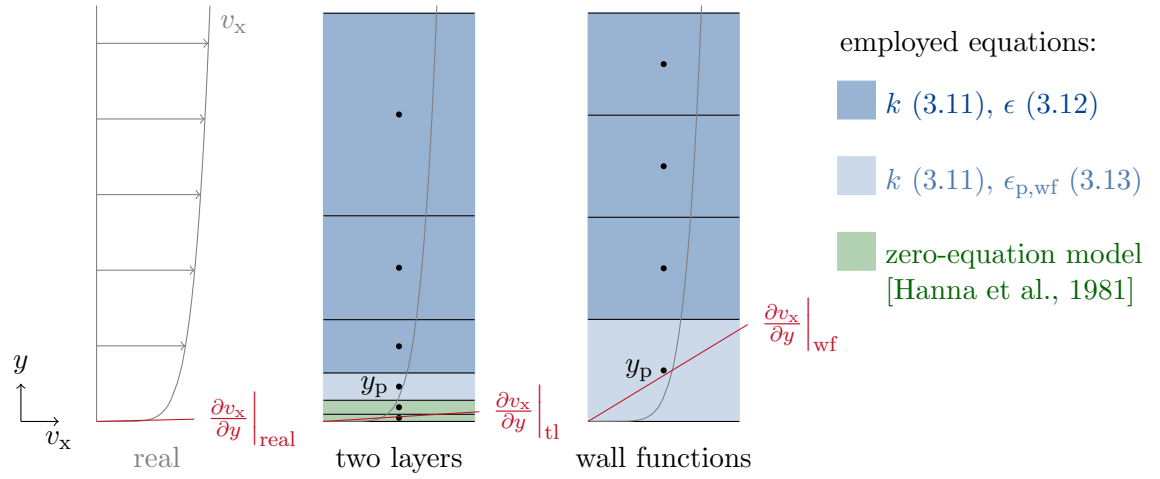

Figure 3.3: Comparison of two-layer and wall-function approaches.

velocity can be calculated, even though the velocity gradients are not appropriately resolved with the actual discretization, see Fig. 3.3. At a point "p" inside the turbulent boundary layer, for which the law of the wall holds ($y_p^+ \geq y_{threshold}^+ = 50$), the dissipation is fixed by the wall function:

$$\varepsilon_{p,wf} = \frac{{u_{\tau,nom}}^3}{\kappa\, y_p} \,. \tag{3.13}$$

This formulation after Pope [2006] uses the nominal friction velocity $u_{\tau,nom} = C_\mu^{0.25} k_p^{0.5}$. The boundary condition for the main velocity/momentum component can be set by comparing the actual velocity (v_x) to the nominal velocity ($v_{x,nom}$) calculated from the law of the wall. Then, the turbulent shear stress can be specified as:

$$\tau_{t,xy} = {u_{\tau,nom}}^2 \frac{v_x}{v_{x,nom}} = \frac{v_x u_{\tau,nom} C_\mu^{0.25} k_p^{0.5}}{v_{x,nom}} = \frac{v_x C_\mu^{0.25} k_p^{0.5}}{u_{nom}^+} = \frac{v_x C_\mu^{0.25} k_p^{0.5}}{1/\kappa \ln(y_p^+) + C} \,. \tag{3.14}$$

For k, zero normal-gradient boundary conditions are set at the wall. In addition, the local equilibrium hypothesis is utilized: *"the production of k and its dissipation rate are assumed to be equal in the wall-adjacent control volume"* [ANSYS, Inc., 2009a]. The important part is to ensure that the center of the near-wall grid cell is inside the log-law region and the viscous sublayer is below the resolution of the discretization. Not resolving the viscous sublayer can be a good compromise between the computational effort and the accuracy of the results, cf. Pope [2006] and section B.3. Aside from the presented method, other strategies to implement wall functions exist in literature, e.g. Wilcox [2006], Versteeg and Malalasekra [2009]. A literature overview on more complex wall functions is given in the Bachelor's Thesis Scholz [2014].

Two Layers: If the viscous sublayer is resolved, the wall friction velocity can be approximated by the velocity gradient at the wall (Fig. 3.3). However, the k-ε equations can only be used in the turbulent, high-Reynolds region of the flow and not throughout the entire simulation domain. The lower bound is still indicated by the above-mentioned criterion ($y^+_{\mathrm{threshold}}$). In the region near the wall, which does not fulfill this criterion and where the flow is affected by viscous forces, a zero-equation turbulence model is used to calculate ν_t. Again, the dissipation value in the first cell which fulfills the y^+-criterion is fixed by:

$$\varepsilon_{\mathrm{p,wf}} = \frac{{u_\tau}^3}{\kappa\, y_\mathrm{p}}\,,$$

and k gets a zero-gradient boundary condition toward the near-wall region. The momentum balance equation receives a classical no-slip condition at the wall. Approaches with a less strict criterion are proposed by Menter [1994] who use more advanced blending functions to continuously go from the k-ε model to a one or two-equation turbulence model near the wall.

Others: The k-ε models of the renormalization group (RNG) are deduced by a more strict derivation out of the Navier-Stokes equations, e.g. Yakhot and Orszag [1986]. Durbin [1991] discusses a near-wall closure without introducing damping functions as they are used e.g. for the low-Re k-ε model which is discussed in the next section.

Low-Re K-Epsilon (low-Re k-ε) The low-Re k-ε models add extra terms or modify the coefficients of the high-Re k-ε model to account for the near-wall behavior. A good overview and comparison of these models is given by Patel et al. [1985]. They conclude that the model by Chien [1982], which is presented here, performs considerably better than others. The turbulent kinetic energy balance is identical with the one from the k-ε model (3.11), but the dissipation includes a damping function (D_ε):

$$\varepsilon = \tilde{\varepsilon} + D_\varepsilon\,, \tag{3.15}$$

and thus the equation for k can be written as:

$$\frac{\partial\,(k)}{\partial t} + \nabla\cdot(\boldsymbol{v}_\mathrm{g} k) - \nabla\cdot\left(\left(\nu_\mathrm{g} + \frac{\nu_\mathrm{t}}{\sigma_\mathrm{k}}\right)\nabla k\right) - 2\nu_\mathrm{t}\mathbf{S}\cdot\mathbf{S} + \tilde{\varepsilon} + D_\varepsilon = 0\,. \tag{3.16}$$

The dissipation balance is changed by introducing additional functions (E_k, f_1, and f_2) to account for a damping towards the wall:

$$\frac{\partial\,(\tilde{\varepsilon})}{\partial t} + \nabla\cdot(\boldsymbol{v}_\mathrm{g}\tilde{\varepsilon}) - \nabla\cdot\left(\left(\nu_\mathrm{g} + \frac{\nu_\mathrm{t}}{\sigma_\varepsilon}\right)\nabla\tilde{\varepsilon}\right) - C_{1\tilde{\varepsilon}} f_1 \frac{\tilde{\varepsilon}}{k} 2\nu_\mathrm{t}\mathbf{S}\cdot\mathbf{S} + C_{2\tilde{\varepsilon}} f_2 \frac{\tilde{\varepsilon}^2}{k} - E_\mathrm{k} = 0\,. \tag{3.17}$$

Also, the kinematic eddy viscosity ν_t is dampened by f_μ:

$$\nu_\mathrm{t} = C_\mu f_\mu \frac{k^2}{\tilde{\varepsilon}} \,. \tag{3.18}$$

The auxiliary and damping functions are defined as:

$$D_\varepsilon = 2\nu_\mathrm{g} k / y^2 \,, \quad E_\mathrm{k} = -2\nu_\mathrm{g} \frac{\tilde{\varepsilon}}{y^2} \exp\left(-0.5 y^+\right) \,,$$

$$f_1 = 1 \,, \quad f_2 = 1 - 0.22 \exp\left(-\left(\frac{Re_\mathrm{t}}{6}\right)^2\right) \,, \quad f_\mu = 1 - \exp\left(-0.0115 y^+\right) \,, \quad Re_\mathrm{t} = \frac{k^2}{\nu\tilde{\varepsilon}} \,.$$

Finally, the model is closed with the following constants:

$$\sigma_\mathrm{k} = 1.00 \,,\ \sigma_\varepsilon = 1.30 \,,\ C_{1\tilde{\varepsilon}} = 1.35 \,,\ C_{2\tilde{\varepsilon}} = 1.80 \,,\ C_\mu = 0.09 \,.$$

K-Omega (k-ω)[4] The k-ω models are another group of models which allows for using the same equations in the turbulent flow and near the walls. In these models, the transport of turbulent kinetic energy is considered together with the turbulence frequency. As reported by Pope [2006] and Wilcox [2006], the earliest versions of k-ω turbulence models were proposed by Kolmogorov [1942] and Saffman [1970]. Later, David C. Wilcox and co-authors were the main driving forces for the k-ω models, but also other popular contributions to k-ω models are made, e.g. by Menter [1994]. In this thesis, the version published in Wilcox [2008] is presented. The turbulent kinetic energy balance equation is given by:

$$\frac{\partial\left(k\right)}{\partial t} + \nabla\cdot\left(\boldsymbol{v}_\mathrm{g} k\right) - \nabla\cdot\left(\left(\nu_\mathrm{g} + \sigma_\mathrm{k}\frac{k}{\omega}\right)\nabla k\right) - 2\nu_\mathrm{t}\mathbf{S}\cdot\mathbf{S} + \beta_k k\omega = 0 \,. \tag{3.19}$$

The balance equation for the turbulence frequency is:

$$\frac{\partial\left(\omega\right)}{\partial t} + \nabla\cdot\left(\boldsymbol{v}_\mathrm{g}\omega\right) - \nabla\cdot\left(\left(\nu_\mathrm{g} + \sigma_\omega\frac{k}{\omega}\right)\nabla\omega\right) - \alpha_\omega\frac{\omega}{k}2\nu_\mathrm{t}\mathbf{S}\cdot\mathbf{S} + \beta_\omega\omega^2 - \frac{\sigma_\mathrm{d}}{\omega}\nabla k\cdot\nabla\omega = 0 \,. \tag{3.20}$$

The eddy viscosity is then calculated by:

$$\nu_\mathrm{t} = \frac{k}{\tilde{\omega}} \,. \tag{3.21}$$

[4]The k-ω model used in this work builds upon an implementation performed in a supervised Master's Thesis, E. Coltman: Numerical investigation of turbulent flow around obstacles and evaporating porous media, *Master's Thesis*, Universität Stuttgart, 2017.

According to the model presented in Wilcox [2008], the following closure constants and relations are used:

$$\alpha_\omega = 0.52\,,\ \sigma_\mathrm{k} = 0.6\,,\ \sigma_\omega = 0.5\,,\ \beta_\mathrm{k} = 0.09\,,\ \beta_\omega = 0.0708\,,$$

$$\tilde{\omega} = \max\left\{\omega,\, 0.875\sqrt{\frac{2\mathbf{S}\cdot\mathbf{S}}{\beta_\mathrm{k}}}\right\}\,,\ \sigma_\mathrm{d} = \begin{cases} 0 & ,\text{ if }\ \nabla k\cdot\nabla\omega \le 0 \\ 0.125 & ,\text{ if }\ \nabla k\cdot\nabla\omega > 0 \end{cases}.$$

The boundary conditions for k and ω are presented in Wilcox [1988]. The condition for k is set as a Dirichlet condition at the wall, whereas the condition for ω would lead to an infinite value and thus ω_p is set in the first cell away from the wall (p):

$$k_\mathrm{wall} = 0\,,\ \omega_\mathrm{p} = \frac{6\nu_\mathrm{g}}{\beta_\omega y_\mathrm{p}}\,.$$

3.1.2.3 One-Equation Models

In this work, the model published by Spalart and Allmaras [1992] is used. However, after further developments, a newer version can be found in Allmaras et al. [2012], but also earlier versions of one-equation models are available, e.g. Baldwin and Barth [1990]. This one-equation model transports the quantity $\tilde{\nu}$, just called working variable [Allmaras et al., 2012]. This working variable already has the units of the eddy viscosity and can be converted via a model function (f_v1):

$$\nu_\mathrm{t} = \tilde{\nu} f_\mathrm{v1}\,.$$

Wilcox [2006] and Versteeg and Malalasekra [2009] propose that the correction terms which account for the transition or trip, might be dropped from the original equations, such that the balance equation simplifies to:

$$\frac{\partial\tilde{\nu}}{\partial t} + \nabla\cdot(\tilde{\nu}\boldsymbol{v}) - c_\mathrm{b1}\tilde{S}\tilde{\nu} - \frac{1}{\sigma_{\tilde{\nu}}}\nabla\cdot([\nu+\tilde{\nu}]\,\nabla\tilde{\nu}) - \frac{c_\mathrm{b2}}{\sigma_{\tilde{\nu}}}\left|\nabla\tilde{\nu}\right|^2 + c_\mathrm{w1} f_\mathrm{w}\frac{\tilde{\nu}^2}{y^2} = 0\,. \tag{3.22}$$

This balance equation is linked to the flow geometry by the distance to the closest wall (y). Further, the model uses the following functions and expressions:

$$\chi = \frac{\tilde{\nu}}{\nu}\,,\ f_\mathrm{v1} = \frac{\chi^3}{\chi^3 + c_\mathrm{v1}^3}\,,\ f_\mathrm{v2} = 1 - \frac{\chi}{1+f_\mathrm{v1}\chi}\,,$$

$$f_\mathrm{w} = g_\mathrm{w}\left(\frac{1+c_\mathrm{w3}^6}{g_\mathrm{w}^6 + c_\mathrm{w3}^6}\right)^{\frac{1}{6}}\,,\ g_\mathrm{w} = r_\mathrm{w} + c_\mathrm{w2}(r_\mathrm{w}^6 - r_\mathrm{w})\,,\ r_\mathrm{w} = \min\left[\frac{\tilde{\nu}}{\tilde{S}\kappa^2 y^2}, 10\right]\,.$$

Here, a modified mean effective strain rate ($\tilde{S}$) based on the mean rotation rate tensor ($\boldsymbol{\Omega}$) is used:

$$\tilde{S} = \sqrt{2\boldsymbol{\Omega}\cdot\boldsymbol{\Omega}} + \frac{\tilde{\nu}}{\kappa^2 y^2} f_{\mathrm{v2}}\,,\ \boldsymbol{\Omega} = \frac{1}{2}\left(\nabla \boldsymbol{v}_{\mathrm{g}} - \nabla \boldsymbol{v}_{\mathrm{g}}^{\mathsf{T}}\right)\,.$$

Finally, the model is closed with the following constants:

$$\sigma_{\tilde{\nu}} = {}^2\!/_3\,,\ c_{\mathrm{b1}} = 0.1355\,,\ c_{\mathrm{b2}} = 0.622\,,$$

$$c_{\mathrm{v1}} = 7.1\,,\ c_{\mathrm{w1}} = \frac{c_{\mathrm{b1}}}{\kappa^2} + \frac{1 + c_{\mathrm{b2}}}{\sigma_{\tilde{\nu}}}\,,\ c_{\mathrm{w2}} = 0.3\,,\ c_{\mathrm{w3}} = 2\,.$$

3.1.2.4 Zero-Equation Models[5]

The zero-equation turbulence models (also named algebraic turbulence models) are the first generation of turbulence models. Two different groups are presented in the following: mixing-length models with one algebraic equation for the entire domain and two-layer approaches with a switching mechanism.

Mixing-Length Models The first mixing-length model was proposed by L. Prandtl at the begin of the 20th century. In analogy to the kinetic gas theory, it assumes a proportionality of the main flow velocity gradient and the eddy viscosity (see also Fig. 3.2):

$$\nu_{\mathrm{t}} = l_{\mathrm{mix}}^2 \left|\frac{\partial v_{\mathrm{x}}}{\partial y}\right|\,, \tag{3.23}$$

which is the mixing length $l_{\mathrm{mix}} = \kappa y$. Here, y is equivalent to the wall-normal distance and v_{x} denotes the main velocity component. This model was improved by van Driest [1956], who changed the mixing length such that the eddy viscosity is dampened near the wall:

$$l_{\mathrm{mix}} = \kappa y \left[1 - \exp\left(-y^+/26\right)\right]\,. \tag{3.24}$$

This model was again improved by Hanna et al. [1981], they corrected the asymptotic behavior of the Reynolds shear stress:

$$l_{\mathrm{mix}} = \kappa y \frac{1 - \exp\left(-y^+/26\right)}{\sqrt{1 - \exp(-0.26 y^+)}}\,. \tag{3.25}$$

[5] Parts of the zero-equation models and their implementations are revised versions of T. Fetzer: Numerical analysis of the influence of turbulence on exchange processes between porous-medium and free flow, *Master's Thesis*, Universität Stuttgart, 2012 and a supervised Master's Thesis, P. Samantray: Implementation of advanced algebraic turbulence models on a staggered grid, *Master's Thesis*, Universität Stuttgart, 2014.

Two-Layer Models Baldwin and Lomax [1978] presented a model in which the eddy viscosity depends on two equations which are valid in different areas of the flow:

$$\nu_\mathrm{t} = \begin{cases} \nu_\mathrm{inner} = l_\mathrm{mix}^2 \left|\boldsymbol{\omega}\right| & y < y_\mathrm{cross} \\ \nu_\mathrm{outer} = 0.02688 F_\mathrm{wake} F_\mathrm{kleb} & y \geq y_\mathrm{cross} \end{cases} . \tag{3.26}$$

The switching point y_cross is defined as the smallest value of y at which $\mu_\mathrm{inner} = \mu_\mathrm{outer}$. For the inner region, Van Driest's expression of the mixing length is used (3.24). Instead of the velocity gradient, the magnitude of the vorticity ($|\boldsymbol{\omega}|$) is applied:

$$|\boldsymbol{\omega}| = \sqrt{\left(\frac{\partial v_\mathrm{x}}{\partial y} - \frac{\partial v_\mathrm{y}}{\partial x}\right)^2 + \left(\frac{\partial v_\mathrm{y}}{\partial z} - \frac{\partial v_\mathrm{z}}{\partial y}\right)^2 + \left(\frac{\partial v_\mathrm{z}}{\partial x} - \frac{\partial v_\mathrm{x}}{\partial z}\right)^2} . \tag{3.27}$$

However, in the case of a parallel flow field, all mean gradients despite $\partial v_\mathrm{x}/\partial y$ are negligible. For the calculation of the eddy viscosity in the outer region, the following additional functions are necessary:

$$F_\mathrm{wake} = \min \begin{cases} y_\mathrm{Fmax} F_\mathrm{max} \\ 0.25 y_\mathrm{Fmax} \frac{(\Delta U)^2}{F_\mathrm{max}} \end{cases} \tag{3.28}$$

$$F = y \left|\boldsymbol{\omega}\right| \left[1 - \exp\left(-y^+/26\right)\right] \tag{3.29}$$

$$F_\mathrm{max} = \max\left\{F\right\} \tag{3.30}$$

$$y_\mathrm{Fmax} = y(F_\mathrm{max}) \tag{3.31}$$

$$\Delta \boldsymbol{v} = \sqrt{v_\mathrm{x,max}^2 + v_\mathrm{y,max}^2 + v_\mathrm{z,max}^2} - \sqrt{v_\mathrm{x,min}^2 + v_\mathrm{y,min}^2 + v_\mathrm{z,min}^2} \tag{3.32}$$

$$F_\mathrm{kleb} = \left[1 + 5.5 \left(\frac{0.3y}{y_\mathrm{Fmax}}\right)^6\right]^{-1} . \tag{3.33}$$

A similar zero-equation turbulence model with a two-layer approach is proposed by Cebeci and Smith [1974]. Because of their similarity, the Cebeci and Smith model is not further evaluated in this work. Mavriplis [1990] showed how these two-layer models can be implemented for non-flat geometries on unstructured grids.

3.1.2.5 Boundary Layer Models

The last approach is based on the boundary layer theory which is intensively discussed in Schlichting and Gersten [2006]. In analogy to the viscous region in the law of the wall, in which the velocity gradient and thus the viscous shear are relatively constant, it is assumed that the same holds for the component and energy transport. The flow field is assumed to be composed of a laminar, diffusion-dominated and a turbulent, fully-mixed sublayer, see

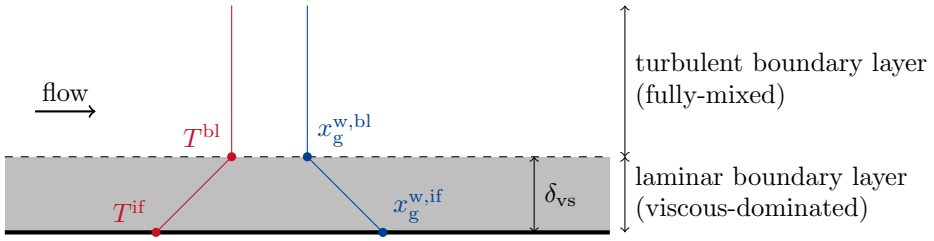

Figure 3.4: Schematic sketch of necessary information for approximating the flux across the laminar boundary layer, after Bird et al. [2007] and Fetzer et al. [2016]. Note that the boundary layer thicknesses might be different for mass, momentum, and energy.

Fig. 3.4. The concentration or temperature in the turbulent layer is assumed to be constant and equals to the known value at the inflow boundary, the concentration and temperature gradient can be calculated by knowing the boundary layer thickness. The edge of the viscous sublayer can be estimated with[6]:

$$\delta_{\mathrm{vs}} = \frac{y_{\mathrm{vs}}^{+} \nu_{\mathrm{g}}}{u_{\tau}} \,. \tag{3.34}$$

Depending on the source, the end of the viscous sublayer is in between $5 < y_{\mathrm{vs}}^{+} < 11$. According to White [2011], the wall shear stress $\tau_{\mathrm{g,xy,wall}}$ and thus the wall friction velocity u_{τ} is given by:

$$\tau_{\mathrm{g,xy,wall}} = \frac{c_{\mathrm{f}} \varrho_{\mathrm{g}} v_{\mathrm{x,max}}^{2}}{2} \,, u_{\tau} = \sqrt{\frac{\tau_{\mathrm{g,xy,wall}}}{\varrho_{\mathrm{g}}}} \,.$$

Different empirical formulations for the skin friction coefficient (c_{f}) can be found in literature, e.g. Schlichting and Gersten [2006], Truckenbrodt [2008a,b], Pope [2006]. These skin friction coefficients will be discussed in the context of surface roughness in section 3.3.5. Finally, this yield the following expression for the sublayer thickness:

$$\delta_{\mathrm{vs}} = \frac{y_{\mathrm{vs}}^{+} \nu_{\mathrm{g}}}{v_{\mathrm{x,max}} \sqrt{c_{\mathrm{f}}/2}} \,. \tag{3.35}$$

3.1.3 Component Mass Balance

The mass-based balance equation for transporting a component κ in the free flow is:

$$\frac{\partial \left(\varrho_{\mathrm{g}} X_{\mathrm{g}}^{\kappa} \right)}{\partial t} + \nabla \cdot \left(\varrho_{\mathrm{g}} X_{\mathrm{g}}^{\kappa} \boldsymbol{v}_{\mathrm{g}} \right) + \nabla \cdot \boldsymbol{j}_{\mathrm{mass,eff}}^{\kappa,\mathrm{ff}} = 0 \,. \tag{3.36}$$

[6] CFD Online proposes this procedure to estimate the y^{+} value for the grid generation, `https://www.cfd-online.com/Wiki/Y_plus_wall_distance_estimation`, accessed on January 04, 2018.

For simplicity, the effective diffusive-dispersive flux ($\boldsymbol{j}^{\kappa,\mathrm{ff}}_{\mathrm{mass,eff}}$) is used. This flux combines the molecular transport by diffusion and the dispersive transport by turbulent fluctuations:

$$\boldsymbol{j}^{\kappa,\mathrm{ff}}_{\mathrm{mass,eff}} = \boldsymbol{j}^{\kappa,\mathrm{ff}}_{\mathrm{mass,g}} + \boldsymbol{j}^{\kappa,\mathrm{ff}}_{\mathrm{mass,t}} = -D^{\kappa}_{\mathrm{g}} \varrho_{\mathrm{mol,g}} M^{\kappa} \nabla x^{\kappa}_{\mathrm{g}} - D_{\mathrm{t}} \varrho_{\mathrm{mol,g}} M^{\kappa} \nabla x^{\kappa}_{\mathrm{g}} \,. \tag{3.37}$$

Note that the only difference between laminar and turbulent flow with respect to component transport is that there are no turbulent dispersive fluxes, hence $\boldsymbol{j}^{\kappa,\mathrm{ff}}_{\mathrm{mass,t}} = 0$. For turbulent flow, the eddy viscosity can be converted to the eddy diffusivity (D_{t}) by the turbulent Schmidt number, $Sc_{\mathrm{t}} = \nu_{\mathrm{t}}/D_{\mathrm{t}}$. Even though a value of 0.7 is a common choice for Sc_{t}, Flesch et al. [2002] and Tominaga and Stathopoulos [2007] report a wide range of values. Tominaga and Stathopoulos [2007] analyze the turbulent Schmidt numbers for urban flow, resulting in values between 0.2 and 1.3 which are discussed with respect to their influence. Flesch et al. [2002] conclude that a value of 0.6 is appropriate for tracer plumes above a bare ground, by evaluating their experiments.
An option to reduce the model complexity is to assume composition independent fluid properties. This allows for decoupling flow and transport equation as e.g. used in Masson et al. [2016]. In this work, a model that does not consider a feedback from the component mass transport to the momentum transport is called *transport* model.

3.1.4 Energy Balance

The energy transport in the free flow is modeled with the following balance equation:

$$\frac{\partial \left(\varrho_{\mathrm{g}} u_{\mathrm{g}}\right)}{\partial t} + \nabla \cdot \left(\varrho_{\mathrm{g}} h_{\mathrm{g}} \boldsymbol{v}_{\mathrm{g}}\right) + \sum_{\kappa \in \{\mathrm{w,a}\}} \nabla \cdot \left(h^{\kappa}_{\mathrm{g}} \boldsymbol{j}^{\kappa,\mathrm{ff}}_{\mathrm{mass,eff}}\right) - \nabla \cdot \left(\lambda_{\mathrm{eff}} \nabla T\right) = 0 \,. \tag{3.38}$$

In which the specific internal energy (u_{g}) is included in the storage term, and a transport of enthalpy by the diffusive-dispersive fluxes: $h^{\kappa}_{\mathrm{g}} \boldsymbol{j}^{\kappa,\mathrm{ff}}_{\mathrm{mass,eff}}$. In addition to the conductive flux inside the fluid, a turbulent conductive flux is considered. Both are lumped in an effective flux:

$$\boldsymbol{f}_{\mathrm{eff}} = \lambda_{\mathrm{eff}} \nabla T = \lambda_{\mathrm{g}} \nabla T + \lambda_{\mathrm{t}} \nabla T \,. \tag{3.39}$$

The relation between the eddy viscosity and the eddy thermal conductivity (λ_{t}) is expressed by the turbulent Prandtl number: $Pr_{\mathrm{t}} = \nu_{\mathrm{t}} \varrho_{\alpha} c_{\mathrm{p},\alpha} / \lambda_{\mathrm{t}}$. Wilcox [2006] proposes $Pr_{\mathrm{t}} \approx 0.9$ for boundary layers. According to Bird et al. [2007] and references therein values of 0.7 to 0.9 for gas flow in conduits and 0.85 for circular tubes are proposed. However, Cebeci [1973] reports a value of 1.22 for air at high Reynolds numbers.

3.2 Porous Medium

The fundamental upscaled models for flow in porous media are well-established and were proposed between the mid of the 19th century to the beginning of the 20th century. All models presented here are based on the assumptions of (i) gas and liquid as mobile phases, (ii) a rigid and isotropic porous medium, (iii) Fickian diffusion without dispersion, (iv) unique capillary pressure–saturation relationship (no hysteresis), and (v) local thermodynamic equilibrium. Further details on porous-medium models can be found in textbooks as Bear [1988], Helmig [1997].

3.2.1 Mass and Momentum Balance

For balancing mass inside the porous medium, the porosity and the saturation have to be considered for the storage term:

$$\sum_{\alpha\in\{\mathrm{l,g}\}} \left(\phi \frac{\partial \left(\varrho_\alpha S_\alpha\right)}{\partial t} + \nabla \cdot \left(\varrho_\alpha \boldsymbol{v}_\alpha\right) + \sum_{\kappa\in\{\mathrm{w,a}\}} \nabla \cdot \boldsymbol{j}^{\kappa,\mathrm{pm}}_{\mathrm{mass},\alpha} \right) = 0\,. \tag{3.40}$$

In contrast to the free flow, where the Navier-Stokes equations are used for balancing momentum, different upscaled models are available for flow in a porous medium.

3.2.1.1 Darcy Law

The maybe most important experiments concerning flow in porous media, were performed by Henry Darcy in 1856. He applied a gradient in fluid pressure and measured the flow through soil samples. Finally, he found a proportionality factor between the pressure difference and the velocity, which is called Darcy law:

$$\boldsymbol{v}_\alpha = -\frac{k_{\mathrm{r},\alpha} K}{\mu_\alpha} \left(\nabla p_\alpha - \varrho_\alpha \boldsymbol{g}\right)\,. \tag{3.41}$$

This equation is valid for creeping flow with $Re_{\mathrm{pore}} < 1$. It considers an intrinsic permeability K which is only a property of the porous medium. In general, the intrinsic permeability is a tensor, but can be simplified as a scalar for isotropic porous media. For single-phase flow, the relative permeability $k_{\mathrm{r},\alpha}$ equals one. The parametrization of $k_{\mathrm{r},\alpha}$ for multi-phase flow is explained in section 2.5.2.

3.2.1.2 Richards Equation

Richards [1931] proposes a simplification of the Darcy law for flow in the unsaturated zone. Assuming that the gas phase is more mobile than the liquid phase ($\mu_\mathrm{g} \ll \mu_\mathrm{l}$), differences in gas-phase pressure equilibrate immediately and no pressure gradient evolves. Thus, the gas-phase pressure equals the pressure in the atmosphere and the liquid-phase pressure corresponds to the capillary pressure. Based on this assumption, neither gas-phase flow nor transport therein is considered in the model. It is obvious that this poses problems e.g. when diffusive transport of water vapor in absence of liquid water is important, see Szymkiewicz [2013]. Vanderborght et al. [2017] and references therein discuss remedies for this problem. One option is to model an increased mobility of liquid water for low water saturations.

3.2.1.3 Dupuit-Forchheimer Equation

The above-mentioned laws are only valid for creeping flow ($Re_\mathrm{pore} < 1$). If inertia effects cannot be entirely neglected, based on findings by Dupuit in 1863 and Forchheimer in 1901, the so-called Dupuit-Forchheimer equation can be used for single-phase flow, cf. Nield and Bejan [2017]:

$$(\nabla p_\alpha - \varrho_\alpha \boldsymbol{g}) = -\frac{\mu_\alpha}{K}\boldsymbol{v}_\alpha - \frac{\varrho_\alpha C_\mathrm{F}}{\sqrt{K}}\left|\boldsymbol{v}_\alpha\right|\boldsymbol{v}_\alpha\,. \tag{3.42}$$

The last term in this equation represents the additional inertia forces, for which Nield and Bejan [2017] and references therein propose a constant Forchheimer coefficient $C_\mathrm{F} = 0.55$. However, there is no common sense how to transfer this single-phase equation to multi-phase conditions: e.g. Wu [2002], Skjetne and Auriault [1999], and Nuske [2014] propose different equations. In this thesis, the approach from Nuske [2014] is used, in which the relative permeabilities are included:

$$(\nabla p_\alpha - \varrho_\alpha \boldsymbol{g}) = -\frac{\mu_\alpha}{k_{\mathrm{r},\alpha} K}\boldsymbol{v}_\alpha - \frac{\varrho_\alpha C_\mathrm{F}}{\sqrt{K} k_{\mathrm{r},\alpha}}\left|\boldsymbol{v}_\alpha\right|\boldsymbol{v}_\alpha\,. \tag{3.43}$$

3.2.2 Component Mass Balance

The mass-based balance equation for transporting a component κ in the porous medium is:

$$\sum_{\alpha\in\{\mathrm{l,g}\}}\left(\phi\frac{\partial\left(\varrho_\alpha S_\alpha X_\alpha^\kappa\right)}{\partial t} + \nabla\cdot\left(\varrho_\alpha X_\alpha^\kappa \boldsymbol{v}_\alpha\right) + \nabla\cdot\boldsymbol{j}^{\kappa,\mathrm{pm}}_{\mathrm{mass},\alpha}\right) = 0\,. \tag{3.44}$$

If the equations for all components are summed-up, the total mass-balance (3.40) is gained.

3.2.3 Energy Balance

With the assumption of local thermodynamic equilibrium, the temperature in one REV is the same for all phases and thus only one energy balance is required:

$$\sum_{\alpha\in\{\mathrm{l,g}\}} \left(\phi \frac{\partial \left(\varrho_\alpha S_\alpha u_\alpha \right)}{\partial t} + \nabla \cdot \left(\varrho_\alpha h_\alpha \boldsymbol{v}_\alpha \right) \right) + (1-\phi)\, \varrho_\mathrm{s} c_\mathrm{s} \frac{\partial T}{\partial t} - \nabla \cdot \left(\lambda^\mathrm{pm} \nabla T \right) = 0\,. \tag{3.45}$$

Properties of the solid matrix material are indicated by the subscript (s). It is assumed that the imposed empirical model for the effective thermal conductivity (λ^pm) includes the conductive energy fluxes as well as the energy fluxes transported by diffusive-dispersive mass fluxes, see e.g. Roth [2012], Lu et al. [2011] for a detailed discussion of this topic.

3.3 Interface

This section presents the conditions for coupling mass, momentum, and energy transport across a porous-medium free-flow interface. In addition to the coupling conditions for each balance equation, possible simplifications are presented which can be included in the coupling or can be applied as dynamic boundary conditions when simulating only one subdomain. In the second part, it is shown how a rough interface can be considered in the model.

The interface coupling conditions are based on the assumptions of local thermodynamic equilibrium and the continuity of fluxes. This is a common approach in literature, see e.g. Moeckel [1975], Layton et al. [2002], Mosthaf et al. [2011]. The coupling conditions for a non-isothermal multi-phase multi-component system, are based on the work presented in Mosthaf et al. [2011] and Fetzer et al. [2016]. Vanderborght et al. [2017] describes different modeling techniques for coupled or uncoupled porous-medium and free flow simulations.

The conditions are classified by the involved balance equations. Mosthaf et al. comprise the conditions for the momentum and the total mass balances as mechanical equilibrium, the conditions for the component mass balances as chemical equilibrium, and the conditions for the energy balances as thermal equilibrium. The coupling conditions presented here differ from previous versions [Mosthaf et al., 2011, Fetzer et al., 2016] by the diffusive-dispersive fluxes which are considered in the mass-based total mass balance. In addition, it differs from Mosthaf et al. [2011] by the ability of the diffusive-dispersive fluxes inside the free flow to transport enthalpy.
In the following, the normal vector ($\boldsymbol{n}$) is pointing outside of the respective subdomain and thus $\boldsymbol{n}^\mathrm{ff} = -\boldsymbol{n}^\mathrm{pm}$.

3.3.1 Total Mass Balances

The condition for coupling the total mass states that the fluxes of (3.1) and (3.40) are equal:

$$\left[\left(\varrho_{\mathrm{g}}\boldsymbol{v}_{\mathrm{g}}+\sum_{\kappa\in\{\mathrm{w,a}\}}\boldsymbol{j}^{\kappa}_{\mathrm{mass,eff}}\right)\cdot\boldsymbol{n}\right]^{\mathrm{ff,if}}=-\left[\left(\sum_{\alpha\in\{\mathrm{l,g}\}}\left(\varrho_{\alpha}\boldsymbol{v}_{\alpha}+\sum_{\kappa\in\{\mathrm{w,a}\}}\boldsymbol{j}^{\kappa}_{\mathrm{mass},\alpha}\right)\right)\cdot\boldsymbol{n}\right]^{\mathrm{pm,if}}. \tag{3.46}$$

No liquid water can exist in the free flow and a net non-zero liquid-phase flux from the porous-medium side corresponds to a direct vaporization or condensation.

3.3.2 Momentum Balances

The momentum flux condition can be split into two parts. The normal part assumes continuity of normal stresses. For the tangential part, different slip conditions may be employed: coupled to the porous-medium flow [Beavers and Joseph, 1967], coupled to the porous-medium permeability [Saffman, 1971], or standard wall functions for turbulence models.

3.3.2.1 Normal Component

The coupling condition for normal momentum depends on the chosen porous-medium model. For Darcy flow [cf. Mosthaf et al., 2011] or Forchheimer flow [cf. Cimolin and Discacciati, 2013, Whitaker, 1996], the normal stresses are continuous across the interface:

$$\left[\left(\varrho_{\mathrm{g}}\boldsymbol{v}_{\mathrm{g}}\boldsymbol{v}_{\mathrm{g}}^{\intercal}-\boldsymbol{\tau}_{\mathrm{eff}}+p_{\mathrm{g}}\mathbf{I}\right)\boldsymbol{n}\right]^{\mathrm{ff,if}}=-\left[\left(p_{\mathrm{g}}\mathbf{I}\right)\boldsymbol{n}\right]^{\mathrm{pm,if}}. \tag{3.47}$$

The potential pressure jump, $p_{\mathrm{g}}^{\mathrm{ff,if}}\neq p_{\mathrm{g}}^{\mathrm{pm,if}}$, results from the different model concepts in the two subdomains.

3.3.2.2 Tangential Components

The free flow and the flow in the porous medium can be linked by the condition proposed by Beavers and Joseph [1967]:

$$\left[\left(-\frac{\sqrt{K}}{\alpha_{\mathrm{BJ}}}\left(\nabla\boldsymbol{v}_{\mathrm{g}}\right)\boldsymbol{n}-\boldsymbol{v}_{\mathrm{g}}\right)\cdot\boldsymbol{t}_{i}\right]^{\mathrm{ff,if}}=\left[-\boldsymbol{v}\cdot\boldsymbol{t}_{i}\right]^{\mathrm{pm,if}}. \tag{3.48}$$

This condition was originally derived for laminar single-phase flow, but work by Hahn et al. [2002] indicates that it also works for turbulent flow.

Saffman Simplification This work uses the simplification proposed by Saffman. It assumes that the tangential flow in the porous medium is negligible for the exchange of momentum, because: $[\boldsymbol{v} \cdot \boldsymbol{t}_i]^{\mathrm{pm,if}} \approx 0$. Therefore, the condition can be used as a free-flow boundary condition only, as it does not depend on porous-medium processes:

$$\left[\left(-\frac{\sqrt{K}}{\alpha_{\mathrm{BJ}}}\left(\nabla \boldsymbol{v}_{\mathrm{g}}\right)\boldsymbol{n} - \boldsymbol{v}_{\mathrm{g}}\right) \cdot \boldsymbol{t}_i\right]^{\mathrm{ff,if}} = 0\,. \tag{3.49}$$

If this condition is extended such that multi-phase flow effects are included, the resulting slip-velocity of the free gas flow is decreased, see Fritsch [2014].

Wall Functions As discussed earlier, wall functions for the k-ε model are necessary, if the discretization is coarse and the near-wall region is not resolved appropriately. In this case, the simplification of no-slip conditions, $[\boldsymbol{v}_{\mathrm{g}} \cdot \boldsymbol{t}_i]^{\mathrm{ff,if}} = 0$, is made and the standard wall functions for the k-ε model are used, see (3.14).

3.3.3 Component Mass Balances

For a component κ, chemical equilibrium in terms of continuity of mass fractions is applied:

$$\left[X_{\mathrm{g}}^{\kappa}\right]^{\mathrm{ff,if}} = \left[X_{\mathrm{g}}^{\kappa}\right]^{\mathrm{pm,if}}\,. \tag{3.50}$$

Mosthaf et al. [2011] write that, in general, it should be asked for continuity in chemical potential. But, due to the unavoidable pressure jump, this would also result in jumps in mass or mole fractions. The continuity of the respective component fluxes is given by:

$$\left[\left(\varrho_{\mathrm{g}} X_{\mathrm{g}}^{\kappa} \boldsymbol{v}_{\mathrm{g}} + \boldsymbol{j}_{\mathrm{mass,eff}}^{\kappa}\right) \cdot \boldsymbol{n}\right]^{\mathrm{ff,if}} = -\left[\sum_{\alpha \in \{\mathrm{l,g}\}} \left(\varrho_{\alpha} X_{\alpha}^{\kappa} \boldsymbol{v}_{\alpha} + \boldsymbol{j}_{\mathrm{mass},\alpha}^{\kappa}\right) \cdot \boldsymbol{n}\right]^{\mathrm{pm,if}}\,. \tag{3.51}$$

Resistance Term Models The total mass flux over the interface can be simplified by using one-dimensional transfer resistance models. This can be done via forward estimations or backward fitting, cf. Vanderborght et al. [2017], Fetzer et al. [2017c] and reference therein. Resistance term models can be used to downscale findings of a full complex to a less complex model (one-dimensional or porous medium only). If the total water mass flux or evaporation

rate is known, the mass transfer resistance (r_{mass}) can be fitted by evaluating the mole fraction at the interface and at a reference height:

$$\left[\left(\varrho_{\mathrm{g}} X_{\mathrm{g}}^{\kappa} \boldsymbol{v}_{\mathrm{g}} + \boldsymbol{j}_{\mathrm{mass,eff}}^{\kappa}\right) \cdot \boldsymbol{n}\right]^{\mathrm{ff,if}} = -\frac{1}{r_{\mathrm{mass}}} \varrho_{\mathrm{mol,g}} M^{\kappa} \left(x_{\mathrm{g}}^{\kappa,\mathrm{if}} - x_{\mathrm{g}}^{\kappa,\mathrm{ref}}\right) . \tag{3.52}$$

Boundary Layer Models Under the assumption that (i) diffusion through the viscous sublayer is the limiting factor for mass transfer and (ii) boundary layers form and the flow is fully mixed outside the viscous sublayer, the diffusive fluxes in eq. (3.51) can be replaced by:

$$\left[\boldsymbol{j}_{\mathrm{mass,eff}}^{\kappa} \cdot \boldsymbol{n}\right]^{\mathrm{ff,if}} = -D_{\mathrm{g}}^{\kappa} \varrho_{\mathrm{mol,g}} M^{\kappa} \frac{x_{\mathrm{g}}^{\kappa,\mathrm{if}} - x_{\mathrm{g}}^{\kappa,\mathrm{bl}}}{\delta_{\mathrm{vs}}} . \tag{3.53}$$

The mole fraction gradient is build with a prescribed value at the edge of the boundary layer, the implicitly calculated value at the interface, and a boundary layer thickness (see Fig. 3.4).

Wall Functions For two-equation turbulence models, the already mentioned wall functions can be used to approximate the fluxes at the interface. According to the ANSYS Fluent Theory's guide [ANSYS, Inc., 2009a] and in analogy to the momentum wall function (3.14), the wall function for a component κ can be formulated as:

$$\left[\boldsymbol{j}_{\mathrm{mass,eff}}^{\kappa} \cdot \boldsymbol{n}\right]^{\mathrm{ff,if}} = -\frac{\left(x_{\mathrm{g}}^{\kappa,\mathrm{if}} - x_{\mathrm{g,p}}^{\kappa}\right) \varrho_{\mathrm{mol,g}} M^{\kappa} C_{\mu}^{0.25} k_{\mathrm{p}}^{0.5}}{Sc_{\mathrm{t}} \left(1/\kappa \ln(y_{\mathrm{p}}^{+} E) + \mathcal{S}\right)} . \tag{3.54}$$

This wall function uses the law of the wall, thus point "p" has to be located in the turbulent log law region ($y_{\mathrm{p}}^{+} \gtrapprox 30$). The log-law constant is $E = 9.793$ and equals the integration constant $C \approx 5.5 \approx 1/\kappa \ln(E)$. The $\mathcal{S}$-function is identical to the $\mathcal{P}$-function used in the temperature wall function (3.60), with the difference, that instead of Prandtl numbers Schmidt numbers are used. For typical Schmidt numbers, e.g. $Sc_{\mathrm{t}} = 0.7$ and $Sc_{\mathrm{g}} = 0.63$, this results in a value of $\mathcal{S} = -0.897$.

Mass Transfer Models Until here, the diffusive fluxes across the interface are independent of the saturation. Mosthaf et al. [2014] present different model concepts which include the saturation at the interface or near-interface cell and analyze how these models affect the evaporation rate.

3.3.4 Energy Balances

Finally, the coupling conditions are completed by ensuring continuity of temperature:

$$[T]^{\mathrm{ff,if}} = [T]^{\mathrm{pm,if}} \,, \tag{3.55}$$

and energy fluxes:

$$\left[\left(\varrho_{\mathrm{g}} h_{\mathrm{g}} \boldsymbol{v}_{\mathrm{g}} + \sum_{\kappa\in\{\mathrm{w,a}\}} h_{\mathrm{g}}^{\kappa} \boldsymbol{j}_{\mathrm{mass,eff}}^{\kappa} - \lambda_{\mathrm{eff}} \nabla T\right) \cdot \boldsymbol{n}\right]^{\mathrm{ff,if}} = -\left[\left(\sum_{\alpha\in\{\mathrm{l,g}\}} \varrho_{\alpha} h_{\alpha} \boldsymbol{v}_{\alpha} - \lambda \nabla T\right) \cdot \boldsymbol{n}\right]^{\mathrm{pm,if}} . \tag{3.56}$$

Resistance Term Models If the total energy flux is known, the energy transfer resistance (r_{energy}) for a one-dimensional resistance term model can be fitted by evaluating the temperature at the interface and at a reference height:

$$\left[\left(\varrho_{\mathrm{g}} h_{\mathrm{g}} \boldsymbol{v}_{\mathrm{g}} + \sum_{\kappa\in\{\mathrm{w,a}\}} h_{\mathrm{g}}^{\kappa} \boldsymbol{j}_{\mathrm{mass,eff}}^{\kappa} - \lambda_{\mathrm{eff}} \nabla T\right) \cdot \boldsymbol{n}\right]^{\mathrm{ff,if}} = -\frac{1}{r_{\mathrm{energy}}} \lambda_{\mathrm{g}} \left(T^{\mathrm{if}} - T^{\mathrm{ref}}\right) . \tag{3.57}$$

Boundary Layer Models In similarity to the component boundary layer model it is assumed that (i) conduction through the viscous sublayer is the limiting factor for energy transfer and (ii) boundary layers form and the flow is fully mixed outside the viscous sublayer. Hence, in addition to the diffusive fluxes, the conductive fluxes in eq. (3.56) can be replaced by:

$$[(\lambda_{\mathrm{eff}} \nabla T) \cdot \boldsymbol{n}]^{\mathrm{ff,if}} = -\lambda_{\mathrm{g}} \frac{T^{\mathrm{if}} - T^{\mathrm{bl}}}{\delta_{\mathrm{vs}}} \,. \tag{3.58}$$

This formulation requires a fully-mixed temperature at the boundary layer edge, the interface temperature, and a boundary layer thickness as model input (see Fig. 3.4).

Wall Functions More literature is available for temperature wall functions than for component wall functions. Equivalent descriptions of such wall functions are found in Versteeg and Malalasekra [2009], ANSYS, Inc. [2009a], and Defraeye et al. [2010], Defraeye [2011]:

$$[(\lambda_{\mathrm{eff}} \nabla T) \cdot \boldsymbol{n}]^{\mathrm{ff,if}} = -\frac{\left(T^{\mathrm{if}} - T_{\mathrm{p}}\right) \varrho c_{\mathrm{p}} C_{\mu}^{0.25} k_{\mathrm{p}}^{0.5}}{Pr_{\mathrm{t}} \left(1/\kappa \ln(y_{\mathrm{p}}^{+} E) + \mathcal{P}\right)} \,. \tag{3.59}$$

Again, the wall function should only be applied for y_p^+ being inside the turbulent region, however some authors apply it just outside the viscous sublayer $y_\mathrm{p}^+ \gtrapprox 11$. According to Malin [1987] different $\mathcal{P}$-functions exist in literature to represent the resistance of heat transfer (or mass transfer if Schmidt numbers are used) through the viscous sublayer. Here, the $\mathcal{P}$-function after Jayatilleke is used (see Malin [1987], Versteeg and Malalasekra [2009] and reference therein):

$$\mathcal{P} = 9.24 \left[\left(\frac{Pr_\mathrm{g}}{Pr_\mathrm{t}} \right)^{3/4} - 1 \right] \left[1 + 0.28 \exp\left(-0.007^{Pr_\mathrm{g}/Pr_\mathrm{t}} \right) \right] , \tag{3.60}$$

which results in $\mathcal{P} = -0.6711$ for typical Prandtl numbers, e.g. $Pr_\mathrm{t} = 0.8$ and $Pr_\mathrm{g} = 0.74$.

3.3.5 Roughness[7]

Sand-grain roughness may affect the boundary layer development and thus the diffusion-dominated transport near the interface. When rough surfaces are considered, at least two different cases have to be considered: hydraulically smooth and rough surfaces, cf. section 2.6.1. This section presents two concepts how the sand-grain roughness of the porous medium can be included in coupled models. Both concepts are originally derived for roughness elements on an impermeable plate and for both concepts the determination of a characteristic sand-grain roughness length k_s is critical.

3.3.5.1 Eddy-Viscosity Models

The first sand-grain roughness parametrization builds upon the eddy-viscosity concept. Cebeci [1978] writes that the wall distance and thus the eddy viscosity can be modified with the sand-grain roughness parametrization as published by Rotta [1962]:

$$y_\mathrm{wall} = y + y_\mathrm{rough} , \tag{3.61}$$

$$y_\mathrm{rough} = 0.9 \frac{\nu}{u_\tau} \left[\sqrt{k_\mathrm{s}^+} - k_\mathrm{s}^+ \exp\left(-k_\mathrm{s}^+/6 \right) \right] . \tag{3.62}$$

The application range of this concept is limited to transitionally and fully rough surfaces, the lower limit corresponds to hydrodynamically smooth surfaces:

$$4.535 < k_\mathrm{s}^+ = \frac{u_\tau k_\mathrm{s}}{\nu} < 2000 . \tag{3.63}$$

[7] This section is based on T. Fetzer, K. M. Smits, and R. Helmig: Effect of Turbulence and Roughness on Coupled Porous-Medium/Free-Flow Exchange Processes, *Transport in Porous Media*, 114(2):395–424, 2016. doi: 10.1007/s11242-016-0654-6; but also provides some additional information to this publication.

This concept is also used by Kuznetsov and Becker [2004] to analyze how energy transfer is altered due to the sand-grain roughness parameter.

3.3.5.2 Boundary Layer Models

As already discussed in section 3.1.2.5, the friction coefficient can be used to recalculate the boundary layer thickness. The problem is that above fully rough surfaces, the viscous boundary layer does not exist or is already fully merged inside the porous medium ($\delta_{\mathrm{vs}} < k_{\mathrm{s}}$). Thus, no boundary condition via boundary layer models can be defined. For hydraulically smooth surfaces, Truckenbrodt [2008b] proposes the following equation:

$$c_{\mathrm{f,hydr.\ smooth}} = 0.523 \left[\ln \left(0.06 \frac{v_{\mathrm{x}}^{\infty}\, x}{\nu} \right) \right]^{-2} . \tag{3.64}$$

In the case of hydraulically smooth surfaces, the viscous boundary layer is larger than the roughness elements ($\delta_{\mathrm{vs}} > k_{\mathrm{s}}$) and thus c_{f} is unaffected by k_{s}. In addition, Truckenbrodt [2008b] presents a formula for fully rough surfaces:

$$c_{\mathrm{f,rough}} = \left[1.89 - 1.62 \log \left({}^{k_{\mathrm{s}}}/_{x} \right) \right]^{-2.5} . \tag{3.65}$$

This model can only be used under the assumption that (i) equation (3.65) is also valid in the transition region even though a small bump occurs, see Fig. 3.5, (ii) a viscous sublayer still exists in the transition region. With the help of Fig. 3.5, the smooth and rough model can be combined via $c_{\mathrm{f}} = \max \left(c_{\mathrm{f,rough}}, c_{\mathrm{f,hydr.\ smooth}} \right)$.

The second approach uses the Darcy friction factor (f). Colebrook and White [Colebrook, 1939] developed an empirical formulation for flow in pipes or ducts which is converted to an explicit formulation by Haaland [1983]:

$$c_{\mathrm{f}} = \frac{f}{4} = \frac{1}{4} \left(-\frac{1.8}{n_{\mathrm{H}}} \log \left[\left(\frac{k_{\mathrm{s}}}{3.75\, d_{\mathrm{hy}}} \right)^{1.11 n_{\mathrm{H}}} + \left(\frac{6.9}{Re_{\mathrm{d}}} \right)^{n_{\mathrm{H}}} \right] \right)^{-2} , \tag{3.66}$$

Haaland suggests $n_{\mathrm{H}} = 3$ to obtain a more abrupt transition between the limiting regimes of smooth and fully rough cases. This formulation is valid for fully developed flow, thus the boundary layer thickness does not depend on the run-length, see Fig. 3.6. Again, $\delta_{\mathrm{vs}} > k_{\mathrm{s}}$ has to be ensured.

In addition to all these limitations, the c_{f}–expressions are empirical and alternative formulations exist which lead to different results and finally the resulting boundary layer strongly depends on the chosen y^{+} value, see (3.35).

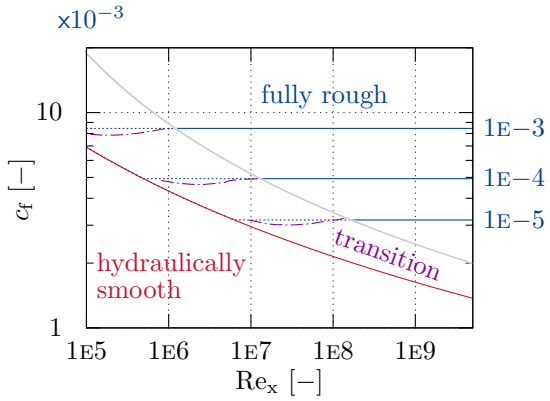

Figure 3.5: Friction coefficients for different Reynolds numbers, after Truckenbrodt [2008b]. The red line is valid for hydraulically smooth regimes (3.64), the solid blue lines are valid for fully rough surfaces (3.65), the magenta lines are valid in the transition region.

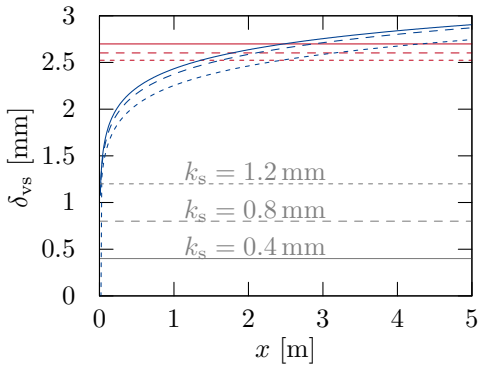

Figure 3.6: Boundary layer thicknesses according to friction coefficient models for $v_{x,g} = 1\,\mathrm{m/s}$ and $y^+ = 10$. The gray lines indicate the roughness heights for the respective line type. The red lines follow (3.66), the blue lines use the maximum of (3.64) and (3.65).

4 Numerical Model

First, this chapter illustrates two different spatial discretization schemes together with their numerical coupling concepts. Then, the discretization in time is explained, different aspects regarding the implementation are looked at, and the used software is presented.

4.1 Discretization in Space

Two spatial discretization methods for coupled porous-medium free-flow problems are used in this thesis. The first uses a vertex-centered finite-volume method (box) in both domains. The second employs a cell-centered finite-volume method (CCFV) in the porous medium and a staggered-grid or marker-and-cell finite-volume method (MAC) in the free flow. Fig. 4.1 visualizes the location of the primary variables (also called unknowns or degrees of freedom) for both discretization types. The porous-medium velocities are secondary variables because they are calculated with the Darcy or Forchheimer law (cf. section 3.2.1). For both methods and both domains, an upwinding scheme is used for the advective terms and an averaging for the diffusive and conductive terms.

4.1.1 Box–Box Coupling

For this coupling method, the box discretization method is used in both domains. First, a finite-element mesh is constructed for the entire domain. Then all barycenters of neighboring finite elements are connected via the midpoints of the faces between them. These faces form different finite-volume boxes. At the porous-medium free-flow interface the boxes are cut in two halves, each of them belonging to one subdomain, see Fig. 4.1.

4.1.1.1 Free-Flow and Porous-Medium Domains

For a detailed information about the used box method it is referred to Masson et al. [1994] and Mosthaf et al. [2014] for the free flow and to Huber and Helmig [2000] for the porous medium.

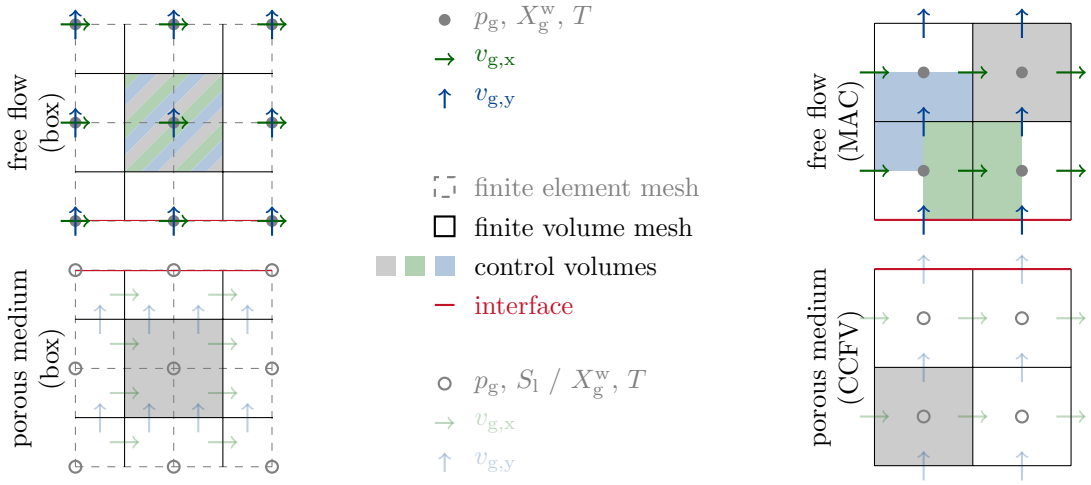

Figure 4.1: Spatial discretization methods and locations of the primary variables (p_g^{ff}, $\boldsymbol{v}_g^{ff}$, $X_g^{w,ff}$, T^{ff}, p_g^{pm}, S_l^{pm} or $X_g^{w,pm}$, T^{pm}). Left: box–box coupling, right: MAC–CCFV coupling. The common interface between the free-flow and the porous-medium domain is given at the boundary of both domains to highlight the available primary variables.

The box method is a co-located method which means that all primary variables are located at the same spot and share the same control volume. Modeling the free flow on co-located grids may lead to unphysical pressure oscillations, e.g. Versteeg and Malalasekra [2009]. For low Reynolds number flows, this can partially be avoided by stabilization terms as implemented in an earlier version of this model, see Mosthaf et al. [2014]. The advective fluxes between two finite-volume boxes are evaluated with a first-order upwind scheme. The gradients in primary variables are evaluated using the Ansatz functions of the finite-element mesh. For diffusive fluxes, the respective coefficients are harmonic or distance-weighted arithmetic averages at the flux evaluation point.

4.1.1.2 Coupling

The first use of the box–box coupling concept for evaporation problems is mentioned in Mosthaf et al. [2011]. In addition, Baber et al. [2012] give detailed information about the numerical implementation. The coupling conditions presented in section 3.3 are implemented in a way, that the primary variables from the porous medium are either used to set the respective ones in the free flow ($X_g^{w,pm}$, T^{pm}) or used inside the condition for the normal momentum flux (p_g^{pm}). The mass and energy fluxes are calculated from the free-flow side and then set for the porous-medium side.

4.1.2 MAC–CCFV Coupling

In contrast to the box–box coupling, this coupling uses two different discretization schemes with different locations of the primary variables.

4.1.2.1 Free-Flow and Porous-Medium Domains

To avoid the above-mentioned pressure oscillations, the free-flow equations are discretized using the marker-and-cell scheme, cf. Harlow and Welch [1965] and Versteeg and Malalasekra [2009]. The scalar primary variables (p_g^ff, $X_\mathrm{g}^\mathrm{w,ff}$, T^ff) are located at the center of each finite-volume cell. The velocity components ($v_{\mathrm{g},i}^\mathrm{ff}$) and their control volumes are shifted to the faces, see Fig. 4.1. For a more detailed description of the free-flow discretization it is referred to Grüninger et al. [2017]. All porous-medium primary variables are located at the cell center. The fluxes are calculated with a two-point flux approximation using a first-order upwind scheme for advective fluxes and harmonic or distance-weighted arithmetic coefficients for diffusive fluxes. The most important point to mention is that the normal velocity is the only primary variable located on the porous-medium free-flow interface.

4.1.2.2 Coupling[8]

Despite the normal velocity component, none of the primary variables is located at the interface (cf. Fig. 4.2). Therefore, the implementation of the coupling conditions is not straightforward. First, for the momentum coupling conditions, the interface gas-phase pressures ($p_\mathrm{g}^\mathrm{ff,if}$, $p_\mathrm{g}^\mathrm{pm,if}$) and the tangential velocities ($v_{\mathrm{g},\mathrm{t}_i}^\mathrm{ff,if} := \boldsymbol{v}_\mathrm{g}^\mathrm{ff,if} \cdot \boldsymbol{t}_i$) are missing. Second, for component and energy transport, the gradients in mole fractions and temperature cannot be formulated based one subdomain alone, but range over both domains. Third, continuity of mole fractions and temperature has to be imposed implicitly.
In the following, first the momentum coupling conditions are examined. Afterward, the different coupling methods (CM) proposed and compared in Fetzer et al. [2017b] are presented. It is started with CM4, the method closest to the continuous coupling conditions presented in section 3.3. Then, from CM3 to CM1, more and more assumptions are made to simplify the discretized coupling conditions.

[8] This section bases on T. Fetzer, C. Grüninger, B. Flemisch, and R. Helmig: On the Conditions for Coupling Free Flow and Porous-Medium Flow in a Finite Volume Framework, *Finite Volumes for Complex Applications VIII*, Hyperbolic, Elliptic and Parabolic Problems (FVCA 8, Lille, France, June 2017):347–356, 2017. doi: 10.1007/978-3-319-57394-6_37.

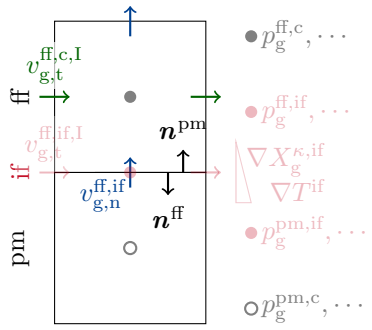

Figure 4.2: Location of primary variables in the two subdomains and at the coupling interface. Unavailable primary variables at the coupling interface are marked in lighter red.
Adapted by permission from Springer Customer Service Centre GmbH: Springer eBook *On the Conditions for Coupling Free Flow and Porous-Medium Flow in a Finite Volume Framework* by Thomas Fetzer, Christoph Grüninger, Bernd Flemisch, and Rainer Helmig ©2017.

On the Tangential Momentum Condition For the tangential momentum, $v_{g,t_i}^{ff,if}$ occurs two times in the Saffman condition (3.49), which can be reformulated to:

$$v_{g,t_i}^{ff,if} = \frac{\beta_{BJS} v_{g,t_i}^{ff,c}}{1 + \beta_{BJS}}, \tag{4.1}$$

with the help of an auxiliary function β_{BJS}:

$$\beta_{BJS} := -\frac{\sqrt{K}}{\alpha_{BJ}} \frac{1}{(\boldsymbol{x}^{ff,c} - \boldsymbol{x}^{ff,if}) \cdot \boldsymbol{n}^{ff}}. \tag{4.2}$$

The superscripts indicate whether the quantity is located at the interface (if) or inside the cell (c). Finally, $v_{g,t_i}^{ff,if}$ can be set as a solution-dependent Dirichlet condition for the i-th tangential momentum balance.

On the Normal Momentum Condition For coupling normal momentum (3.47), both pressures ($p_g^{ff,if}$ and $p_g^{pm,if}$) are unknown. In addition, they may be different due to the different model concepts. The key question is to specify $p_g^{pm,if}$. First, this is necessary to couple the normal momentum balance in the free flow with flow processes inside the porous medium and second, $p_g^{pm,if}$ already corresponds to the right hand side of the coupling condition. For single-phase, single-component systems, as presented in Rybak et al. [2015], recalculating $p_g^{pm,if}$ from the total mass flux condition (3.46) and Darcy's law (3.41) is straightforward. For multi-phase systems this is not possible without further assumptions, see CM3–CM1. It is emphasized, that the recalculated $p_g^{pm,if}$ only serves as a coupling condition to the free-flow side and is not used to calculate fluxes inside the porous medium.

Coupling via an Interface Solver (CM4) The idea of this method is to make as few assumptions concerning interface conditions as possible. For each calculation of the fluxes across the interface, a local system of equations which involves equations (3.46), (3.51), and (3.56) is solved. The continuity of mole/mass fractions (3.50) and temperature (3.55) are integrated into this system of equations and thus the additional local primary variables are: $p_{\mathrm{g}}^{\mathrm{pm,if}}$, $S_{\mathrm{l}}^{\mathrm{if}}$ or $X_{\mathrm{g}}^{\kappa,\mathrm{if}}$, and T^{if}. Now, the diffusive fluxes can be formulated for each subdomain separately. After convergence, the continuity of fluxes is guaranteed and $p_{\mathrm{g}}^{\mathrm{pm,if}}$ is used to specify the normal momentum condition.
The advantages of this method, compared to the following ones, are: (i) it is more accurate as the gradients at the interface are better resolved and (ii) it can consider co-current flow of the liquid phase and the gas phase for estimating the normal momentum flux and thus the interface gas pressure.
However, it also bears some disadvantages. First, the switch from a two-phase system to a one-phase system poses numerical problems: if $S_{\mathrm{l}}^{\mathrm{if}}$ drops below $S_{\mathrm{r,l}}$, the liquid wetting phase becomes immobile and as no storage term is included, the solution does not longer depend on the local primary variable $S_{\mathrm{l}}^{\mathrm{if}}$. To avoid this, a gradual switch to CM3 is implemented around $S_{\mathrm{r,l}}$. When the one-phase system is reached in a cell ($S_{\mathrm{l}}^{\mathrm{c}} = 0$), then, the local system of equations is solved with $X_{\mathrm{g}}^{\kappa,\mathrm{if}}$ as the primary variable. Second, a slope-limiter for the solution of the local primary variable may has to be applied. This is necessary at the beginning of a simulation, when the processes and state variables inside the porous medium and the free flow are far from their equilibrium state. Third, it might be computationally more demanding than the other methods.

Gas Momentum Coupling (CM3) This and all following methods avoid the additional, local system of equations. They assume that the gradients of mole/mass fractions and temperature can be built across the interface:

$$\nabla X_g^{\kappa,\mathrm{if}} = \frac{X_g^{\kappa,\mathrm{ff,c}} - X_g^{\kappa,\mathrm{pm,c}}}{\boldsymbol{x}^{\mathrm{ff,c}} - \boldsymbol{x}^{\mathrm{pm,c}}}\,, \quad \nabla T^{\mathrm{if}} = \frac{T^{\mathrm{ff,c}} - T^{\mathrm{pm,c}}}{\boldsymbol{x}^{\mathrm{ff,c}} - \boldsymbol{x}^{\mathrm{pm,c}}}\,.$$

The respective fluxes are then specified by the free-flow side. This assumption already involves the continuity of mole fractions and temperature. Still, the gas-phase pressure at the interface has to be recalculated using (3.41) and (3.46). It is assumed that the diffusive-dispersive fluxes do not have a considerable effect on the resulting pressure at the interface and thus the coupling condition can be simplified to:

$$\left[\varrho_{\mathrm{g}} \boldsymbol{v}_{\mathrm{g}}^{\mathrm{if}} \cdot \boldsymbol{n}\right]^{\mathrm{ff}} = \left[\sum_{\alpha\in\{\mathrm{l,g}\}} \varrho_\alpha \frac{k_{\mathrm{r},\alpha} K}{\varrho_\alpha \nu_\alpha} \left(\frac{p_\alpha^{\mathrm{if}} - p_\alpha^{\mathrm{c}}}{(\boldsymbol{x}^{\mathrm{if}} - \boldsymbol{x}^{\mathrm{c}}) \cdot \boldsymbol{n}} - \varrho_\alpha \boldsymbol{g} \cdot \boldsymbol{n}\right)\right]^{\mathrm{pm}}. \tag{4.3}$$

The main assumption of this approach, in comparison to CM2, is: $v_{\mathrm{g}}^{\mathrm{pm,if}} \gg v_{\mathrm{l}}^{\mathrm{pm,if}}$. In other words, the contribution of the liquid-phase flow on the resulting gas-phase pressure at the interface is negligible. This means that all liquid-phase terms in (4.3) are dropped and the gas-phase pressure at the interface becomes:

$$p_{\mathrm{g}}^{\mathrm{pm,if}} = \frac{\left[\varrho_{\mathrm{g}} \boldsymbol{v}_{\mathrm{g}}^{\mathrm{if}} \cdot \boldsymbol{n}\right]^{\mathrm{ff}} + \left[\frac{k_{\mathrm{r,g}} K}{\nu_{\mathrm{g}}} \varrho_{\mathrm{g}} \boldsymbol{g} \cdot \boldsymbol{n}\right]^{\mathrm{pm}}}{\frac{k_{\mathrm{r,g}} K}{\nu_{\mathrm{g}}}} \left(\boldsymbol{x}^{\mathrm{pm,if}} - \boldsymbol{x}^{\mathrm{pm,c}}\right) \cdot \boldsymbol{n}^{\mathrm{pm}} + p_{\mathrm{g}}^{\mathrm{pm}} \,. \tag{4.4}$$

In contrast to CM2, (i) a fully liquid-saturated system acts as an impermeable barrier to the free gas-phase flow, (ii) no additional assumptions about the liquid state are required and (iii) the lowest gas-flow resistance $\left({}^{k_{\mathrm{r,g}}}/_{\nu_{\mathrm{g}}}\right)^{-1}$ and thus the highest gas velocities are found for $S_{\mathrm{l}} < S_{\mathrm{r,l}}$.

Total Momentum Coupling (CM2) As for CM3, the gas-phase pressure at the interface is recalculated using (4.3). In (4.3), the liquid-phase pressure at the interface $p_{\mathrm{l}}^{\mathrm{pm,if}}$ is not known, because it depends on the unknown liquid-phase saturation $S_{\mathrm{l}}^{\mathrm{pm,if}}$. In this method, the main assumption is that there is no difference in liquid-phase saturation between the cell and the interface: $S_{\mathrm{l}}^{\mathrm{pm,if}} = S_{\mathrm{l}}^{\mathrm{pm,c}}$. This simplification results in the same pressure difference for both phases and thus the same gradients contributing to the liquid-phase and the gas-phase flux. With this simplification, the interface gas-phase pressure can be expressed as:

$$p_{\mathrm{g}}^{\mathrm{pm,if}} = \frac{\left[\varrho_{\mathrm{g}} \boldsymbol{v}_{\mathrm{g}}^{\mathrm{if}} \cdot \boldsymbol{n}\right]^{\mathrm{ff}} + \left[\sum_{\alpha\in\{\mathrm{l,g}\}} \frac{k_{\mathrm{r},\alpha} K}{\nu_\alpha} \varrho_\alpha \boldsymbol{g} \cdot \boldsymbol{n}\right]^{\mathrm{pm}}}{\sum_{\alpha\in\{\mathrm{l,g}\}} \frac{k_{\mathrm{r},\alpha} K}{\nu_\alpha}} \left(\boldsymbol{x}^{\mathrm{pm,if}} - \boldsymbol{x}^{\mathrm{pm,c}}\right) \cdot \boldsymbol{n}^{\mathrm{pm}} + p_{\mathrm{g}}^{\mathrm{pm,c}} \,. \tag{4.5}$$

However, this method predicts the highest gas velocities, for the lowest gas-flow resistance $\left(\sum_{\alpha\in\{\mathrm{l,g}\}} {}^{k_{\mathrm{r},\alpha}}/_{\nu_\alpha}\right)^{-1}$, which is found for a liquid-filled system ($S_{\mathrm{l}} > 1 - S_{\mathrm{r,g}}$).

Simple Momentum Coupling (CM1) This method assumes no gas-phase pressure gradient: $p_{\mathrm{g}}^{\mathrm{pm,if}} = p_{\mathrm{g}}^{\mathrm{pm,c}}$. Once the discretization is fine enough, this should be a good approximation of the gas-phase pressure at the interface. For coarse grids or high fluxes, the pressure and thus the flow resistance at the interface is over- or underestimated (depending on the direction of the flow). The reason for this behavior is the neglected feedback between the mass flux across and the resulting pressure at the interface. The absence of this feedback leads to difficulties in predicting flow at corner cells of the porous medium. In this case, the influx over one face can leave via the other face without affecting the pressure in the porous medium cell and thus the momentum exchange to the free flow.

4.2 Discretization in Time

For the time discretization a fully implicit Euler method is used. In this work, a monolithic matrix containing both subdomains and the coupling conditions is linearized and solved by the Newton method in each time step. The time step size is variable and depends on the convergence of the Newton method in the previous time step. Each Newton step is solved with the help of a direct solver, see Appendix C. Grüninger [2017] investigates the use of iterative solvers.

4.3 Implementation

This section presents the software concepts and modules in which the turbulent free flow and the coupling conditions are implemented. Afterward, some aspects regarding the implementation of the turbulence models are mentioned.

4.3.1 Software

The model is implemented in the framework of the open-source simulator DuMu^{x} (DUNE for Multi -phase, -physics, -component, -scale Flow in Porous Media), see Flemisch et al. [2011]. DuMu^{x} bases on the core modules of DUNE (Distributed and Unified Numerics Environment), see Bastian et al. [2008b,a] and Blatt et al. [2016]. DUNE provides grid management tools, local functions, and different solvers or backends. Further, this thesis requires the modules DUNE-PDELab and DUNE-MultiDomain [Müthing, 2015].

DuMu^{x} already provides the box method (free flow and porous-medium flow), the CCFV discretization (porous-medium flow), and the box–box coupling framework basing on DUNE-PDELab and DUNE-MultiDomain. In the scope of this thesis, the MAC scheme was implemented in DUNE-PDELab, mainly because it supports mixed degree-of-freedom handling for element and intersection centers. The coupling conditions are implemented within the framework of DUNE-MultiDomain. All code is open-source and online-available[9], all details about the used software versions are listed in Appendix C.

[9] T. Fetzer: *dumux-Fetzer2018a (PhD thesis)*, `https://git.iws.uni-stuttgart.de/dumux-pub/Fetzer2018a`, accessed on March 5, 2018.

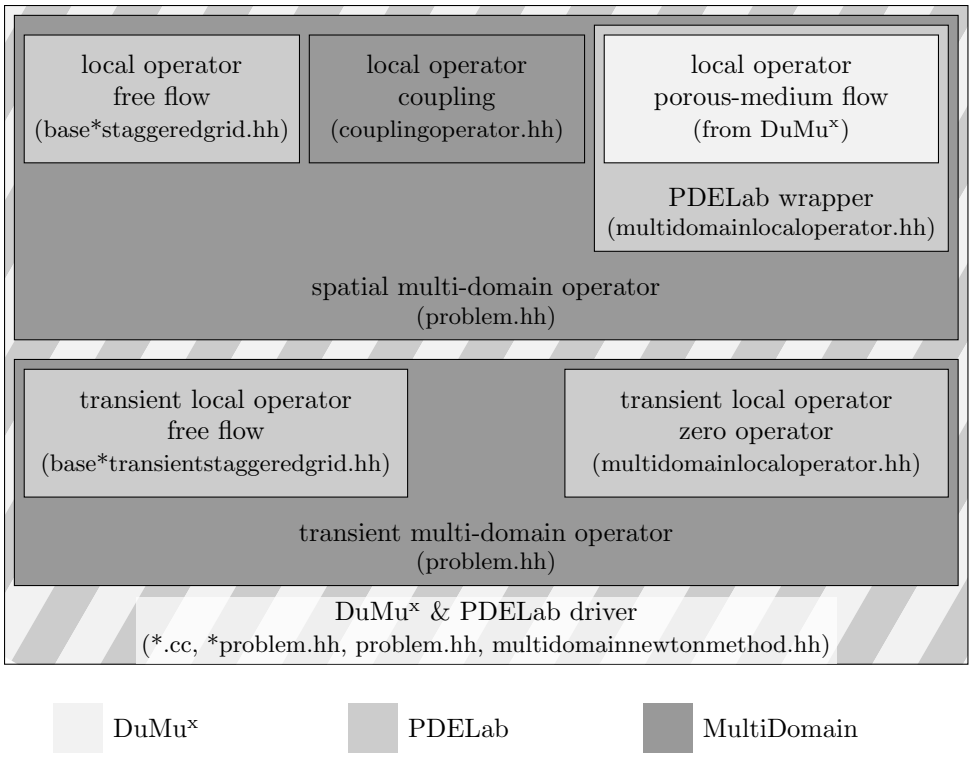

Figure 4.3: Software structure for coupling DuMu^x, Dune-PDELab, and Dune-MultiDomain for coupled free-flow and porous-medium flow simulations.
Adapted from Grüninger et al. [2017], changes: colors and legend position, Creative Commons license: `https://creativecommons.org/licenses/by/4.0`.

4.3.2 Software Coupling[10]

Dune-MultiDomainGrid and Dune-MultiDomain [Müthing, 2015] extend Dune-PDELab for multi-physics and multi-domain simulations. Dune-MultiDomainGrid can subdivide a given grid and handle the subdomains like grids of their own. Additionally, it offers an iterator over the coupling interfaces. Dune-MultiDomain uses this structure and applies so-called local operators to each subdomain and the coupling interface. The free-flow subdomain local operator is the MAC scheme implemented in Dune-PDELab. The porous-medium subdomain local operator is the DuMu^x-based CCFV code. As DuMu^x local operators are incompatible to Dune-PDELab and MultiDomain, a wrapper to tunnel the residual and Jacobian computation to Dune-PDELab has to be provided, see Fig. 4.3.

The DuMu^x porous-medium model has an internal state that stores the variable switch (if

[10] This section is based on C. Grüninger, T. Fetzer, B. Flemisch, and R. Helmig: Coupling DuMuX and DUNE-PDELab to investigate evaporation at the interface between Darcy and Navier-Stokes flow, *Stuttgart Research Centre for Simulation Technology (SRC SimTech)*, Preprint Series (2017):1, 2017. doi: `10.18419/opus-9360`.

one phase vanished and consequently a different primary variable must be used). To update its internal state and to check for variable switches, the DuMu^x model gets a copy of the solution vector after every Newton step. A variable switch alters the associated value in the solution vector, see Class et al. [2002], and as a consequence, the solution vector has to be copied back. The solution vector cannot be reused by passing a reference, because the degree of freedom ordering differs: DuMu^x has one solution vector entry for every element, and the entry is a vector of all element unknowns. In contrast, DUNE-PDELab uses a flat vector and calculates the according indices. Additionally, the solution vector created by DuMu^x is too large, as it is not aware of the subdomains and it considers all elements. In a pre-simulation grid iteration, all elements in the porous-medium subdomain are collected in a vector and used for indirect accesses to the DuMu^x solution vector. The function to copy the degrees of freedom is part of the problem and is passed as a lambda function to the Newton method.

4.3.3 Turbulence Modeling and Wall Handling

This thesis focuses on the effects of wall-bounded turbulence. All turbulence models presented in Chapter 3 depend to some degree on properties at the wall or the wall distance. Some models, as the two-layer models, also require the determination of switching positions. First, the algorithm for determining the wall sections and wall-related quantities is explained. Then the different methods for zero-equation and two-equation two-layer models are compared.

Wall Variables The pseudo C++-code in Fig. 4.4 visualizes how to identify, for each element inside the free flow domain, a wall intersection, its respective wall element, and the wall distance. These relations are determined once at the beginning of the simulation. During the simulation this relation is necessary, e.g. to calculate y^+ or to identify switching positions. The algorithm allows wall distances with the shortest absolute distance to the wall, regardless of the grid orientation (`predefinedWallAxis` $= -1$) or the shortest distance along a specified coordinate axis (`predefinedWallAxis` ≥ 0). This method is inspired by Mavriplis [1990], who propose a kind of wall section strategy for the Baldwin-Lomax model on unstructured grids.

Switching Positions The flow-chart in Fig. 4.5 compares how the switching positions or wall-function regions are determined. For the Baldwin-Lomax model this is necessary to properly calculate the eddy viscosity based on the values for the inner and the outer region. For the k-ε model this is necessary to identify: (i) at which boundaries and cells the wall function have to be used or (ii) in which cells a zero-equation model should be used instead of the k and ε equations. It is possible to update the switching positions after each Newton

or each time step. In the case of strongly unsteady flow, updating after each time step may lead to oscillations.

```
void initializeSimulation()
{
  // 1) Prepare vectors containing wall relevant values.
  //    Later (e.g. postStepRoutine), values are called and written by using
  //    the ID of the element or the ID of the wallElement.
  std::vector<double> wallDistance(numElements);
  std::vector<int> correspondingWallElementID(numElements);
  std::vector<double> yPlus(numElements);
  std::vector<double> velocityGradient(numElements);
  std::vector<type> wallVariable1(numElements); // e.g. isWall, isMatchingPoint
  ...

  // 2) Retrieve:
  //    - All IDs of elements sharing a wall-intersection
  //    - The coordinates of all wall-intersections.
  std::vector<int> wallElementIDs;
  std::vector<std::array<dim, double>> wallCoordinates;
  // Loop over all elements.
    // Loop over all intersections of each element.
      // Check if intersection is on a wall.
        wallElementIDs.push_back(element.ID());
        wallCoordinates.push_back(intersection.coordinates());

  // 3) Search for the shortest wall distance and store the respective element ID.
  // Loop over all elements.
    // Loop over all wallElementIDs (index i).
      double distance = two_norm(element.coordinates - wallCoordinates[i]);
      if (predefinedWallAxis > 0)
      {
        distance = abs(element.coordinates[predefinedWallAxis]
                       - wallCoordinates[i][predefinedWallAxis]);
      }
      if (distance < wallDistance[element.ID()])
      {
        wallDistance[element.ID()] = distance;
        correspondingWallElementID[element.ID()] = wallElementIDs[i];
      }
}

void postStep() // called after a time step or Newton step
{
  ...
  double uStar = sqrt(kinematicViscosity
                      * velocityGradient[correspondingWallElementID[element.ID()]]);
  yPlus[element.ID()] = wallDistance[element.ID()] * uStar;
  ...
}

private:
  int predefinedWallAxis;
  double kinematicViscosity;
  ...
```

Figure 4.4: Pseudo code for determining the wall distance and the treatment of wall-related properties.

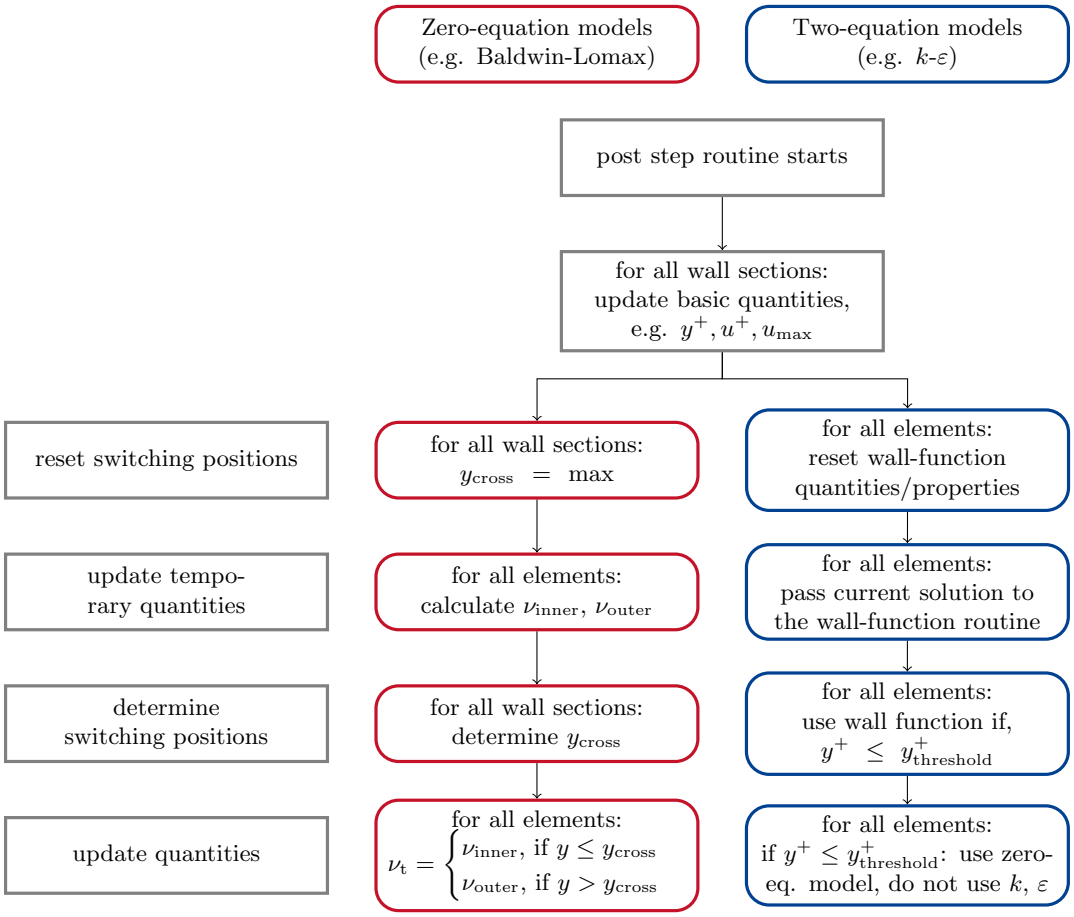

Figure 4.5: Flow chart implementation of switching positions and wall-function regions.

5 Results and Discussion

In this chapter, different simulation results are presented and discussed. It is started with proving the implemented free-flow model concept in section 5.1. Afterward, the attention is drawn to coupled porous-medium free-flow problems. First, different discretization techniques, model concepts, model simplifications, and model parameters are investigated in section 5.2. Then, section 5.3 compares simulation results with results from laboratory experiments. Finally, section 5.4 analyzes the influence of roughness, resulting from heterogeneities, the sand grains, or porous obstacles.

The definition of boundary conditions for such coupled problem setups is quite complex. For improving the readability of the setup sketches, Tab. 5.1 contains predefined sets of boundary conditions. The inflow boundary conditions for the turbulence models are always calculated by a procedure proposed in ANSYS, Inc. [2009b] or Versteeg and Malalasekra [2009]:

$$\tilde{\nu}_{\mathrm{in}} = \sqrt{\frac{3}{2}} v_{\mathrm{x}} I \, \ell \, , \quad k_{\mathrm{in}} = \frac{3}{2} \left(v_{\mathrm{x}} I \right)^2 \, , \quad \varepsilon_{\mathrm{in}} = C_{\mu}^{3/4} \frac{k_{\mathrm{in}}^{3/2}}{\ell} \, , \quad \omega = \frac{k_{\mathrm{in}}^{1/2}}{C_{\mu}^{1/4} \ell} \, .$$

The turbulence intensity (I) and the turbulent length scale (ℓ) can be estimated by:

$$I = \frac{\sqrt{2/3k}}{v_{\mathrm{mean}}} \approx 0.16 Re_{d_{\mathrm{hy}}}^{-0.125} \, , \quad \ell = 0.07 d_{\mathrm{hy}} \, .$$

5.1 Validation of the Free-Flow Code

In this first study, all free-flow turbulence models which are implemented in the scope of this thesis are tested for their proper functionality, see App. B. The respective models are successfully validated with different testing methods: analytical, numerical, and physical (see Tab. 5.2). The selection of respective testing methods is done according to common practice and to available literature data.

domain	type	default	exception
free flow	inflow	Dirichlet	total mass balance is outflow
	outflow	zero-gradient	p is Dirichlet
	symmetry	zero-gradient	$v_\mathrm{n} = 0$
	wall	no-flow	$\boldsymbol{v} = 0$, $\tilde{\nu} = 0$
			k-ε (wall functions): see p. 40ff
			Low-Re k-ε: $k = 0$, $\tilde{\varepsilon} = 0$
			k-ω: see p. 43ff
interface	coupling	see p. 51ff	$\tilde{\nu}$, k, ε, and ω same as free-flow wall
porous medium	symmetry	no-flow	-
	wall	no-flow	-
	const. T wall	no-flow	T is Dirichlet
	insulated wall	no-flow	energy is solution-dependent Neumann

Table 5.1: Definition of boundary condition types for coupled problems. For any primary variable φ, *Dirichlet* means the value on the boundary is fixed, *solution-dependent Neumann* means the boundary flux depends on the current solution, the cell properties, and the fixed value on the boundary, *zero-gradient* means $\partial\varphi/\partial x_\mathrm{n} = 0$, and *no-flow* means $q^\varphi_\mathrm{adv} + q^\varphi_\mathrm{diff} = 0$.

		analytical (section B.1)	numerical (section B.2)	physical (section B.3)
box	Navier-Stokes		✓	
	zero-equation models			✓
MAC	Navier-Stokes	✓	✓	
	zero-equation models			✓
	one-equation models			✓
	two-equation models	✓	✓	✓

Table 5.2: Overview on successfully performed validation cases for the implemented free-flow models.

5.2 Analysis of the Model Concepts

In this section, different model concepts, model simplifications, and discretization methods are compared with the help of simple test cases. Tab. 5.3 provides a short overview on the available model concepts. These concepts are then analyzed with respect to their effect on the exchange fluxes, grid convergence, and computational costs.

5.2.1 Coupling Model Concepts

The differences between a box–box coupling and the different methods for the CCFV–MAC coupling are highlighted with the help of two different setups. The first features a predomi-

model name	description of the free-flow model	discretization
Navier-Stokes	Navier-Stokes	box or MAC
transport	v^{ff}, p^{ff}, $\varrho_{\mathrm{g}}^{\mathrm{ff}}$, and ν_{t} are predefined	box
BL	porous medium only, boundary conditions (3.53) and (3.58)	box
0-Eq.	Baldwin and Lomax [1978] (for experiments), Hanna et al. [1981] (for parameter/model analyses)	box or MAC
1-Eq.	Spalart and Allmaras [1992]	MAC
k-ε (two layers)	Launder and Sharma [1974], near wall ($y^+ < 50$): Hanna et al. [1981]	MAC
k-ε (wall functions)	Launder and Sharma [1974], near wall/coupling: wall functions (3.54) and (3.59)	MAC
Low-Re k-ε	Chien [1982]	MAC
k-ω	Wilcox [2008]	MAC

Table 5.3: Definition of the model names and available discretization methods. All models use a non-isothermal two-component fluid phase and are coupled to a non-isothermal two-phase two-component Darcy model for the porous medium, see section 3.2 and section 3.3.

nantly interface-parallel flow, whereas in the second case the free flow is directed normal to the interface.

Coupled Interface-Parallel Flow For the interface-parallel flow, the exchange through the evolving boundary layers is of key importance. Therefore, the setup defined in Fig. 5.1 and Tab. 5.4 is designed to compare the convergence of steady-state stage-I evaporation rates for the different coupling methods under laminar conditions (modeled with the Navier-Stokes equations) and turbulent conditions (modeled with the 0-Eq. model). A start-up distance of 1 m for the free flow is used to minimize the inlet effects, especially the eddy-viscosity profiles of the different turbulence models are quite different near the inlet. The length of the porous-medium section is chosen such that the slip velocity at the interface and the total evaporation rate do not change with increasing length. The setup uses the quartz sand properties specified in Mosthaf et al. [2014], see soil #1 in Tab. A.1. The domain is discretized with 20×32 cells: $n_{\mathrm{x<1\,m}} = 4$, $n_{\mathrm{x>1\,m}} = 16$, $n_{\mathrm{y}}^{\mathrm{pm}} = 16$, $n_{\mathrm{y}}^{\mathrm{ff}} = 16$. Performing a classical grid convergence study by doubling the number of cells in each direction is difficult because a fine discretization is required at the interface. Therefore, grading factors are chosen such that the height of the smallest cells at the interface are halved in comparison to the previous grading factor ($g_{\mathrm{y}} = \{1.025, 1.109, 1.187, 1.263, 1.339, 1.415, 1.494, 1.575, 1.659\}$).

Fig. 5.2 compares the steady-state stage-I evaporation rates for different grading factors and thus the smallest cells at the interface. For the laminar case, the convergence of all

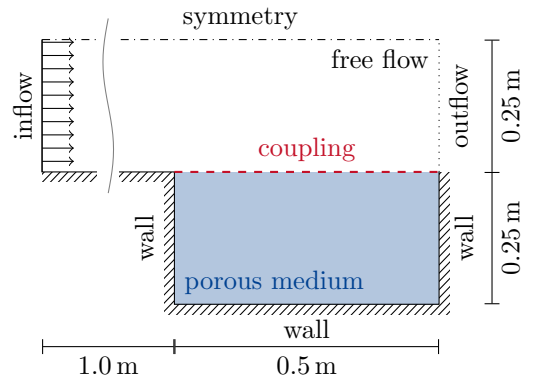

Figure 5.1: Simulation setup for the parallel flow case.

parameter	value
$\boldsymbol{v}_g^{ff}$ [m/s] (laminar)	$(0.035, 0)^\intercal$
$\boldsymbol{v}_g^{ff}$ [m/s] (turbulent)	$(3.5, 0)^\intercal$
p_g^{ff} [Pa]	1E5
$X_g^{w,ff}$ [–]	0.008
T^{ff} [K]	298.15
soil type	#1
p_g^{pm} [Pa]	1E5
S_l^{pm} [–]	0.98
T^{pm} [K]	298.15

Table 5.4: Initial and boundary conditions for the parallel flow case.

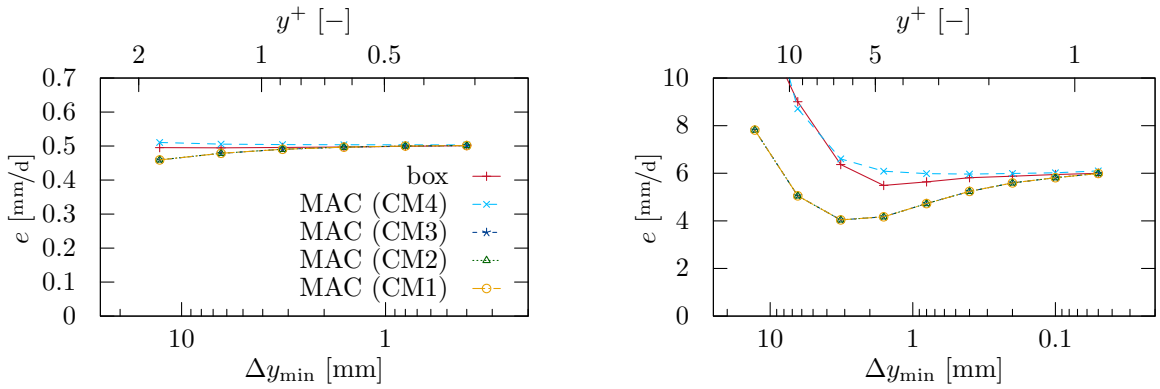

Figure 5.2: Convergence of steady-state stage-I evaporation rates for the parallel flow case (left: laminar, right: turbulent). The dimensionless wall distance (y^+) is calculated based on the wall friction velocity (u_τ) obtained from the simulation with the smallest cells size.

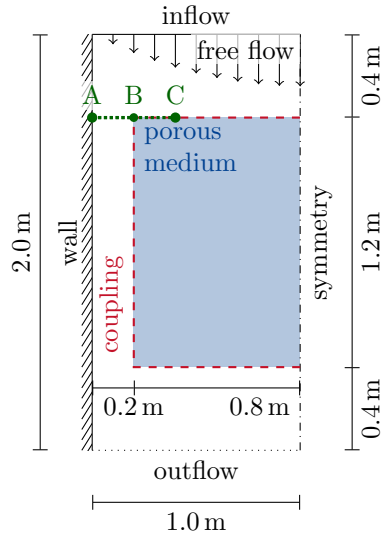

Figure 5.3: Simulation setup for the normal flow case, after Fetzer et al. [2017b].

parameter	value
$v_{g,x}^{ff}$ [m/s]	0
$v_{g,y}^{ff}$ [m/s]	$-0.016\,x^2$
p_g^{ff} [Pa]	1E5
$X_g^{w,ff}$ [–]	0.0005
T^{ff} [K]	303.15
soil type	#2
p_g^{pm} [Pa]	1E5
S_l^{pm} [–]	0.85
T^{pm} [K]	293.15

Table 5.5: Initial and boundary conditions for the normal flow case, after Fetzer et al. [2017b].

methods is comparable. The box method performs a little better, which is attributed to the fact that for a coarser discretization the additional degree of freedom at the interface is more important. When turbulence is considered, it is seen that the box method and the coupling using CM4 have a better grid convergence behavior (for this interface-focused grid refinement). This indicates the importance of an appropriate modeling of the interface processes. For a sufficiently fine discretization, the results for all methods are comparable. This discretization depends more on the dimensionless wall distance y^+ than on the absolute distance. For approximating the evaporation rates, a good modeling of the processes in the viscous sublayer with at least one cell inside the viscous sublayer ($y^+ < 5$) seems to be inevitable. The simpler coupling methods CM1–CM3, require the smallest cells to be located inside $y^+ \approx 1$ for both cases, laminar and turbulent.

Coupled Interface-Normal Flow[11] The setup depicted in Fig. 5.3 and Tab. 5.5 is designed to magnify the difference between CM1–CM3 as their main difference is in the normal momentum exchange. For this test case, a standard grid refinement procedure is used. Staring with a grid using 5×5 cells, in each refinement step (RS) the number of cells in each direction is doubled. This test case is only performed for the Navier-Stokes model ($Re_{\text{max,d}} = 1000$).

[11] The results presented here are an update of those published in: T. Fetzer, C. Grüninger, B. Flemisch, and R. Helmig: On the Conditions for Coupling Free Flow and Porous-Medium Flow in a Finite Volume Framework, *Finite Volumes for Complex Applications VIII*, Hyperbolic, Elliptic and Parabolic Problems (FVCA 8, Lille, France, June 2017):347–356, 2017. doi: 10.1007/978-3-319-57394-6_37.

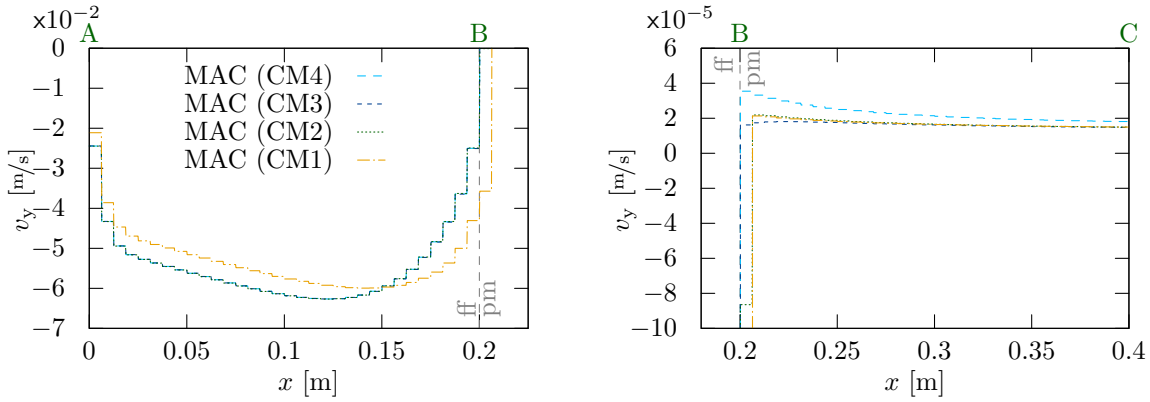

Figure 5.4: Velocity profiles for the normal flow case[11], refinement step 5. Left, for the free flow section (A–B in Fig. 5.3). Right, above the porous-medium section (B–C in Fig. 5.3).

	above ff				above pm				above pm (ref CM4)		
RS	CM1	CM2	CM3	CM4	CM1	CM2	CM3	CM4	CM1	CM2	CM3
0	0.567	0.180	0.179	dnc	4.821	0.968	0.910	dnc	804.9	0.975	0.930
1	0.352	0.258	0.257	0.257	3.761	0.904	0.812	0.723	638.4	0.922	0.860
2	0.214	0.203	0.202	0.202	2.786	0.785	0.652	0.497	489.4	0.822	0.732
3	0.112	0.126	0.125	0.125	1.928	0.607	0.394	0.234	364.9	0.682	0.536
4	0.056	0.066	0.065	0.065	1.102	0.418	0.144	0.116	255.2	0.578	0.350
5	ref	ref	ref	ref	ref	ref	ref	ref	164.5	0.594	0.239

Table 5.6: Relative l^2-errors of vertical velocities[11]. Different refinement steps (RS) are compared to a reference solution (ref) on the finest grid of each coupling method. One simulation did not converge (dnc).

As the focus is on normal momentum exchange, the velocity profiles in normal (here vertical) direction are compared along the line A–B–C, see Fig. 5.3. The results presented here slightly differ to the previous version published in Fetzer et al. [2017b] due to changes in the underlying equations, improvements of the CM4 algorithm, and a shorter simulated time. The only qualitative difference is that similar run times are achieved for all coupling methods (not shown). Fig. 5.4 shows that CM1 fails to predict an acceptable free-flow velocity profile, the velocity above the first porous-medium cell is almost as high as in the free-flow channel. Still, all coupling methods show a good grid convergence against themselves for the free flow, cf. Tab. 5.6. Analyzing the grid convergence of the velocity profiles above the porous medium, CM2 performs worse than CM3, but even CM3 does not convergence against the reference solution obtained with CM4. For a dry case (not shown here), the velocity profiles above the porous medium are almost identical for CM2–CM4.

5.2.2 Free-Flow Model Concepts

Two different types of model concepts are analyzed for turbulent conditions with the help of the parallel-flow setup described in section 5.2.1. First, different simplifications of the coupled porous-medium and free-flow model with respect to the representation of the turbulent free flow are compared. Then, the impact of turbulence models of different complexity on the evaporation rate is investigated. If not stated otherwise, the MAC implementation with CM4 is used from hereon.

Model Simplifications Simplifications of the porous-medium model are not subject of this study and are more thoroughly discussed in Vanderborght et al. [2017] and Fetzer et al. [2017c]. Here, the focus is on the effect of different simplifications of the turbulent free-flow model on the resulting evaporation rate.
The transport model uses a pre-simulation step for calculating the flow field and the turbulent quantities. This pre-simulation step may account for complex geometries and their feedback on the flow field. Afterward, in the coupled simulation, no momentum balances are solved and the transport of water mass and energy is calculated with the help of the given flow field.
The k-ε (wall functions) model only works for a flat interface and a coarse interface-normal discretization, when the cell center of the interface-adjacent free-flow cell is inside the turbulent region. To keep the interface-normal/vertical grading consistent with the other simulations, the number of cells in the free-flow region is reduced to 5 cells in vertical direction, resulting in a minimum cell height of $\Delta y \approx 10\,\mathrm{mm}$.
The boundary layer models (BL) avoid a detailed modeling of the free-flow processes by using the boundary layer information to specify one-dimensional boundary conditions for mass and energy at the top of the porous-medium domain.

The evaporation process for the different simplifications is quite similar, but the predicted stage-I evaporation rates differ, see Fig. 5.5 (left). For this plot, the BL models use $y^+ = 15$ to estimate the boundary layer thickness. This value is fitted to this specific setup with a porous-medium section with a length of 0.5 m. A value of $y^+ = 30$, which corresponds to the beginning of the log law region (cf. Tab. 2.2), would lead to similar results as by the k-ε (wall functions) model. The quality of the k-ε (wall functions) model depends on the length of the porous-medium section. The advantage of the 0-Eq., the k-ε (wall functions), and the transport model is their ability to predict lateral variation in free-flow conditions. This becomes visible when the length of the porous-medium section is increased from 0.5 m to 128 m, see Fig. 5.5 (right). The BL models predict almost no variation in evaporation rate and are especially not able to predict the decrease in rate for long porous-medium sections ($\gtrapprox 100\,\mathrm{m}$). Then, the free flow approaches a relative humidity of 100% and no more evaporation can take place.

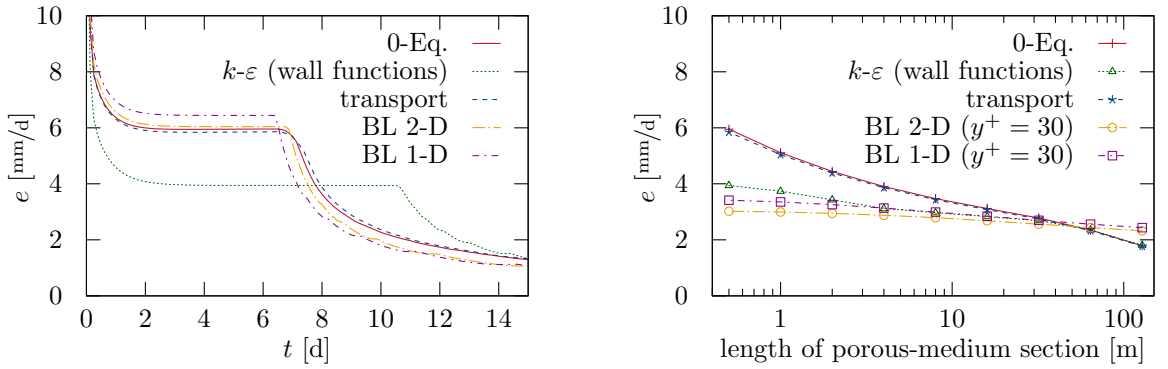

Figure 5.5: Temporal evolution of the evaporation rate for different model simplifications (left). Effect of the length of the porous-medium section on the steady-state stage-I evaporation rate for different model simplifications (right). Note that in the right plot a different y^+-value is used for the BL models.

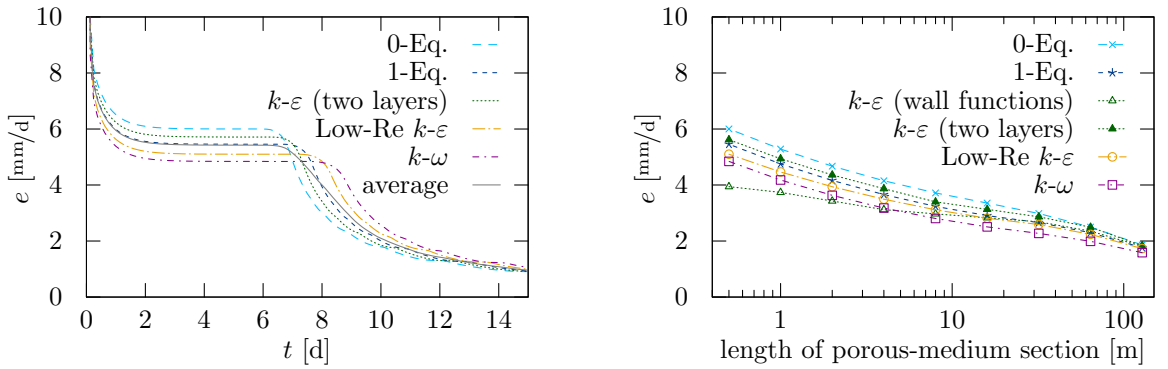

Figure 5.6: Temporal evolution of the evaporation rate for different turbulence models (left). Effect of the length of the porous-medium section on the steady-state stage-I evaporation rate for different turbulence models (right).

Nevertheless, the BL models are attractive as they provide a considerable speed-up, see Tab. 5.7. Their simulation times are less than 3% of the 0-Eq. model. Also, the transport model shows a speed-up, even though it is not yet optimized (an explicit time discretization scheme and less solution-dependent fluid properties could be used). For the k-ε (wall functions) model, half of the speed-up is caused by differences in the implementation of the box and the MAC scheme, the other half originates from less cells inside the free-flow region.

Turbulence Models Fig. 5.6 (left) indicates a qualitatively similar behavior for the different turbulence models, but differences in predicted stage-I evaporation rates (±12% compared to their average rate). The key factor for this behavior is the usage of different damping functions for the eddy viscosity which is important for a correct prediction of its value in the near-wall

	model name	simulation time [s]	relative sim. time	assemble time [s]	solve time [s]	#time steps	#Newton steps
MAC	0-Eq.	722.5	0.51	568	138	562	2320
	1-Eq.	828.4	0.59	646	177	571	2337
	k-ε (two layers)	883.7	0.63	647	210	536	2228
	k-ε (wall func.)	371.0	0.26	345	22	477	1794
	Low-Re k-ε	1015.9	0.72	708	288	582	2405
	k-ω	1003.2	0.71	712	282	572	2385
box	0-Eq.	1412.1	1.00	1115	265	815	3914
	transport	862.9	0.61	808	39	798	3870
	BL 2-D	40.3	0.03	29	7	429	1285
	BL 1-D	1.0	0.00	1	0	454	1528

Table 5.7: Simulation run times and properties for different model concepts. Different turbulence models are compared for the MAC scheme (top) and different model simplifications for the box method (bottom). The relative simulation times are calculated compared to the 0-Eq. box model.

region, cf. Pope [2006, p. 434]. For the 0-Eq., the 1-Eq., and the k-ε (two layers) model the eddy viscosity does not approach a zero value in the viscous sublayer as fast as for the Low-Re k-ε or the k-ω model and thus higher rates are predicted. If the porous-medium section is made longer, the differences in the prediction of the steady-state stage-I evaporation rate persist but become smaller once the free flow becomes saturated with water vapor. Other results, which are not shown here, indicate that the differences between the models increase if the free flow is shorter or is coupled to the porous medium from the beginning, then inlet effects are visible. These inlet effects are especially important for the k-ε (wall functions) model for which three remarks are made.

First, if inlet effects are present, properly matching the y^+-criterion is difficult, as the required height for the free-flow cells might vary along the flow direction. Further, the boundary layers for mass, momentum, and energy might differ significantly and influence the quality of the wall functions.

Second, the evaporation rate of the Low-Re k-ε model is 29% higher compared to the rate of the k-ε (wall functions) model for the shortest setup in Fig. 5.6 (right). Defraeye et al. [2010] reported a mismatch of 50% for heat fluxes from a cube immersed in a turbulent free flow. However, one can see that this discrepancy strongly depends on the length of the porous-medium section and, in this case, for sections longer than 2 m, the k-ε (wall functions) model does not behave much different than turbulence models which resolve the viscous sublayer.

Third, grid convergence results shown in Fig. 5.7 (left) indicate that as long as the near-interface cell is in the turbulent region ($\Delta y_{\min} > 10\,\text{mm}$ in this case), the evaporation rate increases linearly in a double logarithmic plot for the k-ε (wall functions) model, whereas for

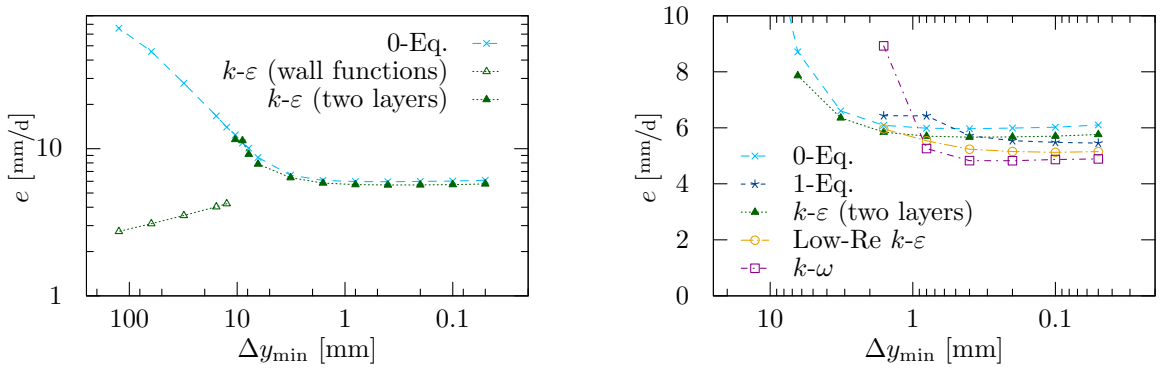

Figure 5.7: Convergence of steady-state stage-I evaporation rates under grid refinement for coarse grids (left) and fine grids (right).

the 0-Eq. model it decreases linearly in a double logarithmic plot. At the best approximation of the k-ε (wall functions) model, the final evaporation rate of the k-ε (two layers) model is underestimated by 27%. In contrast, if the same discretization is used for the 0-Eq. model the final rate is overestimated by 229%. In terms of the vertical water vapor and temperature profiles, the coarse-grid 0-Eq. profiles are not a good approximation of the fine-grid profiles (not shown).

With respect to the grid convergence of the stage-I evaporation rates, see Fig. 5.6 (right), the 0-Eq. and k-ε (two layers) results are comparable as the k-ε (two layers) model uses a zero-equation turbulence model in the near-wall region. The other models show a worse grid convergence in terms of the minimum required cell size (0-Eq./k-ε (two layers): 1.6 mm, Low-Re k-ε/k-ω: 0.4 mm, and 1-Eq.: 0.2 mm).

In terms of run-times, the fastest model which resolves the viscous sublayer is the 0-Eq. model, see Tab. 5.7. It has the least computational effort, because of the lowest number of primary variables (no additional partial differential equation has to be solved). For reasons caused by the implementation, the box models can only use a criterion which is based on the maximum relative shift of any primary variable. Thus, the comparison of simulation times between box and MAC models is of limited value.

5.2.3 Model Parameters

This study analyzes the influence of different model parameters. The effect of the turbulent Schmidt number, the turbulent Prandtl number, and the Beavers-Joseph coefficient is investigated. Four different velocities (0.035 m/s, 0.35 m/s, 1.75 m/s, 3.5 m/s) and thus Reynolds numbers (600, 6 000, 30 000, 60 000) are investigated with the parallel-flow setup presented in Fig. 5.1.

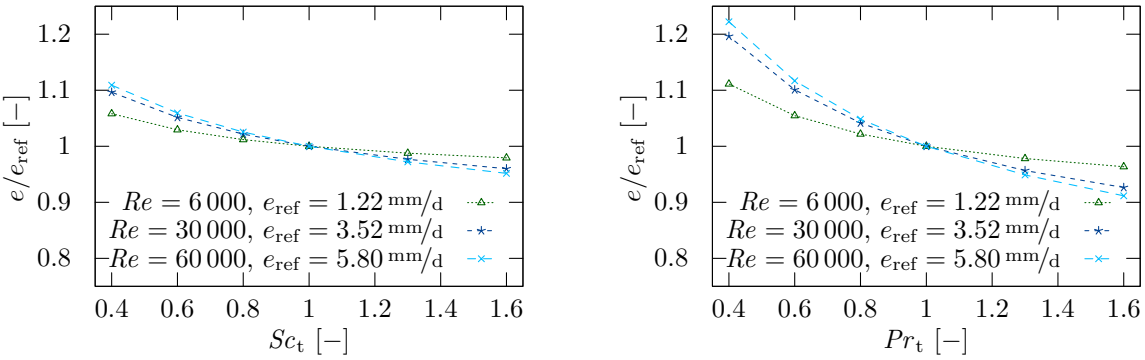

Figure 5.8: Effect of turbulent Schmidt (left) and turbulent Prandtl (right) numbers on steady-state stage-I evaporation rates.

Turbulent Schmidt and Prandtl Numbers So far, it is assumed that $Sc_{\text{t}} = Pr_{\text{t}} = 1$, but depending on the flow geometry, different values can be chosen. Fig. 5.8 shows the effect when varying each of these numbers separately. If the absolute numbers are compared, it can be seen, that the turbulent Prandtl numbers (right figure) have a stronger effect on the evaporation rates than the Schmidt numbers (left figure). But, for the typical ranges of values (as discussed in section 3.1: $Sc_{\text{t}} = 0.2$ to 0.7 and $Pr_{\text{t}} = 0.7$ to 0.9), the influence of both numbers is approximately the same. Further, their effect increases with increasing Reynolds numbers. Here, the porous medium is considered perfectly insulated and thus the main supply of energy is from the free flow in which energy transport strongly depends on the turbulent Prandtl number. If the energy supply across the walls of the porous-medium container increases, the effect of the turbulent Prandtl number may decrease.

Beavers-Joseph According to literature, the Beavers-Joseph coefficient is reported to be in the range of 0.1 to 4 [Beavers and Joseph, 1967] or 0.3 to 2.5 [Nield and Bejan, 2017, and reference therein]. Smaller coefficients have the same effect on the free-flow velocity at the interface ($v_{\text{g,x}}^{\text{if}}$) as increasing the permeability of the porous medium. Fig. 5.9 (left) indicates that the influence of the Beavers-Joseph coefficient on this velocity is linear in a double logarithmic plot for a large range ($v_{\text{g,x}}^{\text{if}} \lessapprox 0.2 \cdot v_{\text{g,x}}^{\text{ref}}$). Of course, the velocity at the interface is bounded by the free stream velocity. The resulting interface-parallel velocities show a good agreement between the box and MAC discretization.
For low Beavers-Joseph coefficients, there is a significant influence on the evaporation rate, see Fig. 5.9 (right). Under turbulent conditions, the influence is decreasing with higher Reynolds numbers. Comparing the left and the right plot, shows that the evaporation rates stop increasing at roughly the same region at which the interface velocities deviate from the linear behavior (at least for the MAC scheme). It is obvious, that changes in the interface velocity changes the flow field and thus the velocity gradients. For zero-equation turbulence models,

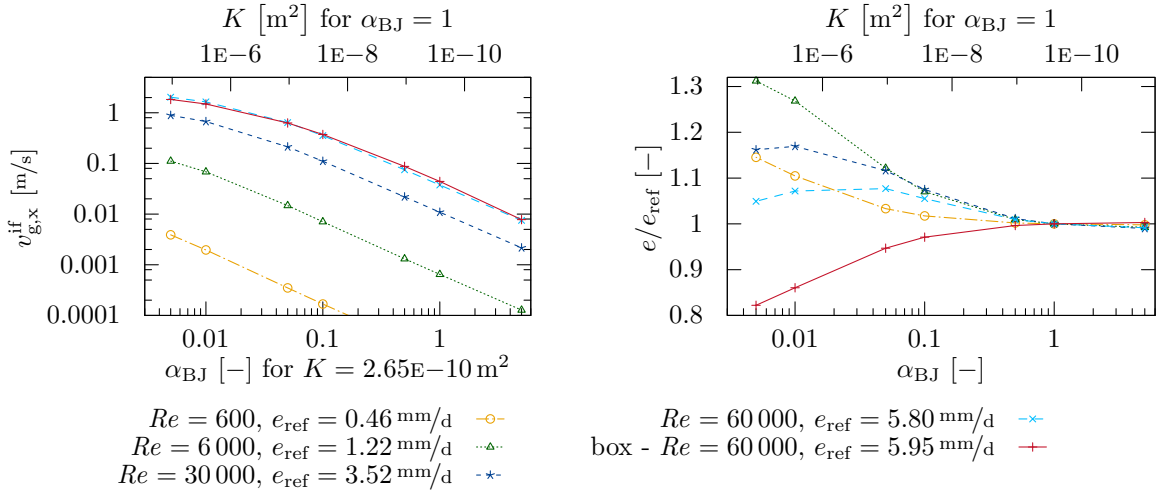

Figure 5.9: Effect of the Beavers-Joseph coefficient on the interface-parallel velocity (left) and on steady-state stage-I evaporation rates (right).

the velocity gradients are used to calculate the eddy-viscosity distribution. Thus, higher interface-parallel velocities (deviation from the no-slip condition) lead to smaller velocity gradients and a smaller contribution of the eddy viscosity on the exchange fluxes. However, a different behavior can be observed for the box method. The resulting oscillations in the velocity field also pertain the interface-normal velocities. These velocities are up to 2 orders of magnitude higher than the average velocities for the MAC scheme. It is hypothesized that these oscillations in combination with higher interface-parallel velocities for lower Beavers-Joseph coefficients lead to a lowering of the evaporation rates.
In Fritsch [2014], a modified version of the Beavers-Joseph condition is implemented to account for multi-phase effects, but it does not show a considerable effect on the evaporation rates. This can be explained, as for stage-I, when the evaporation rate is limited by the free-flow conditions, it would result in an almost no-slip condition (the liquid phase will not be moved by the shear stresses applied from the free-flow gas phase) and for stage-II, when the original condition is yield, the interface velocity does not affect the evaporation rates.

5.2.4 Summary

In this first analysis, the importance of an appropriate interface discretization is shown for two cases: a mainly interface-parallel flow and flow normal toward a porous medium. The box method and the MAC scheme with CM4 show a comparable convergence behavior. Under turbulent conditions, the smallest cell at the interface has to be inside $y^+ < 5$ to prove grid convergence in this setup. This requirement is not too strong and may be a good suggestion

for other cases. Wilcox [2006, Ch.7.6] writes that *"it is imperative to require"* $y^+ < 1$ for turbulence models which integrate through the viscous sublayer; this is only not the case for the k-ε (wall functions) and the BL models. The coupling methods CM1–CM3 can be applied for fine discretizations ($y^+ < 1$) and lead to the same results, if no relevant interface-normal flow is present.

The stage-I evaporation rates of the investigated turbulence models differ by about ±12% with respect to their mean rate. They also differ in their grid convergence of steady-state stage-I evaporation rates and their simulation times. Simplifying the free-flow model is possible under certain conditions, e.g. the BL models provide a good and fast first approximation for simple geometries, but involve fitting parameters with a strong influence. The k-ε (wall functions) model also features some speed-up but the accuracy of the stage-I evaporation rate depends on the optimization of the grid and the length of the porous-medium section. The transport model, in which the flow field is solved in a pre-simulation step, shows the best results for a simplified model and it might also be used for more complex geometries.

The parameter study reveals similar effects when varying the turbulent Schmidt and Prandtl numbers. If they are changed from 1 to a lower, more geometry-specific value, the evaporation rate increases. For a large range of Beavers-Joseph coefficients (especially all values in a physically meaningful range) there is a log-log-linear relation between the Beavers-Joseph coefficient and the interface-parallel velocity. The relative increase in the evaporation rate is the largest for low Reynolds numbers in a turbulent regime and low Beavers-Joseph coefficients. However, very low Beavers-Joseph coefficients decrease the evaporation rate again. Different behaviors are observed for the box and the MAC discretization. The box method shows a decrease in evaporation rate for lower coefficients, whereas the MAC scheme shows an increase. It has to be said, that the box method reveals large oscillations in both, the interface-normal and the interface-parallel velocity components, which have a strong influence on the resulting exchange fluxes.

5.3 Comparison with Experiments

In this section, modeling results are compared and analyzed with the help of laboratory experiments. Although enough experiments, which couple porous-medium and free-flow processes, exist in literature, only a small number is suited for the validation of the presented numerical model concept. The main reasons are: (i) the soil sample evaporates into a laminar free flow or the open lab atmosphere [e.g. Lehmann et al., 2008, Shokri et al., 2010, Smits et al., 2012, Zhang et al., 2015], (ii) the free flow is too complex [e.g. Belhamri and Fohr [1996] include laminar to turbulent transitions or Song et al. [2014] include inlet/jet effects], (iii) lack of available geometrical information, input parameters, or measured data [e.g. Sugita and

Kishii, 2002], or (iv) radiation, precipitation, or other processes inside the porous medium are involved [e.g. Yamanaka et al., 1997, Fujimaki et al., 2006, Wanphen and Nagano, 2009, Jambhekar et al., 2015].

For stage-I evaporation, the free-flow conditions and especially the energy supply are crucial. Therefore, the analysis focuses on matching evaporation rates and temperature evolutions. Plotting the evaporation rates highlights differences during stage-I, when high evaporation rates prevail. If one aims at comparing integral values or stage-II behavior, cumulative mass loss plots are helpful. Fetzer et al. [2016] and Grüninger [2017] indicate that the problem setup, e.g. the thermal boundary conditions and the considered geometry or dimensionality, has a strong effect on the resulting transfer fluxes For this reason, the dimension at which the problem is considered (2-D vs. 3-D) and the thermal boundary conditions: (i) a perfectly insulated porous medium (*perfectly insulated walls*), (ii) a solution dependent energy transfer across the porous-medium walls (*insulated walls*), and (iii) constant temperatures at the porous-medium walls (*const. T walls*) are analyzed. Of course, the porous-medium properties also contribute to the characteristics of the evaporation process. This is comprehensively analyzed in Mosthaf et al. [2014].

In general, the basic experimental setups are comparatively similar. For all experiments, the simulation setup is a variation of the parallel-flow setup in Fig. 5.1. Tab. 5.8 lists the different setups with their geometrical information, porous-medium properties, boundary conditions, and initial conditions. In all cases, it is most difficult to specify the position at which the free-flow conditions are measured (start-up length) and the vertical profiles of velocity, relative humidity, and temperature. Therefore, spatially constant values are set at the inflow boundary and the start-up length is specified according to estimations based on the respective publication. First, the model is compared to the experiments by Mosthaf et al. [2014] to analyze how the changes in the underlying numerical model affect the simulation results. If not stated otherwise, all simulations for this section are run with the Baldwin-Lomax 0-Eq. model using the MAC discretization with CM4 and $Sc_\mathrm{t} = Pr_\mathrm{t} = 1$.

5.3.1 Mosthaf et al. [2014]

Mosthaf et al. [2014] perform evaporation experiments in which water evaporates from an insulated, rectangular, sand-filled Plexiglas box into a free air flow through a circular pipe. A Styrofoam insulation is applied around this box to minimize the heat loss. The soil sample is located on a balance which is used to determine the mass loss and thus the evaporation rate. Thermocouples inside the sand box and the windtunnel are used to monitor the temperature evolution over the experiment height and the run time.

		Mosthaf et al. [2014]	Davarzani et al. [2014]	Belleghem et al. [2014]	Lu et al. [2005]	Trautz [2015]	Haghighi and Or [2015]
free flow	type	pipe	duct	n.a.	duct	duct	open
	length	n.a.	3.72 m	250 mm[Be1]	175 mm[Lu1]	7.5 m	1.2 m
	height	–	0.26 m	10 mm	35 mm[Lu1]	1.0 m	1.2 m
	depth	–	0.09 m	70 mm	n.a.	1.0 m	0.2 m
	d or d_{hy}[(a)]	0.5 m	0.134 m	17.5 mm	35 mm	1.0 m	0.343 m
	v_{x}	3.5 m/s	1.2 m/s	2.3 m/s	1.89 m/s	0.8 m/s[Tr1]	0.7 / 3.5 m/s
	Re	116 666	10 911	2 683	4 410	53 333	16E3 / 80E3
	T	298.1 K	314.0 K	296.9 K	321.0 K	298.1 K	296.0 K
	RH	0.40	0.065	0.44	0.33	0.22	0.30
	$X_{\mathrm{g}}^{\mathrm{w}}$	0.0080	0.0032	0.0081	0.0231	0.0050	0.0052
porous medium	type	rectang.	rectang.	rectang.	cylinder	rectang.	rectang.
	length/diameter	0.25 m	0.25 m	90 mm	45 mm	7.3 m	1.0 m
	height	0.25 m	0.25 m	10 mm	15 mm	1.1 m	1.0 m
	depth	0.08 m	0.09 m	30 mm	–	0.09 m	0.3 m
	material	sand, #1	sand, #3	brick, #4	quartz, #5	sand, #3	sand, #1
	S_{w}	0.98	0.98	0.97	0.90	0.99	0.975[Ha1]
	T	298.1 K	300.8 K	296.9 K	289.8 K	298.1 K	296.0 K[Ha2]
	T_{bulb}[(b)]	289.4 K	292.7 K[Da1]	289.1 K	305.2 K	286.0 K	286.1 K
simulation	n_{x} (above pm)	30	25	9	16	18	15
	$n_{\mathrm{y}}^{\mathrm{pm}}$, $n_{\mathrm{y}}^{\mathrm{ff}}$	31, 31	25, 25	20, 15	8, 11	11, 15	7, 8
	$g_{\mathrm{y}}^{\mathrm{ff}}$	1.13	1.2	1.15	1.4	1.62	varies
	$\Delta y_{\mathrm{min}}^{\mathrm{ff}}$	0.75 mm	0.27 mm	0.10 mm	0.50 mm	0.50 mm	0.71 mm
	y_{min}^{+}	3.8	0.5	0.7	1.9	0.65	1.3 / 2.4

[(a)] The hydraulic diameter is defined as $d_{\mathrm{hy}} := {}^{4\,\mathrm{area}}/_{\mathrm{perimeter}}$.
[(b)] Wet bulb temperatures are calculated via an online tool (`https://www.weather.gov/epz/wxcalc_rh`, accessed on December 28, 2017).
[Da1] Based on average values for two days: $T^{\mathrm{ff}} = 314.5\,\mathrm{K}$ and $RH = 0.10$.
[Be1] Estimated from Belleghem et al. [2014, Fig. 3].
[Lu1] Estimated from the scale of the pm in Lu et al. [2005, Fig. 1].
[Tr1] Personal communication by A. Trautz [2017 and 2018].
[Ha1] $S_{\mathrm{w}} = 0.95$ is used for the simulations.
[Ha2] Estimated from Haghighi and Or [2015, Fig. 5].

Table 5.8: Overview on the specifications of the experiment setups.

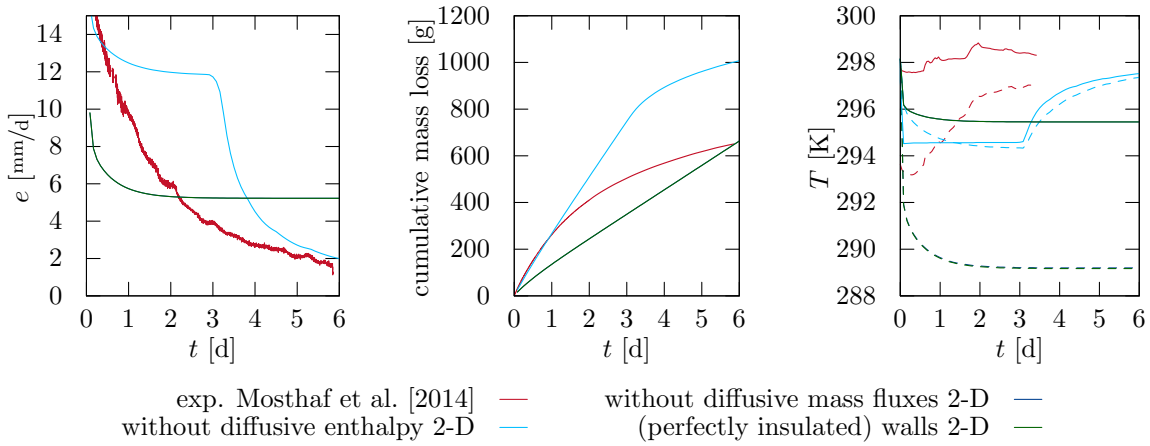

Figure 5.10: Comparison of simulation results to experiments by Mosthaf et al. [2014]. Evaporation rate (left), cumulative water mass loss (center), and temperature (right) are shown over time. The temperature is measured in the center of the windtunnel system, 1 mm below (dashed) and 1 mm above (solid) the interface.

As already said, the model presented in this work bases on the model presented in Mosthaf et al. [2011, 2014], but with two main differences: (i) diffusive fluxes of gas components transport their enthalpy (*diffusive enthalpy*) and (ii) diffusive mass fluxes are considered in the total mass balance as they, in contrast to the diffusive molar fluxes, do not cancel out (*diffusive mass fluxes*). The effect of these two changes are compared in Fig. 5.10. Further, the simulation setup differs from the one specified in Mosthaf et al. [2014]. They use a parabolic velocity profile, here a block profile is set 25 cm upstream of the porous medium. In addition, only the lower half of the pipe is modeled by applying symmetry boundary conditions at the center line.

The results in Fig. 5.10 show that incorporating the diffusive mass fluxes into the total mass balance does not alter the results (blue and green lines). But when not including the diffusive enthalpy fluxes, two-times higher evaporation rates are simulated. These higher rates result from less energy transfer between the porous-medium and the free flow (the water vapor mass is transported into the free flow, but not the energy portion associated with it). The consequences are higher porous-medium temperatures with higher saturation vapor pressures. An additional effect is then, that during the stage-I evaporation process, the smallest temperatures do not occur at the interface but at some distance inside the free-flow region, see Fig. 5.10 (right).
From the cumulative mass loss plot, it is visible that in addition to the failure in predicting stage-I evaporation rates, also the duration of stage-I is overestimated (2 days in the experiments, 3 to 8 days for the simulations). The cumulative mass loss at the end of stage-I is predicted to be almost double the mass loss reported by the experiments. For a more detailed

discussion on reasons for this behavior and the effect of different porous-medium properties it is referred to Mosthaf et al. [2014].

It is summarized that the experimental data can hardly be reproduced. The simulated evaporation rate, the cumulative mass loss, and the temperature show different temporal evolutions compared to the experiments. The determination of porous-medium properties and their reproducibility due to different filling procedures and operating persons is already mentioned to be critical in Mosthaf [2014] (compare results from Mosthaf et al. [2014] and Shahraeeni et al. [2012]). Mosthaf [2014] also mentions the strong assumption which is made by simulating in 2-D even though 3-D wall effects exist in the porous medium. In addition, Grüninger [2017] shows that a 3-D pipe enhances the exchange fluxes.

5.3.2 Davarzani et al. [2014]

Davarzani et al. [2014] perform evaporation experiments from a quartz sand into a free gas flow through a rectangular duct at four different velocities (0.55 m/s, 1.22 m/s, 3.0 m/s, and 3.65 m/s). The free flow is induced by a fan positioned downstream of the porous medium inside the windtunnel; the velocity is the measured with a Pitot tube. All inflow conditions are continuously monitored at an upstream position. These data sets are used to specify time-dependent boundary conditions for the simulations. As the previous experiments, also here the evaporation rate is measured via the mass loss monitored by a balance. The focus of the measurements is on processes inside the porous medium, especially the temperature and saturation evolution with a spatial resolution of 5 cm in each direction. Here, this setup is used to make a more comprehensive analysis regarding the effect of the energy boundary conditions around the porous medium.

The evaporation rates and cumulative mass loss plots shown in Fig. 5.11 (top) indicate a good agreement for stage-I and stage-II evaporation rates, but a too short stage-I or a too drastic transition to stage-II. The usage of a 2-D vs. a 3-D simulation setup hardly affects the results with a perfect insulation or constant temperature walls, but makes a difference for the insulated case. Then, the 3-D setup tends toward the case with constant temperature walls and the 2-D setup tends toward the perfect insulation, which makes sense as the energy input is reduced. The cumulative mass loss indicates the importance of the energy boundary conditions around the porous medium for the stage-I and stage-II evaporation behavior. The effect of fixing the temperature at the walls is an increase in stage-I evaporation rates caused by the better energy supply. If the porous medium is perfectly insulated and the air inside the windtunnel is warmer than around the porous medium, the stage-II evaporation rates increase, because the porous medium is heated by the free flow. For setups at this scale this

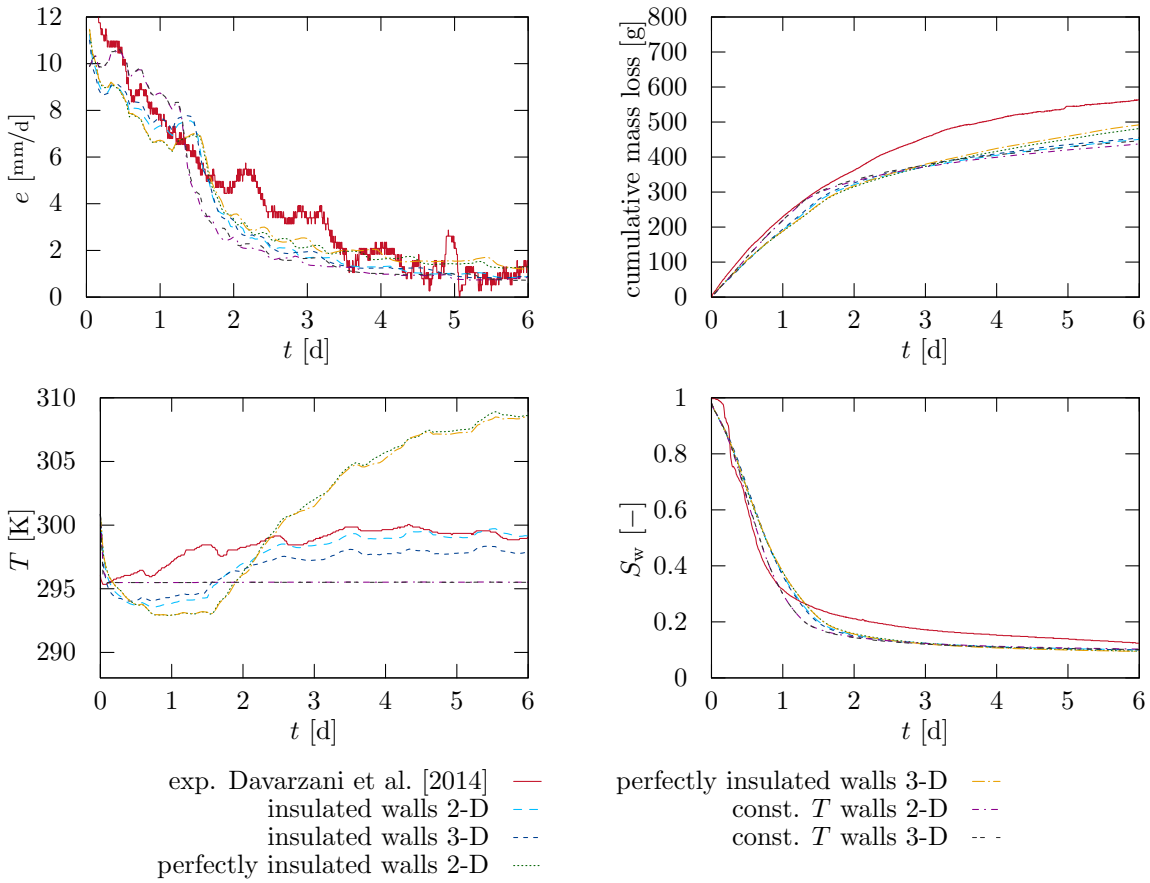

Figure 5.11: Comparison of simulation results to experiments by Davarzani et al. [2014]. The top row shows the evaporation rate (left) and the cumulative mass loss (right) over time. The bottom row shows the temperature (left) and liquid water saturation (right) over time. Temperature and saturation are measured in the center of the porous medium, 2.5 cm below the interface.

means, that a substantial amount of energy is supplied or extracted through the walls of the (insulated) porous-medium box.
The temporal temperature evolution in the center of the porous medium 2.5 cm below the interface shows that both extreme scenarios cannot predict the correct behavior, see Fig. 5.11 (bottom left). The case which includes an insulation, qualitatively reflects the fluctuations seen in the experiments and approaches the final stage-II temperature. The data sets from temperature and saturation sensors only show a little variation inside one row and therefore only one data set is compared with the simulations. For the sensor in the middle of the first row of sensors, there is a good qualitative agreement between the measured and the simulated saturation evolution Fig. 5.11 (bottom right). The match between data from experiments and simulations is worse for the other sensors in vertical directions.

Possible error sources are the definition of free-flow boundary conditions, especially those for the velocity. In comparison to the previous experiments, no flow straighteners are used and the wind is induced by a downstream-located fan. However, for the simulations a block-shaped velocity profile entering the upstream part of the windtunnel is assumed. The influence of the position at which a block profile is assumed is analyzed in Fetzer et al. [2016]. Further, a strong modeling assumption is that the temperature of the air flow is already constant over position at the inflow boundary and therefore no heater section is modeled.

5.3.3 Belleghem et al. [2014]

The experiment by Belleghem et al. [2014] is conducted to improve the understanding of moisture-transport related damages in building envelopes. A unique feature of this experiment, compared to the other experiments investigated here, is that it uses brick instead of sand as a porous medium. The rectangular brick sample is embedded in a Plexiglas and extruded polystyrene foam (XPS) insulation and exposed to flow through a wider, rectangular windtunnel. The water mass loss is tracked via a balance and different thermocouples are installed to measure the temperature evolution over time in vertical direction.

The results visualized in Fig. 5.12 show an excellent agreement in terms of the cumulative mass loss. The development of the evaporation rate, stage-I to stage-II transition, and the total water mass loss are predicted quite accurately. The temperature data indicates the importance of the energy supplied through the side walls of the brick insulation, which can only be modeled in 3-D. However, due to the low Reynolds number ($Re \approx 2683$), even the maximum values of the eddy viscosity are still in the same magnitude as the fluid viscosity.

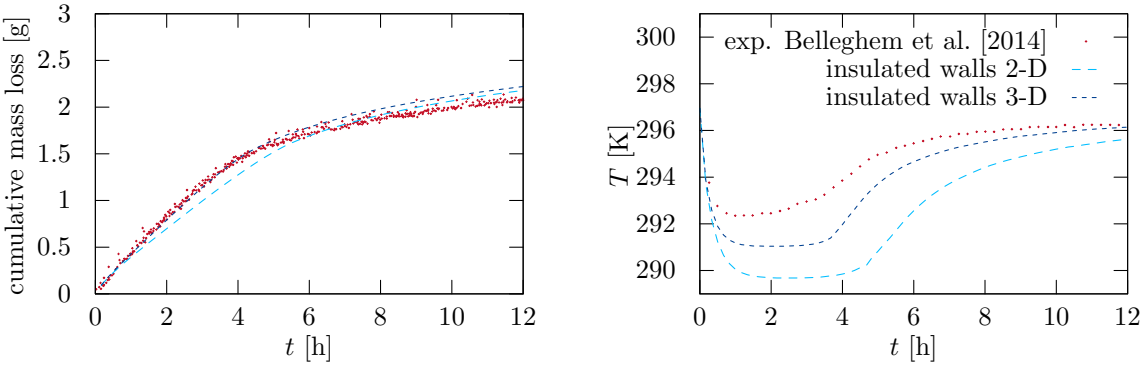

Figure 5.12: Comparison of simulation results to experiments by Belleghem et al. [2014]. Cumulative water mass loss (left) and temperature (right) are shown over time. The temperature is measured in the center of the brick, 10 mm below the interface.

5.3.4 Lu et al. [2005]

Lu et al. [2005] are interested in controlling the convective drying of porous media which is important in many areas, c.f. also Chapter 1. This experiment uses a sand-filled cylindrical container which is connected to a windtunnel and weighted via a balance. The dimensions and shape of this windtunnel are not further specified. It is assumed to be rectangular; length and height are extracted from the schematic sketch in Lu et al. [2005, Fig. 1]. The resulting Reynolds number ($Re \approx 4410$) is quite low, but the experiment features a comparatively high atmospheric demand, due to a large temperature difference ($T^{\mathrm{ff}} - T^{\mathrm{pm}} \approx 31\,\mathrm{K}$) and a lower relative humidity ($\mathrm{RH} = 0.33$). Lu et al. [2005] provide various temperature measurements, but also moisture content data. The moisture content of the porous medium is defined as:

$$MC = \frac{\text{water mass}}{\text{total mass}} = \frac{\phi S_\mathrm{l} \varrho_\mathrm{l} X_\mathrm{l}^\mathrm{w} + \phi S_\mathrm{g} \varrho_\mathrm{g} X_\mathrm{g}^\mathrm{w}}{\phi S_\mathrm{l} \varrho_\mathrm{l} + \phi S_\mathrm{g} \varrho_\mathrm{g} + (1-\phi)\varrho_\mathrm{s}} \tag{5.1}$$

The plots in Fig. 5.13 show improved results for the 3-D compared to the 2-D simulation. However, the stage-I evaporation rates are underestimated by the simulations and thus the temperature rise of the initially cooler porous medium is overestimated. Qualitatively, the evolution in moisture content and temperature can be met. The start of stage-II evaporation can be attributed to the temperature rise (e.g. at 5.2 h for the 3-D setup) and a kink in the moisture content data. This time is approximated by the 3-D simulation with a difference of 0.5 h. The porous-medium sample is very thin, this forces a short stage-II and a complete drying of the sample (final moisture content approaches zero). Due to a lack of data for the stage-II evaporation, hardly any conclusion can be drawn with respect to that stage.

It has to be mentioned, that the limited flexibility of the discretization method only allows

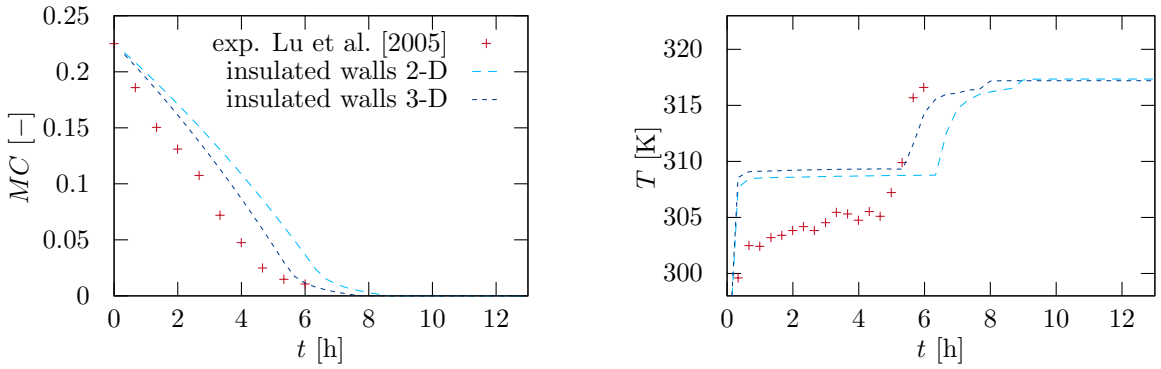

Figure 5.13: Comparison of simulation results to experiments by Lu et al. [2005]. Moisture content (left) and temperature (right) evolution are shown over time. The temperature is measured 8 mm below the interface, due to missing information, it is assumed that the measurements takes place along the center line of the cylinder.

a coarse approximation of the cylindrical sand box with rectangular cells. An insulation is indicated in the experiment setup [Lu et al., 2005, Fig. 1], but without any additional information. Thus, these properties are estimated from the figure scale and Plexiglas walls are assumed. Further, the size of the windtunnel is undefined and thus it is chosen such that the length and depth of the domain only have a small influence.

5.3.5 Trautz [2015]

This experiment is run with the largest soil-atmosphere windtunnel equipment of this comparison study. The width of the porous-medium container is in similar size as the previous experiments, but it is longer and especially of smaller width than the windtunnel. This data set provides 3×3 measurements of porous-medium temperatures and water saturations with high temporal resolutions. In addition, the surface conditions are measured at three locations. Trautz [2015] uses the same sand as Davarzani et al. [2014], but due to different packing and compaction mechanisms, the resulting properties are different. For simplicity, the properties specified in Davarzani et al. [2014] are used (soil #3).

Fig. 5.14 (left) shows two evaporation rates, which are obtained by two different means. Trautz [2015] uses data from infrared radiometers and a surface energy balance based on the publication by Shahraeeni and Or [2010]. Then, the evaporation rates at three different locations at the soil surface are calculated, see Trautz [2015, Fig. 7.6]. The author of this thesis has extracted these evaporation rates from the mentioned figure and has calculated, via a length-based average, the total evaporation rate for the entire porous medium (red line). The second procedure uses the saturation data provided in Trautz [2015, Fig. 7.4] to recalculate

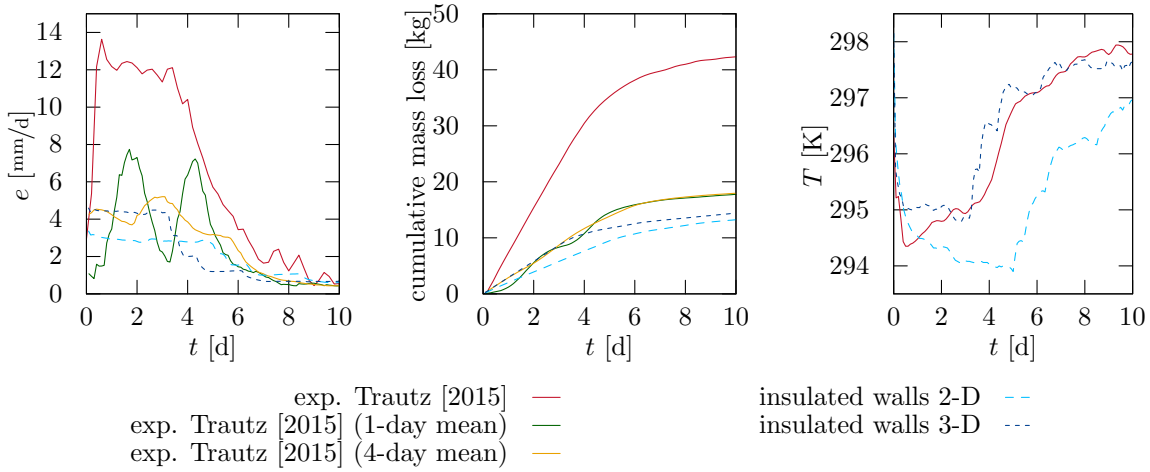

Figure 5.14: Comparison of simulation results to experiments by Trautz [2015]. The evaporation rate (left), the cumulative mass loss (center), and the surface temperature (right) evolution is shown over time. In the left two figures, the red lines are obtained via a surface energy balance, cf. Shahraeeni and Or [2010]. The green and the yellow lines are calculated via the saturation measurements in the first two rows of sensors. The temperature is measured at $x = 4.82\,\mathrm{m}$ on the soil surface.

the mass loss and thus the evaporation rate on an hourly basis. This is possible because all sides of the tanks are closed[12], the system is initially fully saturated, and no saturation decrease in the third row of sensors until day 10 is observed. In this case, this technique can only rely on two rows of sensors. As a consequence, even the data set which uses an averaging interval of one day shows two distinct peaks (green line). These peaks occur when the saturation at the respective sensors decreases. Therefore, the evaporation rate at a specific time might be of limited expressiveness and is better approximated by a large averaging interval (orange line). However, the difference between the evaporation rates from surface energy balance and from saturation measurement is around factor three. Based on the simulation results and after discussion with the author of the experiments, the saturation-based data is assumed to be more reliable.

The cumulative mass loss, Fig. 5.14 (center), indicates a good prediction of stage-I and stage-II evaporation rates. As in most of the other experiment comparisons, the duration of stage-I is not predicted correctly.

The surface temperature results, Fig. 5.14 (right), are in a good agreement for both stages and the transition, especially under the consideration of the uncertainty of the sensor measurements, which is $\pm 0.5\,\mathrm{K}$ [Trautz, 2015].

This setup clearly has to be simulated in 3-D. The energy supply through the side walls of the porous-medium tank, which could theoretically be modeled by a source term in a 2-D setup, is

[12] Personal communication by A. Trautz [2017 and 2018].

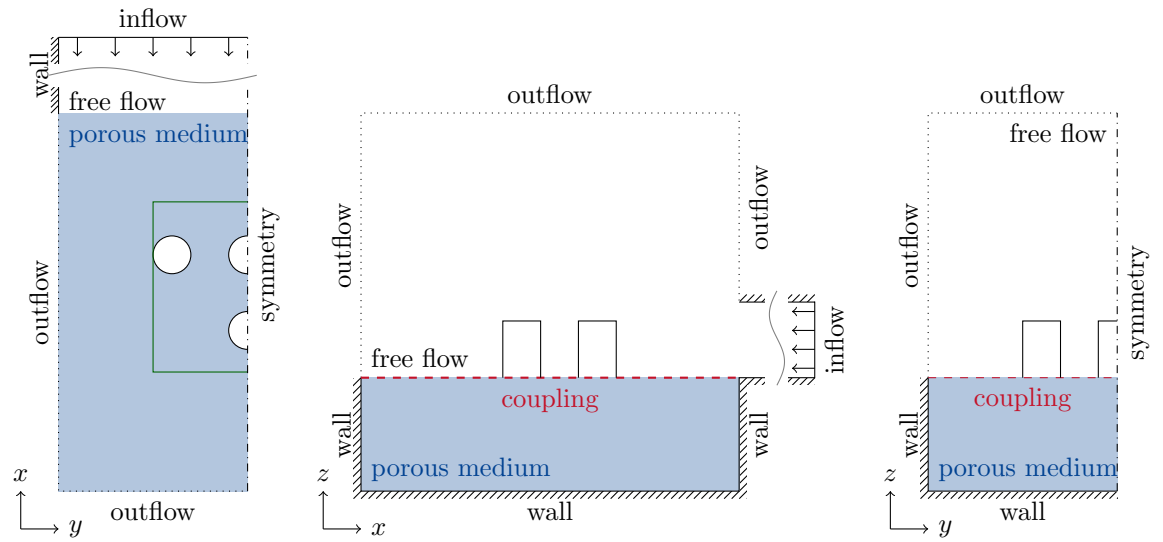

Figure 5.15: Simulation setup for the experiments by Haghighi and Or [2015]. Top view (left), side view (center), and front view (right) of the 3-D simulation setup are shown together with the associated boundary condition types.

crucial for predicting stage-I evaporation rates and for sustaining higher surface temperatures. What is not shown here, is the importance of the soil properties. Other simulation runs with different soil properties for the used sand may lead to a different duration of stage-I. In addition, because of the low evaporation rate and the large tank, the initial water content in the model has a distinct influence on the duration of stage-I.

5.3.6 Haghighi and Or [2015]

In order to test the model against a more complex scenario, the experiment by Haghighi and Or [2015] is chosen. They perform multiple experiment runs with flow around 'bluff bodies', which are cylindrical obstacles placed on an initially water-wet sand. Haghighi and Or investigate the influence of different obstacle configurations (flat, 1, 4, and 9) in combination with three different velocities (0.7 m/s, 1.8 m/s, and 3.5 m/s) on the resulting evaporation rates and surface temperature distributions. Flow is induced by fans, evolves in a small chamber and then flows over the sand box. The velocity field is measured by ultrasonic anemometers at the end of the test section and the atmospheric conditions are measured in the center of the chamber. The weight loss is measured with a balance including 4 measurement units.

The simulation setup depicted in Fig. 5.15 is considerably more complex than in the previous experiments. One consequence is that the Low-Re k-ε model is applied instead of a 0-Eq. model. The Low-Re k-ε is chosen because of a better convergence behavior than the k-ω

	$v_{g,x}$ [m/s]	e^{mean} [kg/h]		
		flat	1 obstacle	4 obstacles
exp.	0.7	0.12 (0.05)	0.13 (0.05)	0.18 (0.08)
sim.	0.7	0.11	0.11	0.12
exp.	3.5	0.25 (0.10)	0.33 (0.08)	0.60 (0.13)
sim.	3.5	0.22	0.25	0.28

Table 5.9: Comparison of evaporation rates to experiments by Haghighi and Or [2015]. Values in parenthesis indicate the standard deviation of 4-5 runs for each configuration.

model. Due to limited computational power and available memory, the setup includes a symmetry boundary along the center line of the experiments and the number of grid cells is rather small. The area of each cylinder is resolved by 6×6 cells and a large grading factor ($g_z = 3.5$) is applied in vertical direction. With the aim to compare the different obstacle setups without changing the spatial grid, the resolution is limited by the case including the most obstacles (here 4) and results in a grid which reveals areas with an unnecessary high number of cells for the cases with less obstacle.

Tab. 5.9 compares the mean evaporation rate over the entire duration of the experiment. The evaporation rates for the flat surface are in good agreement with the experiment results. For the low velocity case, the simulation results are always within the measurement uncertainty. For the high velocity case, they are just inside this range for 1 obstacle, but for 4 obstacles the evaporation rate is strongly underestimated. For both velocities, the increase in evaporation rate associated with the increase in obstacles is underestimated.

The surface temperatures of experiments and simulations are compared for two selected configurations in Fig. 5.16. Already for 1 obstacle and a low velocity, grid artifacts are visible, e.g. rectangular temperature patterns around the obstacle. Qualitatively, the simulation can prescribe the cooler and warmer areas upstream of the obstacle and the region of obstacle influence. Downstream, more deficiencies are visible, the area directly behind the obstacle, the shape of the cooling plume, and the outer areas. The temperature difference between the simulations and the experiments is about $\pm 1.0\,\mathrm{K}$ for lower velocities and less obstacles. For a higher velocity and in combination with more obstacles, the temperature difference between simulations and experiments increases to roughly $\pm 1.5\,\mathrm{K}$.

The major part of these discrepancies can be attributed to the free-flow side. First, the numerical method (implicit and first-order upwind) may not be the most appropriate for modeling flow around such obstacles. Second, the discretization is too coarse to resolve the shape of the cylinders and the processes around them. Third, better free-flow models would lead to a better description of the turbulent flow field, e.g. more turbulence resulting from the

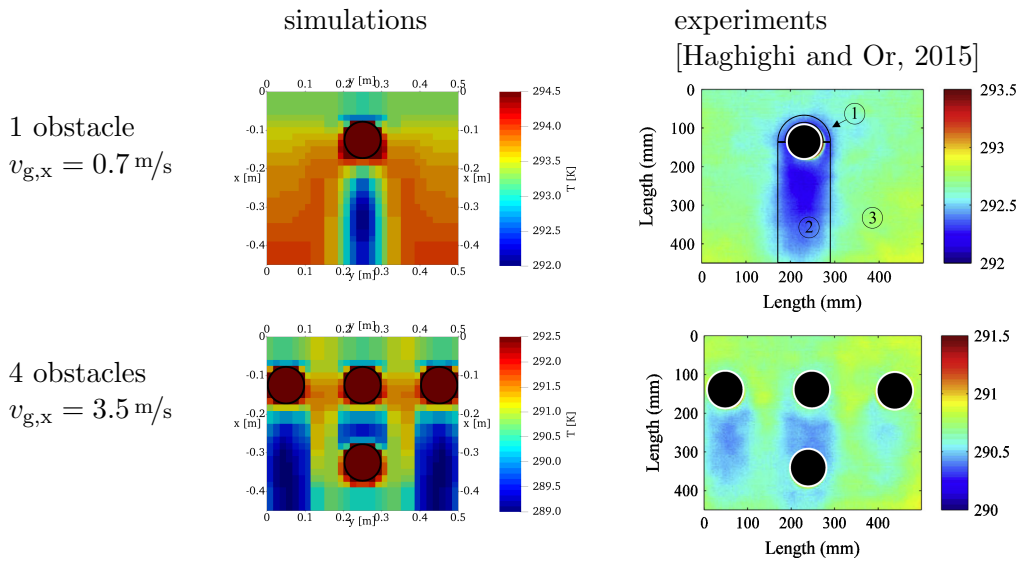

Figure 5.16: Comparison of surface temperatures to experiments by Haghighi and Or [2015]. Surface temperature are extracted at the end of the simulation, the time at which the surface temperatures are measured in the experiments was not given. *Note:* (i) the figures do not use the same temperature ranges, (ii) the figures extracted from Haghighi and Or [2015] show a mismatch in x-y-ratio.
Results of the experiments are reprinted from *Interactions of bluff-body obstacles with turbulent airflows affecting evaporative fluxes from porous surfaces*, 530, Erfan Haghighi and Dani Or, Journal of Hydrology, 14, ©2015, with permission from Elsevier.

cylinder surface and thus enhanced turbulent exchange with higher evaporation rates. One first step to circumvent this problem would be a transport model. Then, the turbulent free flow has to be solved once via a two-equation turbulence model or more advanced turbulence models from external software can be used. In addition, a higher spatial resolution can be achieved.

The conversion from an experiment to a simulation setup bears some uncertainties. From images in Haghighi and Or [2015], it seems as there is a small step from the chamber onto the soil surface and also the soil surface is disturbed around the cylinders. In addition, the velocity is measured at the end of the domain but set as inflow condition inside the chamber. The porous medium is simplified by not integrating the water inflow from the bottom of the domain and applying perfect insulation around the sand box. In reality there might be an imperfect insulation and also the sand is connected to a Mariotte bottle to maintain a constant water level, which leads to an inflow of water and its associated energy. However, even if no water is supplied, the surface will not dry-out completely, the observed saturation decrease is $\Delta S_\mathrm{l} = 0.4$. Finally, the boundary conditions in the free flow are quite undefined and the effect of the assumed outflow conditions has to be analyzed.

		tolerance	Mosthaf et al. [2014]	Davarzani et al. [2014]	Belleghem et al. [2014]	Lu et al. [2005]	Trautz [2015]	Haghighi and Or [2015]
stage-I	duration of stage-I	10%	↑	↓	✓	✓	↓	n.a.
	e	10%	↓	✓	✓	↓	✓	(✓)
	T^{pm}	1 K	↓	↓	✓	↑	✓	(✓)
	T^{pm} compared to T_{bulb}	0.2 K	✓	✓	n.r.	n.r.	n.r.	n.r.
stage-II	cumulative mass loss	10%	↑	↓	✓	✓	↓	n.a.
	e	visual	✓	✓	✓	n.a.	✓	n.a.
	T^{pm}	1 K	↓	✓	✓	✓	✓	n.a.

Table 5.10: Qualitative summary of a comparison study to various laboratory experiments. If available, the 'insulated walls 3-D' simulation results are taken. The 'perfectly insulated walls' cases are taken for the wet-bulb temperature comparison. It is indicated, whether experimental data is not available (n.a.) or simulation sets are not run (n.r.), e.g. perfect insulation for wet-bulb comparison. Values in parentheses are based on the outcome of the majority of the investigated setups.

5.3.7 Summary

In this section, six different laboratory experiments are used to compare and analyze simulation results. The importance of changes in the model concepts, boundary conditions, and dimensionality is highlighted. The results are qualitatively summarized in Tab. 5.10 with respect to stage-I/stage-II transition, evaporation rates, and temperatures. For all setups with a perfect insulation, the difference between simulated and expected wet-bulb temperatures is below 0.2 K or 0.1%. In general, the evaporation rates and the temperatures in stage-II are in good agreement. The cumulative mass loss is not predicted correctly, mainly because of problems in predicting the stage-I to stage-II transition. The stage-I evaporation rates are in a good agreement for most of the investigated setups. However, the temporal evolution of the evaporation rates and the temporal and spatial temperature evolution can be improved. The quality of simulated stage-I temperatures strongly depends on the available information about the energy supply through the walls of the porous-medium container.

Three main error sources are detected from the simulation side: (i) the (free-flow) discretization, (ii) the porous-medium properties, and (iii) the boundary conditions for the simulation or in other words the transfer from laboratory to numerical experiments. The deficiencies

in the numerical (free-flow) concept are obvious in the last example, in which the free-flow field is not resolved accurately enough, but also for the experiments with a cylindrical pipe or cylindrical porous-medium container, the results can be improved with a better discretization. Analyzing the effect of the Reynolds number on the simulation results would be interesting. Here, the experiment with the lowest Reynolds number shows the best match. However, in that study, many other conditions are also changed (e.g. brick instead of sand), so the influence of the Reynolds number on the quality of the simulation results is not clear. A correct description of the free flow is strongly connected to the definition of boundary conditions. For all experiments, block-shaped inflow conditions are assumed and often this inflow location is guessed. In addition, important information about the free flow, the porous-medium, or the room conditions are missing, e.g. Lu et al. [2005] keep the information about the windtunnel quite short. A correct system setup and boundary conditions are not only a problem for the free flow, but also for the porous medium. This comparison study includes examples in which the results are clearly improved by using 3-D instead of 2-D simulations. The 2-D simulation results could be improved by including a source term which accounts for the energy supply through the walls, e.g. for the experiments by Belleghem et al. [2014] the main difference between 2-D and 3-D is in the temperature evolution. As already discussed in Mosthaf et al. [2014], the porous-medium properties have a distinct influence on the shape of the evaporation rate and mismatches in the duration of stage-I might be attributed to them. For sand, the filling and compaction procedures result in different porous-medium properties or local heterogeneities for even the same material. These local heterogeneities influence the processes at various interfaces, e.g. between the porous medium and the free flow, but also near the walls of the porous medium, cf. Haghighi et al. [2013], Mosthaf [2014].
Despite all those error sources, only one publication provides error estimations based on multiple runs for the same experiment setup [Haghighi and Or, 2015].

5.4 Investigation of Roughness

The last part highlights the effect of the roughness of porous media. This includes cases with sharp heterogeneities, sand-grain roughnesses, and porous obstacles.

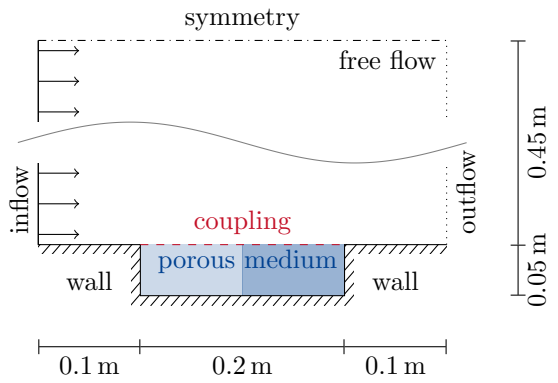

Figure 5.17: Simulation setup for the heterogeneity roughness case, after Fetzer et al. [2017c].

parameter	value
$\boldsymbol{v}_g^{ff}$ [m/s]	$(1.0, 0)^\intercal$
p_g^{ff} [Pa]	1E5
$X_g^{w,ff}$ [−]	0.0055
T^{ff} [K]	293
soil type	#6 and #7
p_g^{pm} [Pa]	1E5
S_l^{pm} [−]	0.97
T^{pm} [K]	293

Table 5.11: Initial and boundary conditions for the heterogeneity roughness case, after Fetzer et al. [2017c].

5.4.1 Heterogeneity Roughness[13]

To investigate the effect of soil types (e.g. silt and sandy loam) and its orientation on evaporation, simulations are run in which two soil blocks are placed adjacent to each other as seen in Fig. 5.17.

Impact of Heterogeneities in the Porous Medium Fig. 5.18 (left) shows the evaporation rates from homogeneous and heterogeneous test cases. For the homogeneous silt case, a steady state evaporation rate is obtained during the first day that remains constant until day 3.5 when the evaporation rate decreases. Feedbacks between free and porous-medium flow result in higher humidities as the air flows along the test section, the evaporation rate from the downstream half of the test section is smaller than from the upstream half. The evaporation rate from the upstream part decreases a little earlier than the downstream part, which leads to a short peak in evaporation from the downstream part. Since the initial water distribution is uniform in the simulation domain, this illustrates that lateral water flow in the porous medium compensated for the higher evaporation losses in the upstream part. Lateral variations in air humidity and temperature in the free flow, which lead to lateral variations in evaporation rate, also induce lateral liquid flow in the porous medium.
In the heterogeneous test cases, the initial evaporation rates are only depending on their position (atmospheric conditions) and not on the soil type (porous-medium properties). However, the sandy loam section's evaporation rate starts to decrease earlier than evaporation from the

[13]This section is, in a longer version, already published in: T. Fetzer, J. Vanderborght, K. Mosthaf, K. M. Smits, and R. Helmig: Heat and water transport in soils and across the soil-atmosphere interface: 2. Numerical analysis, *Water Resources Research*, 53(2):1080–1100, 2017. doi: 10.1002/2016WR019983. The journal publication presents quantitatively different results which are caused by the usage of a different turbulence model and a bug in the calculation of the thermal conductivity in DuMu^x 2.9.

finer silty part, related to the differences in soil hydraulic properties. This falling rate period correlates to the soil entering into stage II evaporation. The decrease in evaporation from the sandy loam is accompanied by an increase in evaporation from the silt part. The silt material functions as a wick that drained water from the adjacent sandy loam resulting in a longer sustained high evaporation from the silt material than in the homogeneous silty test case. This behavior is also demonstrated in lab experiments Lehmann and Or [2009]. The second smaller decrease in evaporation rate from the sandy loam around day 4.5 (green, dotted) occurs when the liquid water flow to the evaporation front in the sandy loam soil driven by gradients in capillary forces is reduced by the limited water supply due to the no-flow bottom boundary condition of the box. With a deeper porous-medium box, the decrease would be continuous. Also, the second drop in evaporation rate from the sandy loam surface corresponds with a further increase in evaporation rate from the silt surface, despite the drying of the silt surface. After the second increase of evaporation from the silt, also the silt starts drying out. This shows that for a heterogeneous surface, the evaporation rate may locally increase and become even larger than from a homogeneous surface. The relative increase in evaporation from the silt part is larger when it is located downstream of the sandy loam part. In this case, the temperature and humidity of the air that flows over the silt part, respectively, increase and decrease when the evaporation from the upstream part decreases.

When the finer silt part is upstream of the sandy loam, the evaporation rate from the silt also increases when evaporation from the sandy loam part decreases. This indicates that, in this case, lateral mixing in the air increased temperature and reduced humidity in the upstream direction above the silt part. Another potential reason is the lateral heat flux in the porous medium, which increases the temperature at the surface of the silt soil when evaporation from the sandy loam part changed.

Impact of Lateral Gradients in the Free Flow To evaluate the influence of changes in lateral gradients in the free flow above a drying heterogeneous porous medium on the evaporation, the one-dimensional aerodynamic resistances r_{mass} are derived in a first step:

$$q^{\mathrm{w}}_{\text{1-D}} = \varrho_{\mathrm{mol,g}} M^{\mathrm{w}} \frac{x^{\mathrm{w,if}}_{\mathrm{g}} - x^{\mathrm{w,ref}}_{\mathrm{g}}}{r_{\mathrm{mass}}} = \frac{\varrho^{\mathrm{w,if}}_{\mathrm{g}} - \varrho^{\mathrm{w,ref}}_{\mathrm{g}}}{r_{\mathrm{mass}}} \,. \tag{5.2}$$

These resistances are subsequently used to calculate the evaporation rates from the heterogeneous porous medium when evaporation of one of the parts ceased (after day 3.5) and compared to those of the fully-coupled 0-Eq. model (fc):

$$q^{\mathrm{w}}_{\mathrm{fc}} = - \left[\left(\varrho_{\mathrm{g}} X^{\mathrm{w}}_{\mathrm{g}} \boldsymbol{v}_{\mathrm{g}} + \boldsymbol{j}^{\mathrm{w}}_{\mathrm{mass,eff}} \right) \cdot \boldsymbol{n} \right]^{\mathrm{ff,if}} \,. \tag{5.3}$$

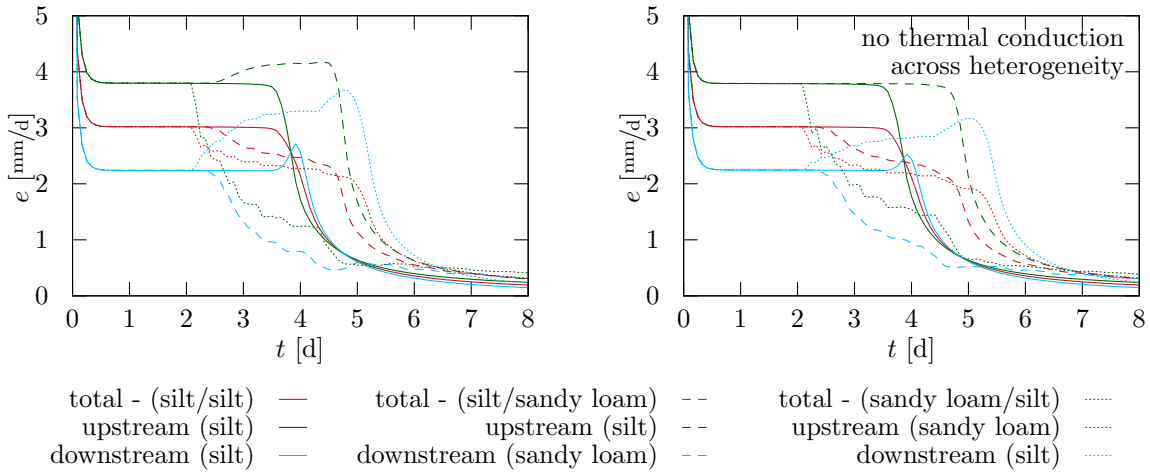

Figure 5.18: Evaporation rates from a homogeneous soil and a soil with a heterogeneity in the horizontal direction[13]. Red lines represent the average evaporation rates across the interface, green lines from the upstream part, and blue lines from the downstream part. Full lines are evaporation rates for the homogeneous case (both parts are silt), dashed lines for the first heterogeneous case (upstream part: silt, downstream part: sandy loam), and dotted lines for the second heterogeneous case (upstream part: sandy loam, downstream part: silt).

For the upstream part, the evaporation rates are fairly well reproduced using the one-dimensional aerodynamic resistances, see Tab. 5.12. This indicates that the air humidity and air temperature profiles in the upstream part are mainly defined by the vapor concentration and temperature at the porous-medium surface and in the inflowing air. The increase in evaporation rate from the upstream silt part when the evaporation from the downstream sandy loam part ceases could be linked to an increase in vapor concentration and temperature at the porous medium surface. Whether this increase in surface temperature and vapor concentration can be predicted based on the lateral heat transfer in the porous medium alone still needs to be investigated. When the dry and less-evaporating sandy loam part is upstream, its lower evaporation rate could also be reproduced fairly well from the surface vapor concentration and the one-dimensional aerodynamic resistance. The conditions in the free flow in the downstream part, that being vertical profiles of air humidity and temperature, are strongly influenced by evaporation from the upstream part and changed when the evaporation from this part changed. These temporal changes in air humidity profiles due to changing evaporation rates in upstream parts from heterogeneous surfaces could not be represented by one-dimensional aerodynamic resistances that are derived for other evaporation conditions in the upstream part.

setup	parameter	upstream	downstream
silt/silt	$\varrho_{\mathrm{g}}^{\mathrm{w}}$ [kg/m³]	10.4E−3	10.4E−3
	q^{w} [kg/m²s]	4.32E−5	2.59E−5
	r_{mass} [s/m]	89.0	151.1
silt/sand	$\varrho_{\mathrm{g}}^{\mathrm{w}}$ [kg/m³]	10.7E−3	9.3E−3
	$q_{\mathrm{fc}}^{\mathrm{w}}$ [kg/m²s]	4.77E−5	1.12E−5
	$q_{\mathrm{1\text{-}D}}^{\mathrm{w}}$ [kg/m²s]	4.73E−5	1.85E−5
sand/silt	$\varrho_{\mathrm{g}}^{\mathrm{w}}$ [kg/m³]	7.9E−3	10.9E−3
	$q_{\mathrm{fc}}^{\mathrm{w}}$ [kg/m²s]	1.65E−5	3.75E−5
	$q_{\mathrm{1\text{-}D}}^{\mathrm{w}}$ [kg/m²s]	1.52E−5	2.89E−5
	$q_{\mathrm{1\text{-}D}}^{\mathrm{w}}$ [kg/m²s]		4.91E−5*

Table 5.12: Average vapor concentrations and evaporation fluxes at the surface of the homogeneous/heterogeneous porous medium after 3.5 days of evaporation[13]. The one-dimensional aerodynamic resistances, that are derived from evaporation fluxes and vapor concentrations ($\varrho_{\mathrm{g}}^{\mathrm{w}} = \varrho_{\mathrm{mol,g}} M^{\mathrm{w}} x_{\mathrm{g}}^{\mathrm{w}} = \varrho_{\mathrm{g}} X_{\mathrm{g}}^{\mathrm{w}}$) using the fully-coupled 0-Eq. model (fc) for the homogeneous setup, are used to calculate the one-dimensional fluxes of the heterogeneous setups (1-D). The inflow vapor concentration is $\varrho_{\mathrm{g}}^{\mathrm{w,ref}} = 6.5\mathrm{E}{-3}\,\mathrm{kg/m^3}$. The value marked with * uses r_{mass} from the upstream part.

Impact of Lateral Heat Fluxes in the Porous Medium In Fig. 5.18 (right), simulated evaporation rates are shown for the case that conductive heat transfer between up and downstream parts are blocked. Then, the increase in evaporation from the silt parts at the time when the evaporation from the sandy loam parts decreases is clearly less. When conductive heat transfer between the silt and sandy loam blocks is blocked, the evaporation rate in the upstream silt block (green, dashed) does not increase when the evaporation from the downstream sandy loam part decreases. This demonstrates that the increase in evaporation from the upstream silt part when the evaporation from the downstream sandy loam part decreases is due to conductive heat fluxes in the porous medium rather than heat transfer through the air flow. The increase in evaporation rates from the downstream silt block is to larger portion related to the change in atmospheric conditions, especially the relative humidity of the approaching air.

5.4.2 Sand-Grain Roughness

In Fetzer et al. [2016], the effect of roughness is analyzed for different model concepts when applied to the experiment published in Davarzani et al. [2014]. Here, the emphasis is on the effect for different velocities (0.35 m/s, 1.75 m/s, 3.5 m/s) and thus Reynolds numbers (6 000, 30 000, 60 000). Therefore, the parallel-flow setup specified in Fig. 5.1 is changed by applying various sand-grain roughness lengths (0.25 mm to 8 mm). To minimize inlet effects, it is

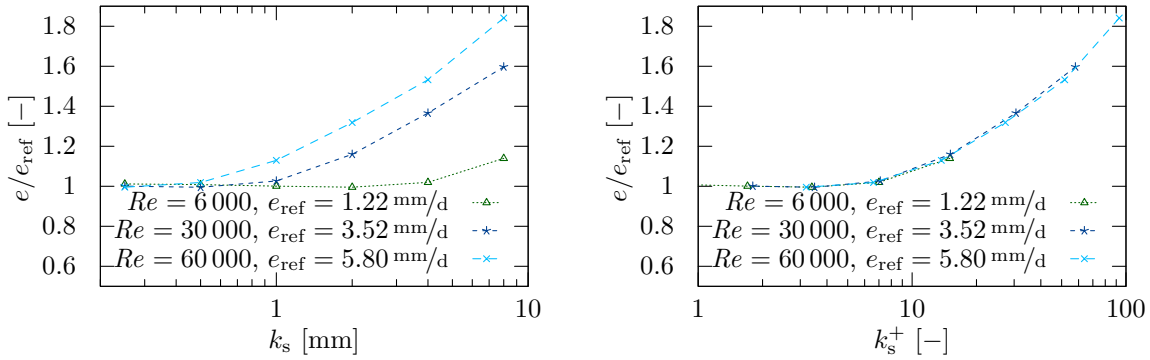

Figure 5.19: Effect of the sand-grain roughness on steady-state stage-I evaporation rates. The left figure shows the dependency on the absolute sand-grain roughness length, whereas the right figure relates the evaporation rate to the dimensionless sand-grain roughness.

assumed that the sand-grain roughness does not only exist at the interface, but at the entire bottom of the free-flow simulation domain. It has to be mentioned, that all considered sand-grain roughness lengths are larger than the smallest cell at the bottom of the domain. This is an inconsistency for these sets of simulations but as the main interest is not on the velocity evolution or velocity distribution inside this region but on the integral, mainly diffusion-limited exchange fluxes, it is assumed that the model still gives qualitatively meaningful results.

As expected, the results in Fig. 5.19 (left) show that larger roughness lengths lead to higher evaporation rates, as turbulent effects move closer toward the interface. Basing the relative evaporation rates on the dimensionless sand-grain roughness k_{s}^{+}, as plotted in Fig. 5.19 (right), shows how the increase in evaporation only depends on this parameter. The used roughness concept is, as already written, only applicable in the range of $4.535 < k_{\mathrm{s}}^{+} = \frac{u_\tau k_{\mathrm{s}}}{\nu} < 2000$. Even if the lower bound is violated, the results are almost identical with those of a smooth surface. This leads to two additional conclusions. First, for small Reynolds numbers ($Re \lessapprox 50\,000$) the roughness length has to be relatively high, especially larger than they exist in natural soils, e.g. this sand (#1) has a sand grain diameter range of $d_{\mathrm{min}} = 0.3\,\mathrm{mm}$ to $d_{\mathrm{max}} = 0.9\,\mathrm{mm}$. Compared to the results presented for the turbulent Schmidt and Prandtl numbers (Fig. 5.8), for the largest Reynolds number and the mentioned grain size range, the effects are in a similar order of magnitude. Second, as already discussed, boundary layer models which include the effect of roughness are only meaningful in the small transition region between hydrodynamically smooth surfaces (no effects due to the sand-grain roughness) and rough surfaces (viscous boundary layer moves into the porous medium). The findings of the fully-coupled 0-Eq. model indicate, that in this range the effect of roughness is minor.

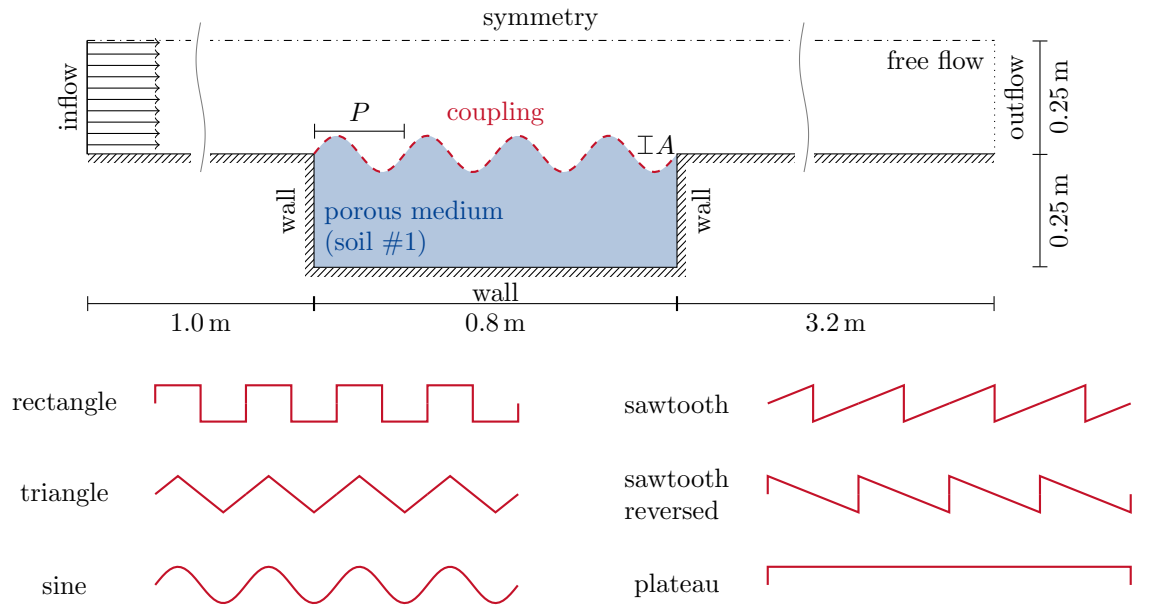

Figure 5.20: Simulation setup for analyzing the influence of porous obstacles. The different shapes used in this study are shown. The height of an obstacle is defined by its amplitude, A. Here, one obstacle corresponds to one period, P. In addition, the plateau shape is used as an extreme case.

5.4.3 Obstacle Roughness

In the last study, the influence of different interface shapes/porous obstacles is analyzed. This study comprises different obstacle heights, obstacle lengths, and obstacle shapes. The investigated setup here differs from the previous reference setup and is shown in Fig. 5.20. The initial and boundary condition values correspond to the turbulent conditions presented in Tab. 5.5. The reasons for the changes are that a longer porous medium is needed to evaluate the influence of different numbers of porous obstacles and the windtunnel has to be long enough to ensure a proper outflow condition on the right. On the top of the windtunnel, a symmetry boundary condition is applied. Of course, all conclusions drawn in this section depend on the height of the free flow channel above the porous medium. For industrial production or filtration processes, this might be a realistic setup, as the porous medium will likely be attached to the windtunnel from more than one side. This contrasts with flow over ploughed soil under outdoor conditions, then the reduction in cross-section area is negligible. The area around the obstacles is resolved with $\Delta x = 10\,\text{mm}$ and $\Delta y = 2.5\,\text{mm}$. All simulations are performed with the Low-Re k-ε model using CM3 (theoretically CM4 can be used, but results in tiny time steps for the reasons listed in section 4.1.2.2). The reference setup (ref) has 4 obstacles ($P = 0.2\,\text{m}$) with an amplitude of $A = 40\,\text{mm}$ and a sine shape.

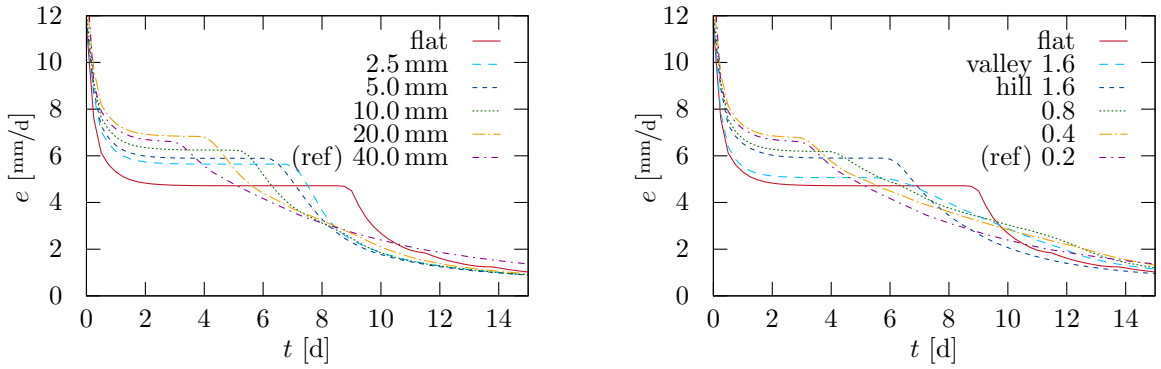

Figure 5.21: Evaporation rates for different obstacle heights (left) and lengths (right).

Fig. 5.21 (left) shows that already small perturbations of the flat surface lead to higher stage-I evaporation rates. The increase in steady-state stage-I evaporation rates is less than compared to the increase caused by a sand grain-roughness model (the relative increases are e.g. for $A = k_s = 2.5\,\text{mm}$: 1.2 vs. 1.4, and for $A = k_s = 10\,\text{mm}$: 1.3 vs. 1.9 (extrapolated)). If the obstacle height increases, at least three different effects can be reported. First, for higher obstacles, the deflection of the flow at the first obstacle is stronger and the flow requires a longer distance to reattach to the top-level of the obstacles. Here, the symmetry boundary condition has a considerable effect, as the flow is forced through a smaller channel which increases the mean velocity therein (the cross-section compared to the flat surface is reduced from 99% for 2.5 mm to 84% for 40 mm). Second, higher obstacles reduce the availability of water at the top level. The capillary forces are too weak to overcome gravity and pull water from the bottom of the porous-medium box, cf. Lehmann et al. [2008]. And third, also the area of the cavities in between two hills increases and the vortices inside change their behavior. These three effects may lead to the following observations. The stage-I evaporation rate does not monotonously increase with height, but reach a maximum for obstacles of 20 mm height in this setup. In contrast to the rate, the duration of stage-I does monotonously decrease with height. Analyzing the cumulative mass loss (not shown here) indicates that for higher obstacles, less water did evaporate when the transition to stage-II is reached. The transition to stage-II is smoother for higher obstacles. An interesting observation is that the stage-II evaporation rate is noticeably higher for the highest obstacles.

In Fig. 5.21 (right) the influence of different obstacle periods is shown. The period also influences the number of obstacles and care must be taken, whether the observed effects are caused by changing the period and thus the shape of the obstacles or the number of obstacles. As for the obstacle height, the minimum stage-I evaporation rate is predicted for the flat surface. Even the valley part of half an obstacle shows an increased rate. Driving forces for this behavior are (i) a significant downward and upward flow, (ii) a higher porous-medium

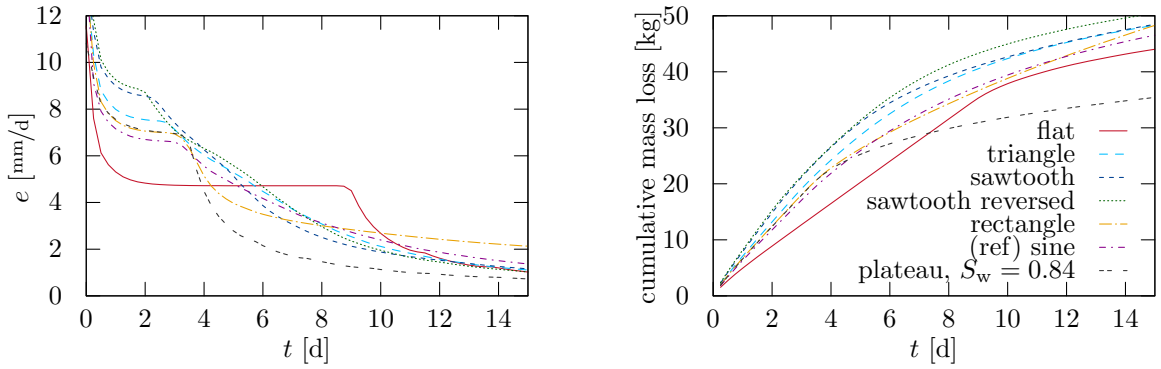

Figure 5.22: Evaporation rates (left) and cumulative mass losses (right) for different obstacle shapes.

free-flow interface, and (iii) higher eddy diffusivities in vicinity of the interface. It makes sense that having only the hill part of half an obstacle shows a higher rate than the valley. The free flow better follows the obstacle at the beginning, there, the air is saturated with water vapor. In addition, the increase in mean flow velocity caused by the cross-section reduction is almost 30%. What seems counter-intuitive is that the duration of stage-I is almost identical for both cases. This is explained, by initially setting a constant saturation of 0.98, thus ∼17% more water is available for the hill compared to the valley. Unfortunately using the same amount of water as for the reference case is not possible, otherwise the initial water saturation for the valley setup would be greater than one. However, it would lead to a shorter stage-I for the hill setup and longer stage-I for the valley setup. It is observed that the maximum stage-I evaporation rate is not reached for the shortest period (most obstacles). Shorter periods lead to steeper slopes, less favorable flow configurations, and more deflection effects. The duration of stage-I seems to converge against a minimum value for shorter periods. Also, the stage-II evaporation rates seem to approach a maximum for the shorter periods. Including cavities leads to smoother transitions to stage-II, but without any obvious trend.

The effects of different obstacle shapes are shown in Fig. 5.22. Each shape features different factors which influence the flow field and the exchange behavior. The main factors forming the shape of the evaporation process are (i) the distribution of the eddy diffusivity, (ii) the interface area available for exchange, and (iii) the flow field (especially the formation of cavity flow). The sine shape has the least edges, these edges are responsible for the creation of turbulent kinetic energy, because of stronger velocity gradients. Therefore, the sine shape has the lowest stage-I evaporation rate. The rectangles have the largest surface area on the top level, which on the one hand increase the area for exchange of water vapor and energy, but on the other hand slows down the free flow, due to the almost no-slip condition. If the rectangles are compared to the plateau case with adapted water content, it is seen that they show the same stage-I behavior. This indicates that the stage-I behavior is significantly influenced by

the properties of the first obstacle. The triangle and the sawtooth show a more favorable flow configuration, still featuring the sharp edges. Compared to the triangle, the slope of the first sawtooth obstacle is half of the triangle one and the distance to the top is doubled, which can explain the higher evaporation rates. The flow fields depicted in Fig. 5.23 show that for the reversed sawtooth setup the flow deflection by the first obstacle directly feeds into the second one which may explain the highest evaporation rates.
When looking at the cumulative mass loss in Fig. 5.22 (right), it can be seen, that one effect of increased top-level area is that the stage-II begins for a smaller water mass loss (especially visible for the rectangle and the plateau). If one is interested in a fast drying of the material, the flat surface performs worst in the beginning, due to the low stage-I evaporation rate, but it improves as time proceeds in stage-I. In stage-II, the importance of cavity flow for the exchange behavior and the evaporation process can be seen when comparing the rectangle and the plateau evaporation rates, then the rectangles show higher evaporation rate. From Fig. 5.23 it can be seen that for stage-II (14 days), the rectangle setup has the largest interface area in combination with available liquid water. This explains the high stage-II rates, as the diffusive transport in the porous medium is slower than the advective-diffusive transport inside the cavities.
Including the Forchheimer extension does not alter the results and therefore is not shown here. At the first rectangle, the average velocity normal to the interface is $v_{\mathrm{g,n}} = 0.0034\,\mathrm{m/s}$. The difference between Darcy and Forchheimer results is less than 0.1%. Even for a conservative estimation of the pore diameter ($d_{\mathrm{pore}} = 10\,\mathrm{mm}$), the resulting Reynolds number is in the validity range for the Darcy law ($Re_{\mathrm{pore}} = 0.22 < 1$).

This study shows that the shape of the surface has a significant effect on all stages of the evaporation process. Compared to the flat surface, all tested configurations show a higher stage-I evaporation rate, but also a shorter stage-I. The stage-I evaporation rate is strongly affected by inlet effects and the properties of the first obstacles. The main factor for an increased stage-II evaporation rate is the enhanced transport inside the cavities.
However, this study uses a quite coarse discretization and the obstacle shapes could be better resolved, which may lead to different results. With respect to the simulation of the free flow field, the same suggestions as for simulating the experiment by Haghighi and Or [2015] can be made.

5.4.4 Summary

This section analyzes the effect of three different kinds of roughness on the evaporation behavior. Heterogeneities in porous-medium properties lead to a heterogeneous distribution of fluxes. These fluxes lead to compensation mechanisms, e.g. lateral exchange of mass and

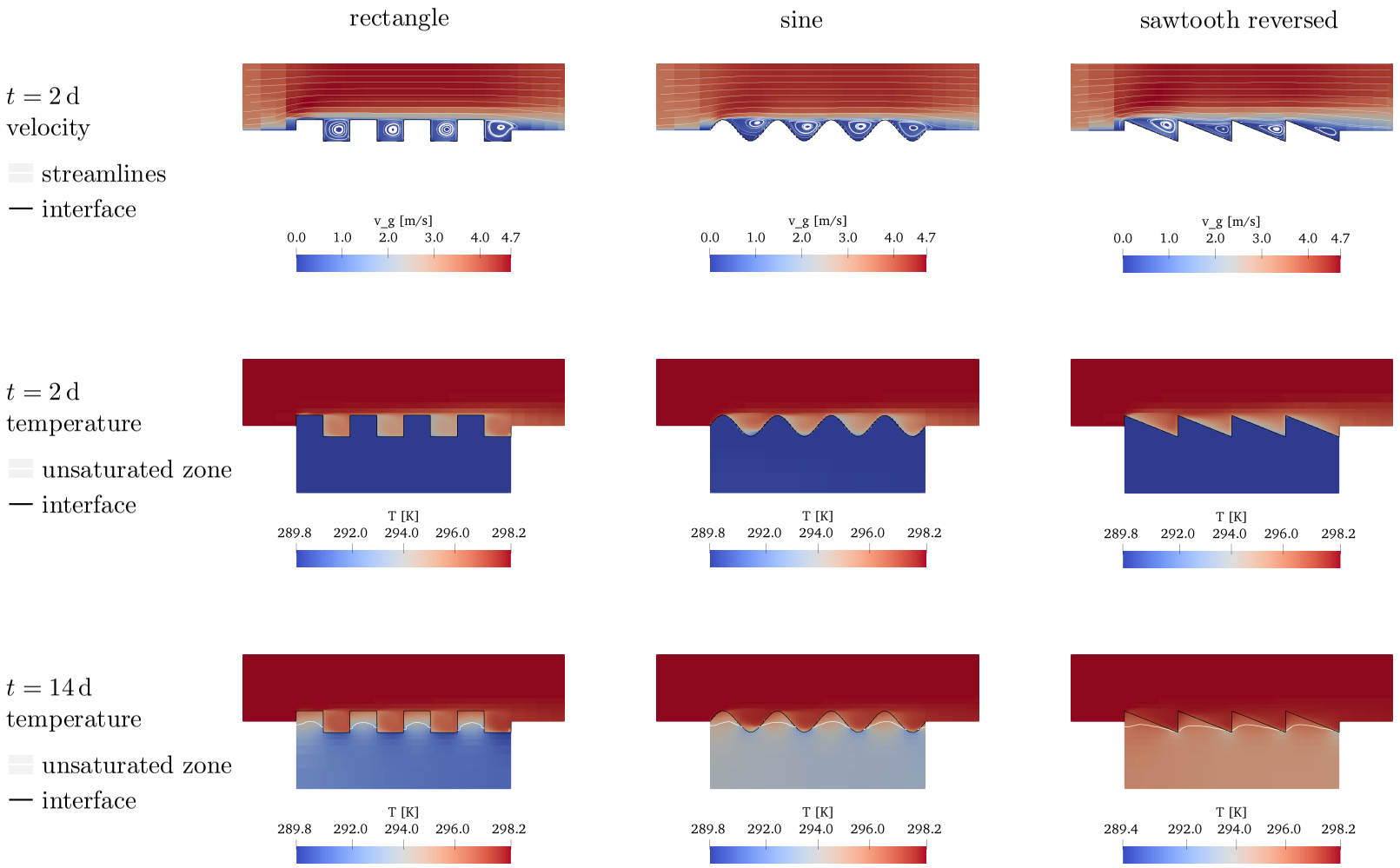

Figure 5.23: Velocity and temperature evolutions for different obstacle shapes. The location of the interface is given by the black line. In the first row, the white lines show the stream lines in the free flow. In the second and third row, the white lines indicate the end of the zone containing liquid water.

energy inside the soil. Because of these processes, a high evaporation rate can be maintained and the stage-I to stage-II transition is altered in comparison to the transition behavior for homogeneous media.

Including a sand-grain roughness concept from classical fluid dynamics leads to higher stage-I evaporation rates. The increase in stage-I evaporation rates fully depends on the dimensionless parameter k_s^+. However, due to the required fine discretization at the interface, the sand-grain roughness height is of the same magnitude as the smallest grid cells. In addition, there is no unique definition of the sand-grain roughness for a fully permeable medium and this concept does not account for the effect of flow normal at and tangential to a porous interface.

If the shape of the porous-medium surface is changed by porous obstacles of different heights, lengths, or shapes the stage-I evaporation rate is increased. For a certain water content, the duration of stage-I is affected by the height of the obstacles which limits the capillary transport of liquid water to the surface. Compared to the flat surface, the stage-II evaporation rate is enhanced by a more efficient transport inside the valleys/cavities in between obstacles. For a small number of objects, as used here, the flow deflection around the first obstacle influences the results.

6 Summary

The focus of this thesis is on improving the model concept for multi-phase porous-medium flow coupled to a turbulent free flow, both including multi-component and energy transport. As outlined in the introduction, such coupled interactions are relevant for different kinds of applications from a variety of different research fields.

It is aimed to develop an REV-scale two-domain concept which can handle two models in two separated subdomains and to couple them via appropriate coupling conditions at a sharp interface. One goal is to perform this coupling without introducing additional degrees of freedom on the interface. An existing porous-medium model, using the equations by Darcy or Forchheimer and discretized with the cell-centered finite volume method, is coupled to a (Reynolds-Averaged) Navier-Stokes model discretized with a marker-and-cell scheme (also known as staggered grid), cf. Grüninger et al. [2017]. In this framework, eddy-viscosity based turbulence models of different complexity are presented and implemented. In addition, simplifications of the coupling conditions are introduced and discussed. The implementation is performed using the software modules DuMu$^{\text{x}}$ and Dune. A fully implicit Euler method is used and the resulting monolithic matrix is solved with a Newton method and the help of a direct linear solver.

In the previous chapter, several concepts, parameters, and setups are investigated. In a first step, the developed model concepts and coupling methods are compared to a previous work which uses the box method for spatial discretization, cf. Mosthaf [2014]. The results for both discretization methods are in a good agreement. In contrast, the presented coupling methods for the new discretization concept reveal differences. The investigated turbulence models produce differences in stage-I evaporation rates of $\pm 12\%$ compared to their mean rate. Simplifications of the free-flow model concept can speed-up the simulations and still, under specific conditions, preserve the quality of the results. Afterward, analyses of the turbulent Schmidt number, the turbulent Prandtl number, and the Beavers-Joseph coefficient show an influence of up to $+10\%$ on stage-I evaporation rates when each value is varied from unity to other physical meaningful values.
In a second study, the model results are compared to different evaporation experiments from the literature and show a good qualitative and quantitative agreement. Most difficulties are

observed in reproducing the temperature evolution over time, or the transition from stage-I to stage-II. The results show that the model predictions are sensitive to the boundary conditions, the considered model dimension, and the porous-medium properties (see also Mosthaf [2014]). Further, they reveal the deficiencies of the used implementation, which are the inflexible axis-parallel grid without local refinements and the memory-intense solving of the monolithic matrix.
Finally, the effects of three different kinds of roughness are analyzed: heterogeneities, roughness resulting from the sand-grains and from porous obstacles. The roughness of the porous medium has a strong influence on the entire evaporation process and may add additional stages to the typical evaporation stages known from flat and homogeneous media.

6.1 Conclusions

Based on the previous analyses and with respect to the research hypotheses, the following conclusions are drawn.

Discretizations and Interface Model Concepts The discretization around the interface is important; grid convergence of stage-I evaporation rates can only be shown for near-interface cells with a height of $\Delta y^+ < 5$ (if a local system of equations is solved, CM4). The proposed coupling methods which avoid additional degrees of freedom on the interface (CM1 to CM3) converge against the same results for mainly interface-parallel flow, but require a finer discretization $\Delta y^+ < 1$. For flow normal toward a porous medium with multiple mobile phases, all methods produce different results, because of the different ways to account for the phases' resistance to flow. For one-phase porous-medium systems, CM2 to CM4 are identical with respect to their normal-momentum coupling conditions.

Turbulence Models and Simplifications The presented fully-coupled model concept is quite complex and in some cases simplifications are desirable. All presented simplifications are shown to speed-up the simulation. One-dimensional boundary layer models can be used as boundary conditions for the porous medium. These models give a good first estimation but are limited to specific cases, e.g. flat, homogeneous porous media. Another option is to simulate the transport of water vapor and energy on a given flow field (neglecting the feedback on the momentum transport), this should also work for more complicated setups. Wall functions for the k-ε model are especially helpful for larger setups. Further, the choice of the turbulence model affects the predicted stage-I evaporation rates.

Processes and Properties in Vicinity of the Interface The influence of the turbulent Prandtl number and the turbulent Schmidt number on the stage-I evaporation rate is in a similar range as the effect of the different turbulence models. Adapting these dimensionless numbers to the geometry of a specific problem may improve the quality of the model prediction. Compared to the influence of those two numbers, the effect of the Beavers-Joseph coefficient is minor. The comparison of simulation results with data from various experiments and the case of a sharp heterogeneity without conductive energy transfer indicate the importance of the energy transport inside the porous medium, but also across the porous-medium free-flow interface or the insulation of the porous-medium. A model which includes the sand-grain roughness of an impermeable surface, is tested for its usage in the application of evaporation through a permeable interface. It can be seen that the dimensionless sand-grain roughness length k_s^+ is a better indicator for the influence on the stage-I evaporation rate than the absolute roughness length k_s. Nevertheless, if an influence is present, the roughness length is already above the minimum required discretization length. Finally, different porous obstacles are analyzed. Any change to the flat surface increases the stage-I evaporation rate, but also leads to a shorter duration of stage-I. The area which is available for free-flow porous-medium exchange inside one cavity between two porous obstacles has a distinct influence on the stage-II evaporation rate.

6.2 Outlook

This thesis considers some of the points which are mentioned in the outlook of Mosthaf [2014] or Grüninger [2017], but also shows perspectives for further research.

Numerical Model Concept Many improvements are possible with respect to the numerical model concept. First, the discretization of the free flow is not able to adequately resolve geometric features and areas with highly dynamic processes. Consequences are an unnecessary fine grid in unimportant areas and a large matrix. Adapting the grid to relevant areas, either at the beginning or during the simulation, would help to reduce the computational costs and improve the model predictions. In addition to that, Mortar concepts could be used to allow for different discretizations in both domains at the interface. A third improvement would be achieved by solving the matrix with an iterative solver, such that a parallelization of the code is possible, cf. Grüninger [2017]. Fourth, the eddy-viscosity turbulence models (like k-ε or k-ω) are a popular choice for turbulence models but could be improved by using Reynolds stress models or large eddy simulations.

Simplifications This work proposes some possible simplifications, but the reported speed-up can be increased by simplifying the material laws or their computations, by simplifying flow and transport inside the porous medium [Vanderborght et al., 2017, Defraeye et al., 2010], by decoupling the interactions in time [Rybak et al., 2015], in space [Masson et al., 2016], or between the different transport processes (e.g. tracer components). In addition to the previous points, neglecting the influence of mass and energy transport on the momentum transport would allow to use free-flow fields from external software as OpenFOAM.

Experiments and Comparison Study Even though a lot of experiments are available in literature, many of them lack a precise description of the investigated setup or error estimations based on multiple runs. A comparison with such experiments is inevitable to prove or further develop a model concept. An alternative is to compare simulations based on averaged models (RANS/REV) to simulations which resolve all details (DNS), but this is not yet possible for non-isothermal, multi-phase, multi-component flow and transport. Comparing model results for flow through and over porous obstacles with experiments would be interesting, cf. Suga et al. [2013], Yang et al. [2018].

Relevant Processes Especially under outdoor conditions, turbulent pressure fluctuations will affect the porous-medium flow and enhance the component transport (known as turbulent pumping), e.g. Maier et al. [2012], Rutten [2015]. These pressure fluctuations are below the time-scale of the turbulence models used here. Therefore, either more detailed turbulence models have to be used or this effect has to be upscaled to RANS and REV models.
Applications with fast advection and high mass or energy transfer rates, as evaporation from porous media, eventually violate the assumptions of local thermodynamic equilibrium. Some studies are already performed, e.g. Nuske et al. [2014] and Trautz et al. [2015], but the effect of the turbulent free flow is not yet sufficiently analyzed.
The importance of processes at the interface is highlighted in this thesis. Many other interface-related processes exist, e.g. the wet-pore patterns influence the stage-I to stage-II transition [Haghighi et al., 2013, Mosthaf et al., 2014], the formation of drops in a fuel cell [Baber et al., 2016], or turbulent pumping. Replacing the sharp interface by lower-scale model concepts, as pore-network models [cf. Beyhaghi et al., 2016], might be helpful to analyze the effect of these processes.
From the perspective of an environmental engineer and with respect to outdoor conditions, including plants [Heck, 2016, Koch et al., 2018], salt transport [Jambhekar et al., 2015], radiation [Mosthaf, 2014], diurnal cycles (in wind speed, temperature, relative humidity), or precipitation is interesting.

A Soil Properties

Tab. A.1 summarizes the soils and their properties used for the simulations in this thesis. Fig. A.1 provides visualizations of the capillary pressure and relative permeability functions using the parametrization by van Genuchten [1980]. For the experiment by Lu et al. [2005], the missing soil parameters are calculated with the help of the following relations:

Kozeny-Carman Equation Bear [1988] gives an equation after Kozeny and Carman which relates the permeability to the median sand grain diameter and the porosity:

$$K = \frac{d_{50}^2}{180} \frac{\phi^3}{(1-\phi)^2} \,. \tag{A.1}$$

Leverett-J Function According to Leverett [1941], a function $J(S_\mathrm{w})$ exists to scale capillary pressure–saturation curves. The formulation here is taken from Bear [1988] and includes the surface tension (σ) and the contact angle (Θ):

$$J(S_\mathrm{w}) = \sqrt{\frac{K}{\phi}} \frac{p_\mathrm{c}(S_\mathrm{w})}{\sigma \cos\Theta} \,. \tag{A.2}$$

Lu et al. [2005] give a formulation for $J(S_\mathrm{w})$:

$$J(S_\mathrm{w}) = 0.364(1 - \exp(-40(1-S))) + 0.221(1-S) + 0.005/(S - S_{\mathrm{r,w}}) \,, \tag{A.3}$$

which can be used together with (A.1) and (A.2) to obtain a capillary pressure–saturation relationship. This method should be handled with care because Lu et al. [2005] do not provide proper sources for their equations. Therefore, this method is only used to obtain a similar data set as in Lu et al. [2005]. For this purpose, a contact angle of $\Theta = 60°$ and a surface tension of $\sigma = 72\,{}^{\mathrm{mN}}/_{\mathrm{m}}$ are assumed.

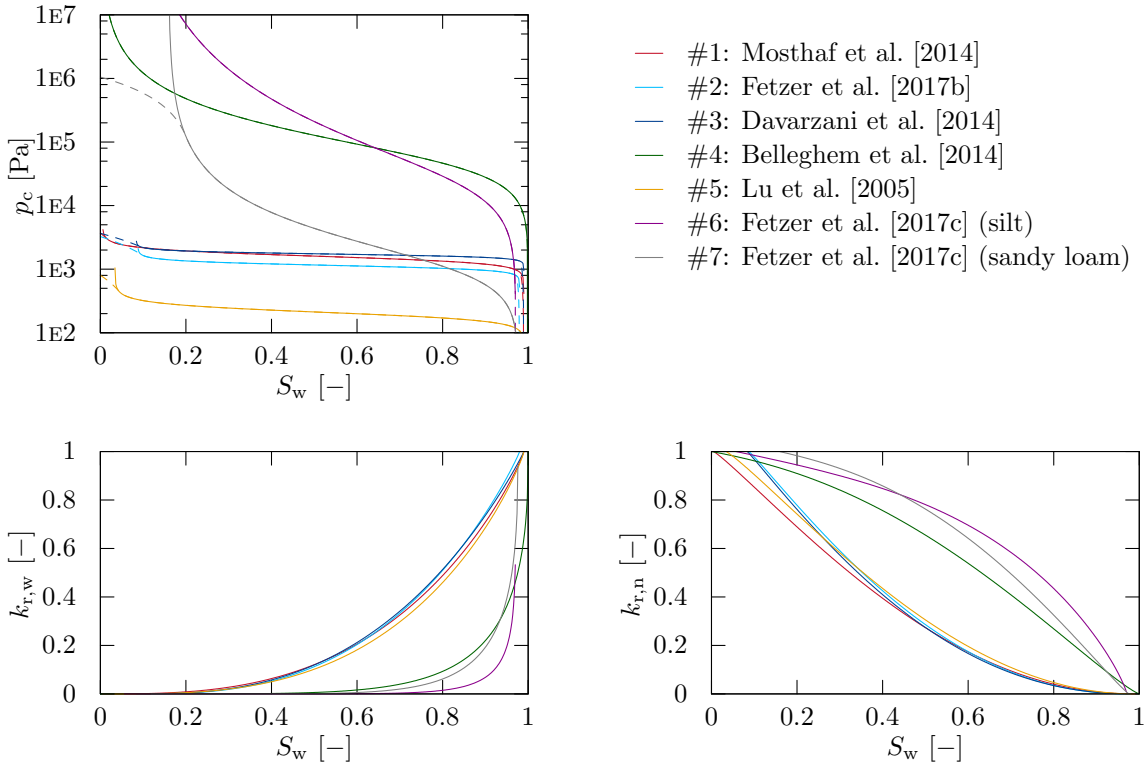

Figure A.1: Capillary pressures (top left) and relative permeabilities (bottom) of the used soils. The dashed curves include regularizations for low and high saturations ($S_{w,eff} < 0.01$ or $0.99 < S_{w,eff}$).

soil type	#1 quartz sand	#2 –	#3 quartz sand	#4 brick	#5 quartz part.	#6 silt	#7 sandy loam
d [mm]	0.3 to 0.9	–	$d_{50} = 0.52$	–	1.0 to 1.5	–	–
K $\left[\mathrm{m}^2\right]$	2.65E−10	3.87E−10	1.08E−10	1.12E−15	2.89E−9	1.08E−12	1.13E−12
ϕ [−]	0.41	0.32	0.33	0.13	0.46	0.35	0.41
$S_{\mathrm{r,w}}$ [−]	0.005	0.0875	0.084	0.0	0.034	0.057	0.159
$S_{\mathrm{r,n}}$ [−]	0.01	0.02	0.01	0.0	0.01	0.029	0.024
α_{VG} $\left[1/\mathrm{Pa}\right]$	6.37E−4	8.77E−4	5.80E−4	1.728E−5	4.90E−3	4.28E−5	8.16E−4
n_{VG} [−]	8.0	12.7	17.8	1.755	6.84	1.32	1.65
λ_{s} $\left[\mathrm{W}/(\mathrm{m\,K})\right]$	5.3	5.26	5.9	1.6	5.9	5.9	5.9
c_{s} $\left[\mathrm{K}/(\mathrm{kg\,K})\right]$	790	790	790	840	790	790	790
ϱ_{s} $\left[\mathrm{kg}/\mathrm{m}^3\right]$	2700	2700	2660	2087	2700	2700	2700
α_{BJ} [−]	1.0	1.0	1.0	1.0	1.0	1.0	1.0

Table A.1: Summary of the soil properties used in this thesis.

B Code Validation

The purpose of this chapter is to summarize and present the performed validation tests. The validation is performed to check the main functionality of the DuMu$^{\text{x}}$ MAC-discretization code written for this thesis, if not said otherwise, the results use this discretization method.

B.1 Analytical

Analytical tests are performed for the Stokes, Navier-Stokes, the k-ε, and the k-ω model.

B.1.1 Stokes [Donea and Huerta, 2003]

In this test case, known source terms for the mass and momentum balance trigger the desired analytical solution of the stationary Stokes equation, cf. Donea and Huerta [2003, p. 306]. The equations are solved on a square domain $\Omega = [0, 1\,\text{m}] \times [0, 1\,\text{m}]$ with constant values of $\nu = 1\,\text{m}^2/\text{s}$ and $\varrho = 1\,\text{kg}/\text{m}^3$ and Dirichlet boundary conditions everywhere. The resulting l^2-error norms are shown in Tab. B.1 and visualized in Fig. B.1.

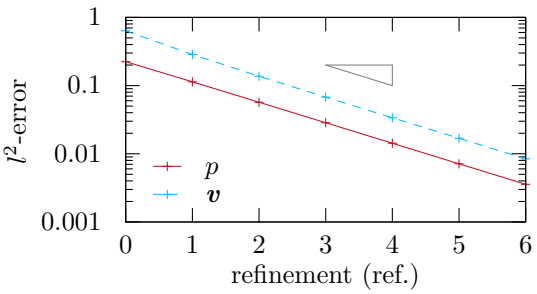

Figure B.1: Relative l^2-error convergence for pressure (p) and velocity ($\boldsymbol{v}$) for the test case by Donea and Huerta [2003].

ref.	cells	$l^2(p)$	$l^2(\boldsymbol{v})$
0	4^2	2.24E-1	6.35E-1
1	8^2	1.13E-1	2.86E-1
2	16^2	5.69E-2	1.37E-1
3	32^2	2.85E-2	6.77E-2
4	64^2	1.42E-2	3.37E-2
5	128^2	7.13E-3	1.68E-2
6	256^2	3.56E-3	8.43E-3

Table B.1: Relative l^2-error norms for pressure (p) and velocity ($\boldsymbol{v}$) for the test case by Donea and Huerta [2003].

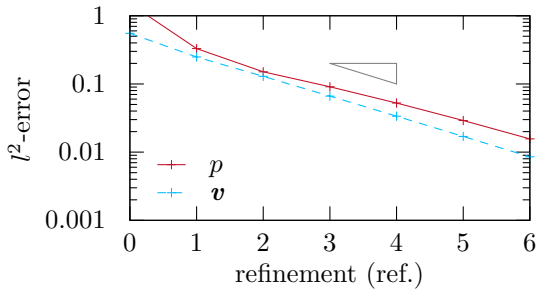

Figure B.2: Relative l^2-error convergence for pressure (p) and velocity ($\boldsymbol{v}$) for the test case by Kovasznay [1947].

ref.	cells	$l^2(p)$	$l^2(\boldsymbol{v})$
0	4^2	1.50E0	5.52E-1
1	8^2	3.30E-1	2.48E-1
2	16^2	1.50E-1	1.29E-1
3	32^2	9.09E-2	6.61E-2
4	64^2	5.24E-2	3.36E-2
5	128^2	2.90E-2	1.69E-2
6	256^2	1.56E-2	8.54E-3

Table B.2: Relative l^2-error norms for pressure (p) and velocity ($\boldsymbol{v}$) for the test case by Kovasznay [1947].

B.1.2 Navier-Stokes [Kovasznay, 1947]

Kovasznay [1947] poses a source-term free solution of the stationary Navier-Stokes equation for $Re = 40$. The equations are solved on a square domain $\Omega = [-0.5, -0.5\,\mathrm{m}] \times [1.0, 1.5\,\mathrm{m}]$ with constant values of $\nu = 0.025\,\mathrm{m^2/s}$ and $\varrho = 1\,\mathrm{kg/m^3}$. The boundary conditions for velocity are set to Dirichlet everywhere. For pressure, Outflow conditions are used everywhere, expect for the lower left cell which gets a Dirichlet value. The resulting l^2-error norms are shown in Tab. B.2 and visualized in Fig. B.2.

B.1.3 Two-Equation Turbulence Models

For testing the k-ε and the k-ω turbulence models, 1-D tests with predefined analytical solutions are run:

$$v = 2x\,, \tag{B.1}$$

$$p = 2 - 2x\,, \tag{B.2}$$

$$k = 1 + x^2\,, \tag{B.3}$$

$$\varepsilon = 2 - x^2\,, \tag{B.4}$$

$$\text{or } \omega = 2 - x^2\,. \tag{B.5}$$

The analytical solutions are inserted in the respective balance equations and the correct solutions are triggered by the adapting the source terms. The problems are solved on a domain $\Omega = [0\,\mathrm{m}] \times [1\,\mathrm{m}]$ with constant values of $\nu = 1\,\mathrm{m^2/s}$ and $\varrho = 1\,\mathrm{kg/m^3}$ and Dirichlet boundary conditions everywhere. The resulting l^2-error norms are shown in Tab. B.3, Fig. B.3, Tab. B.4, and Fig. B.4.

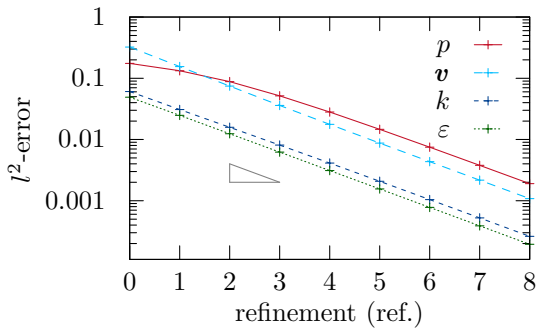

Figure B.3: Relative l^2-error convergence for pressure (p), velocity (v), turbulent kinetic energy (k), and dissipation (ε) for the k-ε test case.

ref.	$l^2(p)$	$l^2(\boldsymbol{v})$	$l^2(k)$	$l^2(\varepsilon)$
0	1.74E-1	3.23E-1	6.07E-2	4.91E-2
1	1.32E-1	1.55E-1	3.08E-2	2.47E-2
2	8.82E-2	7.44E-2	1.58E-2	1.24E-2
3	5.16E-2	3.60E-2	8.10E-3	6.22E-3
4	2.80E-2	1.76E-3	4.11E-3	3.11E-3
5	1.46E-3	8.73E-3	2.07E-3	1.55E-3
6	7.48E-3	4.34E-3	1.04E-3	7.77E-4
7	3.78E-3	2.16E-3	5.23E-4	3.88E-4
8	1.90E-3	1.08E-3	2.62E-4	1.94E-4

Table B.3: Relative l^2-error norms for pressure (p), velocity (v), turbulent kinetic energy (k), and dissipation (ε) for the k-ε test case.

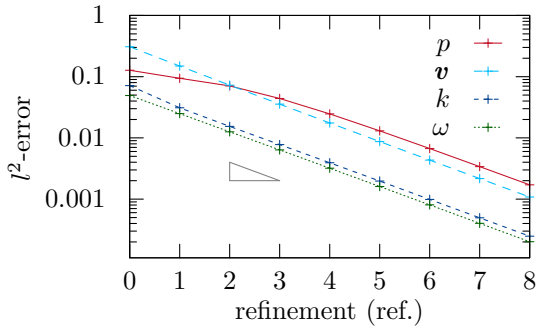

Figure B.4: Relative l^2-error convergence for pressure (p), velocity (v), turbulent kinetic energy (k), and turbulence frequency (ω) for the k-ω test case.

ref.	$l^2(p)$	$l^2(\boldsymbol{v})$	$l^2(k)$	$l^2(\omega)$
0	1.27E-1	3.08E-1	7.13E-2	4.91E-2
1	9.41E-2	1.49E-1	3.09E-2	2.49E-2
2	7.06E-2	7.25E-2	1.54E-2	1.25E-2
3	4.40E-2	3.55E-2	7.77E-3	6.36E-3
4	2.46E-2	1.75E-2	3.92E-3	3.19E-3
5	1.30E-2	8.70E-3	1.97E-3	1.60E-3
6	6.70E-3	4.33E-3	9.88E-4	8.04E-4
7	3.39E-3	2.16E-3	4.95E-4	4.02E-4
8	1.71E-3	1.08E-3	2.47E-4	2.01E-4

Table B.4: Relative l^2-error norms for pressure (p), velocity (v), turbulent kinetic energy (k), and turbulence frequency (ω) for the k-ω test case.

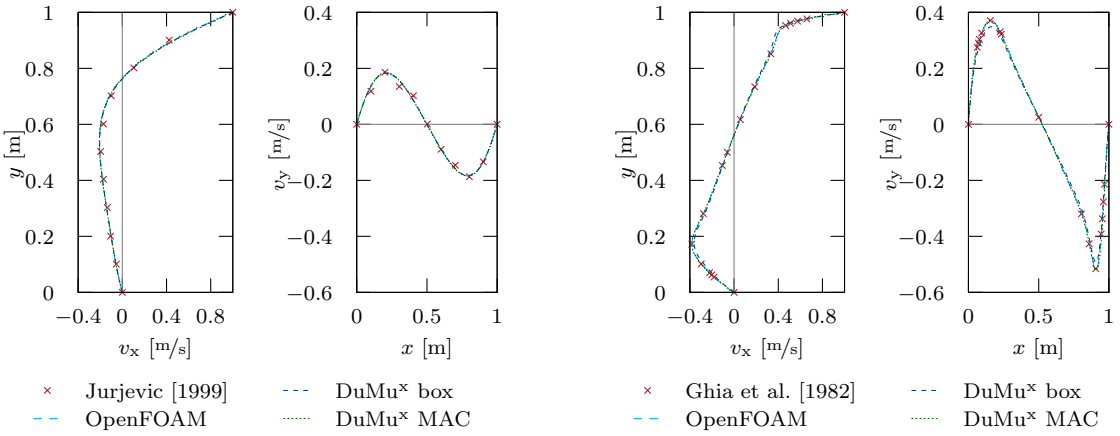

Figure B.5: Vertical and horizontal velocity profiles through the center lines of the cavity. The profiles are compared to numerical results by OpenFOAM and to experimental results by Jurjevic [1999] for $Re = 1$ (left) and to numerical results by Ghia et al. [1982] for $Re = 1000$ (right).

B.2 Numerical

For the numerical test cases, setups available in literature are taken and, together with results from OpenFOAM, compared to results obtained using DuMu^x.

B.2.1 Navier-Stokes (Lid-Driven Cavity Flow)

A velocity of $v_x = 1\,\mathrm{m/s}$ is imposed on the top of a cavity sized $\Omega = [0, 0\,\mathrm{m}] \times [1, 1\,\mathrm{m}]$ with 128×128 cells. On the sides and the bottom no-slip conditions are applied. In the lower left cell, a Dirichlet value for pressure is set, everywhere else outflow conditions are applied. Two different cases ($Re = 1$ and $Re = 1000$) are tested and compared. The fluid properties for $Re = 1$ are: $\nu = 1\,\mathrm{m^2/s}$, $\varrho = 1\,\mathrm{kg/m^3}$. For $Re = 1000$ they are: $\nu = 0.001\,\mathrm{m^2/s}$, $\varrho = 1\,\mathrm{kg/m^3}$. Vertical and horizontal velocity profiles through the center of the cavity are compared for the box method and the MAC scheme. As references, numerical results by OpenFOAM and experimental results by Jurjevic [1999] for $Re = 1$ and numerical results by Ghia et al. [1982] for $Re = 1000$ are given, see Fig. B.5.

B.2.2 K-Epsilon (Mixinglayer)

This test case is inspired by a setting shown in Mohammadi and Pironneau [1994, p. 74f]. Because they do not specify the domain size and the boundary values, we choose a domain size of $\Omega = [0, 3\,\mathrm{m}] \times [-0.3, 0.3\,\mathrm{m}]$ and equidistant grid with of 100×40 cells. At the right side

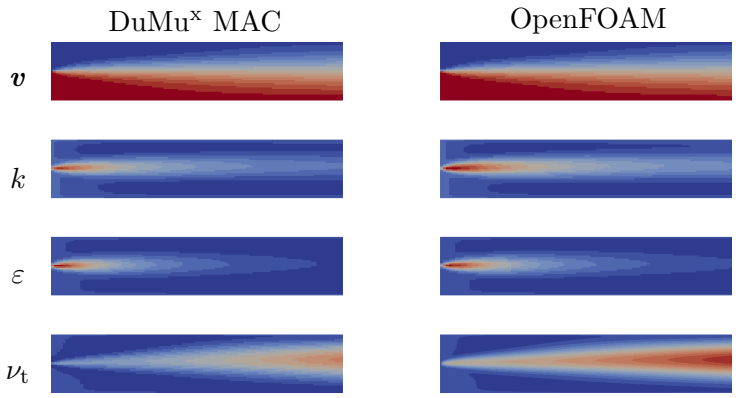

Figure B.6: Contour surfaces for the mixinglayer test case, after Mohammadi and Pironneau [1994]. Results are shown for the DuMu$^{\text{x}}$ MAC scheme and OpenFOAM.

outflow for $\boldsymbol{v}$, k, and ε and Dirichlet for p are applied and the other way around for all other boundaries. The constants as specified in 3.1.2.2 are used, the initial and boundary values are:

$$\boldsymbol{v} = \begin{cases} (2,0\,\mathrm{m/s})^\intercal, & \text{if } y < 0 \\ (1,0\,\mathrm{m/s})^\intercal, & \text{else} \end{cases}, \tag{B.6}$$

$$p = 1\text{E}5\,\mathrm{Pa}\,, \tag{B.7}$$

$$k = 0.001\,\mathrm{m^2/s^2}\,, \tag{B.8}$$

$$\varepsilon = 0.001\,\mathrm{m^2/s^3}\,. \tag{B.9}$$

The fluid properties are constant with: $\nu = 0.00706\,\mathrm{m^2/s}$ and $\varrho = 1.19\,\mathrm{kg/m^3}$. Fig. B.6 shows contour surfaces for $\boldsymbol{v}$, k, ε, and ν_t.

B.3 Physical (Pipe Flow, Laufer [1954])

Laufer [1954] performs a laboratory experiment in which air flows through a pipe at $Re = 50\,000$. This experiment is simulated using a 2-D setup with a domain $\Omega = [0,0\,\mathrm{m}] \times [10, 0.2469\,\mathrm{m}]$. On the top and on the bottom no-slip conditions, and if necessary wall functions, are applied. On the left, Dirichlet conditions with a constant velocity of $\boldsymbol{v} = (2.5, 0\,\mathrm{m/s})^\intercal$ is given, whereas the boundary conditions on the right are outflow. The problem is discretized using 25×50 cells with a grading of 1.2 in vertical direction from each wall to the center. For testing the wall functions of the k-ε model, an equal-spaced discretization with 20 cells in vertical direction is used. Fig. B.7 shows the resulting velocity profiles for different turbulence models.

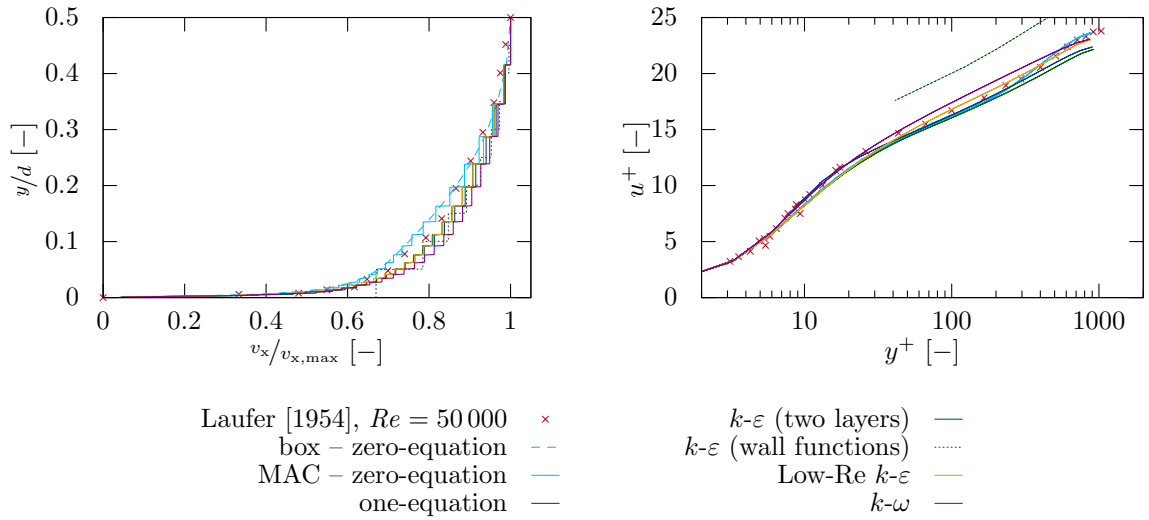

Figure B.7: Velocity profiles for the pipe flow experiments by Laufer [1954]. The velocity profiles are taken at steady state ($t = 100\,\mathrm{s}$, $x = 8.0\,\mathrm{m}$). The velocity is scaled by the maximum velocity (left) and the wall friction velocity (right). The experiment data points for the right plot are extracted from Truckenbrodt [2008a, Fig. 2.42].

C Software and Hardware

The simulation results presented in this thesis are achieved using the open-source numerical toolboxes DuMu^x and DUNE. Tab. C.1 lists all required modules and Tab. C.2 provides a list with other pre-compiled programs or library necessary for running the simulations. For unix systems, a script which installs all necessary modules can be found at `https://git.iws.uni-stuttgart.de/dumux-pub/Fetzer2018a/raw/master/installFetzer2018a.sh` [14].

The main module of this thesis (dumux-Fetzer2018a) has the following structure. First, the release version of dumux has to be adapted with the patches provided in `patches`. The `appl/multidomain` folder contains the problem specific source code for the presented results in Ch. 5, whereas `appl/staggeredgrid` contains all basic MAC models. `bin/jobfiles` contains script files to re-run all used simulations and scripts for all post-processing in `bin/scripts`. In `dumux`, the basic transport model and input/output helper files are located. The plot of material laws and fluid properties are performed by executables built from the `material` folder. For re-simulating the OpenFOAM results, the files in `openfoam` can be used. The data sets of which all plots and pictures in Ch. 5 are made of can be found in `results`. Note that these data sets can be automatically reproduced by running the scripts from the `bin` folder. Finally, `test` contains setups which ensure the basic functionality of the code. Some of these setups are presented in Ch. B.

All simulation for which the simulation times and properties are given, are run on a Linux computer using openSUSE 13.2 (Linux 3.16.7-35-default, kde 4.14.9), with four CPU cores (Intel® Core™ i5-5300U @ 2.3GHz) and RAM of ≈11.85GB.

[14] Script was accessed on June 19, 2018

module	version/branch	commit	website	reference
dumux	2.12.0	`8888c221`	https://git.iws.uni-stuttgart.de/dumux-repositories/dumux.git	Fetzer et al. [2017a]
dumux-Fetzer2018a	master		https://git.iws.uni-stuttgart.de/dumux-pub/Fetzer2018a	
dune-common	releases/2.4	`23e56898`	https://gitlab.dune-project.org/core/dune-common.git	Blatt et al. [2016]
dune-geometry	releases/2.4	`4330ebc9`	https://gitlab.dune-project.org/core/dune-geometry.git	
dune-grid	releases/2.4	`6d74754d`	https://gitlab.dune-project.org/core/dune-grid.git	e.g. Bastian et al. [2008b]
dune-istl	releases/2.4	`c29b037d`	https://gitlab.dune-project.org/core/dune-istl.git	
dune-localfunction	releases/2.4	`cf91cc81`	https://gitlab.dune-project.org/core/dune-localfunctions.git	
dune-multidomain	releases/2.0	`e3d52982`	https://github.com/smuething/dune-multidomain.git	
dune-multidomaingrid	releases/2.3	`3b829b7a`	https://github.com/smuething/dune-multidomaingrid.git	
dune-pdelab	releases/2.0	`19c782ee`	https://gitlab.dune-project.org/pdelab/dune-pdelab.git	
dune-typetree	releases/2.3	`ecffa10c`	https://gitlab.dune-project.org/staging/dune-typetree.git	

Table C.1: List of used DuMu^{x} and DUNE modules as basis for the developed code. The required versions for recompiling the executables and reproducing the results of this thesis are given. Note that the release version of dumux has to be patched by patches provided in dumux-Fetzer2018a. Websites were accessed on March 6, 2018.

program	version	type	website	reference
clang	3.5.0	compiler	http://clang.llvm.org	
gnuplot	5.0.0	graphing utility	http://www.gnuplot.info	
OpenFOAM	2.3.0	CFD toolbox	http://openfoam.org	
superLU	4.3	linear solver	http://crd-legacy.lbl.gov/ xiaoye/SuperLU/	Li [2005]
umfpack	5.7.1	linear solver	http://faculty.cse.tamu.edu/davis/suitesparse.html	Davis [2004]

Table C.2: List of used programs and libraries versions. Websites were accessed on January 3, 2018.

Bibliography

B. Ahrenholz, J. Niessner, R. Helmig, and M. Krafczyk. Pore-scale determination of parameters for macroscale modeling of evaporation processes in porous media. *Water Resources Research*, 47(7):W07543, 2011. doi: 10.1029/2010WR009519.

S. R. Allmaras, F. T. Johnson, and P. R. Spalart. Modifications and Clarifications for the Implementation of the Spalart-Allmaras Turbulence Model. In *Seventh International Conference on Computational Fluid Dynamics (ICCFD7)*, 2012.

S. Aluwihare and K. Watanabe. Measurement of Evaporation on Bare Soil and Estimating Surface Resistance. *Journal of Environmental Engineering*, 129(12):1157–1168, 2003. doi: 10.1061/(ASCE)0733-9372(2003)129:12(1157).

P. S. Andersen, W. M. Kays, and R. J. Moffat. The Turbulent Boundary Layer on a Porous Plate: An Experimental Study of the Fluid Mechanics for Adverse Free-Stream Pressure Gradients. Report HMT-15, Department of Mechanical Engineering, Stanford University, 1972.

ANSYS, Inc. *ANSYS FLUENT 12.0 - Theory Guide*, 2009a.

ANSYS, Inc. *ANSYS FLUENT 12.0 - User's Guide*, 2009b.

J. E. Armstrong, E. O. Frind, and R. D. McClellan. Nonequilibrium mass transfer between the vapor, aqueous, and solid phases in unsaturated soils during vapor extraction. *Water Resources Research*, 30(2):355–368, 1994. doi: 10.1029/93WR02481.

S. Assouline, K. Narkis, and D. Or. Evaporation from partially covered water surfaces. *Water Resources Research*, 46(10):W10539, 2010. doi: 10.1029/2010WR009121.

J.-L. Auriault. About the Beavers and Joseph Boundary Condition. *Transport in Porous Media*, 83(2):257–266, 2010. doi: 10.1007/s11242-009-9435-9.

K. Baber. *Coupling free flow and flow in porous media in biological and technical applications: From a simple to a complex interface description*. PhD thesis, University of Stuttgart, 2014. doi: 10.18419/opus-594.

K. Baber, K. Mosthaf, B. Flemisch, R. Helmig, S. Müthing, and B. Wohlmuth. Numerical scheme for coupling two-phase compositional porous-media flow and one-phase compositional free flow. *IMA Journal of Applied Mathematics*, 77(6):887–909, 2012. doi: 10.1093/imamat/hxs048.

K. Baber, B. Flemisch, and R. Helmig. Modeling drop dynamics at the interface between free and porous-medium flow using the mortar method. *International Journal of Heat and Mass Transfer*, 99:660–671, 2016. doi: 10.1016/j.ijheatmasstransfer.2016.04.014.

B. S. Baldwin and T. J. Barth. A one-equation turbulence transport model for high Reynolds number wall-bounded flows. NASA Technical Memorandum 102847, NASA, 1990.

B. S. Baldwin and H. Lomax. Thin Layer Approximation and Algebraic Model for Seperated Turbulent Flows. *ACM Trans Math Software*, 78–257:1–9, 1978. doi: 10.2514/6.1978-257.

J. Bardina, P. Huang, T. Coakley, J. Bardina, P. Huang, and T. Coakley. Turbulence modeling validation. In *28th Fluid Dynamics Conference, Fluid Dynamics and Co-located Conferences*. American Institute of Aeronautics and Astronautics, 1997. doi: 10.2514/6.1997-2121.

P. Bastian, M. Blatt, A. Dedner, C. Engwer, R. Klöfkorn, R. Kornhuber, M. Ohlberger, and O. Sander. A Generic Grid Interface for Parallel and Adaptive Scientific Computing. Part II: Implementation and Tests in DUNE. *Computing*, 82(2–3):121–138, 2008a. doi: 10.1007/s00607-008-0004-9.

P. Bastian, M. Blatt, A. Dedner, C. Engwer, R. Klöfkorn, M. Ohlberger, and O. Sander. A Generic Grid Interface for Parallel and Adaptive Scientific Computing. Part I: Abstract Framework. *Computing*, 82(2–3):103–119, 2008b. doi: 10.1007/s00607-008-0003-x.

J. Bear. *Dynamics of fluids in porous media*. Dover Publ., New York, 1988. ISBN 0-486-65675-6.

G. S. Beavers and D. D. Joseph. Boundary conditions at a naturally permeable wall. *Journal of Fluid Mechanics*, 30(1):197–207, 1967. doi: 10.1017/S0022112067001375.

G. S. Beavers, E. M. Sparrow, and B. A. Masha. Boundary Condition at a Porous Surface Which Bounds a Fluid Flow. *AIChE Journal*, 20(3):596–597, 1974. doi: 10.1002/aic.690200323.

A. Belhamri and J.-P. Fohr. Heat and mass transfer along a wetted porous plate in an air stream. *AIChE Journal*, 42(7):1833–1843, 1996. doi: 10.1002/aic.690420705.

M. V. Belleghem, M. Steeman, H. Janssen, A. Janssens, and M. D. Paepe. Validation of a coupled heat, vapour and liquid moisture transport model for porous materials implemented in CFD. *Building and Environment*, 81:340–353, 2014. doi: 10.1016/j.buildenv.2014.06.024.

S. Beyhaghi, Z. Xu, and K. M. Pillai. Achieving the Inside–Outside Coupling During Network Simulation of Isothermal Drying of a Porous Medium in a Turbulent Flow. *Transport in Porous Media*, 114(3):823–842, 2016. doi: 10.1007/s11242-016-0746-3.

R. B. Bird, W. E. Stewart, and E. N. Lightfoot. *Transport Phenomena*. Wiley, New York, 2 edition, 2007. ISBN 978-0-470-11539-8.

M. Blatt, A. Burchardt, A. Dedner, C. Engwer, J. Fahlke, B. Flemisch, C. Gersbacher, C. Gräser, F. Gruber, C. Grüninger, D. Kempf, R. Klöfkorn, T. Malkmus, S. Müthing, M. Nolte, M. Piatkowski, and O. Sander. The Distributed and Unified Numerics Environment, Version 2.4. *Archive of Numerical Software*, 4(100):13–29, 2016. doi: 10.11588/ans.2016.100.26526.

B. Blocken, T. Stathopoulos, and J. Carmeliet. CFD simulation of the atmospheric boundary layer: wall function problems. *Atmospheric Environment*, 41(2):238–252, 2007. doi: 10.1016/j.atmosenv.2006.08.019.

M. J. Blunt, B. Bijeljic, H. Dong, O. Gharbi, S. Iglauer, P. Mostaghimi, A. Paluszny, and C. Pentland. Pore-scale imaging and modelling. *Advances in Water Resources*, 51:197–216, 2013. doi: 10.1016/j.advwatres.2012.03.003.

J. V. Boussinesq. Essai sur la théorie des eaux courantes. *Memoires Acad. des Sciences*, 23 (1):1–680, 1877.

W. P. Breugem and B. J. Boersma. Direct numerical simulations of turbulent flow over a permeable wall using a direct and a continuum approach. *Physics of Fluids*, 17(2):025103, 2005. doi: 10.1063/1.1835771.

H. C. Brinkman. A calculation of the viscous force exerted by a flowing fluid on a dense swarm of particles. *Applied Scientific Research*, 1(1):27–34, 1949. doi: 10.1007/BF02120313.

T. Broecker, W. Elsesser, K. Teuber, I. Özgen, G. Nützmann, and R. Hinkelmann. High-resolution simulation of free-surface flow and tracer retention over streambeds with ripples. *Limnologica*, 68:46–58, 2018. doi: 10.1016/j.limno.2017.06.005.

R. H. Brooks and A. T. Corey. Hydraulic Properties of Porous Media. Technical report, Colorado State University, Fort Collins, Colorado, 1964.

W. Brutsaert. *Evaporation into the Atmosphere: Theory, History, and Applications*, volume 1. D. Reidel Publishing Company, Dordrecht, 1982. ISBN 90-277-1247-6. doi: 10.1007/978-94-017-1497-6.

R. Buccolieri, C. Gromke, S. D. Sabatino, and B. Ruck. Aerodynamic effects of trees on pollutant concentration in street canyons. *Science of The Total Environment*, 407(19): 5247–5256, 2009. doi: 10.1016/j.scitotenv.2009.06.016.

T. Cebeci. A Model for Eddy Conductivity and Turbulent Prandtl Number. *Journal of Heat Transfer*, 95(2):227–234, 1973. doi: 10.1115/1.3450031.

T. Cebeci. Calculation of Incompressible Rough-Wall Boundary Layer Flows. *AIAA Journal*, 16(7):730–735, 1978. doi: 10.2514/3.7571.

T. Cebeci and A. M. O. Smith. *Analysis of turbulent boundary layers*. Academic Press, New York, 1974. ISBN 0-12-164650-5.

CFD Online. www.cfd-online.com, 2017.

L. Chen, S. Wang, G. Li, C.-H. Lin, and T. Zhang. CFD modeling of moisture accumulation in the insulation layers of an aircraft. *Applied Thermal Engineering*, 102:1141–1156, 2016. doi: 10.1016/j.applthermaleng.2016.04.048.

K.-Y. Chien. Predictions of Channel and Boundary-Layer Flows with a Low-Reynolds-Number Turbulence Model. *AIAA Journal*, 20(1):33–38, 1982. doi: 10.2514/3.51043.

F. Cimolin and M. Discacciati. Navier-Stokes/Forchheimer models for filtration through porous media. *Applied Numerical Mathematics*, 72:205–224, 2013. doi: 10.1016/j.apnum.2013.07.001.

H. Class. *Theorie und numerische Modellierung nichtisothermer Mehrphasenprozesse in NAPL-kontaminierten porösen Medien*. PhD thesis, Technische Universität Braunschweig, 2001. doi: 10.18419/opus-223.

H. Class. Models for non-isothermal compositional gas-liquid flow and transport in porous media. Habilitation, University of Stuttgart, 2007. doi: 10.18419/opus-299.

H. Class, R. Helmig, and P. Bastian. Numerical simulation of non-isothermal multiphase multicomponent processes in porous media.: 1. An efficient solution technique. *Advances in Water Resources*, 25(5):533–550, 2002. doi: 10.1016/S0309-1708(02)00014-3.

C. F. Colebrook. Turbulent flow in pipes, with particular reference to the transition region between smooth and rough pipe laws. *Journal of the Institution of Civil Engineers*, 11(4): 133–156, 1939. doi: 10.1680/ijoti.1939.13150.

T. J. Craft, A. V. Gerasimov, H. Iacovides, and B. E. Launder. Progress in the generalization of wall-function treatments. *International Journal of Heat and Fluid Flow*, 23(2):148–160, 2002. doi: 10.1016/S0142-727X(01)00143-6.

W. Dahmen, T. Gotzen, S. Müller, and M. Rom. Numerical simulation of transpiration cooling through porous material. *International Journal for Numerical Methods in Fluids*, 76(6):331–365, 2014. doi: 10.1002/fld.3935.

B. Das, J. Hendrickx, and B. Borchers. Modeling transient water distributions around landmines in bare soils. *Soil Science*, 166(3):163–173, 2001. doi: 10.1097/00010694-200103000-00002.

D. B. Das, V. Nassehi, and R. J. Wakeman. A finite volume model for the hydrodynamics of combined free and porous flow in sub-surface regions. *Advances in Environmental Research*, 7(1):35–58, 2002. doi: 10.1016/S1093-0191(01)00108-3.

H. Davarzani, K. M. Smits, R. M. Tolene, and T. Illangasekare. Study of the effect of wind speed on evaporation from soil through integrated modeling of the atmospheric boundary layer and shallow subsurface. *Water Resources Research*, 50(1):1–20, 2014. doi: 10.1002/2013WR013952.

T. A. Davis. Algorithm 832: UMFPACK V4.3—an Unsymmetric-pattern Multifrontal Method. *ACM Transactions on Mathematical Software*, 30(2):196–199, 2004. doi: 10.1145/992200.992206.

M. J. S. de Lemos. Turbulent Flow Around Fluid–Porous Interfaces Computed with a Diffusion-Jump Model for k and ε Transport Equations. *Transport in Porous Media*, 78 (3):331–346, 2009. doi: 10.1007/s11242-009-9379-0.

T. Defraeye. *Convective heat and mass transfer at exterior building surfaces*. PhD thesis, Katholieke Universiteit Leuven, 2011.

T. Defraeye, B. Blocken, and J. Carmeliet. CFD analysis of convective heat transfer at the surfaces of a cube immersed in a turbulent boundary layer. *International Journal of Heat and Mass Transfer*, 53(1–3):297–308, 2010. doi: 10.1016/j.ijheatmasstransfer.2009.09.029.

T. Defraeye, B. Blocken, and J. Carmeliet. Analysis of convective heat and mass transfer coefficients for convective drying of a porous flat plate by conjugate modelling. *International Journal of Heat and Mass Transfer*, 55(1–3):112–124, 2012a. doi: 10.1016/j.ijheatmasstransfer.2011.08.047.

T. Defraeye, B. Blocken, D. Derome, B. Nicolai, and J. Carmeliet. Convective heat and mass transfer modelling at air–porous material interfaces: Overview of existing methods and relevance. *Chemical Engineering Science*, 74:49–58, 2012b. doi: 10.1016/j.ces.2012.02.032.

F. Diaz, C. C. Jimenez, and M. Tejedor. Influence of the thickness and grain size of tephra mulch on soil water evaporation. *Agricultural Water Management*, 74(1):47–55, 2005. doi: 10.1016/j.agwat.2004.10.011.

M. Discacciati and A. Quarteroni. Navier-Stokes/Darcy Coupling: Modeling, Analysis, and Numerical Approximation. *Revista Matematica Complutense*, 22(2):315–426, 2009. doi: 10.5209/rev_REMA.2009.v22.n2.16263.

M. Discacciati, P. Gervasio, and A. Quarteroni. Interface control domain decomposition methods for heterogeneous problems. *International Journal for Numerical Methods in Fluids*, 76(8):471–496, 2014. doi: 10.1002/fld.3942.

M. Discacciati, P. Gervasio, A. Giacomini, and A. Quarteroni. The Interface Control Domain Decomposition Method for Stokes–Darcy Coupling. *SIAM Journal on Numerical Analysis*, 54(2):1039–1068, 2016. doi: 10.1137/15M101854X.

J. Donea and A. Huerta. *Finite Element Methods for Flow Problems*, volume 1. Wiley, 2003. ISBN 978-0-470-01382-3. doi: 10.1002/0470013826.ch6.

Y. Dong, J. S. McCartney, and N. Lu. Critical Review of Thermal Conductivity Models for Unsaturated Soils. *Geotechnical and Geological Engineering*, 33(2):207–221, 2015. doi: 10.1007/s10706-015-9843-2.

P. A. Durbin. Near-wall turbulence closure modeling without "damping functions". *Theoretical and Computational Fluid Dynamics*, 3(1):1–13, 1991. doi: 10.1007/BF00271513.

E. Fattahi, C. Waluga, B. Wohlmuth, U. Rüde, M. Manhart, and R. Helmig. Lattice Boltzmann methods in porous media simulations: From laminar to turbulent flow. *Computers & Fluids*, 140:247– 259, 2016. doi: 10.1016/j.compfluid.2016.10.007.

R. T. Ferrell and D. M. Himmelblau. Diffusion coefficients of nitrogen and oxygen in water. *Journal of Chemical & Engineering Data*, 12(1):111–115, 1967. doi: 10.1021/je60032a036.

T. Fetzer. Numerical analysis of the influence of turbulence on exchange processes between porous-medium and free flow. Diploma thesis, University of Stuttgart, 2012.

T. Fetzer, K. M. Smits, and R. Helmig. Effect of Turbulence and Roughness on Coupled Porous-Medium/Free-Flow Exchange Processes. *Transport in Porous Media*, 114(2):395–424, 2016. doi: 10.1007/s11242-016-0654-6.

T. Fetzer, B. Becker, B. Flemisch, D. Gläser, K. Heck, T. Koch, M. Schneider, S. Scholz, and K. Weishaupt. DuMuX 2.12.0, 2017a.

T. Fetzer, C. Grüninger, B. Flemisch, and R. Helmig. *On the Conditions for Coupling Free Flow and Porous-Medium Flow in a Finite Volume Framework*, pages 347–356. Finite Volumes for Complex Applications VIII - Hyperbolic, Elliptic and Parabolic Problems: FVCA 8, Lille, France, June 2017. Springer International Publishing, Cham, 2017b. ISBN 978-3-319-57394-6. doi: 10.1007/978-3-319-57394-6_37.

T. Fetzer, J. Vanderborght, K. Mosthaf, K. M. Smits, and R. Helmig. Heat and water transport in soils and across the soil-atmosphere interface: 2. Numerical analysis. *Water Resources Research*, 53(2):1080–1100, 2017c. doi: 10.1002/2016WR019983.

A. Fick. Ueber Diffusion. *Annalen der Physik*, 170(1):59–86, 1855. doi: 10.1002/andp.18551700105.

S. Finsterle. Inverse Modellierung zur Bestimmung hydrogeologischer Parameter eines Zweiphasensystems. VAW Mitteilungen 121, ETH Zürich, 1993.

B. Flemisch, M. Darcis, K. Erbertseder, B. Faigle, A. Lauser, K. Mosthaf, S. Müthing, P. Nuske, A. Tatomir, M. Wolff, and R. Helmig. DuMuX: DUNE for Multi-{Phase, Component, Scale, Physics, ...} Flow and Transport in Porous Media. *Advances in Water Resources*, 34(9):1102–1112, 2011. doi: 10.1016/j.advwatres.2011.03.007.

T. K. Flesch, J. H. Prueger, and J. L. Hatfield. Turbulent Schmidt number from a tracer experiment. *Agricultural and Forest Meteorology*, 111(4):299–307, 2002. doi: 10.1016/S0168-1923(02)00025-4.

M. Fritsch. Analysis of Processes and Properties at a Porous-Medium Free-Flow Interface with the Application of Evaporation. Masther's thesis, University of Stuttgart, 2014. Supervisors: R. Helmig and T. Fetzer.

H. Fujimaki, T. Shimano, M. Inoue, and K. Nakane. Effect of a Salt Crust on Evaporation from a Bare Saline Soil. *Vadose Zone Journal*, 5(4):1246–1256, 2006. doi: 10.2136/vzj2005.0144.

A. Furman. Modeling Coupled Surface–Subsurface Flow Processes: A Review. *Vadose Zone Journal*, 7(2):741–756, 2008. doi: 10.2136/vzj2007.0065.

U. Ghia, K. N. Ghia, and C. T. Shin. High-Re solutions for incompressible flow using the Navier-Stokes equations and a multigrid method. *Journal of Computational Physics*, 48 (3):387–411, 1982. doi: 10.1016/0021-9991(82)90058-4.

P. Grassmann and F. Widmer. *Einführung in die thermische Verfahrenstechnik*. de Gruyter, Berlin, 2 edition, 1974. ISBN 3-11-004214-2.

C. Grüninger. *Numerical Coupling of Navier-Stokes and Darcy Flow for Soil-Water Evaporation*. PhD thesis, University of Stuttgart, 2017.

C. Grüninger, T. Fetzer, B. Flemisch, and R. Helmig. Coupling DuMuX and DUNE-PDELab to investigate evaporation at the interface between Darcy and Navier-Stokes flow. Preprint Series 2017 – 1, Stuttgart Research Centre for Simulation Technology (SRC SimTech), University of Stuttgart, 2017. doi: 10.18419/opus-9360.

V. Gurau, T. A. Zawodzinski, Jr., and J. A. Mann, Jr. Two-Phase Transport in PEM Fuel Cell Cathodes. *Journal of Fuel Cell Science and Technology*, 5(2):021009–021009–12, 2008. doi: 10.1115/1.2821597.

S. E. Haaland. Simple and Explicit Formulas for the Friction Factor in Turbulent Pipe Flow. *Journal of Fluids Engineering*, 105(1):89–90, 1983. doi: 10.1115/1.3240948.

E. Haghighi and D. Or. Interactions of bluff-body obstacles with turbulent airflows affecting evaporative fluxes from porous surfaces. *Journal of Hydrology*, 530:103–116, 2015. doi: 10.1016/j.jhydrol.2015.09.048.

E. Haghighi, E. Shahraeeni, P. Lehmann, and D. Or. Evaporation rates across a convective air boundary layer are dominated by diffusion. *Water Resources Research*, 49(3):1602–1610, 2013. doi: 10.1002/wrcr.20166.

S. Hahn, J. Je, and H. Choi. Direct numerical simulation of turbulent channel flow with permeable walls. *Journal of Fluid Mechanics*, 450:259–285, 2002. doi: 10.1017/S0022112001006437.

O. T. Hanna, O. C. Sandell, and P. R. Mazet. Heat and Mass Transfer in Turbulent Flow Under Conditions of Drag Reduction. *AIChE Journal*, 27(4):693–697, 1981. doi: 10.1002/aic.690270424.

N. S. Hanspal, A. N. Waghode, V. Nassehi, and R. J. Wakeman. Numerical Analysis of Coupled Stokes/Darcy Flows in Iindustrial Filtrations. *Transport in Porous Media*, 64(1):73–101, 2006. doi: 10.1007/s11242-005-1457-3.

F. H. Harlow and J. E. Welch. Numerical Calculation of Time-Dependent Viscous Incompressible Flow of Fluid with Free Surface. *Physics of Fluids*, 8(12):2182–2189, 1965. doi: 10.1063/1.1761178.

K. Heck. Numerical and experimental investigation of soil-root interactions. Masther's thesis, University of Stuttgart, 2016. Supervisors: R. Helmig, B. Flemisch, N. Schröder, T. Fetzer, and A. Trautz.

R. Helmig. *Multiphase Flow and Transport Processes in the Subsurface: A Contribution to the Modeling of Hydrosystems*. Springer, Berlin, 1997. ISBN 978-3-540-62703-6.

R. Huber and R. Helmig. Node-centered finite volume discretizations for the numerical simulation of multiphase flow in heterogeneous porous media. *Computers & Geosciences*, 4(2): 141–164, 2000. doi: 10.1023/A:1011559916309.

IAPWS. Revised Release on the IAPWS Industrial Formulation 1997 for the Thermodynamic Properties of Water and Steam. Technical Report IAPWS R7-97(2012), The International Association for the Properties of Water and Steam, Lucerne, Switzerland, 2007.

IAPWS. Release on the IAPWS Formulation 2008 for the Viscosity of Ordinary Water Substance. Technical Report IAPWS R12-08, The International Association for the Properties of Water and Steam, Berlin, Germany, 2008.

IAPWS. Release on the IAPWS Formulation 2011 for the Thermal Conductivity of Ordinary Water Substance. Technical Report IAPWS R15-11, The International Association for the Properties of Water and Steam, Plzeň, Czech Republic, 2011.

O. Iliev and V. Laptev. On numerical simulation of flow through oil filters. *Computing and Visualization in Science*, 6(2):139–146, 2004. doi: 10.1007/s00791-003-0118-8.

A. Jamarani, M. Maerefat, N. F. Jouybari, and M. E. Nimvari. Thermal Performance Evaluation of a Double-Tube Heat Exchanger Partially Filled with Porous Media Under Turbulent Flow Regime. *Transport in Porous Media*, 120(3):449–471, 2017. doi: 10.1007/s11242-017-0933-x.

V. A. Jambhekar, R. Helmig, N. Schröder, and N. Shokri. Free-Flow–Porous-Media Coupling for Evaporation-Driven Transport and Precipitation of Salt in Soil. *Transport in Porous Media*, 110(2):251–280, 2015. doi: 10.1007/s11242-015-0516-7.

V. A. Jambhekar, E. Mejri, N. Schröder, R. Helmig, and N. Shokri. Kinetic Approach to Model Reactive Transport and Mixed Salt Precipitation in a Coupled Free-Flow–Porous-Media System. *Transport in Porous Media*, 114(2):341–369, 2016. doi: 10.1007/s11242-016-0665-3.

O. Johansen. *Thermal conductivity of soils*. PhD Thesis, (CRREL draft transl. 637, 1977), Norwegian University of Science and Technology, Trondheim, Norway, 1975.

W. P. Jones and B. E. Launder. The prediction of laminarization with a two-equation model of turbulence. *International Journal of Heat and Mass Transfer*, 15(2):301–314, 1972. doi: 10.1016/0017-9310(72)90076-2.

R. Jurjevic. Modelling of two-dimensional laminar flow using finite element method. *International Journal for Numerical Methods in Fluids*, 31(3):601–626, 1999. doi: 10.1002/(SICI)1097-0363(19991015)31:3<601::AID-FLD892>3.0.CO;2-Z.

W. M. Kays, M. E. Crawford, and B. Weigand. *Convective heat and mass transfer*. McGraw-Hill Higher Education, 4 edition, 2009. ISBN 9780071238298.

T. Koch, K. Heck, N. Schröder, B. Flemisch, and R. Helmig. A new model concept for plant-scale soil-root interaction including soil evaporation, growth and transport processes. *Vadose Zone Journal*, accepted, 2018.

A. N. Kolmogorov. The local structure of turbulence in incompressible viscous fluid for very large Reynolds numbers [in Russian]. *Doklady Akademii Nauk SSSR*, 30(4):301–305, 1941.

A. N. Kolmogorov. Equations of turbulent motion in an icompressible Fluid [in Russian]. *Izvestia Academii Nauk USSR: Physics*, 6(1–2):56–58, 1942.

A. N. Kolmogorov. The Local Structure of Turbulence in Incompressible Viscous Fluid for Very Large Reynolds Numbers. *Proceedings: Mathematical and Physical Sciences*, 434 (1890):9–13, 1991.

L. I. G. Kovasznay. Laminar flow behind a two-dimensional grid. *Mathematical Proceedings of the Cambridge Philosophical Society*, 44(1):58–62, 1947. doi: 10.1017/S0305004100023999.

M. Krafczyk, K. Kucher, Y. Wang, and M. Geier. DNS/LES Studies of Turbulent Flows Based on the Cumulant Lattice Boltzmann Approach. In W. E. Nagel, D. H. Kröner, and M. M. Resch, editors, *High Performance Computing in Science and Engineering '14*, pages 519–531. Springer International Publishing, 2015. ISBN 978-3-319-10809-4. doi: 10.1007/978-3-319-10810-0_34.

Y. Kuwata and K. Suga. Lattice Boltzmann direct numerical simulation of interface turbulence over porous and rough walls. *International Journal of Heat and Fluid Flow*, 61: 145–157, 2016. doi: 10.1016/j.ijheatfluidflow.2016.03.006.

A. V. Kuznetsov. Numerical modeling of turbulent flow in a composite porous/fluid duct utilizing a two-layer k–ε model to account for interface roughness. *International Journal of Thermal Sciences*, 43(11):1047–1056, 2004. doi: 10.1016/j.ijthermalsci.2004.02.011.

A. V. Kuznetsov and S. M. Becker. Effect of the interface roughness on turbulent convective heat transfer in a composite porous/fluid duct. *International Communications in Heat and Mass Transfer*, 31(1):11–20, 2004. doi: 10.1016/S0735-1933(03)00197-0.

J. Laufer. The structure of turbulence in fully developed pipe flow. *NACA Report*, 1174: 417–434, 1954.

B. E. Launder and B. I. Sharma. Application of the energy-dissipation model of turbulence to the calculation of flow near a spinning disc. *Letters in Heat and Mass Transfer*, 1(2): 131–137, 1974. doi: 10.1016/0094-4548(74)90150-7.

B. E. Launder and D. B. Spalding. *Mathematical Models of Turbulence*. Acadademic Press, London, 1972.

J. B. Laurindo and M. Prat. Numerical and experimental network study of evaporation in capillary porous media. Drying rates. *Chemical Engineering Science*, 53(12):2257–2269, 1998. doi: 10.1016/S0009-2509(97)00348-5.

W. J. Layton, F. Schieweck, and I. Yotov. Coupling fluid flow with porous media flow. *SIAM Journal on Numerical Analysis*, 40(6):2195–2218, 2002. doi: 10.1137/S0036142901392766.

M. Le Bars and M. G. Worster. Interfacial conditions between a pure fluid and a porous medium: implications for binary alloy solidification. *Journal of Fluid Mechanics*, 550: 149–173, 2006. doi: 10.1017/S0022112005007998.

P. Lehmann and D. Or. Evaporation and capillary coupling across vertical textural contrasts in porous media. *Physical Review E*, 80(4):046318, 2009. doi: 10.1103/PhysRevE.80.046318.

P. Lehmann, S. Assouline, and D. Or. Characteristic lengths affecting evaporative drying of porous media. *Physical Review E*, 77(5):056309, 2008. doi: 10.1103/PhysRevE.77.056309.

E. W. Lemmon and R. T. Jacobsen. Viscosity and Thermal Conductivity Equations for Nitrogen, Oxygen, Argon, and Air. *International Journal of Thermophysics*, 25(1):21–69, 2004. doi: 10.1023/B:IJOT.0000022327.04529.f3.

M. C. Leverett. Capillary Behavior in Porous Solids. *Transactions of the AIME*, 1(5), 1941. doi: 10.2118/941152-G.

X. S. Li. An Overview of SuperLU: Algorithms, Implementation, and User Interface. *ACM Transactions on Mathematical Software*, 31(3):302–325, 2005. doi: 10.1145/1089014.1089017.

F. S. Lien, E. Yee, and Y. Cheng. Simulation of mean flow and turbulence over a 2D building array using high-resolution CFD and a distributed drag force approach. *Journal of Wind Engineering and Industrial Aerodynamics*, 92(2):117–158, 2004. doi: 10.1016/j.jweia.2003.10.005.

S. Lu, T. Ren, Z. Yu, and R. Horton. A method to estimate the water vapour enhancement factor in soil. *European Journal of Soil Science*, 62(4):98–504, 2011. doi: 10.1111/j.1365-2389.2011.01359.x.

T. Lu, P. Jiang, and S. Shen. Numerical and experimental investigation of convective drying in unsaturated porous media with bound water. *Heat and Mass Transfer*, 41(12):1103–1111, 2005. doi: 10.1007/s00231-005-0634-9.

M. Maier, H. Schack-Kirchner, M. Aubinet, S. Goffin, B. Longdoz, and F. Parent. Turbulence Effect on Gas Transport in Three Contrasting Forest Soils. *Soil Science Society of America Journal*, 76(5):1518–1528, 2012. doi: 10.2136/sssaj2011.0376.

M. R. Malin. On the calculation of heat transfer rates in fully turbulent wall flows. *Applied Mathematical Modelling*, 11(4):281–284, 1987. doi: 10.1016/0307-904X(87)90143-0.

C. Manes, D. Pokrajac, V. I. Nikora, L. Ridolfi, and D. Poggi. Turbulent friction in flows over permeable walls. *Geophysical Research Letters*, 38(3):L03402, 2011. doi: 10.1029/2010GL045695.

C. Masson, H. J. Saabas, and B. R. Baliga. Co-located equal-order control-volume finite element method for two-dimensional axisymmetric incompressible fluid flow. *International Journal for Numerical Methods in Fluids*, 18(1):1–26, 1994. doi: 10.1002/fld.1650180102.

R. Masson, L. Trenty, and Y. Zhang. Coupling compositional liquid gas Darcy and free gas flows at porous and free-flow domains interface. *Journal of Computational Physics*, 321:708–728, 2016. doi: 10.1016/j.jcp.2016.06.003.

D. J. Mavriplis. Algebraic Turbulence Modeling for Unstructered and Adaptive Meshes. *AIAA Journal*, 29(12):2086–2093, 1990. doi: 10.2514/3.10845.

T. R. McVicar, M. L. Roderick, R. J. Donohue, L. T. Li, T. G. V. Niel, A. Thomas, J. Grieser, D. Jhajharia, Y. Himri, N. M. Mahowald, A. V. Mescherskaya, A. C. Kruger, S. Rehman, and Y. Dinpashoh. Global review and synthesis of trends in observed terrestrial near-surface wind speeds: Implications for evaporation. *Journal of Hydrology*, 416–417:182–205, 2012. doi: 10.1016/j.jhydrol.2011.10.024.

F. R. Menter. Two-Equation Eddy-Viscosity Turbulence Models for Engineering Applications. *AIAA Journal*, 32(8):1598–1605, 1994. doi: 10.2514/3.12149.

R. J. Millington. Gas diffusion in porous media. *Science*, 130(3367):100–102, 1959. doi: 10.1126/science.130.3367.100-a.

A. S. Modaihsh, R. Horton, and D. Kirkham. Soil-water evaporation suppression by sand mulches. *Soil Science*, 139(4):357–361, 1985. doi: 10.1097/00010694-198504000-00010.

G. P. Moeckel. Thermodynamics of an interface. *Archive for Rational Mechanics and Analysis*, 57(3):255–280, 1975. doi: 10.1007/BF00280158.

B. Mohammadi and O. Pironneau. *Analysis of the K-Epsilon turbulence model*. Wiley, Chichester, 1994. ISBN 0-471-94460-2.

K. Mosthaf. *Modeling and Analysis of Coupled Porous-Medium and Free Flow with Application to Evaporation Processes*. PhD thesis, Universität Stuttgart, 2014. doi: 10.18419/opus-519.

K. Mosthaf, K. Baber, B. Flemisch, R. Helmig, A. Leijnse, I. Rybak, and B. Wohlmuth. A coupling concept for two-phase compositional porous-medium and single-phase compositional free flow. *Water Resources Research*, 47(10):W10522, 2011. doi: 10.1029/2011WR010685.

K. Mosthaf, R. Helmig, and D. Or. Modeling and analysis of evaporation processes from porous media on the REV scale. *Water Resources Research*, 50(2):1059–1079, 2014. doi: 10.1002/2013WR014442.

S. Müthing. *A Flexible Framework for Multi Physics and Multi Domain PDE Simulations*. PhD thesis, Universität Stuttgart, 2015. doi: 10.18419/opus-3620.

V. Nassehi. Modelling of combined Navier–Stokes and Darcy flows in crossflow membrane filtration. *Chemical Engineering Science*, 53(6):1253–1265, 1998. doi: 10.1016/S0009-2509(97)00443-0.

D. A. Nield. The Beavers-Joseph boundary condition and related matters: A historical and critical note. *Transport in Porous Media*, 78(3):537–540, 2009. doi: 10.1007/s11242-009-9344-y.

D. A. Nield and A. Bejan. *Convection in Porous Media*. Springer International Publishing, 5 edition, 2017. ISBN 978-3-319-49562-0. doi: 10.1007/978-3-319-49562-0.

M. E. Nimvari, M. Maerefat, and M. K. El-Hossaini. Numerical simulation of turbulent flow and heat transfer in a channel partially filled with a porous media. *International Journal of Thermal Sciences*, 60:131–141, 2012. doi: 10.1016/j.ijthermalsci.2012.05.016.

P. Nuske. *Beyond local equilibrium: relaxing local equilibrium assumptions in multiphase flow in porous media*. PhD thesis, University of Stuttgart, 2014. doi: 10.18419/opus-597.

P. Nuske, V. Joekar-Niasar, and R. Helmig. Non-equilibrium in multiphase multicomponent flow in porous media: An evaporation example. *International Journal of Heat and Mass Transfer*, 74:128–142, 2014. doi: 10.1016/j.ijheatmasstransfer.2014.03.011.

H. Oertel. *Strömungsmechanik*. Vieweg+Teubner, Wiesbaden, 6 edition, 2011. ISBN 978-3-8348-8110-6. doi: 10.1007/978-3-8348-8110-6.

H. Oertel. *Prandtl - Führer durch die Strömungslehre: Grundlagen und Phänomene*. Springer Vieweg, Wiesbaden, 13 edition, 2012. ISBN 978-3-8348-2315.1. doi: 10.1007/978-3-8348-2315-1.

C. Oldenburg and A. Unger. Coupled vadose zone and atmospheric surface-layer transport of CO_2 from geologic carbon sequestration sites. *Vadose Zone Journal*, 3(3):848–857, 2004. doi: 10.2136/vzj2004.0848.

D. Or, P. Lehmann, E. Shahraeeni, and N. Shokri. Advances in Soil Evaporation Physics – A Review. *Vadose Zone Journal*, 12(4), 2013. doi: 10.2136/vzj2012.0163.

V. C. Patel, W. Rodi, and G. Scheuerer. Turbulence models for near-wall and low Reynolds number flows - A review. *AIAA Journal*, 23(9):1308–1319, 1985. doi: 10.2514/3.9086.

M. H. J. Pedras and M. J. S. de Lemos. Macroscopic turbulence modeling for incompressible flow through undeformable porous media. *International Journal of Heat and Mass Transfer*, 44(6):1081–1093, 2001. doi: 10.1016/S0017-9310(00)00202-7.

H. L. Penman. Natural Evaporation from Open Water, Bare Soil and Grass. *Proceedings of the Royal Society of London A: Mathematical, Physical and Engineering Sciences*, 193 (1032):120–145, 1948. doi: 10.1098/rspa.1948.0037.

D. Pokrajac and C. Manes. Velocity Measurements of a Free-Surface Turbulent Flow Penetrating a Porous Medium Composed of Uniform-Size Spheres. *Transport in Porous Media*, 78(3):367–383, 2009. doi: 10.1007/s11242-009-9339-8.

B. E. Poling, J. M. Prausnitz, and J. P. O'Connell. *The properties of gases and liquids*, volume 5. McGraw-Hill, New York, 2001. ISBN 0070116822. doi: 10.1036/0070116822.

S. B. Pope. *Turbulent flows*. Cambridge University Press, Cambridge, 4 edition, 2006. ISBN 978-0-521-59125-6.

K. N. Potter, R. Horton, and R. M. Cruse. Soil Surface Roughness Effects on Radiation Reflectance and Soil Heat Flux. *Soil Science Society of America Journal*, 51(4):855–860, 1987. doi: 10.2136/sssaj1987.03615995005100040003x.

J. Ren and A. I. Packman. Coupled Stream–Subsurface Exchange of Colloidal Hematite and Dissolved Zinc, Copper, and Phosphate. *Environmental Science & Technology*, 39(17): 6387–6394, 2005. doi: 10.1021/es050168q.

L. A. Richards. Capillary conduction of liquids through porous mediums. *Journal of Applied Physics*, 1(5):318–333, 1931. doi: 10.1063/1.1745010.

W. Rodi, G. Constantinescu, and T. Stoesser. *Large-Eddy Simulation in Hydraulics*. IAHR Monographs. CRC Press, 2013. ISBN 978-1-138-00024-7.

K. Roth. *Soil Physics. Lecture Notes Autumn 2012*. Heidelberg University, Institute of Environmental Physics, 2012.

J. C. Rotta. Turbulent Boundary Layers in Incompressible Flow. *Progress in Aerospace Science*, 2(1):1–219, 1962. doi: 10.1016/0376-0421(62)90014-3.

M. Rutten. *Moisture in the topsoil: From large-scale observations to small-scale process understanding*. PhD thesis, TU Delft, 2015. doi: 10.4233/uuid:89e13a16-b456-4692-92f0-7a40ada82451.

I. Rybak, J. Magiera, R. Helmig, and C. Rohde. Multirate time integration for coupled saturated/unsaturated porous medium and free flow systems. *Computers & Geosciences*, 19(2):299–309, 2015. doi: 10.1007/s10596-015-9469-8.

P. G. Saffman. A model for inhomogeneous turbulent flow. *Proceedings of the Royal Society of London A: Mathematical, Physical and Engineering Sciences*, 317(1530):417–433, 1970. doi: 10.1098/rspa.1970.0125.

P. G. Saffman. On the boundary condition at the surface of a porous medium. *Studies in Applied Mathematics*, 50(2):93–101, 1971. doi: 10.1002/sapm197150293.

M. Sahraoui and M. Kaviany. Slip and no-slip velocity boundary conditions at interface of porous, plain media. *International Journal of Heat and Mass Transfer*, 35(4):927–943, 1992. doi: 10.1016/0017-9310(92)90258-T.

A. G. Salinger, R. Aris, and J. J. Derby. Finite element formulations for large-scale, coupled flows in adjacent porous and open fluid domains. *International Journal for Numerical Methods in Fluids*, 18(12):1185–1209, 1994. doi: 10.1002/fld.1650181205.

H. Schlichting and K. Gersten. *Grenzschicht-Theorie*. Springer, Berlin Heidelberg, 10 edition, 2006. ISBN 978-3-540-23004-5. doi: 10.1007/3-540-32985-4.

E.-U. Schlünder. Über den Mechanismus des ersten Trocknungsabschnittes und seine mögliche Bedeutung für diffusionskontrollierte katalytische Gasphasen-Reaktionen. *Chemie Ingenieur Technik*, 60(2):117–120, 1988. doi: 10.1002/cite.330600209.

K. Schneider-Zapp, O. Ippisch, and K. Roth. Numerical study of the evaporation process and parameter estimation analysis of an evaporation experiment. *Hydrology and Earth System Sciences*, 14(5):765–781, 2010. doi: 10.5194/hess-14-765-2010.

S. Scholz. Study on porous-medium wall functions for k-ε and k-ω turbulence models. Bachelor's thesis, University of Stuttgart, 2014. Supervisors: R. Helmig and T. Fetzer.

E. Shahraeeni and D. Or. Thermo-evaporative fluxes from heterogeneous porous surfaces resolved by infrared thermography. *Water Resources Research*, 46(9):W09511, 2010. doi: 10.1029/2009WR008455.

E. Shahraeeni, P. Lehmann, and D. Or. Coupling of evaporative fluxes from drying porous surfaces with air boundary layer: Characteristics of evaporation from discrete pores. *Water Resources Research*, 48(9):W09525, 2012. doi: 10.1029/2012WR011857.

U. Shavit. Special Issue on "Transport Phenomena at the Interface Between Fluid and Porous Domains". *Transport in Porous Media*, 78(3):327–330, 2009. doi: 10.1007/s11242-009-9414-1.

N. Shokri and D. Or. What determines drying rates at the onset of diffusion controlled stage-2 evaporation from porous media? *Water Resources Research*, 47(9):W09513, 2011. doi: 10.1029/2010WR010284.

N. Shokri, P. Lehmann, and D. Or. Critical evaluation of enhancement factors for vapor transport through unsaturated porous media. *Water Resources Research*, 45(10):W10433, 2009. doi: 10.1029/2009WR007769.

N. Shokri, P. Lehmann, and D. Or. Evaporation from layered porous media. *Journal of Geophysical Research: Solid Earth*, 115(B6):B06204, 2010. doi: 10.1029/2009JB006743.

J. Shukla and Y. Mintz. Influence of land–surface evapotranspiration on the earth's climate. *Science*, 215(4539):1498–1501, 1982. doi: 10.1126/science.215.4539.1498.

E. Skjetne and J.-L. Auriault. High-Velocity Laminar and Turbulent Flow in Porous Media. *Transport in Porous Media*, 36(2):131–147, 1999. doi: 10.1023/A:1006582211517.

K. M. Smits, T. Sakaki, A. Limsuwat, and T. H. Illangasekare. Thermal Conductivity of Sands under Varying Moisture and Porosity in Drainage–Wetting Cycles. *Vadose Zone Journal*, 9(1):172–180, 2010. doi: 10.2136/vzj2009.0095.

K. M. Smits, A. Cihan, T. Sakaki, and T. H. Illangasekare. Evaporation from soils under thermal boundary conditions: Experimental and modeling investigation to compare equilibrium- and nonequilibrium-based approaches. *Water Resources Research*, 47(5): W05540, 2011. doi: 10.1029/2010WR009533.

K. M. Smits, V. V. Ngo, A. Cihan, T. Sakaki, and T. H. Illangasekare. An evaluation of models of bare soil evaporation formulated with different land surface boundary conditions and assumptions. *Water Resources Research*, 48(12):W12526, 2012. doi: 10.1029/2012WR012113.

K. M. Smits, A. Cihan, T. Sakaki, S. E. Howington, J. F. Peters, and T. H. Illangasekare. Soil Moisture and Thermal Behavior in the Vicinity of Buried Objects Affecting Remote Sensing Detection: Experimental and Modeling Investigation. *IEEE Transactions on Geoscience and Remote Sensing*, 51(5):2675–2688, 2013. doi: 10.1109/TGRS.2012.2214485.

W. H. Somerton, J. A. Keese, and S. L. Chu. Thermal behavior of unconsolidated oil sands. *Society of Petroleum Engineers Journal*, 14(5):513–521, 1974. doi: 10.2118/4506-PA.

W.-K. Song, Y.-J. Cui, A. M. Tang, W.-Q. Ding, and T. D. Tran. Experimental study on water evaporation from sand using environmental chamber. *Canadian Geotechnical Journal*, 51 (2):115–128, 2014. doi: 10.1139/cgj-2013-0155.

M. Sophocleous. Interactions between groundwater and surface water: the state of the science. *Hydrogeology Journal*, 10(1):52–67, 2002. doi: 10.1007/s10040-001-0170-8.

P. R. Spalart. Philosophies and fallacies in turbulence modeling. *Progress in Aerospace Sciences*, 74:1–15, 2015. doi: 10.1016/j.paerosci.2014.12.004.

P. R. Spalart and S. R. Allmaras. A one-equation turbulence model for aerodynamic flows. In *Aerospace Sciences Meetings*, pages –. American Institute of Aeronautics and Astronautics, 1992. doi: 10.2514/6.1992-439.

K. Suga. Understanding and Modelling Turbulence Over and Inside Porous Media. *Flow, Turbulence and Combustion*, 96(3):717–756, 2016. doi: 10.1007/s10494-015-9673-6.

K. Suga, S. Tominaga, M. Mori, and M. Kaneda. Turbulence Characteristics in Flows Over Solid and Porous Square Ribs Mounted on Porous Walls. *Flow, Turbulence and Combustion*, 91(1):19–40, 2013. doi: 10.1007/s10494-013-9452-1.

F. Sugita and T. Kishii. Effect of roughness distribution on evaporation processes over non-homogeneous sand surfaces: a wind tunnel investigation. *Hydrological Processes*, 16(11): 2141–2153, 2002. doi: 10.1002/hyp.1147.

S. Suzuki and S. Maeda. On the mechanism of drying of granular bed. *Journal of Chemical Engineering of Japan*, 1(1):26–31, 1968. doi: 10.1252/jcej.1.26.

A. Szymkiewicz. *Mathematical Models of Flow in Porous Media*, pages 9–47. Springer Berlin Heidelberg, Berlin, Heidelberg, 2013. ISBN 978-3-642-23559-7. doi: 10.1007/978-3-642-23559-7_2.

J. Y. Tang and W. J. Riley. A new top boundary condition for modeling surface diffusive exchange of a generic volatile tracer: theoretical analysis and application to soil evaporation. *Hydrology and Earth System Sciences*, 17(2):873–893, 2013. doi: 10.5194/hess-17-873-2013.

N. Targui and H. Kahalerras. Analysis of fluid flow and heat transfer in a double pipe heat exchanger with porous structures. *Energy Conversion and Management*, 49(11):3217–3229, 2008. doi: 10.1016/j.enconman.2008.02.010.

S. W. Thomson. LX. On the equilibrium of vapour at a curved surface of liquid. *Philosophical Magazine*, 42(282):448–452, 1871. doi: 10.1080/14786447108640606.

Y. Tominaga and T. Stathopoulos. Turbulent Schmidt numbers for CFD analysis with various types of flowfield. *Atmospheric Environment*, 41(37):8091–8099, 2007. doi: 10.1016/j.atmosenv.2007.06.054.

A. C. Trautz. *Heat and Mass Transfer in Porous Media under the Influence of Near-Surface Boundary Layer Atmospheric Flow*. PhD thesis, Colorado School of Mines, 2015.

A. C. Trautz, K. M. Smits, and A. Cihan. Continuum-scale investigation of evaporation from bare soil under different boundary and initial conditions: An evaluation of nonequilibrium phase change. *Water Resources Research*, 51(9):7630–7648, 2015. doi: 10.1002/2014WR016504.

E. Truckenbrodt. Grundlagen und elementare Strömungsvorgänge dichtebeständiger Fluide. In *Fluidmechanik*, Klassiker der Technik, pages XXVII, 364. Springer, Berlin Heidelberg, 4 edition, 2008a. ISBN 978-3-540-79017-4. doi: 10.1007/978-3-540-79018-1.

E. Truckenbrodt. Elementare Strömungsvorgänge dichteveränderlicher Fluide. In *Fluidmechanik*, Klassiker der Technik, pages XVII, 414. Springer, Berlin Heidelberg, 4 edition, 2008b. ISBN 978-3-540-79023-5. doi: 10.1007/978-3-540-79024-2_1.

P. W. Unger and D. K. Cassel. Tillage implement disturbance effects on soil properties related to soil and water conservation: a literature review. *Soil and Tillage Research*, 19 (4):363–382, 1991. doi: 10.1016/0167-1987(91)90113-C.

J. van Brakel. *Advances in Drying*, volume 1, chapter Mass transfer in convective drying, pages 217–267. Hemisphere, 1980. ISBN 0-89116-185-6.

E. R. van Driest. On Turbulent Flow Near a Wall. *AIAA Journal*, 23(11):1007–1011, 1956. doi: 10.2514/8.3713.

M. T. van Genuchten. A Closed-form Equation for Predicting the Hydraulic Conductivity of Unsaturated Soils. *Soil Science Society of America Journal*, 44(5):892–898, 1980. doi: 10.2136/sssaj1980.03615995004400050002x.

J. Vanderborght, A. Graf, C. Steenpass, B. Scharnagl, N. Prolingheuer, M. Herbst, H.-J. H. Franssen, and H. Vereecken. Within-Field Variability of Bare Soil Evaporation Derived from Eddy Covariance Measurements Special Section: Patterns. *Vadose Zone Journal*, 9 (4):943–954, 2010. doi: 10.2136/vzj2009.0159.

J. Vanderborght, T. Fetzer, K. Mosthaf, K. M. Smits, and R. Helmig. Heat and water transport in soils and across the soil-atmosphere interface: 1. Theory and different model concepts. *Water Resources Research*, 53(2):1057–1079, 2017. doi: 10.1002/2016WR019982.

N. B. Vargaftik. *Tables on the thermophysical properties of liquids and gases*. Advances in Thermal Engineering. Hemisphere Publishing Corporation, 2 edition, 1975. ISBN 9780470903100.

P. Verboven, D. Flick, B. M. Nicolaï, and G. Alvarez. Modelling transport phenomena in refrigerated food bulks, packages and stacks: basics and advances. *International Journal of Refrigeration*, 29(6):985–997, 2006. doi: 10.1016/j.ijrefrig.2005.12.010.

H. Versteeg and W. Malalasekra. *An Introduction to Computational Fluid Dynamics*. Pearson Education, Harlow, 2 edition, 2009. ISBN 978-0-13-127498-3.

W. R. Walker, J. D. Sabey, and D. R. Hampton. Studies of heat transfer and water migration in soils. Final report. Technical Report DOE/CS/30139-T1, Colorado State University, Fort Collins (USA), 1981.

S. Wanphen and K. Nagano. Experimental study of the performance of porous materials to moderate the roof surface temperature by its evaporative cooling effect. *Building and Environment*, 44(2):338–351, 2009. doi: 10.1016/j.buildenv.2008.03.012.

S. Whitaker. Flow in porous media I: A theoretical derivation of Darcy's law. *Transport in Porous Media*, 1(1):3–25, 1986. doi: 10.1007/BF01036523.

S. Whitaker. The Forchheimer equation: A theoretical development. *Transport in Porous Media*, 25(1):27–61, 1996. doi: 10.1007/BF00141261.

F. M. White. *Fluid mechanics*. McGraw-Hill, New York, 7 edition, 2011. ISBN 978-0-07-131121-2.

Wikipedia. Wikipedia: The Free Encyclopedia, www.en.wikipedia.org, 2017.

D. C. Wilcox. Reassessment of the Scale-Determining Equation for Advanced Turbulence Models. *AIAA Journal*, 26(11):1299–1310, 1988. doi: 10.2514/3.10041.

D. C. Wilcox. *Turbulence Modeling for CFD*. DCW Industries, La Cañada, California, 3 edition, 2006. ISBN 978-1-928729-08-2.

D. C. Wilcox. Formulation of the k-ω Turbulence Model Revisited. *AIAA Journal*, 46(11): 2823–2838, 2008. doi: 10.2514/1.36541.

D. Wildenschild and A. P. Sheppard. X-ray imaging and analysis techniques for quantifying pore-scale structure and processes in subsurface porous medium system. *Advances in Water Resources*, 51:217–246, 2013. doi: 10.1016/j.advwatres.2012.07.018.

Y.-S. Wu. Numerical Simulation of Single-Phase and Multiphase Non-Darcy Flow in Porous and Fractured Reservoirs. *Transport in Porous Media*, 49(2):209–240, 2002. doi: 10.1023/A:1016018020180.

V. Yakhot and S. A. Orszag. Renormalization group analysis of turbulence. I. Basic theory. *Journal of Scientific Computing*, 1(1):3–51, 1986. doi: 10.1007/BF01061452.

T. Yamanaka, A. Takeda, and F. Sugita. A modified surface-resistance approach for representing bare-soil evaporation: Wind tunnel experiments under various atmospheric conditions. *Water Resources Research*, 33(9):2117–2128, 1997. doi: 10.1029/97WR01639.

G. Yang, B. Weigand, A. Terzis, K. Weishaupt, and R. Helmig. Numerical Simulation of Turbulent Flow and Heat Transfer in a Three-Dimensional Channel Coupled with Flow Through Porous Structures. *Transport in Porous Media*, 122(1):145–167, 2018. doi: 10.1007/s11242-017-0995-9.

A. G. Yiotis, I. N. Tsimpanogiannis, A. K. Stubos, and Y. C. Yortsos. Coupling between external and internal mass transfer during drying of a porous medium. *Water Resources Research*, 43(W06403):1–12, 2007. doi: 10.1029/2006WR005558.

C. Zhang, L. Li, and D. Lockington. A physically based surface resistance model for evaporation from bare soils. *Water Resources Research*, 51(2):1084–1111, 2015. doi: 10.1002/2014WR015490.

Institut für Wasser- und Umweltsystemmodellierung
Universität Stuttgart

Pfaffenwaldring 61
70569 Stuttgart (Vaihingen)
Telefon (0711) 685 - 64717/64749/64752/64679
Telefax (0711) 685 - 67020 o. 64746 o. 64681
E-Mail: iws@iws.uni-stuttgart.de
http://www.iws.uni-stuttgart.de

Verzeichnis der Mitteilungshefte

5 Plate, Erich: *Beitrag zur Bestimmung der Windgeschwindigkeitsverteilung in der durch eine Wand gestörten bodennahen Luftschicht*, und
Röhnisch, Arthur; Marotz, Günter: *Neue Baustoffe und Bauausführungen für den Schutz der Böschungen und der Sohle von Kanälen, Flüssen und Häfen; Gestehungskosten und jeweilige Vorteile*, sowie
Unny, T.E.: *Schwingungsuntersuchungen am Kegelstrahlschieber*, 1967

6 Seiler, Erich: *Die Ermittlung des Anlagenwertes der bundeseigenen Binnenschiffahrtsstraßen und Talsperren und des Anteils der Binnenschiffahrt an diesem Wert*, 1967

7 *Sonderheft anläßlich des 65. Geburtstages von Prof. Arthur Röhnisch mit Beiträgen von* Benk, Dieter; Breitling, J.; Gurr, Siegfried; Haberhauer, Robert; Honekamp, Hermann; Kuz, Klaus Dieter; Marotz, Günter; Mayer-Vorfelder, Hans-Jörg; Miller, Rudolf; Plate, Erich J.; Radomski, Helge; Schwarz, Helmut; Vollmer, Ernst; Wildenhahn, Eberhard; 1967

8 Jumikis, Alfred: *Beitrag zur experimentellen Untersuchung des Wassernachschubs in einem gefrierenden Boden und die Beurteilung der Ergebnisse*, 1968

9 Marotz, Günter: *Technische Grundlagen einer Wasserspeicherung im natürlichen Untergrund*, 1968

10 Radomski, Helge: *Untersuchungen über den Einfluß der Querschnittsform wellenförmiger Spundwände auf die statischen und rammtechnischen Eigenschaften*, 1968

11 Schwarz, Helmut: *Die Grenztragfähigkeit des Baugrundes bei Einwirkung vertikal gezogener Ankerplatten als zweidimensionales Bruchproblem*, 1969

12 Erbel, Klaus: *Ein Beitrag zur Untersuchung der Metamorphose von Mittelgebirgsschneedecken unter besonderer Berücksichtigung eines Verfahrens zur Bestimmung der thermischen Schneequalität*, 1969

13 Westhaus, Karl-Heinz: *Der Strukturwandel in der Binnenschiffahrt und sein Einfluß auf den Ausbau der Binnenschiffskanäle*, 1969

14 Mayer-Vorfelder, Hans-Jörg: *Ein Beitrag zur Berechnung des Erdwiderstandes unter Ansatz der logarithmischen Spirale als Gleitflächenfunktion*, 1970

15 Schulz, Manfred: *Berechnung des räumlichen Erddruckes auf die Wandung kreiszylindrischer Körper*, 1970

16 Mobasseri, Manoutschehr: *Die Rippenstützmauer. Konstruktion und Grenzen ihrer Standsicherheit*, 1970

17 Benk, Dieter: *Ein Beitrag zum Betrieb und zur Bemessung von Hochwasserrückhaltebecken*, 1970

18 Gàl, Attila: *Bestimmung der mitschwingenden Wassermasse bei überströmten Fischbauchklappen mit kreiszylindrischem Staublech*, 1971, vergriffen

19 Kuz, Klaus Dieter: *Ein Beitrag zur Frage des Einsetzens von Kavitationserscheinungen in einer Düsenströmung bei Berücksichtigung der im Wasser gelösten Gase*, 1971, vergriffen

20 Schaak, Hartmut: *Verteilleitungen von Wasserkraftanlagen*, 1971

21 *Sonderheft zur Eröffnung der neuen Versuchsanstalt des Instituts für Wasserbau der Universität Stuttgart mit Beiträgen von* Brombach, Hansjörg; Dirksen, Wolfram; Gàl, Attila; Gerlach, Reinhard; Giesecke, Jürgen; Holthoff, Franz-Josef; Kuz, Klaus Dieter; Marotz, Günter; Minor, Hans-Erwin; Petrikat, Kurt; Röhnisch, Arthur; Rueff, Helge; Schwarz, Helmut; Vollmer, Ernst; Wildenhahn, Eberhard; 1972

22 Wang, Chung-su: *Ein Beitrag zur Berechnung der Schwingungen an Kegelstrahlschiebern*, 1972

23 Mayer-Vorfelder, Hans-Jörg: *Erdwiderstandsbeiwerte nach dem Ohde-Variationsverfahren*, 1972

24 Minor, Hans-Erwin: *Beitrag zur Bestimmung der Schwingungsanfachungsfunktionen überströmter Stauklappen*, 1972, vergriffen

25 Brombach, Hansjörg: *Untersuchung strömungsmechanischer Elemente (Fluidik) und die Möglichkeit der Anwendung von Wirbelkammerelementen im Wasserbau*, 1972, vergriffen

26 Wildenhahn, Eberhard: *Beitrag zur Berechnung von Horizontalfilterbrunnen*, 1972

27 Steinlein, Helmut: *Die Eliminierung der Schwebstoffe aus Flußwasser zum Zweck der unterirdischen Wasserspeicherung, gezeigt am Beispiel der Iller*, 1972

28 Holthoff, Franz Josef: *Die Überwindung großer Hubhöhen in der Binnenschiffahrt durch Schwimmerhebewerke*, 1973

29 Röder, Karl: *Einwirkungen aus Baugrundbewegungen auf trog- und kastenförmige Konstruktionen des Wasser- und Tunnelbaues*, 1973

30 Kretschmer, Heinz: *Die Bemessung von Bogenstaumauern in Abhängigkeit von der Talform*, 1973

31 Honekamp, Hermann: *Beitrag zur Berechnung der Montage von Unterwasserpipelines*, 1973

32 Giesecke, Jürgen: *Die Wirbelkammertriode als neuartiges Steuerorgan im Wasserbau*, und Brombach, Hansjörg: *Entwicklung, Bauformen, Wirkungsweise und Steuereigenschaften von Wirbelkammerverstärkern*, 1974

33 Rueff, Helge: *Untersuchung der schwingungserregenden Kräfte an zwei hintereinander angeordneten Tiefschützen unter besonderer Berücksichtigung von Kavitation*, 1974

34 Röhnisch, Arthur: *Einpreßversuche mit Zementmörtel für Spannbeton - Vergleich der Ergebnisse von Modellversuchen mit Ausführungen in Hüllwellrohren*, 1975

35 *Sonderheft anläßlich des 65. Geburtstages von Prof. Dr.-Ing. Kurt Petrikat mit Beiträgen von*: Brombach, Hansjörg; Erbel, Klaus; Flinspach, Dieter; Fischer jr., Richard; Gàl, Attila; Gerlach, Reinhard; Giesecke, Jürgen; Haberhauer, Robert; Hafner Edzard; Hausenblas, Bernhard; Horlacher, Hans-Burkhard; Hutarew, Andreas; Knoll, Manfred; Krummet, Ralph; Marotz, Günter; Merkle, Theodor; Miller, Christoph; Minor, Hans-Erwin; Neumayer, Hans; Rao, Syamala; Rath, Paul; Rueff, Helge; Ruppert, Jürgen; Schwarz, Wolfgang; Topal-Gökceli, Mehmet; Vollmer, Ernst; Wang, Chung-su; Weber, Hans-Georg; 1975

36 Berger, Jochum: *Beitrag zur Berechnung des Spannungszustandes in rotationssymmetrisch belasteten Kugelschalen veränderlicher Wandstärke unter Gas- und Flüssigkeitsdruck durch Integration schwach singulärer Differentialgleichungen*, 1975

37 Dirksen, Wolfram: *Berechnung instationärer Abflußvorgänge in gestauten Gerinnen mittels Differenzenverfahren und die Anwendung auf Hochwasserrückhaltebecken*, 1976

38 Horlacher, Hans-Burkhard: *Berechnung instationärer Temperatur- und Wärmespannungsfelder in langen mehrschichtigen Hohlzylindern*, 1976

39 Hafner, Edzard: *Untersuchung der hydrodynamischen Kräfte auf Baukörper im Tiefwasserbereich des Meeres*, 1977, ISBN 3-921694-39-6

40 Ruppert, Jürgen: *Über den Axialwirbelkammerverstärker für den Einsatz im Wasserbau*, 1977, ISBN 3-921694-40-X

41 Hutarew, Andreas: *Beitrag zur Beeinflußbarkeit des Sauerstoffgehalts in Fließgewässern an Abstürzen und Wehren*, 1977, ISBN 3-921694-41-8, vergriffen

42 Miller, Christoph: *Ein Beitrag zur Bestimmung der schwingungserregenden Kräfte an unterströmten Wehren*, 1977, ISBN 3-921694-42-6

43 Schwarz, Wolfgang: *Druckstoßberechnung unter Berücksichtigung der Radial- und Längsverschiebungen der Rohrwandung*, 1978, ISBN 3-921694-43-4

44 Kinzelbach, Wolfgang: *Numerische Untersuchungen über den optimalen Einsatz variabler Kühlsysteme einer Kraftwerkskette am Beispiel Oberrhein*, 1978, ISBN 3-921694-44-2

45 Barczewski, Baldur: *Neue Meßmethoden für Wasser-Luftgemische und deren Anwendung auf zweiphasige Auftriebsstrahlen*, 1979, ISBN 3-921694-45-0

46 Neumayer, Hans: *Untersuchung der Strömungsvorgänge in radialen Wirbelkammerverstärkern*, 1979, ISBN 3-921694-46-9

47 Elalfy, Youssef-Elhassan: *Untersuchung der Strömungsvorgänge in Wirbelkammerdioden und -drosseln*, 1979, ISBN 3-921694-47-7

48 Brombach, Hansjörg: *Automatisierung der Bewirtschaftung von Wasserspeichern*, 1981, ISBN 3-921694-48-5

49 Geldner, Peter: *Deterministische und stochastische Methoden zur Bestimmung der Selbstdichtung von Gewässern*, 1981, ISBN 3-921694-49-3, vergriffen

50 Mehlhorn, Hans: *Temperaturveränderungen im Grundwasser durch Brauchwassereinleitungen*, 1982, ISBN 3-921694-50-7, *vergriffen*

51 Hafner, Edzard: *Rohrleitungen und Behälter im Meer*, 1983, ISBN 3-921694-51-5

52 Rinnert, Bernd: *Hydrodynamische Dispersion in porösen Medien: Einfluß von Dichteunterschieden auf die Vertikalvermischung in horizontaler Strömung*, 1983, ISBN 3-921694-52-3, *vergriffen*

53 Lindner, Wulf: *Steuerung von Grundwasserentnahmen unter Einhaltung ökologischer Kriterien*, 1983, ISBN 3-921694-53-1, *vergriffen*

54 Herr, Michael; Herzer, Jörg; Kinzelbach, Wolfgang; Kobus, Helmut; Rinnert, Bernd: *Methoden zur rechnerischen Erfassung und hydraulischen Sanierung von Grundwasserkontaminationen*, 1983, ISBN 3-921694-54-X

55 Schmitt, Paul: *Wege zur Automatisierung der Niederschlagsermittlung*, 1984, ISBN 3-921694-55-8, *vergriffen*

56 Müller, Peter: *Transport und selektive Sedimentation von Schwebstoffen bei gestautem Abfluß*, 1985, ISBN 3-921694-56-6

57 El-Qawasmeh, Fuad: *Möglichkeiten und Grenzen der Tropfbewässerung unter besonderer Berücksichtigung der Verstopfungsanfälligkeit der Tropfelemente*, 1985, ISBN 3-921694-57-4, *vergriffen*

58 Kirchenbaur, Klaus: *Mikroprozessorgesteuerte Erfassung instationärer Druckfelder am Beispiel seegangsbelasteter Baukörper*, 1985, ISBN 3-921694-58-2

59 Kobus, Helmut (Hrsg.): *Modellierung des großräumigen Wärme- und Schadstofftransports im Grundwasser*, Tätigkeitsbericht 1984/85 (DFG-Forschergruppe an den Universitäten Hohenheim, Karlsruhe und Stuttgart), 1985, ISBN 3-921694-59-0, *vergriffen*

60 Spitz, Karlheinz: *Dispersion in porösen Medien: Einfluß von Inhomogenitäten und Dichteunterschieden*, 1985, ISBN 3-921694-60-4, *vergriffen*

61 Kobus, Helmut: *An Introduction to Air-Water Flows in Hydraulics*, 1985, ISBN 3-921694-61-2

62 Kaleris, Vassilios: *Erfassung des Austausches von Oberflächen- und Grundwasser in horizontalebenen Grundwassermodellen*, 1986, ISBN 3-921694-62-0

63 Herr, Michael: *Grundlagen der hydraulischen Sanierung verunreinigter Porengrundwasserleiter*, 1987, ISBN 3-921694-63-9

64 Marx, Walter: *Berechnung von Temperatur und Spannung in Massenbeton infolge Hydratation*, 1987, ISBN 3-921694-64-7

65 Koschitzky, Hans-Peter: *Dimensionierungskonzept für Sohlbelüfter in Schußrinnen zur Vermeidung von Kavitationsschäden*, 1987, ISBN 3-921694-65-5

66 Kobus, Helmut (Hrsg.): *Modellierung des großräumigen Wärme- und Schadstofftransports im Grundwasser*, Tätigkeitsbericht 1986/87 (DFG-Forschergruppe an den Universitäten Hohenheim, Karlsruhe und Stuttgart) 1987, ISBN 3-921694-66-3

67 Söll, Thomas: *Berechnungsverfahren zur Abschätzung anthropogener Temperaturanomalien im Grundwasser*, 1988, ISBN 3-921694-67-1

68 Dittrich, Andreas; Westrich, Bernd: *Bodenseeufererosion, Bestandsaufnahme und Bewertung*, 1988, ISBN 3-921694-68-X, *vergriffen*

69 Huwe, Bernd; van der Ploeg, Rienk R.: *Modelle zur Simulation des Stickstoffhaushaltes von Standorten mit unterschiedlicher landwirtschaftlicher Nutzung*, 1988, ISBN 3-921694-69-8, *vergriffen*

70 Stephan, Karl: *Integration elliptischer Funktionen*, 1988, ISBN 3-921694-70-1

71 Kobus, Helmut; Zilliox, Lothaire (Hrsg.): *Nitratbelastung des Grundwassers, Auswirkungen der Landwirtschaft auf die Grundwasser- und Rohwasserbeschaffenheit und Maßnahmen zum Schutz des Grundwassers*. Vorträge des deutsch-französischen Kolloquiums am 6. Oktober 1988, Universitäten Stuttgart und Louis Pasteur Strasbourg (Vorträge in deutsch oder französisch, Kurzfassungen zweisprachig), 1988, ISBN 3-921694-71-X

72 Soyeaux, Renald: *Unterströmung von Stauanlagen auf klüftigem Untergrund unter Berücksichtigung laminarer und turbulenter Fließzustände*,1991, ISBN 3-921694-72-8

73 Kohane, Roberto: *Berechnungsmethoden für Hochwasserabfluß in Fließgewässern mit überströmten Vorländern*, 1991, ISBN 3-921694-73-6

74 Hassinger, Reinhard: *Beitrag zur Hydraulik und Bemessung von Blocksteinrampen in flexibler Bauweise*, 1991, ISBN 3-921694-74-4, vergriffen

75 Schäfer, Gerhard: *Einfluß von Schichtenstrukturen und lokalen Einlagerungen auf die Längsdispersion in Porengrundwasserleitern*, 1991, ISBN 3-921694-75-2

76 Giesecke, Jürgen: *Vorträge, Wasserwirtschaft in stark besiedelten Regionen; Umweltforschung mit Schwerpunkt Wasserwirtschaft*, 1991, ISBN 3-921694-76-0

77 Huwe, Bernd: *Deterministische und stochastische Ansätze zur Modellierung des Stickstoffhaushalts landwirtschaftlich genutzter Flächen auf unterschiedlichem Skalenniveau*, 1992, ISBN 3-921694-77-9, vergriffen

78 Rommel, Michael: *Verwendung von Kluftdaten zur realitätsnahen Generierung von Kluftnetzen mit anschließender laminar-turbulenter Strömungsberechnung*, 1993, ISBN 3-92 1694-78-7

79 Marschall, Paul: *Die Ermittlung lokaler Stofffrachten im Grundwasser mit Hilfe von Einbohrloch-Meßverfahren*, 1993, ISBN 3-921694-79-5, vergriffen

80 Ptak, Thomas: *Stofftransport in heterogenen Porenaquiferen: Felduntersuchungen und stochastische Modellierung*, 1993, ISBN 3-921694-80-9, vergriffen

81 Haakh, Frieder: *Transientes Strömungsverhalten in Wirbelkammern,* 1993, ISBN 3-921694-81-7

82 Kobus, Helmut; Cirpka, Olaf; Barczewski, Baldur; Koschitzky, Hans-Peter: *Versuchseinrichtung zur Grundwasser und Altlastensanierung VEGAS, Konzeption und Programmrahmen*, 1993, ISBN 3-921694-82-5

83 Zang, Weidong: *Optimaler Echtzeit-Betrieb eines Speichers mit aktueller Abflußregenerierung*, 1994, ISBN 3-921694-83-3, vergriffen

84 Franke, Hans-Jörg: *Stochastische Modellierung eines flächenhaften Stoffeintrages und Transports in Grundwasser am Beispiel der Pflanzenschutzmittelproblematik*, 1995, ISBN 3-921694-84-1

85 Lang, Ulrich: *Simulation regionaler Strömungs- und Transportvorgänge in Karstaquiferen mit Hilfe des Doppelkontinuum-Ansatzes: Methodenentwicklung und Parameteridentifikation*, 1995, ISBN 3-921694-85-X, vergriffen

86 Helmig, Rainer: *Einführung in die Numerischen Methoden der Hydromechanik*, 1996, ISBN 3-921694-86-8, vergriffen

87 Cirpka, Olaf: *CONTRACT: A Numerical Tool for Contaminant Transport and Chemical Transformations - Theory and Program Documentation -*, 1996, ISBN 3-921694-87-6

88 Haberlandt, Uwe: *Stochastische Synthese und Regionalisierung des Niederschlages für Schmutzfrachtberechnungen*, 1996, ISBN 3-921694-88-4

89 Croisé, Jean: *Extraktion von flüchtigen Chemikalien aus natürlichen Lockergesteinen mittels erzwungener Luftströmung*, 1996, ISBN 3-921694-89-2, vergriffen

90 Jorde, Klaus: *Ökologisch begründete, dynamische Mindestwasserregelungen bei Ausleitungskraftwerken*, 1997, ISBN 3-921694-90-6, vergriffen

91 Helmig, Rainer: *Gekoppelte Strömungs- und Transportprozesse im Untergrund - Ein Beitrag zur Hydrosystemmodellierung-*, 1998, ISBN 3-921694-91-4, vergriffen

92 Emmert, Martin: *Numerische Modellierung nichtisothermer Gas-Wasser Systeme in porösen Medien,* 1997, ISBN 3-921694-92-2

93 Kern, Ulrich: *Transport von Schweb- und Schadstoffen in staugeregelten Fließgewässern am Beispiel des Neckars*, 1997, ISBN 3-921694-93-0, vergriffen

94 Förster, Georg: *Druckstoßdämpfung durch große Luftblasen in Hochpunkten von Rohrleitungen 1997*, ISBN 3-921694-94-9

95 Cirpka, Olaf: *Numerische Methoden zur Simulation des reaktiven Mehrkomponententransports im Grundwasser*, 1997, ISBN 3-921694-95-7, *vergriffen*

96 Färber, Arne: *Wärmetransport in der ungesättigten Bodenzone: Entwicklung einer thermischen In-situ-Sanierungstechnologie*, 1997, ISBN 3-921694-96-5

97 Betz, Christoph: *Wasserdampfdestillation von Schadstoffen im porösen Medium: Entwicklung einer thermischen In-situ-Sanierungstechnologie*, 1998, SBN 3-921694-97-3

98 Xu, Yichun: *Numerical Modeling of Suspended Sediment Transport in Rivers*, 1998, ISBN 3-921694-98-1, *vergriffen*

99 Wüst, Wolfgang: *Geochemische Untersuchungen zur Sanierung CKW-kontaminierter Aquifere mit Fe(0)-Reaktionswänden,* 2000, ISBN 3-933761-02-2

100 Sheta, Hussam: *Simulation von Mehrphasenvorgängen in porösen Medien unter Einbeziehung von Hysterese-Effekten*, 2000, ISBN 3-933761-03-4

101 Ayros, Edwin: *Regionalisierung extremer Abflüsse auf der Grundlage statistischer Verfahren*, 2000, ISBN 3-933761-04-2, *vergriffen*

102 Huber, Ralf: *Compositional Multiphase Flow and Transport in Heterogeneous Porous Media*, 2000, ISBN 3-933761-05-0

103 Braun, Christopherus: *Ein Upscaling-Verfahren für Mehrphasenströmungen in porösen Medien*, 2000, ISBN 3-933761-06-9

104 Hofmann, Bernd: *Entwicklung eines rechnergestützten Managementsystems zur Beurteilung von Grundwasserschadensfällen*, 2000, ISBN 3-933761-07-7

105 Class, Holger: *Theorie und numerische Modellierung nichtisothermer Mehrphasenprozesse in NAPL-kontaminierten porösen Medien,* 2001, ISBN 3-933761-08-5

106 Schmidt, Reinhard: *Wasserdampf- und Heißluftinjektion zur thermischen Sanierung kontaminierter Standorte*, 2001, ISBN 3-933761-09-3

107 Josef, Reinhold:, *Schadstoffextraktion mit hydraulischen Sanierungsverfahren unter Anwendung von grenzflächenaktiven Stoffen*, 2001, ISBN 3-933761-10-7

108 Schneider, Matthias: *Habitat- und Abflussmodellierung für Fließgewässer mit unscharfen Berechnungsansätzen*, 2001, ISBN 3-933761-11-5

109 Rathgeb, Andreas: *Hydrodynamische Bemessungsgrundlagen für Lockerdeckwerke an überströmbaren Erddämmen*, 2001, ISBN 3-933761-12-3

110 Lang, Stefan: *Parallele numerische Simulation instätionärer Probleme mit adaptiven Methoden auf unstrukturierten Gittern*, 2001, ISBN 3-933761-13-1

111 Appt, Jochen; Stumpp Simone: *Die Bodensee-Messkampagne 2001, IWS/CWR Lake Constance Measurement Program 2001*, 2002, ISBN 3-933761-14-X

112 Heimerl, Stephan: *Systematische Beurteilung von Wasserkraftprojekten,* 2002, ISBN 3-933761-15-8, *vergriffen*

113 Iqbal, Amin: *On the Management and Salinity Control of Drip Irrigation,* 2002, ISBN 3-933761-16-6

114 Silberhorn-Hemminger, Annette: *Modellierung von Kluftaquifersystemen: Geostatistische Analyse und deterministisch-stochastische Kluftgenerierung,* 2002, ISBN 3-933761-17-4

115 Winkler, Angela: *Prozesse des Wärme- und Stofftransports bei der In-situ-Sanierung mit festen Wärmequellen,* 2003, ISBN 3-933761-18-2

116 Marx, Walter: *Wasserkraft, Bewässerung, Umwelt - Planungs- und Bewertungsschwerpunkte der Wasserbewirtschaftung,* 2003, ISBN 3-933761-19-0

117 Hinkelmann, Reinhard: *Efficient Numerical Methods and Information-Processing Techniques in Environment Water,* 2003, ISBN 3-933761-20-4

118 Samaniego-Eguiguren, Luis Eduardo: *Hydrological Consequences of Land Use / Land Cover and Climatic Changes in Mesoscale Catchments*, 2003, ISBN 3-933761-21-2

119 Neunhäuserer, Lina: *Diskretisierungsansätze zur Modellierung von Strömungs- und Transportprozessen in geklüftet-porösen Medien*, 2003, ISBN 3-933761-22-0

120 Paul, Maren: *Simulation of Two-Phase Flow in Heterogeneous Poros Media with Adaptive Methods*, 2003, ISBN 3-933761-23-9

121 Ehret, Uwe: *Rainfall and Flood Nowcasting in Small Catchments using Weather Radar*, 2003, ISBN 3-933761-24-7

122 Haag, Ingo: *Der Sauerstoffhaushalt staugeregelter Flüsse am Beispiel des Neckars - Analysen, Experimente, Simulationen -,* 2003, ISBN 3-933761-25-5

123 Appt, Jochen: *Analysis of Basin-Scale Internal Waves in Upper Lake Constance,* 2003, ISBN 3-933761-26-3

124 Hrsg.: Schrenk, Volker; Batereau, Katrin; Barczewski, Baldur; Weber, Karolin und Koschitzky, Hans-Peter: *Symposium Ressource Fläche und VEGAS - Statuskolloquium 2003, 30. September und 1. Oktober 2003,* 2003, ISBN 3-933761-27-1

125 Omar Khalil Ouda: *Optimisation of Agricultural Water Use: A Decision Support System for the Gaza Strip,* 2003, ISBN 3-933761-28-0

126 Batereau, Katrin: *Sensorbasierte Bodenluftmessung zur Vor-Ort-Erkundung von Schadensherden im Untergrund*, 2004, ISBN 3-933761-29-8

127 Witt, Oliver: *Erosionsstabilität von Gewässersedimenten mit Auswirkung auf den Stofftransport bei Hochwasser am Beispiel ausgewählter Stauhaltungen des Oberrheins*, 2004, ISBN 3-933761-30-1

128 Jakobs, Hartmut: *Simulation nicht-isothermer Gas-Wasser-Prozesse in komplexen Kluft-Matrix-Systemen*, 2004, ISBN 3-933761-31-X

129 Li, Chen-Chien: *Deterministisch-stochastisches Berechnungskonzept zur Beurteilung der Auswirkungen erosiver Hochwasserereignisse in Flussstauhaltungen,* 2004, ISBN 3-933761-32-8

130 Reichenberger, Volker; Helmig, Rainer; Jakobs, Hartmut; Bastian, Peter; Niessner, Jennifer: *Complex Gas-Water Processes in Discrete Fracture-Matrix Systems: Up-scaling, Mass-Conservative Discretization and Efficient Multilevel Solution,* 2004, ISBN 3-933761-33-6

131 Hrsg.: Barczewski, Baldur; Koschitzky, Hans-Peter; Weber, Karolin; Wege, Ralf: *VEGAS - Statuskolloquium 2004,* Tagungsband zur Veranstaltung am 05. Oktober 2004 an der Universität Stuttgart, Campus Stuttgart-Vaihingen, 2004, ISBN 3-933761-34-4

132 Asie, Kemal Jabir: *Finite Volume Models for Multiphase Multicomponent Flow through Porous Media*. 2005, ISBN 3-933761-35-2

133 Jacoub, George: *Development of a 2-D Numerical Module for Particulate Contaminant Transport in Flood Retention Reservoirs and Impounded Rivers,* 2004, ISBN 3-933761-36-0

134 Nowak, Wolfgang: *Geostatistical Methods for the Identification of Flow and Transport Parameters in the Subsurface,* 2005, ISBN 3-933761-37-9

135 Süß, Mia: *Analysis of the influence of structures and boundaries on flow and transport processes in fractured porous media*, 2005, ISBN 3-933761-38-7

136 Jose, Surabhin Chackiath: *Experimental Investigations on Longitudinal Dispersive Mixing in Heterogeneous Aquifers,* 2005, ISBN: 3-933761-39-5

137 Filiz, Fulya: *Linking Large-Scale Meteorological Conditions to Floods in Mesoscale Catchments,* 2005, ISBN 3-933761-40-9

138 Qin, Minghao: *Wirklichkeitsnahe und recheneffiziente Ermittlung von Temperatur und Spannungen bei großen RCC-Staumauern*, 2005, ISBN 3-933761-41-7

139 Kobayashi, Kenichiro: *Optimization Methods for Multiphase Systems in the Subsurface - Application to Methane Migration in Coal Mining Areas*, 2005, ISBN 3-933761-42-5

140 Rahman, Md. Arifur: *Experimental Investigations on Transverse Dispersive Mixing in Heterogeneous Porous Media,* 2005, ISBN 3-933761-43-3

141 Schrenk, Volker: *Ökobilanzen zur Bewertung von Altlastensanierungsmaßnahmen,* 2005, ISBN 3-933761-44-1

142 Hundecha, Hirpa Yeshewatesfa: *Regionalization of Parameters of a Conceptual Rainfall-Runoff Model*, 2005, ISBN: 3-933761-45-X

143 Wege, Ralf: *Untersuchungs- und Überwachungsmethoden für die Beurteilung natürlicher Selbstreinigungsprozesse im Grundwasser,* 2005, ISBN 3-933761-46-8

144 Breiting, Thomas: *Techniken und Methoden der Hydroinformatik - Modellierung von komplexen Hydrosystemen im Untergrund*, 2006, ISBN 3-933761-47-6

145 Hrsg.: Braun, Jürgen; Koschitzky, Hans-Peter; Müller, Martin: *Ressource Untergrund: 10 Jahre VEGAS: Forschung und Technologieentwicklung zum Schutz von Grundwasser und Boden,* Tagungsband zur Veranstaltung am 28. und 29. September 2005 an der Universität Stuttgart, Campus Stuttgart-Vaihingen, 2005, ISBN 3-933761-48-4

146 Rojanschi, Vlad: *Abflusskonzentration in mesoskaligen Einzugsgebieten unter Berücksichtigung des Sickerraumes,* 2006, ISBN 3-933761-49-2

147 Winkler, Nina Simone: *Optimierung der Steuerung von Hochwasserrückhaltebeckensystemen,* 2006, ISBN 3-933761-50-6

148 Wolf, Jens: *Räumlich differenzierte Modellierung der Grundwasserströmung alluvialer Aquifere für mesoskalige Einzugsgebiete*, 2006, ISBN: 3-933761-51-4

149 Kohler, Beate: *Externe Effekte der Laufwasserkraftnutzung*, 2006, ISBN 3-933761-52-2

150 Hrsg.: Braun, Jürgen; Koschitzky, Hans-Peter; Stuhrmann, Matthias: *VEGAS-Statuskolloquium 2006,* Tagungsband zur Veranstaltung am 28. September 2006 an der Universität Stuttgart, Campus Stuttgart-Vaihingen, 2006, ISBN 3-933761-53-0

151 Niessner, Jennifer: *Multi-Scale Modeling of Multi-Phase - Multi-Component Processes in Heterogeneous Porous Media*, 2006, ISBN 3-933761-54-9

152 Fischer, Markus: *Beanspruchung eingeerdeter Rohrleitungen infolge Austrocknung bindiger Böden,* 2006, ISBN 3-933761-55-7

153 Schneck, Alexander: *Optimierung der Grundwasserbewirtschaftung unter Berücksichtigung der Belange der Wasserversorgung, der Landwirtschaft und des Naturschutzes*, 2006, ISBN 3-933761-56-5

154 Das, Tapash: *The Impact of Spatial Variability of Precipitation on the Predictive Uncertainty of Hydrological Models,* 2006, ISBN 3-33761-57-3

155 Bielinski, Andreas: *Numerical Simulation of CO_2 sequestration in geological formations*, 2007, ISBN 3-933761-58-1

156 Mödinger, Jens: *Entwicklung eines Bewertungs- und Entscheidungsunterstützungssystems für eine nachhaltige regionale Grundwasserbewirtschaftung*, 2006, ISBN 3-933761-60-3

157 Manthey, Sabine: *Two-phase flow processes with dynamic effects in porous media - parameter estimation and simulation,* 2007, ISBN 3-933761-61-1

158 Pozos Estrada, Oscar: *Investigation on the Effects of Entrained Air in Pipelines,* 2007, ISBN 3-933761-62-X

159 Ochs, Steffen Oliver: *Steam injection into saturated porous media – process analysis including experimental and numerical investigations*, 2007, ISBN 3-933761-63-8

160 Marx, Andreas: *Einsatz gekoppelter Modelle und Wetterradar zur Abschätzung von Niederschlagsintensitäten und zur Abflussvorhersage, 2007,* ISBN 3-933761-64-6

161 Hartmann, Gabriele Maria: *Investigation of Evapotranspiration Concepts in Hydrological Modelling for Climate Change Impact Assessment*, 2007, ISBN 3-933761-65-4

162 Kebede Gurmessa, Tesfaye: *Numerical Investigation on Flow and Transport Characteristics to Improve Long-Term Simulation of Reservoir Sedimentation*, 2007, ISBN 3-933761-66-2

163 Trifković, Aleksandar: *Multi-objective and Risk-based Modelling Methodology for Planning, Design and Operation of Water Supply Systems*, 2007, ISBN 3-933761-67-0

164 Götzinger, Jens: *Distributed Conceptual Hydrological Modelling - Simulation of Climate, Land Use Change Impact and Uncertainty Analysis*, 2007, ISBN 3-933761-68-9

165 Hrsg.: Braun, Jürgen; Koschitzky, Hans-Peter; Stuhrmann, Matthias: *VEGAS – Kolloquium 2007,* Tagungsband zur Veranstaltung am 26. September 2007 an der Universität Stuttgart, Campus Stuttgart-Vaihingen, 2007, ISBN 3-933761-69-7

166 Freeman, Beau: *Modernization Criteria Assessment for Water Resources Planning; Klamath Irrigation Project, U.S.*, 2008, ISBN 3-933761-70-0

167 Dreher, Thomas: *Selektive Sedimentation von Feinstschwebstoffen in Wechselwirkung mit wandnahen turbulenten Strömungsbedingungen*, 2008, ISBN 3-933761-71-9

168 Yang, Wei: *Discrete-Continuous Downscaling Model for Generating Daily Precipitation Time Series*, 2008, ISBN 3-933761-72-7

169 Kopecki, Ianina: *Calculational Approach to FST-Hemispheres for Multiparametrical Benthos Habitat Modelling,* 2008*,* ISBN 3-933761-73-5

170 Brommundt, Jürgen: *Stochastische Generierung räumlich zusammenhängender Niederschlagszeitreihen*, 2008, ISBN 3-933761-74-3

171 Papafotiou, *Alexandros: Numerical Investigations of the Role of Hysteresis in Heterogeneous Two-Phase Flow Systems*, 2008, ISBN 3-933761-75-1

172 He, Yi: *Application of a Non-Parametric Classification Scheme to Catchment Hydrology*, 2008, ISBN 978-3-933761-76-7

173 Wagner, Sven: *Water Balance in a Poorly Gauged Basin in West Africa Using Atmospheric Modelling and Remote Sensing Information*, 2008, ISBN 978-3-933761-77-4

174 Hrsg.: Braun, Jürgen; Koschitzky, Hans-Peter; Stuhrmann, Matthias; Schrenk, Volker: *VEGAS-Kolloquium 2008 Ressource Fläche III*, Tagungsband zur Veranstaltung am 01. Oktober 2008 an der Universität Stuttgart, Campus Stuttgart-Vaihingen, 2008, ISBN 978-3-933761-78-1

175 Patil, Sachin: *Regionalization of an Event Based Nash Cascade Model for Flood Predictions in Ungauged Basins*, 2008, ISBN 978-3-933761-79-8

176 Assteerawatt, Anongnart: *Flow and Transport Modelling of Fractured Aquifers based on a Geostatistical Approach,* 2008, ISBN 978-3-933761-80-4

177 Karnahl, Joachim Alexander: *2D numerische Modellierung von multifraktionalem Schwebstoff- und Schadstofftransport in Flüssen*, 2008, ISBN 978-3-933761-81-1

178 Hiester, Uwe: *Technologieentwicklung zur In-situ-Sanierung der ungesättigten Bodenzone mit festen Wärmequellen,* 2009, ISBN 978-3-933761-82-8

179 Laux, Patrick: *Statistical Modeling of Precipitation for Agricultural Planning in the Volta Basin of West Africa,* 2009, ISBN 978-3-933761-83-5

180 Ehsan, Saqib: *Evaluation of Life Safety Risks Related to Severe Flooding,* 2009, ISBN 978-3-933761-84-2

181 Prohaska, Sandra: *Development and Application of a 1D Multi-Strip Fine Sediment Transport Model for Regulated Rivers,* 2009, ISBN 978-3-933761-85-9

182 Kopp, Andreas: *Evaluation of CO_2 Injection Processes in Geological Formations for Site Screening,* 2009, ISBN 978-3-933761-86-6

183 Ebigbo, Anozie: *Modelling of biofilm growth and its influence on CO_2 and water (two-phase) flow in porous media,* 2009, ISBN 978-3-933761-87-3

184 Freiboth, Sandra: *A phenomenological model for the numerical simulation of multiphase multicomponent processes considering structural alterations of porous media*, 2009, ISBN 978-3-933761-88-0

185 Zöllner, Frank: *Implementierung und Anwendung netzfreier Methoden im Konstruktiven Wasserbau und in der Hydromechanik*, 2009, ISBN 978-3-933761-89-7

186 Vasin, Milos: *Influence of the soil structure and property contrast on flow and transport in the unsaturated zone*, 2010, ISBN 978-3-933761-90-3

187 Li, Jing: *Application of Copulas as a New Geostatistical Tool*, 2010, ISBN 978-3-933761-91-0

188 AghaKouchak, Amir: *Simulation of Remotely Sensed Rainfall Fields Using Copulas*, 2010, ISBN 978-3-933761-92-7

189 Thapa, Pawan Kumar: *Physically-based spatially distributed rainfall runoff modelling for soil erosion estimation*, 2010, ISBN 978-3-933761-93-4

190 Wurms, Sven: *Numerische Modellierung der Sedimentationsprozesse in Retentionsanlagen zur Steuerung von Stoffströmen bei extremen Hochwasserabflussereignissen*, 2011, ISBN 978-3-933761-94-1

191 Merkel, Uwe: *Unsicherheitsanalyse hydraulischer Einwirkungen auf Hochwasserschutzdeiche und Steigerung der Leistungsfähigkeit durch adaptive Strömungsmodellierung*, 2011, ISBN 978-3-933761-95-8

192 Fritz, Jochen: *A Decoupled Model for Compositional Non-Isothermal Multiphase Flow in Porous Media and Multiphysics Approaches for Two-Phase Flow*, 2010, ISBN 978-3-933761-96-5

193 Weber, Karolin (Hrsg.): *12. Treffen junger WissenschaftlerInnen an Wasserbauinstituten*, 2010, ISBN 978-3-933761-97-2

194 Bliefernicht, Jan-Geert: *Probability Forecasts of Daily Areal Precipitation for Small River Basins,* 2011, ISBN 978-3-933761-98-9

195 Hrsg.: Koschitzky, Hans-Peter; Braun, Jürgen: *VEGAS-Kolloquium 2010 In-situ-Sanierung - Stand und Entwicklung Nano und ISCO -,* Tagungsband zur Veranstaltung am 07. Oktober 2010 an der Universität Stuttgart, Campus Stuttgart-Vaihingen*,* 2010*,* ISBN 978-3-933761-99-6

196 Gafurov, Abror: *Water Balance Modeling Using Remote Sensing Information - Focus on Central Asia,* 2010, ISBN 978-3-942036-00-9

197 Mackenberg, Sylvia: *Die Quellstärke in der Sickerwasserprognose: Möglichkeiten und Grenzen von Labor- und Freilanduntersuchungen,* 2010, ISBN 978-3-942036-01-6

198 Singh, Shailesh Kumar: *Robust Parameter Estimation in Gauged and Ungauged Basins,* 2010, ISBN 978-3-942036-02-3

199 Doğan, Mehmet Onur: *Coupling of porous media flow with pipe flow,* 2011, ISBN 978-3-942036-03-0

200 Liu, Min: *Study of Topographic Effects on Hydrological Patterns and the Implication on Hydrological Modeling and Data Interpolation,* 2011, ISBN 978-3-942036-04-7

201 Geleta, Habtamu Itefa: *Watershed Sediment Yield Modeling for Data Scarce Areas,* 2011, ISBN 978-3-942036-05-4

202 Franke, Jörg: *Einfluss der Überwachung auf die Versagenswahrscheinlichkeit von Staustufen,* 2011, ISBN 978-3-942036-06-1

203 Bakimchandra, Oinam: *Integrated Fuzzy-GIS approach for assessing regional soil erosion risks,* 2011, ISBN 978-3-942036-07-8

204 Alam, Muhammad Mahboob: *Statistical Downscaling of Extremes of Precipitation in Mesoscale Catchments from Different RCMs and Their Effects on Local Hydrology,* 2011, ISBN 978-3-942036-08-5

205 Hrsg.: Koschitzky, Hans-Peter; Braun, Jürgen: *VEGAS-Kolloquium 2011 Flache Geothermie - Perspektiven und Risiken,* Tagungsband zur Veranstaltung am 06. Oktober 2011 an der Universität Stuttgart, Campus Stuttgart-Vaihingen*,* 2011*,* ISBN 978-3-933761-09-2

206 Haslauer, Claus: *Analysis of Real-World Spatial Dependence of Subsurface Hydraulic Properties Using Copulas with a Focus on Solute Transport Behaviour,* 2011, ISBN 978-3-942036-10-8

207 Dung, Nguyen Viet: *Multi-objective automatic calibration of hydrodynamic models – development of the concept and an application in the Mekong Delta,* 2011, ISBN 978-3-942036-11-5

208 Hung, Nguyen Nghia: *Sediment dynamics in the floodplain of the Mekong Delta, Vietnam,* 2011, ISBN 978-3-942036-12-2

209 Kuhlmann, Anna: *Influence of soil structure and root water uptake on flow in the unsaturated zone,* 2012, ISBN 978-3-942036-13-9

210 Tuhtan, Jeffrey Andrew: *Including the Second Law Inequality in Aquatic Ecodynamics: A Modeling Approach for Alpine Rivers Impacted by Hydropeaking,* 2012, ISBN 978-3-942036-14-6

211 Tolossa, Habtamu: *Sediment Transport Computation Using a Data-Driven Adaptive Neuro-Fuzzy Modelling Approach,* 2012, ISBN 978-3-942036-15-3

212 Tatomir, Alexandru-Bodgan: *From Discrete to Continuum Concepts of Flow in Fractured Porous Media,* 2012, ISBN 978-3-942036-16-0

213 Erbertseder, Karin: *A Multi-Scale Model for Describing Cancer-Therapeutic Transport in the Human Lung,* 2012, ISBN 978-3-942036-17-7

214 Noack, Markus: *Modelling Approach for Interstitial Sediment Dynamics and Reproduction of Gravel Spawning Fish,* 2012, ISBN 978-3-942036-18-4

215 De Boer, Cjestmir Volkert: *Transport of Nano Sized Zero Valent Iron Colloids during Injection into the Subsurface*, 2012, ISBN 978-3-942036-19-1

216 Pfaff, Thomas: *Processing and Analysis of Weather Radar Data for Use in Hydrology*, 2013, ISBN 978-3-942036-20-7

217 Lebrenz, Hans-Henning: *Addressing the Input Uncertainty for Hydrological Modeling by a New Geostatistical Method*, 2013, ISBN 978-3-942036-21-4

218 Darcis, Melanie Yvonne: *Coupling Models of Different Complexity for the Simulation of CO_2 Storage in Deep Saline Aquifers*, 2013, ISBN 978-3-942036-22-1

219 Beck, Ferdinand: *Generation of Spatially Correlated Synthetic Rainfall Time Series in High Temporal Resolution - A Data Driven Approach*, 2013, ISBN 978-3-942036-23-8

220 Guthke, Philipp: *Non-multi-Gaussian spatial structures: Process-driven natural genesis, manifestation, modeling approaches, and influences on dependent processes*, 2013, ISBN 978-3-942036-24-5

221 Walter, Lena: *Uncertainty studies and risk assessment for CO_2 storage in geological formations*, 2013, ISBN 978-3-942036-25-2

222 Wolff, Markus: *Multi-scale modeling of two-phase flow in porous media including capillary pressure effects,* 2013, ISBN 978-3-942036-26-9

223 Mosthaf, Klaus Roland: *Modeling and analysis of coupled porous-medium and free flow with application to evaporation processes,* 2014, ISBN 978-3-942036-27-6

224 Leube, Philipp Christoph: *Methods for Physically-Based Model Reduction in Time: Analysis, Comparison of Methods and Application*, 2013, ISBN 978-3-942036-28-3

225 Rodríguez Fernández, Jhan Ignacio: *High Order Interactions among environmental variables: Diagnostics and initial steps towards modeling*, 2013, ISBN 978-3-942036-29-0

226 Eder, Maria Magdalena: *Climate Sensitivity of a Large Lake*, 2013, ISBN 978-3-942036-30-6

227 Greiner, Philipp: *Alkoholinjektion zur In-situ-Sanierung von CKW Schadensherden in Grundwasserleitern: Charakterisierung der relevanten Prozesse auf unterschiedlichen Skalen*, 2014, ISBN 978-3-942036-31-3

228 Lauser, Andreas: *Theory and Numerical Applications of Compositional Multi-Phase Flow in Porous Media*, 2014, ISBN 978-3-942036-32-0

229 Enzenhöfer, Rainer: *Risk Quantification and Management in Water Production and Supply Systems*, 2014, ISBN 978-3-942036-33-7

230 Faigle, Benjamin: *Adaptive modelling of compositional multi-phase flow with capillary pressure*, 2014, ISBN 978-3-942036-34-4

231 Oladyshkin, Sergey: *Efficient modeling of environmental systems in the face of complexity and uncertainty*, 2014, ISBN 978-3-942036-35-1

232 Sugimoto, Takayuki: *Copula based Stochastic Analysis of Discharge Time Series*, 2014, ISBN 978-3-942036-36-8

233 Koch, Jonas: *Simulation, Identification and Characterization of Contaminant Source Architectures in the Subsurface*, 2014, ISBN 978-3-942036-37-5

234 Zhang, Jin: *Investigations on Urban River Regulation and Ecological Rehabilitation Measures, Case of Shenzhen in China*, 2014, ISBN 978-3-942036-38-2

235 Siebel, Rüdiger: *Experimentelle Untersuchungen zur hydrodynamischen Belastung und Standsicherheit von Deckwerken an überströmbaren Erddämmen,* 2014, ISBN 978-3-942036-39-9

236 Baber, Katherina: *Coupling free flow and flow in porous media in biological and technical applications: From a simple to a complex interface description,* 2014, ISBN 978-3-942036-40-5

237 Nuske, Klaus Philipp: *Beyond Local Equilibrium — Relaxing local equilibrium assumptions in multiphase flow in porous media,* 2014, ISBN 978-3-942036-41-2

238 Geiges, Andreas: *Efficient concepts for optimal experimental design in nonlinear environmental systems*, 2014, ISBN 978-3-942036-42-9

239 Schwenck, Nicolas: *An XFEM-Based Model for Fluid Flow in Fractured Porous Media*, 2014, ISBN 978-3-942036-43-6

240 Chamorro Chávez, Alejandro: *Stochastic and hydrological modelling for climate change prediction in the Lima region, Peru*, 2015, ISBN 978-3-942036-44-3

241 Yulizar: *Investigation of Changes in Hydro-Meteorological Time Series Using a Depth-Based Approach*, 2015, ISBN 978-3-942036-45-0

242 Kretschmer, Nicole: *Impacts of the existing water allocation scheme on the Limarí watershed – Chile, an integrative approach*, 2015, ISBN 978-3-942036-46-7

243 Kramer, Matthias: *Luftbedarf von Freistrahlturbinen im Gegendruckbetrieb*, 2015, ISBN 978-3-942036-47-4

244 Hommel, Johannes: *Modeling biogeochemical and mass transport processes in the subsurface: Investigation of microbially induced calcite precipitation*, 2016, ISBN 978-3-942036-48-1

245 Germer, Kai: *Wasserinfiltration in die ungesättigte Zone eines makroporösen Hanges und deren Einfluss auf die Hangstabilität*, 2016, ISBN 978-3-942036-49-8

246 Hörning, Sebastian: *Process-oriented modeling of spatial random fields using copulas*, 2016, ISBN 978-3-942036-50-4

247 Jambhekar, Vishal: *Numerical modeling and analysis of evaporative salinization in a coupled free-flow porous-media system,* 2016, ISBN 978-3-942036-51-1

248 Huang, Yingchun: *Study on the spatial and temporal transferability of conceptual hydrological models*, 2016, ISBN 978-3-942036-52-8

249 Kleinknecht, Simon Matthias: *Migration and retention of a heavy NAPL vapor and remediation of the unsaturated zone*, 2016, ISBN 978-3-942036-53-5

250 Kwakye, Stephen Oppong: *Study on the effects of climate change on the hydrology of the West African sub-region*, 2016, ISBN 978-3-942036-54-2

251 Kissinger, Alexander: *Basin-Scale Site Screening and Investigation of Possible Impacts of CO_2 Storage on Subsurface Hydrosystems*, 2016, ISBN 978-3-942036-55-9

252 Müller, Thomas: *Generation of a Realistic Temporal Structure of Synthetic Precipitation Time Series for Sewer Applications*, 2017, ISBN 978-3-942036-56-6

253 Grüninger, Christoph: *Numerical Coupling of Navier-Stokes and Darcy Flow for Soil-Water Evaporation*, 2017, ISBN 978-3-942036-57-3

254 Suroso: *Asymmetric Dependence Based Spatial Copula Models: Empirical Investigations and Consequences on Precipitation Fields*, 2017, ISBN 978-3-942036-58-0

255 Müller, Thomas; Mosthaf, Tobias; Gunzenhauser, Sarah; Seidel, Jochen; Bárdossy, András: *Grundlagenbericht Niederschlags-Simulator (NiedSim3)*, 2017, ISBN 978-3-942036-59-7

256 Mosthaf, Tobias: *New Concepts for Regionalizing Temporal Distributions of Precipitation and for its Application in Spatial Rainfall Simulation,* 2017, ISBN 978-3-942036-60-3

257 Fenrich, Eva Katrin: *Entwicklung eines ökologisch-ökonomischen Vernetzungsmodells für Wasserkraftanlagen und Mehrzweckspeicher,* 2018, ISBN 978-3-942036-61-0

258 Schmidt, Holger: *Microbial stabilization of lotic fine sediments*, 2018, ISBN 978-3-942036-62-7

259 Fetzer, Thomas: *Coupled Free and Porous-Medium Flow Processes Affected by Turbulence and Roughness – Models, Concepts and Analysis*, 2018, ISBN 978-3-942036-63-4

Die Mitteilungshefte ab der Nr. 134 (Jg. 2005) stehen als pdf-Datei über die Homepage des Instituts: www.iws.uni-stuttgart.de zur Verfügung.